Rutherford
Appleton
Laboratory

RAL-85-110
Volume III

Proceedings of the Eighth Meeting of the International Collaboration
on Advanced Neutron Sources 8 — 12 July 1985

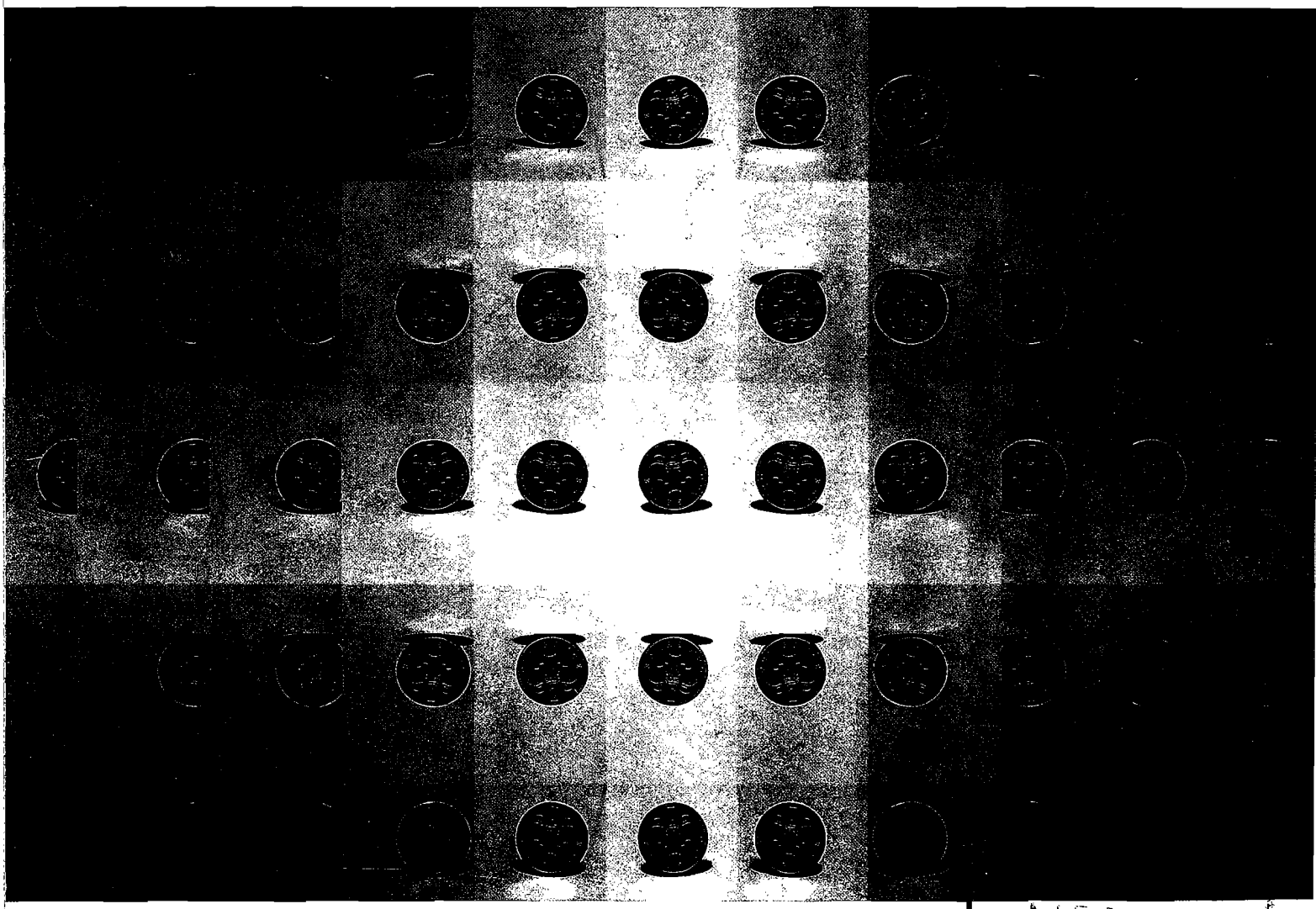

ICANS - VIII

Volume III
Neutron-scattering techniques

RAL-85-110

ICANS-VIII

Proceedings of the Eighth Meeting of the International Collaboration on Advanced Neutron Sources

8-12 July 1985

VOLUME III

Neutron-scattering techniques

Rutherford Appleton Laboratory
Chilton
DIDCOT
Oxfordshire

November 1985

Cover: Kaleidoscopic view along a neutron guide tube section (see page 771)

PREFACE

The eighth meeting of the International Collaboration on Advanced Neutron Sources was hosted by the Rutherford Appleton Laboratory and held at Keble College Oxford, from the 8th to 12th July 1985. The timing, and venue in the UK, were particularly appropriate in view of the contemporaneous start-up of RAL's spallation neutron source.

Following the traditional cycle of programming, ICANS-VIII concentrated on target and moderator systems for accelerator-based sources, and on neutron-scattering instrumentation. Continuing the trend of recent meetings, there was an increasing emphasis on data and results from operating facilities, but amidst the success stories came the announcement of the demise of the SNQ project. The achievements of the Jülich team have been quite remarkable, and other ICANS laboratories will continue to benefit from their work for many years to come.

The meeting also noted with regret the recent passing of Rex Fluharty, formerly of Los Alamos. Rex had been involved with ICANS since its inception, and with his breadth of experience had been a stalwart of the Collaboration, and a valued colleague at numerous international meetings and workshops.

These ICANS-VIII proceedings follow a familiar format, opening with status reports from the participating laboratories. The presentation of subsequent papers adheres more or less to the organisation of the meeting; there has been minimal editing of individual papers in order to facilitate reproduction procedures. Two *ad hoc* workshop sessions held during the meeting, on "Boosters and Delayed Neutrons" and "The Second User Revolution" led by John Carpenter and Peter Egelstaff respectively, have not been recorded here. These sessions highlighted two important issues facing the neutron-scattering community at this time. With many of the new generation sources now becoming operational alongside the more conventional reactor sources, it is timely to ask how we proceed towards the next generation of advanced facilities, while at the same time reappraising the optimal means of exploiting their potential. It was appropriate that the present meeting chose to address these problems, which are certain to feature even more prominantly in future ICANS programmes.

GEORGE C STIRLING
Rutherford Appleton Laboratory
November 1985

Eighth Meeting of the International Collaboration on Advanced Neutron Sources (ICANS-VIII), Oxford, 8-12 July 1985

REGISTERED PARTICIPANTS

B Alefeld	Jülich	M Kohgi	Tohoku
C Andreani	Rome	J Laakmann	Jülich
T W Armstrong	La Jolla	A J Leadbetter	RAL
F Atchison	SIN	G Manning	RAL
J R J Bennett	RAL	F A Morse	LANL
S Biggin	Bristol	R O Nelson	LANL
D E Bohringer	ANL	K Neumann	IKE Stuttgart
T A Broome	RAL	R J Newport	RAL
F Brumwell	ANL	T G Perring	Cambridge
C J Carlile	RAL	G E Ostrowski	ANL
J M Carpenter	ANL	M Paoli	Oxford
B G Chidley	CRNL	J Penfold	RAL
F Cilloco	Frascati	C Petrillo	Perugia
P Cloth	Jülich	D J Picton	Birmingham
H Conrad	Jülich	B H Poulten	RAL
R Cywinski	RAL	V T Pugh	RAL
W I F David	RAL	A V Rauchas	ANL
M Davidovic	Vinca	R A Robinson	LANL
V Drüke	Jülich	H Robinson	LANL
P A Egelstaff	Guelph	G J Russell	LANL
D Filges	Jülich	F Sacchetti	Perugia
W E Fischer	SIN	A W Schulke Jr	ANL
J B Forsyth	RAL	P A Seeger	LANL
R Geick	Würzburg	R N Silver	LANL
P S Goyal	BARC Bombay	H Stechemesser	Jülich
D A Gray	RAL	H Stiller	Jülich
R K Heenan	RAL	G C Stirling	RAL
A W Hewat	ILL	Y Takeda	SIN
W S Howells	RAL	A D Taylor	RAL
Y Ishikawa	Tohoku	I M Thorson	TRIUMF
M W Johnson	RAL	Ch Tschalär	SIN
T J L Jones	RAL	H Tietze	Würzburg
M Kimura	Sendai	R C Ward	RAL
W Kley	JRC Ispra	W G Williams	RAL
K J Knowles	RAL	C G Windsor	AERE
A Kollmar	Jülich	H Wroe	RAL

TABLE OF CONTENTS

VOLUME 1

STATUS REPORTS, NEW CONCEPTS

TARGET SYSTEMS

VOLUME III

SHIELDING, BEAM DEFINITION

CHOPPER SYSTEMS

DETECTORS

DATA ACQUISITION

ANCILLARY DEVICES AND EQUIPMENT

Proceedings of the Eighth Meeting of the International Collaboration on Advanced Neutron Sources (ICANS-VIII)
8-12 July 1985, Rutherford Appleton Laboratory Report RAL-85-110

The Degradation of a Pulsed Neutron Beam by Inelastically Scattering Collimators.

Colin G. Windsor

Materials Physics and Metallurgy Division, B 418 AERE Harwell , OX11 0RA.

Summary. Pulsed neutron beams for neutron scattering experiments are degraded by scattering from the collimators used to define the beam. A simple analytic theory including down-scattering from the collimators is used to estimate the beam-born background from the circular iris collimators usually employed. The results are used to give guidelines for the practical design of collimators.

1. Introduction

The dominant contribution to the neutron scattering background in most neutron scattering experiments comes from neutrons within the instruments's own beam. Some of the possible contributions to this are listed in figure 1. A simple collimator is assumed consisting of circular irises in a cylindrical tube. Consider some of the contributions to the background measured at the point P, just outside the geometric penumbra of the beam.

(i) The transmitted background is the term frequently calculated. These are the neutrons which have not suffered sattering so that their energy is not degraded from that calculated simply from their time of flight.

(ii) The primary scattered background has been intensively studied by algebraic and Monte Carlo methods (1,2). However, a vital feature often neglected is that the scattering processes are inelastic. For higher energy neutrons, the tendency is for down-scattering, so that the scattered velocity v_1 is less then the incident velocity v_0. A neutron arriving at a flight time corresponding to a direct velocity v_d may therefore have left the moderator at a higher or lower neutron energy depending on whether the scattering collimator was nearer the source, or nearer the sample.

(iii) Higher order contributions can arise from neutrons scattered successively from two surfaces, from scattering from one surface followed by transmission through an iris, and so on.

The primary scattered contribution (ii) is the object of special study in this paper. To make analytic progress, the scattering collimator is assumed to be several scattering lengths thick so that its surface can be considered as a moderator.

2. The inelastic scattering from a single collimator ring.

Figure 2 illustrates the simple geometry to which the inelastic theory is applied. A point moderator M emits neutrons with a slowing down spectral flux as a function of wavelength λ given by (3)

$$n_0(\lambda)\ \delta\lambda\ \delta\Omega = \frac{B_0}{\lambda^{1+2\alpha_0}}\ \delta\lambda\ \delta\Omega. \qquad 1.$$

B_0 is a measure of the moderator flux per unit time, per unit wave length per steradian. α_0 is the buckling term, with a value from zero to 0.15 for pulsed source moderators, describing the surface losses from the moderator during slowing down. A point sample S receives neutrons at a distance L from the moderator. The direct flux at the sample between the elastic wavelength λ_d and $\lambda_d+\delta\lambda_d$ is given by

$$n_d(\lambda_d)\ \delta\lambda_d = \frac{B_0}{\lambda_d^{1+2\alpha_0}}\ \frac{\delta\lambda_d}{4\pi L^2} \qquad 2.$$

per unit area per unit time. All background fluxes in this paper will be presented as a background fraction with respect to this direct flux.

Consider next the indirect beam scattered from the inner surface of the iris collimator shown. The iris surface is of radius r, length l and centred at a distance x from the moderator. The solid angle of the iris front aperture seen by the source is

$$\Omega_0 = \frac{\pi r^2}{4\pi(x-l/2)^2}. \qquad 3.$$

The solid angle Ω_0 is unchanged for an extended moderator lying on the sphere shown dashed in figure 2. It follows that if moderator extent is small compared with x, equation 3 applies equally for an extended moderator. The solid angle from the iris back surface Ω_1 is similar with $x+l/2$ in the denominator giving for the incident solid angle subtended by the inner surface.

$$\Delta\Omega_0 = \Omega_0 - \Omega_1 = \frac{r^2 xl}{2[x^2-(l/2)^2]^2} \doteqdot \frac{r^2 l}{2x^3} \qquad 4.$$

provided that $x > l/2$. The area of the iris inner surface is $2\pi rl$, so that the mean flux of neutrons over the inner surface per unit area between wavelengths λ_0 and $\lambda_0+\delta\lambda_0$ is

$$n_0(\lambda_0)\ \delta\lambda_0 = \frac{B_0}{\lambda_0^{1+2\alpha}} \frac{r^2 l}{2x^3} \frac{\delta\lambda_0}{2\pi rl} \qquad 5.$$

Of these neutrons a fraction $A(\lambda_0)$, the albedo, will be scattered back from the same surface of the collimator (3). If the collimator is several scattering lengths thick, the scattered neutrons will emerge equally in all directions. Others may be absorbed and still others scattered further within the material. $A(\lambda_0)$ can be found by experiment or calculated from the scattering cross-sections. It varies from about 15% for a totally coherent scatterer such as polyethylene, though 12 % for iron, to 0.13% for boron carbide.

During the scattering process occuring in the iris, slowing down of the neutrons will be occuring so that the emitted neutrons will be at a generally longer wavelength $\lambda_1 > \lambda_0$. This process occupies some moderation time t_m shown by experiment and theory to be proportional to wavelength (4). The process is exactly analogous to the time delay during slowing down neutrons is the moderator where neutrons emitted at a wavelength λ_0 experience a time delay

$$t_m = C_0\ \lambda_0$$

The constant C_0 is around 10 $\mu s\text{Å}^{-1}$ for hydrogenous materials, but increases to 80 $\mu s\text{Å}^{-1}$ for heavier elements such as iron. The time delay in the shielding material incurred by slowing neutrons down from wavelength λ_0 to wavelength λ_1 will be similar but with a different time constant C_1

$$\Delta t_m = C_1(\lambda_1 - \lambda_0) \qquad 6.$$

Figure 3 illustrates the spectrum of neutrons emitted by incident neutrons of wavelength λ_0. Once again the epithermal distribution of equation 1 is assumed, but with a changed buckling constant α_1 likely to be closer to zero for a thick semi-infinite iris. The total number of emitted neutrons $n_1(\lambda_1)$ from all wavelengths from λ_0 to ∞ must be equal to the number incident $n_0(\lambda_0)\delta\lambda_0$ attenuated by $A(\lambda_0)$.

$$n_0(\lambda_0)\ \delta\lambda_0\ A(\lambda_0) = \int_{\lambda_0}^{\infty} n_1(\lambda_1)d\lambda_1 = \int_{\lambda_0}^{\infty} \frac{B_1}{\lambda_1^{1+2\alpha_1}}\ d\lambda_1 = \frac{B_1}{2\alpha_1 \lambda_0^{2\alpha_1}}. \qquad 7.$$

This expression defines the constant B_1 in the emitted neutron spectrum. The number of neutrons emitted from the inner surface of the collimator within the band λ_1 to $\lambda_1+\delta\lambda_1$ from incident neutrons λ_0 to $\lambda_0+\delta\lambda_0$ is therefore

$$n_1(\lambda_0,\lambda_1)\ \delta\lambda_0\ \delta\lambda_1 = \frac{2\alpha_1 \lambda_0^{2\alpha_1}}{\lambda_1^{1+2\alpha_1}} A(\lambda_0) \frac{B_0}{\lambda_0^{1+2\alpha_0}} \frac{r^2 l}{2x^3} \frac{\delta\lambda_0\ \delta\lambda_1}{2\pi rl}. \qquad 8.$$

If these neutrons are emitted isotropically, the number reaching the sample position will be reduced by the solid angle of the collimator inner surface as seen by the sample $\Delta\Omega_1$. This will be equation 4 with x replaced by $L-x$,

$$n_s(\lambda_0,\lambda_1)\ \delta\lambda_0\ \delta\lambda_1 = \frac{2\alpha_1\lambda_0^{2\alpha_1}}{\lambda_1^{1+2\alpha_1}}\ A(\lambda_0)\ \frac{B_0}{\lambda_0^{1+2\alpha_0}}\ \frac{r^2 l}{2x^3}\ \frac{r^2 l}{2(L-x)^3}\ \frac{\delta\lambda_0\ \delta\lambda_1}{2\pi r l}. \qquad 9.$$

Let us next consider the flight times of the neutrons. The direct neutrons will have a flight time over the path L of

$$t_d = (\frac{mL}{h}+C_0)\ \lambda_d. \qquad 10.$$

The constant $\frac{m}{h}$ is equal to 0.3956 for t in μs, L in cm and λ in Å This flight time is illustrated by the dashed line in figure 4. The inelastically scattered neutrons have a total flight time consisting of an initial delay in the moderator C_0, a flight time to the collimator $mx\lambda_0/h$, a time delay during moderation $C_1(\lambda_1-\lambda_0)$, and a flight time from collimator to sample $m(L-x)\frac{\lambda_1}{h}$, making a total

$$t(\lambda_0,\lambda_1) = \left(\frac{mx}{h} + C_0 - C_1\right)\lambda_0 + \left(\frac{m(L-x)}{h} + C_1\right)\lambda_1 = t_d \qquad 11.$$

The inelastic background to be calculated is the ratio between the indirect and direct neutron fluxes arriving at the sample in the same time interval between t_d and $t_d+\delta t_d$. For direct neutrons this corresponds to neutrons of wavelengths λ_d to $\lambda_d+\delta\lambda_d$. Differentiating equation 10, and using equation 2 this direct flux is seen to be

$$n_d(\lambda_d)\delta\lambda_d = \frac{B_0}{\lambda_d^{1+2\alpha_0}}\ \frac{1}{\frac{mL}{h} + C_0}\ \frac{\delta t_d}{4\pi L^2}. \qquad 12.$$

The inelastically scattered neutron flux is found by intergrating over all incident and scattered wavelengths with the constraint that the total flight time falls between t_d and $t_d+\delta t_d$. Figure 4 illustrates such a set of scattering possibilities. An option is to equate δt_e with the finite δt_1 corresponding to the wavelength spread δt_1 of the scattered neutrons. The incident wavelength spread $\delta\lambda_0$ is made infinitesimal and incorported into an integral over λ_0. From equation 11 the scattered wavelength λ_1 corresponding to a given total time t_d and wavelength λ_0 is given by

$$\lambda_1 = \frac{(L+C_0h/m)\lambda_d - (x+C_0h/m - C_1h/m)\lambda_0}{L - x + C_1h/m}. \qquad 13.$$

At a fixed λ_0 the relationship between δt_d and $\delta\lambda_1$ is given by differentiating as

$$\delta\lambda_1\ (L - x + C_1h/m) = \delta t_d\ h/m\ . \qquad 14.$$

The number of neutrons reaching the sample between times t_d and $t_d+\delta t_d$ is then

$$\int_0^{\lambda_d} n_s(\lambda_0,\lambda_1)d\lambda_0\ \delta\lambda_1 = \frac{\alpha_1 B_0 r^3 l}{4\pi x^3(L-x)^3} \int_0^{\lambda_d} \frac{A(\lambda_0)\ \lambda_0^{2\alpha_1}\ d\lambda_0}{\lambda_0^{1+2\alpha_0}\ \lambda_1^{1+2\alpha_1}}\ \frac{\delta t_d\ h/m}{(L - x + C_1h/m)}\ . \qquad 15.$$

Comparing with equation 12 gives the inelastically scattered fraction. The integral is cast in dimensionless terms with

$$\xi = \frac{x}{L},\quad \rho = \frac{r}{L},\quad \mu = \frac{l}{2L},\quad \nu = \frac{\lambda_0}{\lambda_d},\quad \delta_0 = C_0\ \frac{h}{mL}\quad and\quad \delta_1 = C_1\ \frac{h}{mL}. \qquad 16.$$

Writing it in the form of the albedo A, a geometric term G and the inelastic integral I gives

$$F = A\ G\ I$$

with

$$G = \frac{r^3 l L^2}{x^3 (L - x)^3} = \frac{\rho^3 \mu}{\xi^3 (1 - \xi)^3} \qquad 17.$$

and

$$I = \alpha_1 (1 + \delta_0)(1 - \xi + \delta_1)^{2\alpha_1} \int_0^1 \frac{dv}{v^{1+2\alpha_0-2\alpha_1} [1 + \delta_0 - (\xi+\delta_0-\delta_1)v]^{1+2\alpha_1}}. \qquad 18.$$

An alternative integral is obtained if the integration is performed over scattered wavelengths λ_1 with $\delta\lambda_0$ scaled to give the chosen time interval δt_d. Putting $\varepsilon = \frac{\lambda_1}{\lambda_d}$ as the variable gives the equivalent integral

$$I = \alpha_1 (\xi+\delta_0-\delta_1)^{2\alpha_0-2\alpha_1} \int_1^{(1+\delta_0)/(1-\xi+\delta_1)} \frac{d\varepsilon}{[1 + \delta_0 - (1-\xi+\delta_1)\varepsilon]^{1+2\alpha_0-2\alpha_1} \varepsilon^{1+2\alpha_1}} \qquad 15.$$

A number of interesting features can be noted from evaluating either integral numerically

(i) The geometric term G of equation 17 shows that scattering centres close to either the moderator or sample give a relatively large contribution and so should be used with caution.

(ii) Apart from the albedo term, the scattering fraction is independent of the incident neutron energy in this approximation.

(iii) Figure 5(i) shows the integral evaluated for negligible moderation delay $\delta_0 = \delta_1 = 0$, $\alpha_0 = 0$, and a rapid collimator slowing down $\alpha_1 = 0.5$. The largest contribution to the integral is close to the direct wavelength λ_d. The inelastic integral becomes close to unity, indeed it is exactly unity for the conditions of figure 5(i).

(iv) Figure 5(ii) shows the integral for the more practical case of the moderator buckling $\alpha_0 = 0.15$ and the collimator buckling $\alpha_1 = 0.05$, with $\delta_0 = \delta_1 = 0$. For this example the inelastic integral is appreciably larger than unity. The largest contribution to the integral comes from the shortest wavelenths, and for $\alpha_0 > \alpha_1$ the integral can in principle diverge. In practice the $\frac{1}{\lambda^{1-\alpha_0}}$ divergence cannot continue indefinitely and the integral remains finite. The conclusion remains that any moderating material can become a serious background source if near either the target or the sample area.

(v) The inclusion of a moderation time delay causes a further increase in the value of the inelastic integral. Figure 6(iii) shows its value for negligible moderator delay $\delta_0 = 0.0$, but with appreciable moderation delay in the shielding $\delta_1 = 0.25$. The time-distance plot shows the effect for a moderator to collimator distance $L - x$ equal to the moderation effective moderation distance $C_1 h/m$. The scattered neutron energy is the same for *any* incident neutron energy leading to the appearance of ghost source near the true moderator.

3. The complete collimator

Returning to figure 1, let us consider the conclusions for good collimator design suggested by the present calculations. Numerical estimates will be considered in another report. The aim should be to reduce the background fraction F given roughly by observed

counts at P divided by incident counts at S to the values of order 10^{-6} given by a good reactor small angle spectrometer.

(i) An iris transmission of this order is easy to achieve, at any rate below 1 ev, by a mere 1 cm thickness of boron carbide. Thus it it likely to be the collimator scattering which dominates the observed background.

(ii) The scattering surfaces seen by both moderator and sample area are the main subject of the paper. This surface is clearly reduced by splitting the collimator into a series of relatively thin irises of radius r_i, length l_i at positions x_i. The primary iris scattering function is

$$F = \sum_i \frac{r_i^3 l_i L^2 A_i I_i}{2x_i^3 (L-x_i)^3}. \qquad 20.$$

Consider a 10 m long, 10 cm diameter collimator with irises 10 cm long. The geometric term is only 0.04×10^{-6} for an iris at 5 m but rises to 0.85×10^{-6} at 1 m or 9 m close to the moderator or sample, and to 83×10^{-6} at 20 cm from the moderator or sample. Clearly collimators placed at these positions must be designed with great care, for example by ensuring low albedo by using low hydrogen content B_4C shielding.

(iii) Double scattering processes are potentially almost as large since, as indicated in figure 6, the bright and visible surfaces on adjacent irises can be of much larger area than the edges of the irises. Figure 7 illustrates the calculation of the solid angles subtended by these areas at the moderator and sample

$$\delta\Omega_0 = \frac{\pi(r_i^2 - r^2)}{x_i^2} \qquad \delta\Omega_1 = \frac{\pi(r_j^2 - r^2)}{(L-x_j)^2}.$$

The scattering fraction is seen to have had a contribution

$$\delta\Omega_0 \frac{A_i}{4\pi} \frac{1}{(x_i - x_j)^2} \delta\Omega_1 \frac{A_j}{4\pi}$$

giving for the overall geometric scattering fraction

$$G = \sum_i \sum_{j<i} \frac{r^4(x_i^2 - x_j^2)\left((L-x_i)^2 - (L-x_j)^2\right)L^2}{16x_i^4(L-x_j)^4(x_i-x_j)^2} \qquad 21.$$

and depends on the square of the albedo, and also on a double inelastic integral which we have not evaluated. To estimate this term consider a single pair of surfaces between two adjacent irises at x_i and $x_i - S$. This term is

$$G_{ij} = \frac{r^4(2x_iS - S^2)\left(2(L-x_i)S - S^2\right)L^2}{16x_i^4(L-x_i)^4}. \qquad 22.$$

With the reasonable approximation that the separation S is small compared with x_i or $L-x_i$ this becomes independent of S giving

$$G_{ij} = \frac{r^4 L^2}{4x_i^3(L-x_i)^3}. \qquad 23.$$

The equation closely resembles equation 20 and gives terms of comparable size. It follows that both inside and outside surfaces of the iris should be covered with low albedo surfaces.

(iv) The outer region of the collimator must not be neglected. Neglecting the positional dependence of the albedo and inelasticity integral of a collimator from x_1 to x_2 gives a scattering fraction

$$F = A\ I\ \frac{r^3}{2L^3}\left[\frac{1}{2\xi^2(1-\xi^2)} + \frac{2}{\xi^2(1-\xi)} - \frac{3(2\xi+1)}{\xi^2} + 6\ln\frac{\xi}{1-\xi}\right]_{x_1/L}^{x_2/L}. \qquad 24.$$

This geometry of collimator has been investigated by Soper(5). This fraction can become very serious if the collimator extends close to moderator or sample. For example for a collimator extending from $x_1 = 100$ cm to $x_2 = 900$ cm. for a 10 cm diameter 10 m long collimator the geometric scattering fraction is 8.2×10^{-6}. Inelastic effects can be very important here, as thin boron carbide irises do little to prevent fast neutrons entering this region. Although slow neutrons emitted by the collimator are not directly visible near the sample, they may easily be scattered off an iris surface as in the previous section. The solution is to make the outer region of the collimator from absorbing materials with a low albedo surface.

References

(1) G M Vineyard Phy Rev 96 (1954) 93

(2) V F Sears Adv Phys 24 (1975) 1

(3) C G Windsor Pulsed Neutron Scattering, Taylor and Francis, London, 1981

(4) K H Beckurts and J Wirtz Neutron Physics Springer Verlag, Berlin, 1964

(5) A K Soper, Nucl Inst Meth 212 (1983) 337

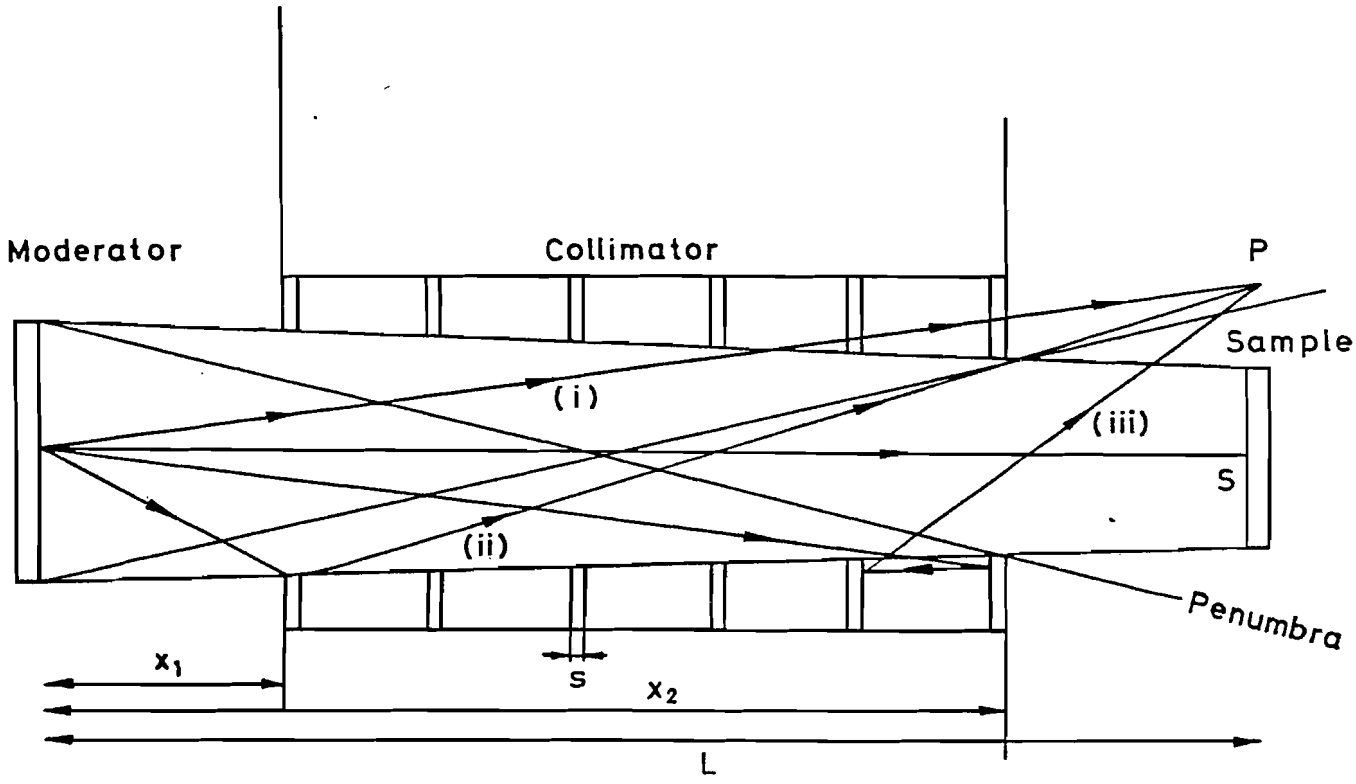

Figure 1. The contributions to the neutron background at a point P just outside the geometric penumbra of the collimator. (i) neutrons transmitted by the collimator (ii) neutrons scattered by the collimator (iii) neutrons doubly-scattered or scattered and transmitted.

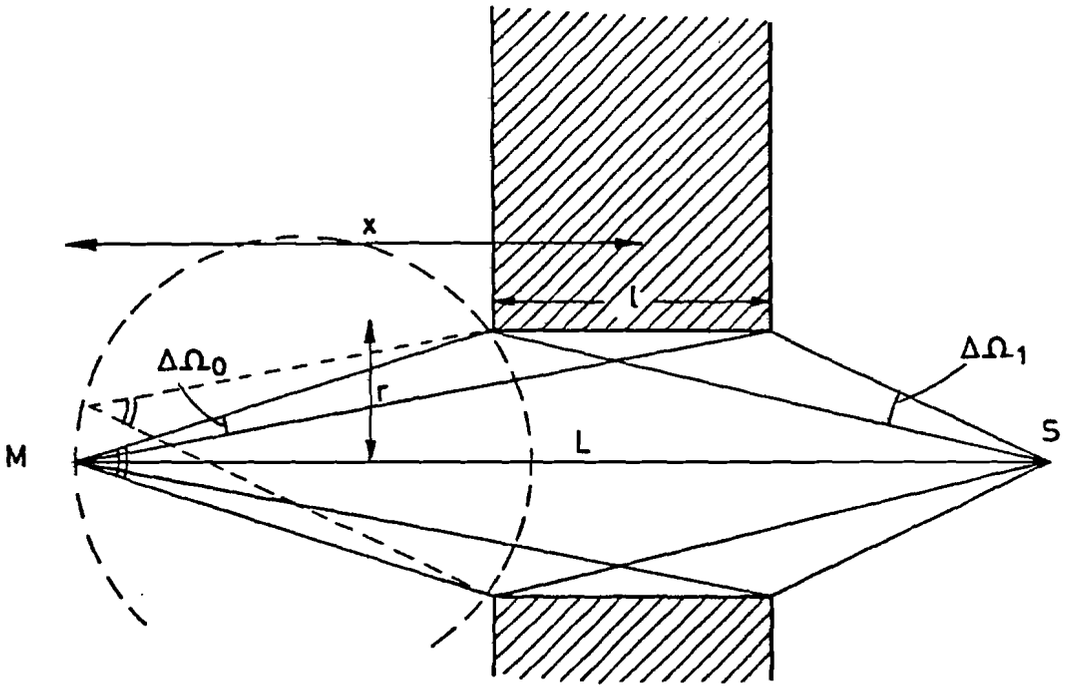

Figure 2. Scattering from a circular iris collimator. A geometric term depends on the incident and scattered solid angles $\Delta\Omega_0$, Δl_1 . An inelasticity term depends on slowing down properties of the moderator and iris.

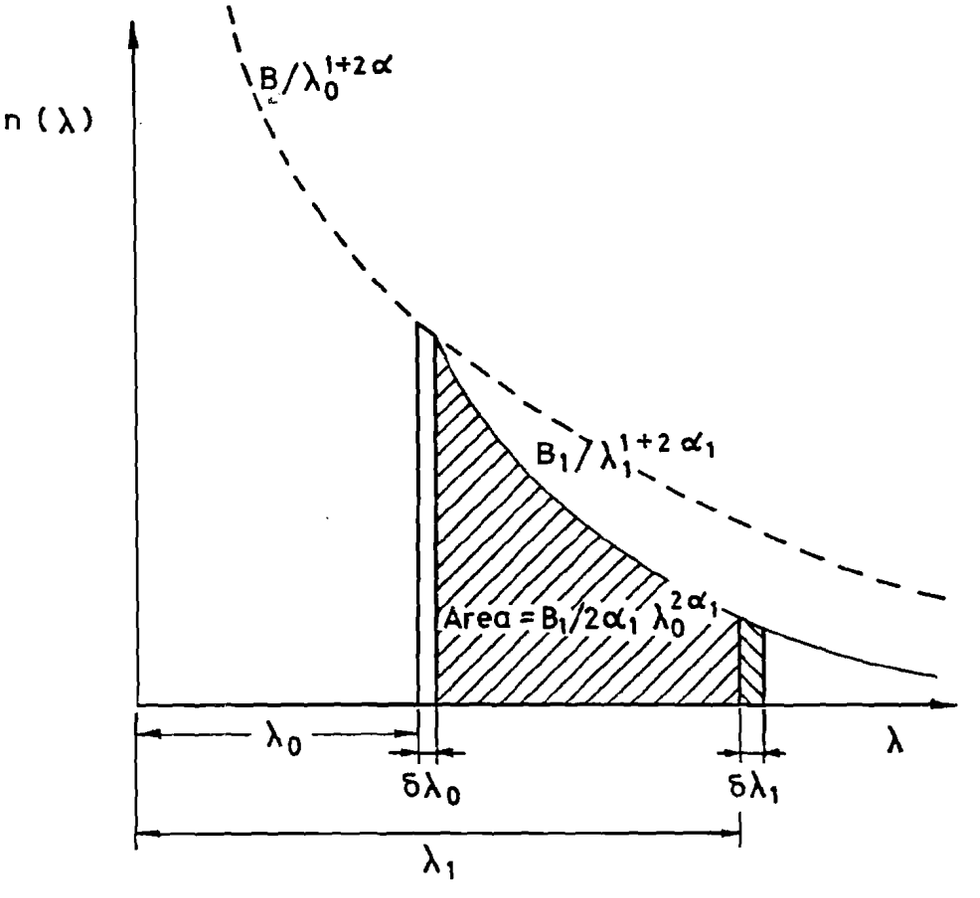

Figure 3. The flux incident on a collimator between wavelengths λ_0 and $\lambda_0+\delta\lambda_0$, is assumed to be partly re-admitted over a range of wavelengths λ_1 from λ_0 to infinity with a slowing down distribution $B_1/\lambda_1^{1+2\alpha_1}$.

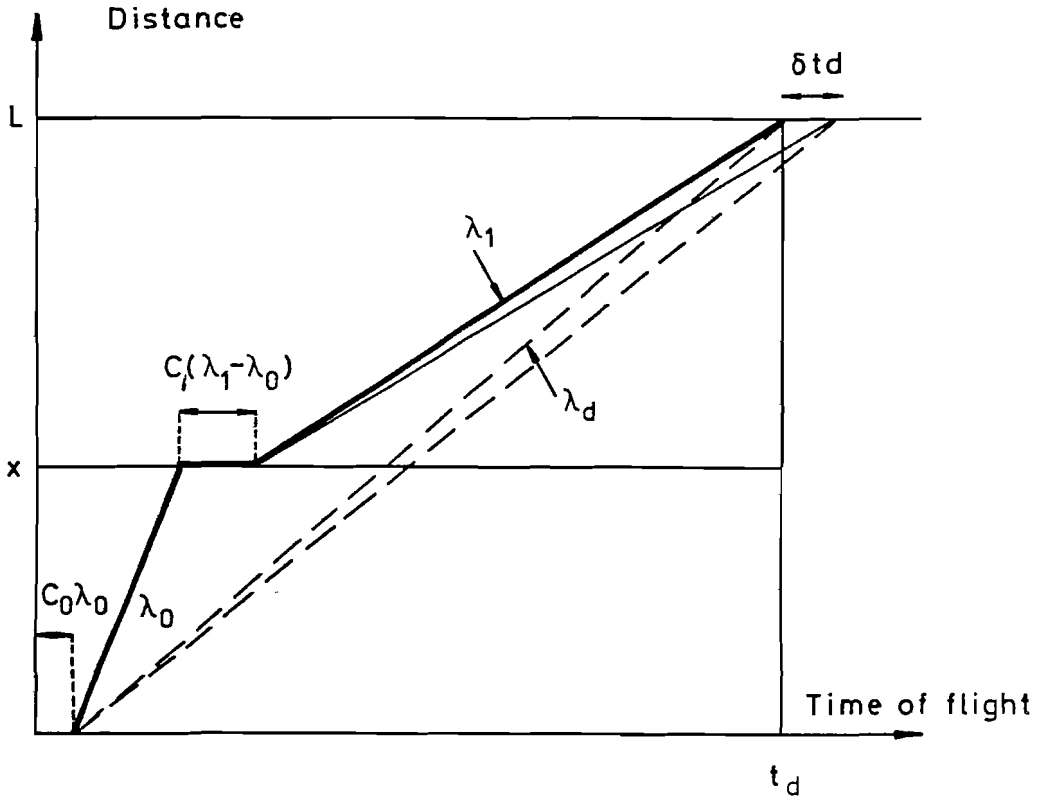

Figure 4. The time/distance diagram for inelastically scattering collimators. Direct neutrons arrive between times t_d and $t_d+\delta t_d$. The set of inelastic neutrons is considered which travel at any wavelength λ_0 to the collimator at x. and then travel to arrive at time t_d with wavelength λ_1 including a moderation time delay proportional to $C_0\lambda_0$ and a delay due to moderation in the shielding proportional to $C_1(\lambda_1-\lambda_0)$.

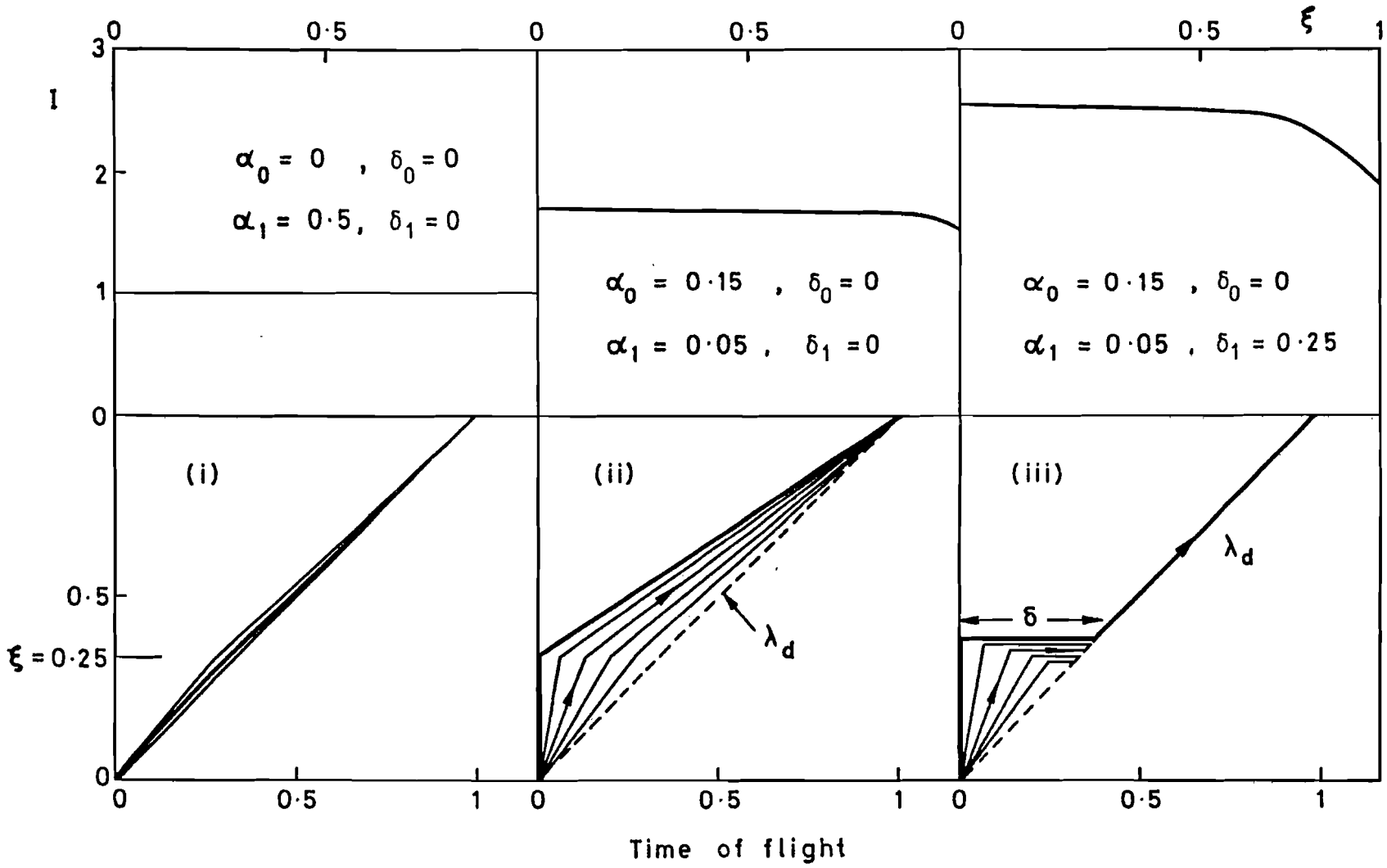

Figure 5. The inelastic integral I evaluated as a function of position down the collimator ξ, with corresponding time/distance diagrams for $\xi=1/3$. (i) if the collimator buckling is relatively large most scattering is elastic and I = 1. (ii) if the moderator buckling exceeds the collimator buckling the integral rises and becomes dominated by incident fast neutrons (iii) with moderation delay in the iris material $\delta_1 = \xi$ the inelastic integral increases, and can give the same scattered energy for all incident energies.

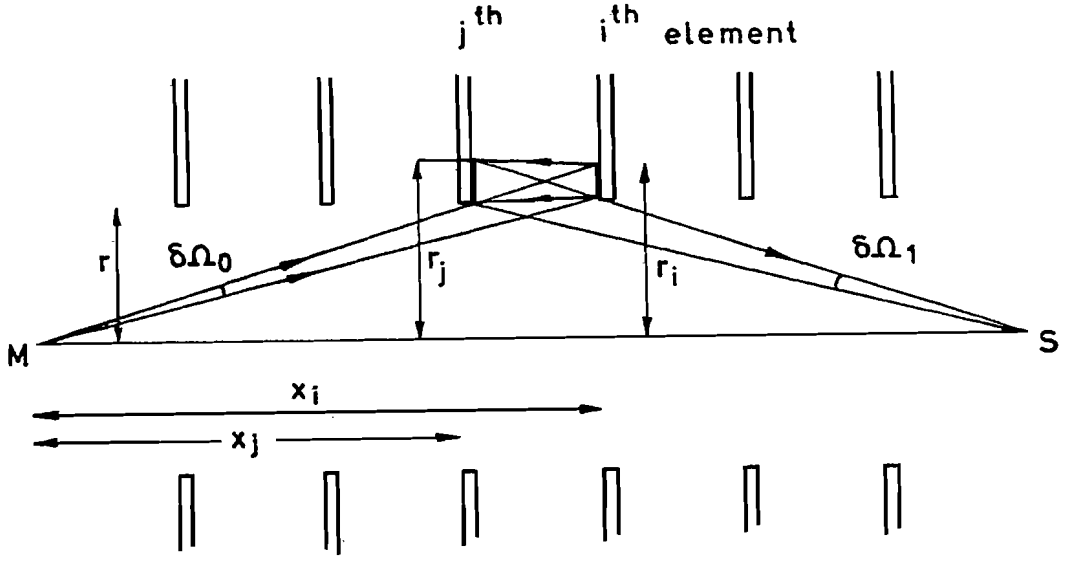

Figure 6. Double scattering from a pair of collimator irises. The *bright* area of radius $r_i = rx_i/x_j$ on the i^{th} iris, reflects back to a *visible* area of radius $r_j = r(L-x_i)/(L-x_j)$ on the j^{th} iris. The increase in these areas with increasing separation between irises exactly cancels the decrease in scattered neutron intensity arising from the inverse square law.

Proceedings of the Eighth Meeting of the International Collaboration on Advanced Neutron Sources (ICANS-VIII)
8-12 July 1985, Rutherford Appleton Laboratory Report RAL-85-110

Analysis of Neutron Streaming in Beam Tubes by a Favourable Coupling of Analytical Solution and S_N-Approximation of Transport Theory*)

K. Neumann, W. Bernnat

Institut für Kernenergetik und Energiesysteme,
Pfaffenwaldring 31, D-7000 Stuttgart 80
Federal Republic of Germany

Abstract

A new method has been developed to treat the particle streaming through enlarged and extremely dimensioned cavities. It uses the analytical solution of the integral transport equation for the cavity zones and the S_N-approximation in the surrounding materials. The method has been applied to study streaming through beam tubes for high energy particle transport. In this context a comparison between different methods for the determination of spatial flux distributions for different beam tube dimensions bas been made.

*) This work was supported by the Kernforschungsanlage Jülich, Institut für Reaktorentwicklung

1 Introduction

The calculation of neutron and photon streaming through enlarged cavities is difficult, if one considers the interactions with the surrounding materials. Use of S_N-method /1/ necessitates high angular discretisation to describe a correct streaming through the cavities. Low orders lead to flux distortions, called "ray-effect" /2/. Other methods (e. g. Monte Carlo, spherical harmonics or first collision source) combined with the S_N-method are more complicated.

The transport equation can be solved analytically in vacuum zones. This solution can be embedded in the S_N-method with boundary conditions for cavity surfaces /3/. At the surface elements the incoming and outgoing directional fluxes are approximated by a polynomial expansion and the solution for the cavity is calculated with this approximation. A program RATRAC (Radiation Transport in Cavities), based on the above mentioned principle, has been developed and coupled with the two-dimensional S_N-code DOT (version 4.2) /4/. The method is realized in r,z-geometry for cylindrical and annular cavities or ducts /5/.

The method has been applied to analyse the streaming effects in beam tubes of the planned SNQ facility and the results have been compared with those from other methods. To show the spatial distributions for varied beam tube diameters the source has been defined.

2 Theory

The solution of the integral transport equation in vacuum (between two points on the cavity surface) is

$$\Phi(\vec{r}_p,\vec{\Omega}) = \Phi(\vec{r}_q,\vec{\Omega}) \tag{1}$$

where $\vec{r}_p$ indicated the target point and $\vec{r}_q$ the source point. From eq. (1) the particle current between the target area element dS_p and the source area element dS_q could be derived as below

$$(\vec{\Omega}\cdot\vec{n}_p)\Phi(\vec{r}_p,\vec{\Omega})d\vec{\Omega}dS_p = (\vec{\Omega}\cdot\vec{n}_p)(\vec{\Omega}\cdot\vec{n}_q)\Phi(\vec{r}_q,\vec{\Omega})\frac{1}{R_{pq}^2}dS_q dS_p \tag{2}$$

R_{pq} is the distance between $\vec{r}_p$ and $\vec{r}_q$.

To get a solution of eq. (2) the angular fluxes are approximated by Legendre polynomials. The functions for the approximation are so chosen that they are orthogonal in the 4 direction quadrants of the S_N-method. For any quadrant the directional flux density is given by

$$\Phi(\vec{r},\vec{\Omega}) = \sum_{\ell}\sum_{n<\ell}\frac{2\ell+1}{\pi}f_\ell^n(\vec{r})Y_\ell^n(\vec{\Omega}) \tag{3}$$

where f_l^n represents the moments of the expansion and Y_l^n are associated Legendre functions of order l, n. Following three orthogonal systems allow above mentioned expansion for cylindrical geometry:

l, n even; (4)

l, n odd surfaces in radial directions; (5)

and

l odd, n even surfaces in axial directions. (6)

In order to formulate a general expression of the directional flux

density at the target point $\vec{r}_p$ in quadrant k the approximation in eq. (3) will be applied to eq. (2). Multiplying eq. (2) with Y_1^n at the target point and integrating over the quadrant k gives

$$\int_{\vec{\Omega}\in Q^k} Y_{\ell_p}^{n_p}(\vec{\Omega})(\vec{\Omega}\cdot\vec{n}_p)\Phi^k(\vec{r}_p,\vec{\Omega})dS_p d\vec{\Omega} = \int_{S_q} Y_{\ell_p}^{n_p}(\vec{\Omega})(\vec{\Omega}\cdot\vec{n}_p)(\vec{\Omega}\cdot\vec{n}_q)\Phi^{k'}(\vec{r}_q,\vec{\Omega})\frac{dS_q dS_p}{R^2_{pq}} \quad . \quad (7)$$

On the left hand side of eq. (7) $(\vec{\Omega}\cdot\vec{n})Y_1^n(\vec{\Omega})$ will be expressed by different recursion formulas for the different surfaces. Use of the orthogonal system (5) in radial direction and of (6) in axial direction results in a system of linear equations for the moments f_1^n at the target point $\vec{r}_p$.

$$A\cdot FP = RP \quad (8)$$

The matrix A contains the constant coefficients of the recursion formulas, F represents a vector with the moments f_1^n and the vector RP gives the solution of the right hand side of eq. (7). The solution of RP can be obtained by using system (4) for the angular dependence of the incoming fluxes.

$$RP_\ell^{nk} = \sum_{G'} \sum_{\ell_q} \sum_{n_q<\ell_q} \sum_{k'} \frac{2\ell_q+1}{\pi} \int_{u_q} f_{\ell_q}^{n_q k'}(\vec{r}_q) \{2 \int_{\psi_q} Y_{\ell_p}^{n_p}(\vec{\Omega}_p) Y_{\ell_q}^{n_q}(\vec{\Omega}_q) \quad (9)$$

$$(\vec{\Omega}\cdot\vec{n}_p)(\vec{\Omega}\cdot\vec{n}_q)\cdot\frac{r_q}{R^2_{pq}}\,d\psi\}du_q dS_p$$

The sums represent the streaming from different surfaces G', out of quadrant k' for the flux approximation l_q, n_q into quadrant k at surface G. The variable u_q means a surface element where $f_{1_q}^{n_q}(\vec{r}_q)$ is constant and the azimuthal angle ψ gives the possible optical view from source surface to the target point.

The coupling of above mentioned solution with the S_N-method needs the formulation of boundary conditions. These are defined by

$$f_{\ell_q}^{n_q k'}(\vec{r}_q) = \sum_{m\in Q^{k'}} \Phi_m(\vec{r}_q)\, w_m \frac{\int_{\Delta\Omega_m} Y_{\ell_q}^{n_q} d\vec{\Omega}}{\int_{\Delta\Omega_m} d\vec{\Omega}} = 4\pi \sum_{m\in Q^{k}} \Phi_m(\vec{r}_q)\, w_m\, Y_{\ell_q}^{n_q}{}_m \qquad (10)$$

for the incoming fluxes. The outgoing fluxes are given by

$$\Phi_m^k(\vec{r}_p) = \sum_{\ell_p} \sum_{n\le\ell_p} \frac{2\ell_p+1}{\pi} f_{\ell_p}^{n_p k}(\vec{r}_p) \frac{\int_{\Delta\Omega_m} Y_{\ell_p}^{n_p}(\vec{\Omega}) d\vec{\Omega}}{\int_{\Delta\Omega_m} d\vec{\Omega}} \quad . \qquad (11)$$

By this formulation of the analytical solution of the integral transport equation and its coupling with S_N-approximation the streaming coefficients can be defined which describe the particle transport in cavities completely and depend only on the geometrical structure of the cavities. These coefficients can be calculated before flux iterations and stored for several problems with the same geometry of cavities. During the flux iteration cycle the treatment of the transport through cavities is reduced to matrix operations, which could be efficiently programmed (vectorized).

For extremely anisotropic outstreaming from cavities additional coefficients have been derived, which couple the instreaming on a source area element (eq. (10)) directly to the S_N-discretization on the target area elements.

By realization of the method following attributes have been included, which support the different scattering properties of the surrounding materials, different geometrical structures and computation technics:

- several different cavities can be defined,

- variable expansion orders on surfaces and quadrants are allowed,

- extremely anisotropic outstreaming can be treated additonally,

- variable S_N-orders are possible,

- coupling of RATRAC and DOT is realized efficiently for reducing computation time.

3 Results

A two-dimensional model in r-z-geometry was set up for the beam tube investigations (Fig. 1). Two cases with beam tube diameters 10 and 20 cm and length 600 cm were considered. Both were surrounded by a homogeneous iron shield of 200 cm diameter and 600 cm length. Since realistic source distributions in space and energy were not available at present state of SNQ project, they were defined artificially. At a distance of 50 cm from the beam tube entrance a constant flat source from r = 0 to r = 10 cm was defined. For this analysis the angular dependence of the source was taken as cosine shaped.

The cross sections for the iron shield have been taken from the high energy library from Los Alamos /6/. The library includes energies from thermal up to 800 MeV. The sources are defined in the 1st. (700 - 800 MeV), in the 15th. (1,2 - 1,0 MeV) and in the 32nd. group (1,235 - 0,454 keV) with the source density 1 n/cm^2. The results of one-group calculations are transferable to multigroups taking care of the ingroup scattering components.

The radial flux densities at the end of the beam tube are shown in Fig. 2 for the source with the highest energy. Two S_N-calculations, with an usual S_8 set and a biased $S_N(166)$ set based on S_{10} and with a fine discretisation in -z direction, have been carried out. A calculation with the coupled method in $S_8/Y_2/D(S_8$ in scattering materials, an order of 2 in the expansions (Y_2) and using the additional coefficients (D) for cavity treatment) has been made. The line of sight results, which consider only the direct streaming from source area to the end of the beam tube, are shown in the same

figure. It can be seen, that the S_8 calculation underestimates the fluxes very much compared with the other results. Use of $S_N(166)$ leads to an underestimation at the centre of the beam tube, but it gives a correct streaming through the outer surface of the beam tube. The solution of the coupled method represents the beam tube streaming exactly according to the line of sight results. For the energy group 1 the self scattering cross section is only 4,8 % of the total cross section, so that the scattering component for the duct streaming is very low. (The library includes only the inelastic scattering for high energies.)

It can be seen that the axial distribution, at r = 10,25 cm (Fig. 3), with $S_N(166)$ leads to some ray effects at the end of the beam tube. The results of the coupled method, using a S_8 set in the material zones are different, because this S_N set is not able to reproduce the extreme anisotropic outstreaming from the beam tube. The particle currents are correct, but the angular distribution of the particles is not adequately represented by a S_8-angular discretisation. To get better results near the beam tube one has to use finer angular discretisation like $S_N(80)/Y_2/D$ in Fig. 3.

An axial distribution at 190 cm (Fig. 4) shows that the differences between $S_N(166)$ and S_8 are less than a factor of two except for the flux distortions for $S_N(166)$ on the source side of the shield.

For the same source group the beam tube diameter is reduced to 10 cm (Fig. 5). A section of 100 cm radius at the end of the beam tube shows the underestimation by the $S_N(166)$ solution by a factor of 80. In contrast to the coupled method a new S_N set must be defined for smaller diameters.

As a last case the source energy has been changed (Fig. 6). The scattering component at the end of the beam tube increases only slightly with lower energies. For the 15th. group it is about 2 % compared to the first group. For the 32nd. group it is about 4 %, which can not be seen due to the logarithmic scale of the curves.

The radial distribution is quite different from those of the higher energies. This is due to decreasing of the mean free path lengths although the self-scattering rate increases from Σ_{g-g}/Σ_T = 0,048 for 700 - 800 MeV to 0,929 for 1,235 - 0,454 keV.

These results show that the new coupled method is able to treat the neutron streaming through extreme dimensional cavities, like beam tubes, without ray-effect. There are no special S_N sets to define for different beam tube dimensions, because the geometry will be analysed automatically from DOT input for generating the streaming coefficients.

Calculation time is more economic than using adjusted S_N sets. The method allows the continuation of the outstreaming at the end of the beam tube also. With variable S_N orders surrounding the beam tube the streaming along the beam tube can be treated by a low order and the outstreaming at the top of the beam tube can be determined exactly by high or biased S_N orders.

4 Literature

/1/ Carlson, B.G.: Solutions of the Transport Equation by S_N-Approximations,
Los Alamos 1953 (LA-1599)

/2/ Lathrop, K.D.: Ray-Effects in Discrete Ordinates Equiations,
Nucl. Sci. Eng. 32, p. 357 - 369 (1968)

/3/ Emendörfer, D.: Randbedingungen für den Neutronenfluß im endlichen Zylinder nach der P_L-Approximation der Transportgleichung.
Nuklonik 5, S. 74 - 82 (1963)

/4/ Rhoades, W.A., Simpson, D.B., Childs, R.L., Engle, W.W. jr.: The DOT-IV Two Dimensional Discrete Ordinates Transport Code with Spacedependent Mesh and Quadrature.
Oak Ridge 1977 (ORNL/TM-5629)

/5/ Neumann, K.: Thesis in preparation

/6/ Wilson, W.B.: Nuclear Data Development and Shield Design for Neutrons Below 60 MeV.
Los Alamos 1978 (LA-7159-T)

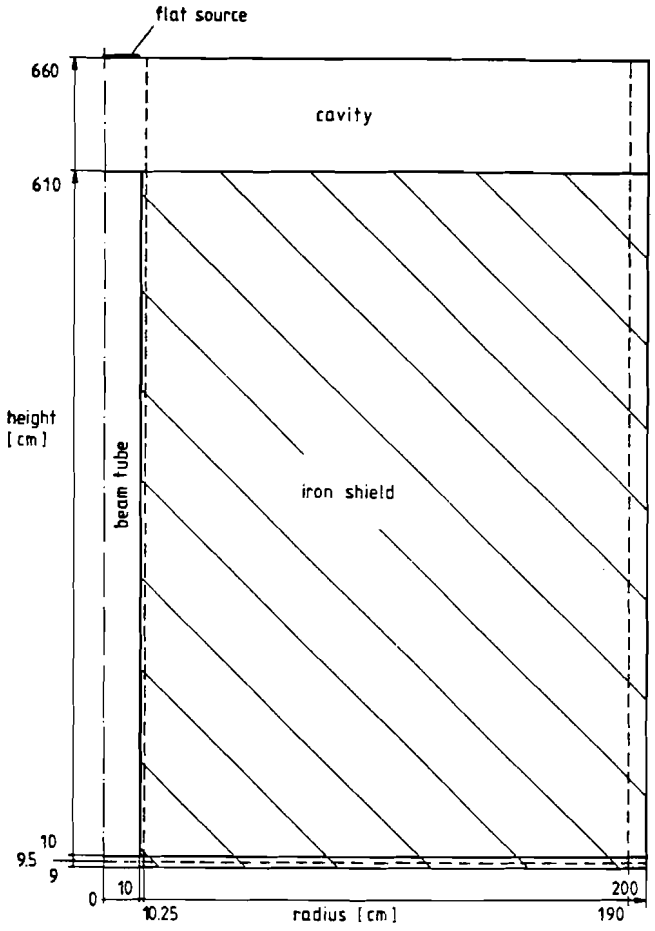

- - - - - - - grid lines for flux comparison

Fig. 1 Geometry of the Model for the Beam Tube Investigations.

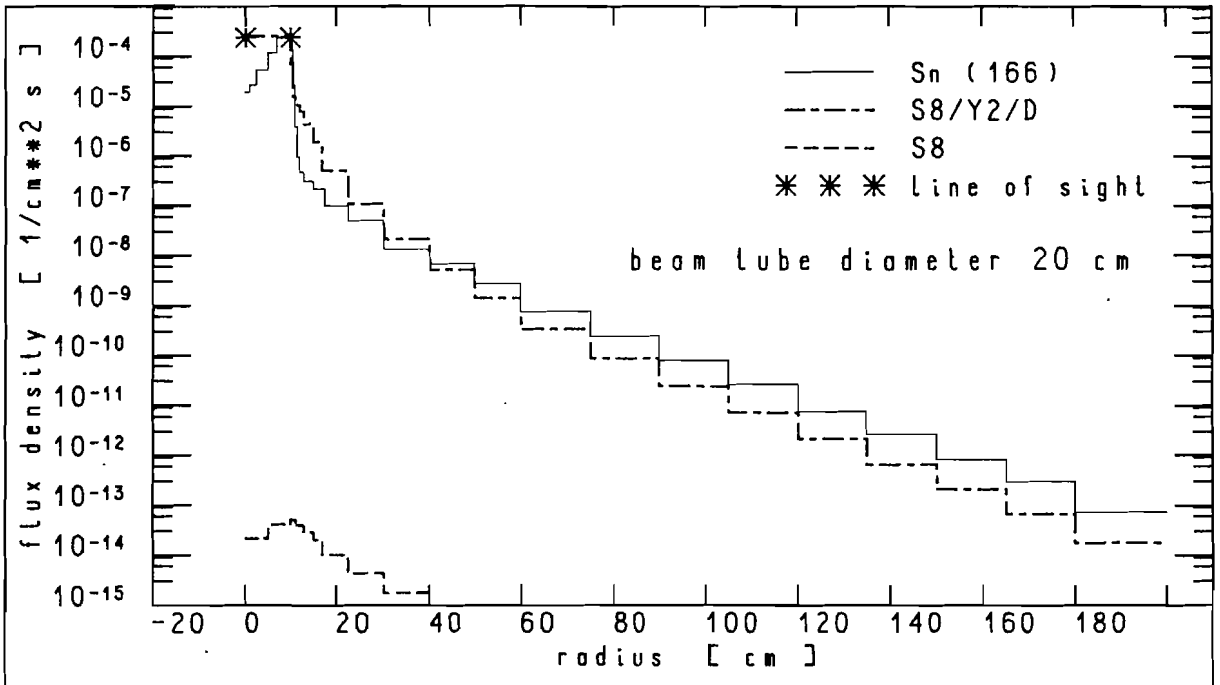

Radial flux distribution at the end of the beam tube (source 700-800 MeV)	IKE Stuttgart
	Fig. 2

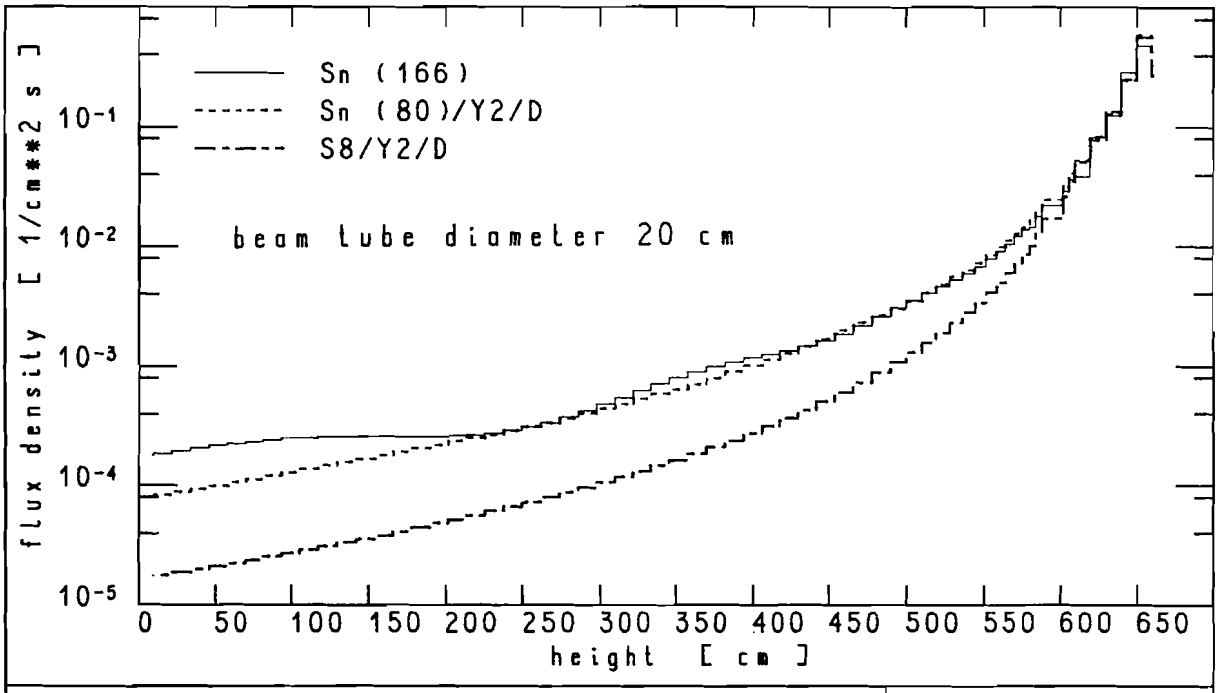

Axial flux distribution along the beam tube at r=10.25 cm (source 700-800 MeV)

IKE Stuttgart

Fig. 3

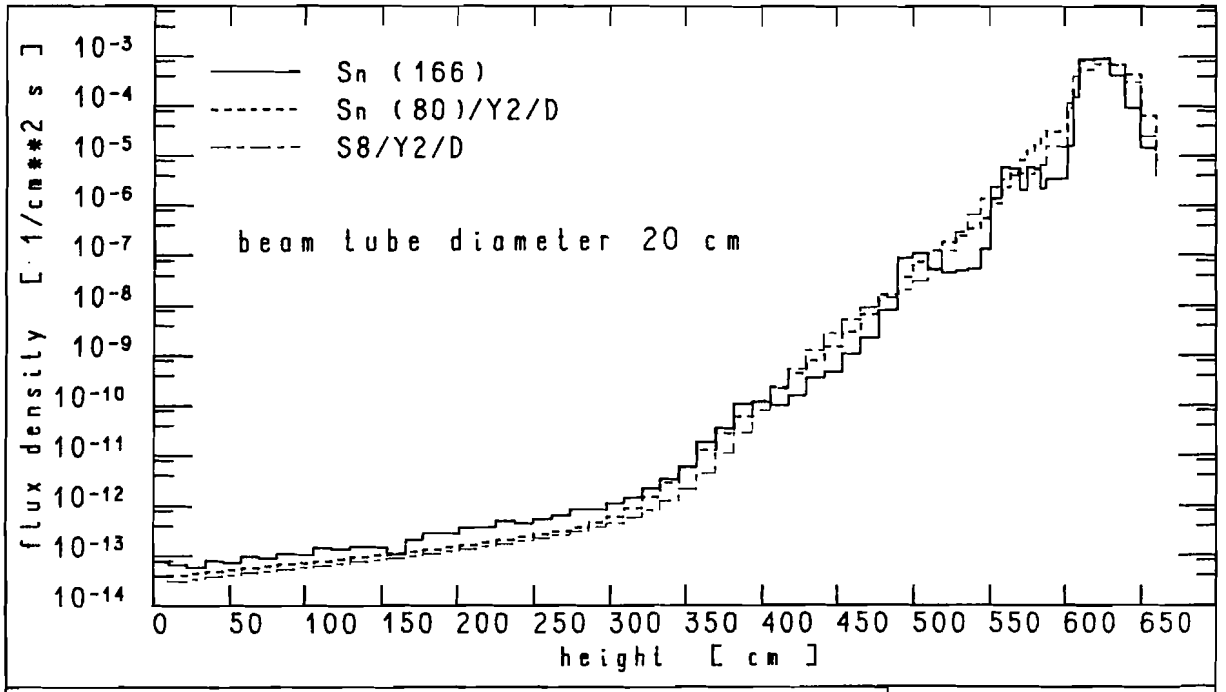

Axial flux distribution along the beam tube at r=190. cm (source 700-800 MeV)

IKE Stuttgart

Fig. 4

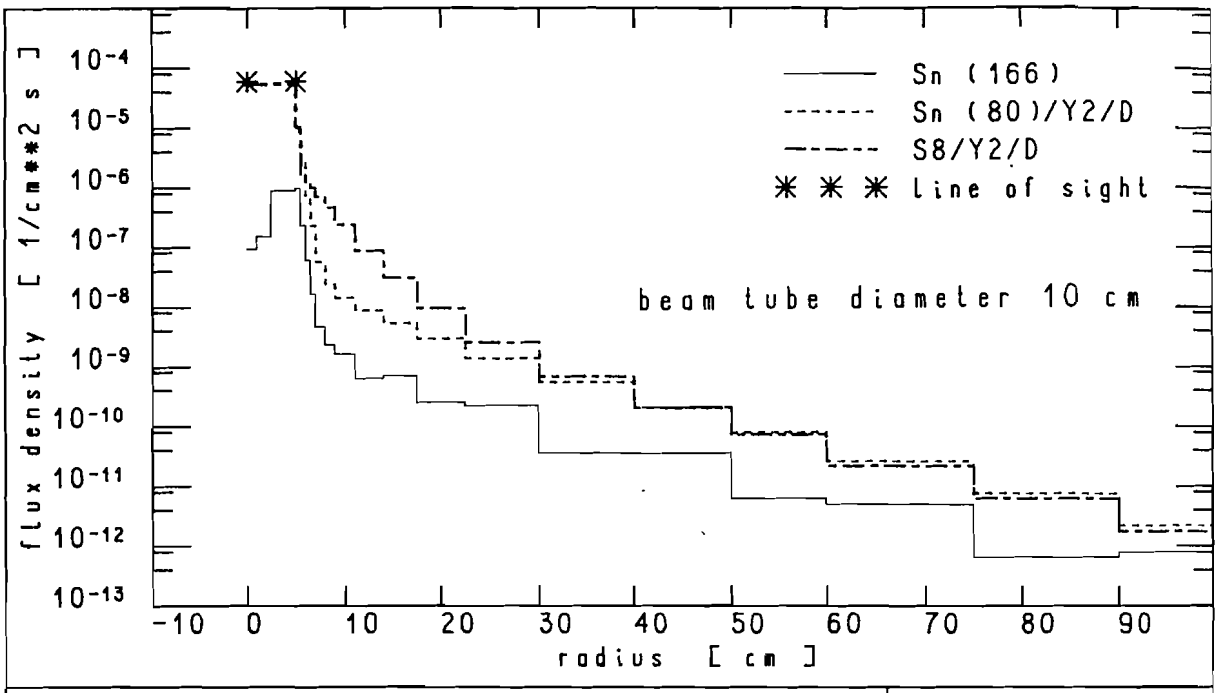

Radial flux distribution at the end of the beam tube (source 700-800 MeV)

IKE Stuttgart

Fig. 5

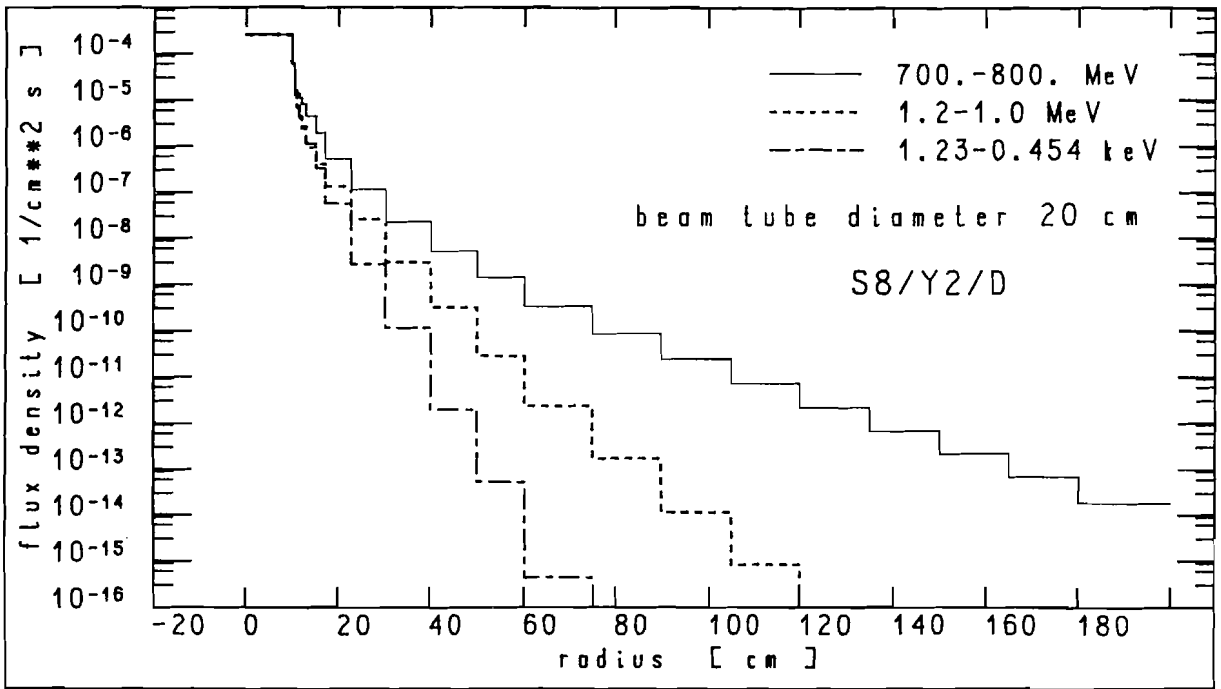

Flux distribution at the end of the beam tube for different source energies

IKE Stuttgart

Fig. 6

Proceedings of the Eighth Meeting of the International Collaboration on Advanced Neutron Sources (ICANS-VIII)
8-12 July 1985, Rutherford Appleton Laboratory Report RAL-85-110

CONSIDERATIONS ON BACKGROUNDS AT SINQ

F Atchison
Swiss Institute for Nuclear Research
CH-5234 Villigen, Switzerland

1 INTRODUCTION.

The SINQ project [1] aims to build a neutron scattering facility for the wavelength range of about 1 to 10 Å based on a continuous spallation neutron source: The end result will be a set of scattering instruments with their associated facilities, operating with a neutron flux comparable to that at a medium flux research reactor. It is our hope that users will be unaware that the source is not a reactor.

Experimentalists have come to terms with background problems at reactors (fast neutrons and gammas) and these problems will also be present at SINQ but accompanied by possible new effects from, (i) a high-energy (E > 10 MeV) tail to the neutron spectrum, (ii) high energy charged particles and (iii) a high-energy tail to the gamma spectrum (from neutral pion decay). It is the aim of this paper to examine what we know of these new background precursors and to see their effect on the design. So far, studies have been restricted to examining the problem of the high energy neutrons.

The principal concern is background at the spectrometers. Unlike pulsed sources where the sample is in the direct beam from the moderator, the continuous type includes a monochromator and it is this which will scatter part of the high-energy neutron contamination of the thermal neutron beam toward the spectrometer. The major worries arise from: (i) Estimation of the high-energy component at the monochromator is very difficult (inaccurate!): (ii) The effect of high-energy neutron contamination on experiments is unknown: (iii) The reduction of background can only be made at the expense of thermal flux.

The sources of high energy neutron contamination are illustrated in Fig 1: It is assumed we know how to build a bulk-shield hence direct shield leakage, ground and sky shine are excluded from the discussion.

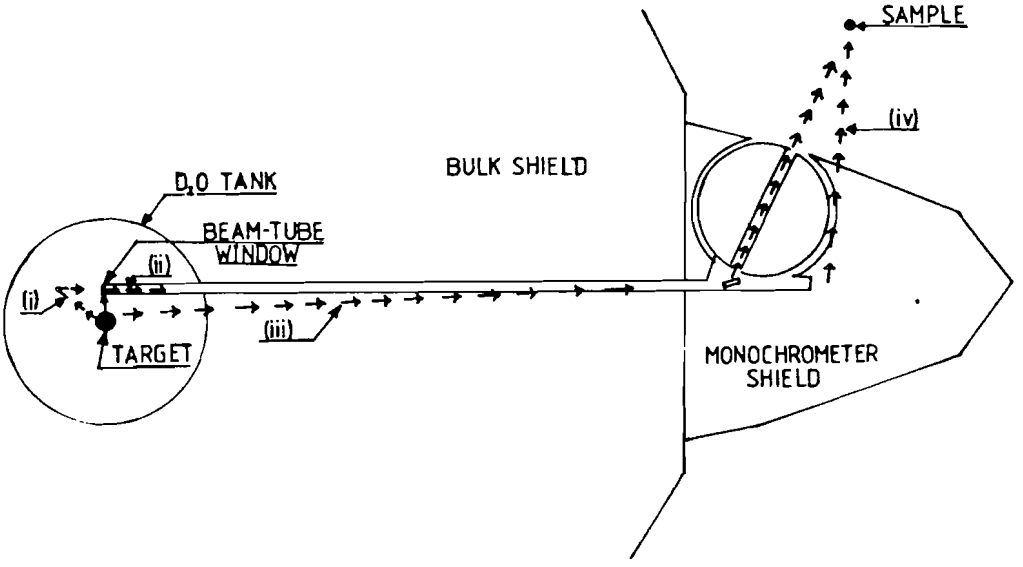

Fig 1: The principal sources of background caused by high-energy neutrons (direct shield leakage, sky and ground shine are neglected; see the text): (i) Scattering by heavy-water in the vicinity of the beam-tube window, (ii) scattering by the beam window, (iii) shield weakening due to the presence of the beam tube, (iv) leakage from the monochromator shielding.

2 THE EFFECT OF HIGH-ENERGY NEUTRONS.

The general consequence of background is to make the source less attractive to the user; reduced instrument resolution; increased experiment time due to more difficult background estimation; less convenient access to instruments. The possible effects may be collected together under three general headings:
(i) Measurement errors: (ii) Limitations on monochromator design: (iii) Radiation protection.

At present, little or nothing is known about the effects on the measurements being made, from having high-energy neutrons incident at the sample. This gives the major problem for design work that no guidance is available about levels of high-energy contamination which might be allowable in the beam from the monochromator. It is hoped that this may be quantified by experiment prior to construction of SINQ.

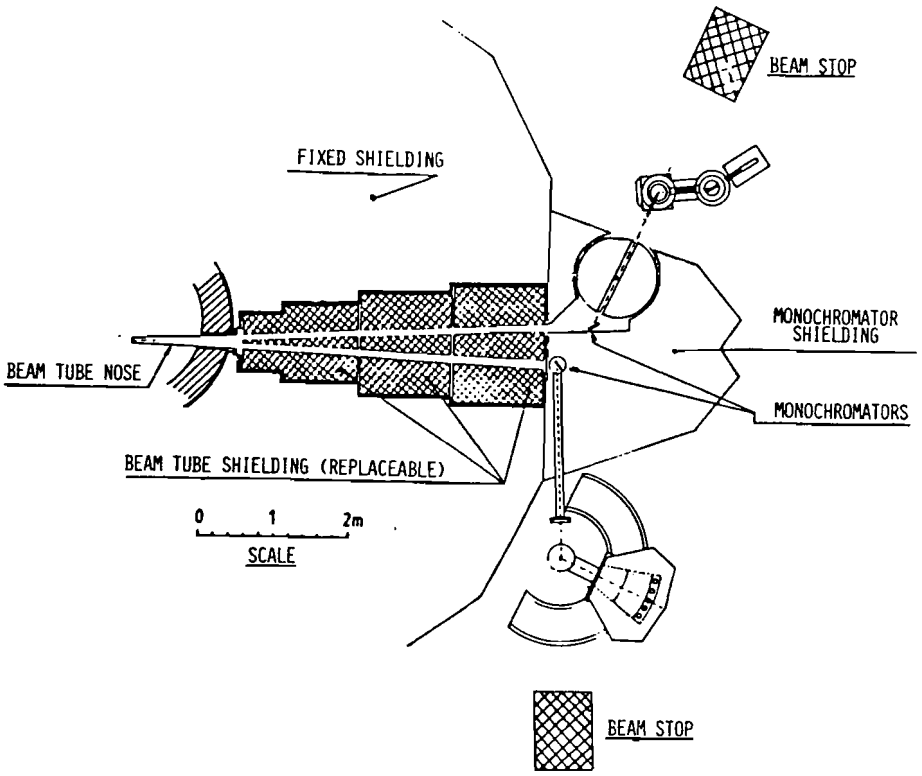

Fig 2: Schematic layout of a beam-tube pair with monochromators and instruments.

2.2 Limitations on monochromator design.

A sketch of a beam-tube pair with monochromators and instruments is shown in Fig 2. The presence of HE neutrons in the beam incident at the monochromator may be summarised as follows:

(a) The monochromator shielding external to the bulk shield will need to be large enough to effectively shield the HE neutrons; this restricts the space available for the instruments and is likely to be costly.

(b) The choice of monochromator crystal and configuration (transmission or reflection mode, single or double) will effect the fraction of HE neutrons scattered into the direction of the instrument. It would be unfortunate to have to restrict the design because of background.

(c) The smallest monochromator take-off angle will be set by the need to keep the monochromated beam out of the HE neutron flux directly passing through the crystal and its spreading out in the shield.

(d) The size of drums for adjustable monochromators will have to be sufficient to shield the HE scattered flux. They could become large hence cause thermal flux loss and be expensive.

(e) Increased activation problems in the monochromator system, hence difficulties with maintenance. HE neutrons tend to cause persistent activation whilst thermal neutrons generally cause short-lived.

2.3 Radiation protection considerations.

The expected thermal flux at the monochromator is of the order of $10^9/(cm^2.sec)$, with about 1% of this scattered toward the instrument by the monochromator. The (localised) equivalent dose of this beam is of the order of 40 rem/hour. A measurement by Cierjacks et al [2] showed a high energy flux of about $1.5 \times 10^7/(cm^2.sec)$ at 6 m along an 8 cm diameter beam tube for an 1mA proton beam incident at the target. The scattered HE neutron intensity into the monochromated beam direction has been estimated [3] to be 4 to 5 orders of magnitude lower than that incident; that is, $< 2 \times 10^3/(cm^2.sec)$ may be scattered toward the instrument and this corresponds to a (localised) equivalent dose of <0.4 rem/hour. This result is considered to be pessimistic compared to the situation expected with SINQ (see section 3.3).

The dose due to the high-energy neutrons should not add significantly to the radiation hazard from the thermal neutrons. The beam scattered by the sample should give doses at 1 m of less than 3 mrem/hour but attention will have to be paid to the provision of adequate shielding around the monochromator and efficient neutron catchers ("get-lost holes") behind the instruments.

3 ESTIMATION OF HIGH-ENERGY NEUTRON FLUXES IN BEAM TUBES.

The calculation of the HE neutron contamination in a beam tube is very difficult. These calculations need to estimate the neutron flux at the end of a narrow channel (50 to 100 cm^2 cross-sectional area) crossing about 5 m of shielding and having scatterers (beam window and D_2O) in the high intensity region close to the target; to allow design decisions, the calculations need to give information on how the contamination varies with pertinent parameters.

The HE flux escaping from the beam tube is considered to come from three principal sources, scattering by D_2O in the vicinity of the beam window, scattering by the window itself and shield weakening due to the beam tube. The Cierjacks et al [2] measurement was made with a geometric arrangement rather different from that being considered for SINQ; being the only experimental measurement available to us it is important to be able to compare it with our situation.

3.1 High-energy neutron scattering into the beam tube.

A first estimate for the variation with position in the moderator of the tangentially scattered HE neutron intensity into a beam-tube by D_2O was unnormalised [4]. A more direct estimate for this effect has been made by Monte-Carlo using the HETC [5] code. The calculation used in-core analysis to collect angular distributions at various positions in the moderator for HE neutrons, using as source a previously calculated target escape distribution. The angular distributions were extrapolated to give an estimate for the component tangential to the target. The calculation results are shown in Fig 3. The results show severe statistical fluctuation, but as a total of about 21 hours computer time was used, prospects of making any significant improvement look bleak.

The results have been used to normalise the previous calculation [4] of D_2O scattering and gives a factor of 5.9×10^{-12} to convert the numbers to units of $/(cm^2.sr.proton)$. The statistical fluctuations of the normalisation calculation give an RMS uncertainty of about 130%. The normalised results have been included into Fig 3 and show, within the uncertainties, reasonable consistency. The variation with position in the moderator of the contribution to HE neutron flux in the beam-tube of D_2O scattering, is shown in Fig 4.

The angular distributions in the moderator have been used to make a first estimate for the contribution of window scattering. The differential scattering cross-section averaged over the HE neutron spectrum from the target has been calculated for Aluminium using the MECCRL code [6]. This differential cross-section is folded with the angular distributions from the moderator calculation and the thickness variation of the window with angle. The estimated contribution as a function of position in the moderator is shown in Fig 5. The calculation also shows that there will be contributions from high-energy protons (about half the values for the HE neutrons), evaporation neutrons (roughly 60% of the HE neutrons) and evaporation protons.

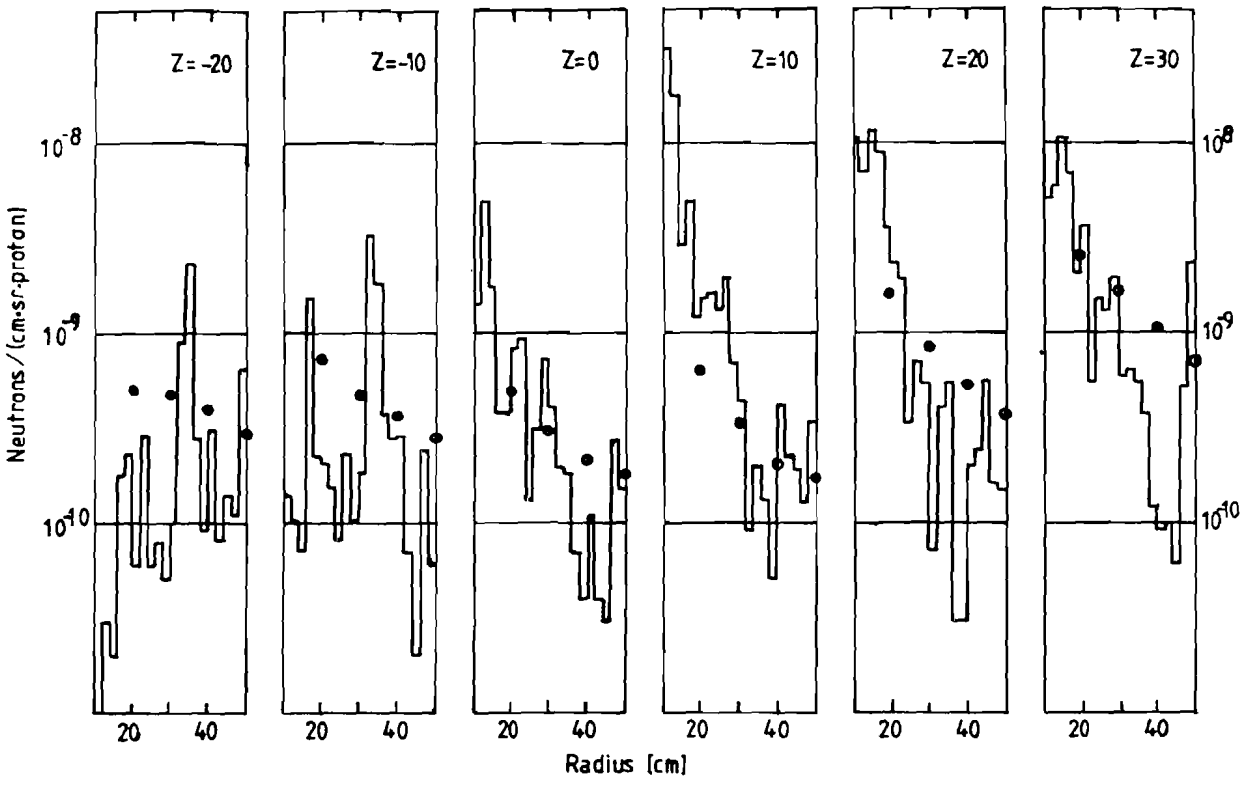

Fig 3: Radial variation of the tangentially scattered high energy neutrons by heavy-water for six positions (Z) relative to the front face of the target. 'o' are the normalised results from the calculation of reference 4.

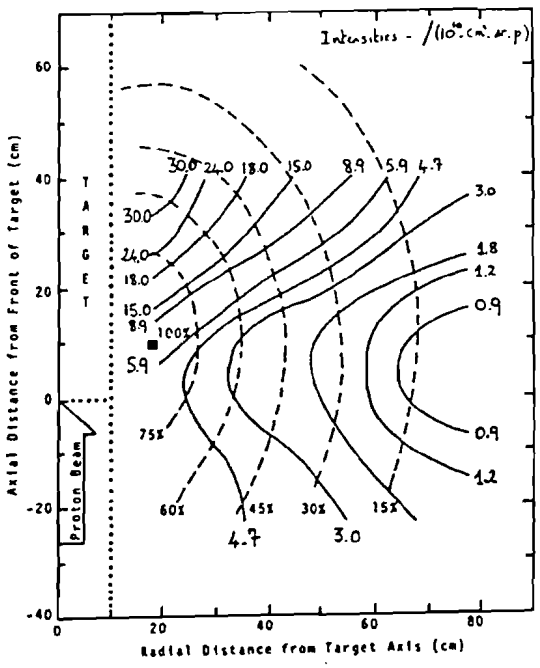

Fig 4:
Contours for the intensity of tangential HE neutron scatters by heavy-water as a function of position in the moderator. The thermal flux distribution is shown for comparison (dashed lines).

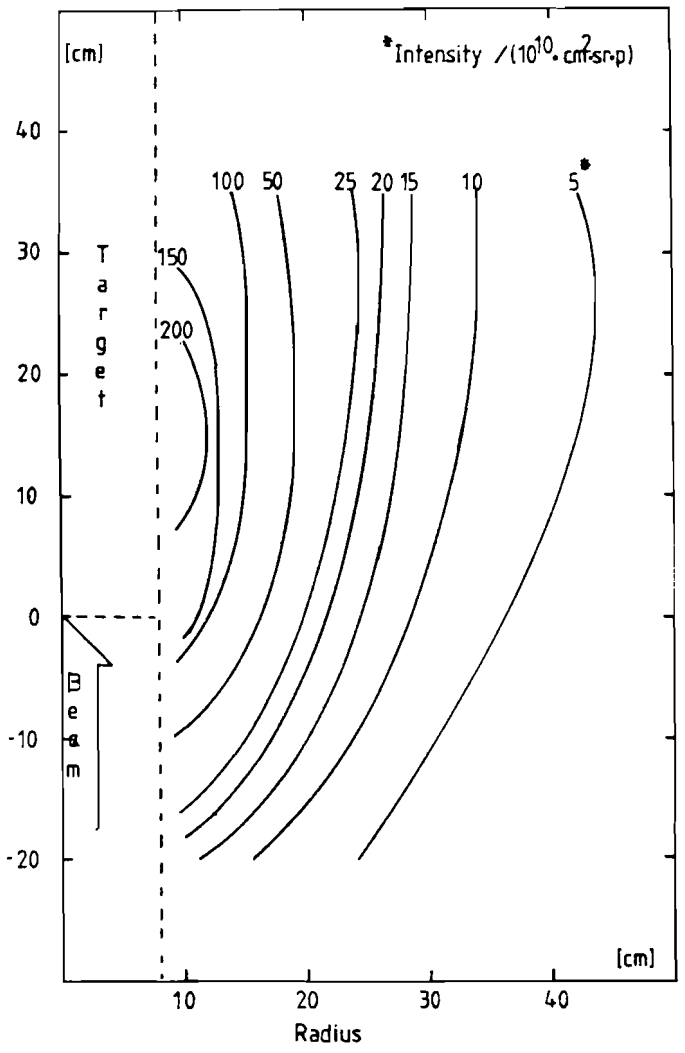

Fig 5: Contours for the intensity of the HE neutrons scattered by a 1 cm thick aluminium window, as a function of position in the moderator.
Note: The scales used for this figure are not the same as those for Fig 4.

3.2 Beam tube shield weakening.

A first estimate, based on the simple exponential shielding model, has been made of the effect of loss of path length in the shielding due to the presence of the beam tube. The calculation uses the simplified geometry illustrated in Fig 6. For SINQ, S = 5m, M = 1m and the neutron fluxes at the monochromator for various size beam tubes and beam tube tip radii are shown in Fig 7.

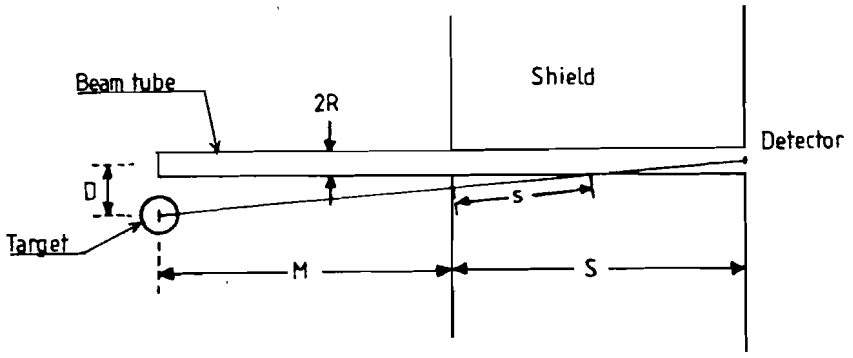

Fig 6: Simple exponential shielding model estimate for the effect of shield weakening due to the presence of a beam tube. The path length in shielding, s, is given by $s = S - (M + S) \times R/D$. Build-up is accounted for by reduction of the distance s by a length σ. For SINQ, the path is in Iron and a shielding length of 17.3cm and a value of σ of 75cm are used.

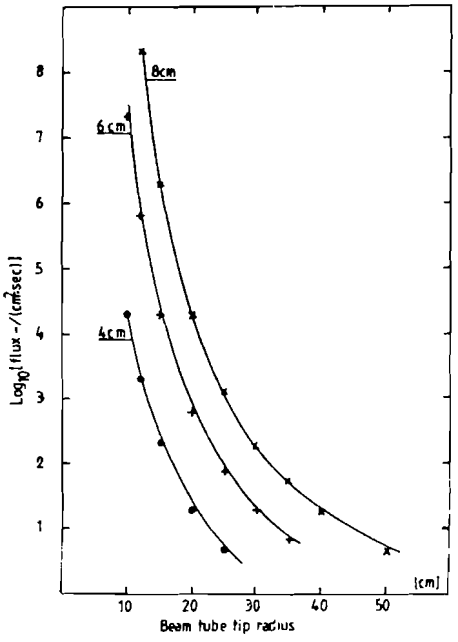

Fig 7:
High energy neutron intensity at the end of a 6m long beam tube due to shield-weakening, as a function of beam-tube tip radius and for SINQ at 1mA. Results for beam tubes of radii 4, 6 and 8cm are shown.

3.3 Comparison with the measurement of Cierjacks et al.

The results of Cierjacks et al [2] show a high energy (E>15 MeV) current at 6m down an 8cm diameter beam tube for 1mA proton current on the target of about 1.5×10^7 /(cm^2.sec). The moderator material used was light-water and the beam tube was at D = 13cm from a 15cm diameter target. The tube itself was at 30° to the target axis.

The results of the calculations presented in sections 3.1 & 3.2 indicate the following contributions:

Scattering by H_2O (taken as = D_2O)	1.7×10^3/(cm^2.sec)
Scattering by Al window (3mm thick)	4.5×10^3/(cm^2.sec)
Beam hole shield weakening	0.9 to 10.0 $\times 10^7$/(cm^2.sec)

The calculated value for the HE neutron contamination is in quite good agreement with the measurement and indicates that the shield weakening dominates; the order of magnitude range in the predicted value reflects the difficulty of choosing values for the parameters of the model used. This is also unfortunate, as in the case of SINQ it is the first two terms which dominate (see section 4.1) and these terms could be increased by factors of several hundred without giving a significant contribution in this case.

4. REDUCTION OF THE EFFECT OF HIGH ENERGY NEUTRON CONTAMINATION.

The pessimistic assumptions of the estimate presented in section 2.3 indicate that the expected HE contamination will not require special extra restrictions on instrument access. The principal problem will be background in the spectrometers from having HE neutrons incident at the sample. Having little guidance about allowable contamination (it ought to be as high as possible or thermal flux will be being wasted), the source parameters available for background reduction will be briefly discussed.

4.1 Beam tube tip radius.

The present design for SINQ requires that this be a fixed parameter for the source. The ideal choice is for a radius in the viscinity of the thermal flux maximum in the moderator but has to be somewhat larger to reduce the fast neutron and gamma contamination and (where appropriate) the power load on cold sources. The current design uses radii of 25, 27 and 30 cm and has two layers of beam-tubes. The estimated HE neutron source strength at a monochromator 6m from the target and for a 1 mA proton current are now tabulated:-

Tip-radius [cm]	D_2O scattering [no/(cm^2.sec)]	Window scattering [no/(cm^2.sec)]	Shield weakening [no/(cm^2.sec)]
25 (lower level)	1500	1100	180
27 (upper level)	1500	3100	100
30 (lower level)	750	700	40
30 (upper level)	1200	3100	40

The present calculation indicates the contamination will be a factor of 3000 to 10000 lower than for the situation measured by Cierjacks et al [2]. This has obvious important consequences on the design for the monochromator shielding and the particularly strong variation of the shield-weakening contribution requires confirmation.

4.2 Beam tube length and aperture.

Reduction of the beam tube aperture will cause reduction of the HE neutron contamination as will increasing the beam tube length. They will also reduce the thermal flux. The design concept includes special equipment boxes in the bulk shield to allow the size and the materials in this region to be changed (see Fig 2). The monochromator and its shielding are added externally to the bulk-shield. In the case of take-off angles greater than 90°, the monochromator will be moved radially to a position outside the limits of the bulk shield to allow space for the instrument.

4.3 Monochromator design.

The predicted 4 to 5 orders of magnitude reduction of the HE contamination scattered to the instrument would seem to give a very low contamination at the sample. The use of distance between monochromator sample and/or double monochromator systems will allow further reduction should the actual contamination be significantly higher than predicted or a very large depression be required for background supression. The loss of thermal flux due to added distance may be partly compensated by use of focusing monochromators.

5 CONCLUSIONS AND DISCUSSION.

The high-energy neutron contamination of the thermal beam at the monochomator will not be known with any great certainty when SINQ starts operation as long as we have to rely on calculation. In a similar way, the effect of high-energy neutrons at the sample on instrument background being extremely uncertain means there is no guidance as to what levels should be aimed for.

The magnitudes for the estimated HE neutrons incident at the sample, indicate that they do not significantly increase the radiation protection problem at the scattering instruments. Removal of the monochromator crystal and the provision of a rather modest shutter, should allow access to the instruments whilst the source is running.

The final decision on what beam tube tip radii should be used is important as it determines the basic high-energy neutron contamination at the monochromator. The predicted large reduction of the shield-weakening term will need confirmation by more exact methods; the inclusion of leakage out of the bulk-shield and into the beam tube may start to become significant at the low levels predicted. There would seem to be sufficient flexability with other variables in the system, to produce low high-energy neutron contamination at the sample; this mitigates the consequence of uncertainty in the estimates but, most likely, will be paid-for by having a final SINQ performance (ie thermal neutron flux) below its potential best.

REFERENCES.

[1] W E Fischer, "Status report on SINQ" - These proceedings.

[2] S Cierjacks et al., Proc. 5th ICANS, Julich 1981. Jul-Conf-45, 215 (1981)

[3] A Furrer (Editor), "Bericht der Diskussionstag uber Neutronenstreuung". AF-SSP-123 (1983)

[4] F Atchison, Proc. 7th ICANS, Chalk River 1983. AECL-8488, 266 (1984)

[5] Radiation Shielding Information Centre code package CCC-178, HETC.

[6] MECCRL is the Intra-nuclear cascade/evaporation code extracted from HETC (see reference 4 for more details).

Proceedings of the Eighth Meeting of the International Collaboration on Advanced Neutron Sources (ICANS-VIII)
8-12 July 1985, Rutherford Appleton Laboratory Report RAL-85-110

DESIGN CALCULATIONS FOR THE SNQ SHIELD

P. Cloth, D. Filges, R.D. Neef, J.M. Zazula*
Institut für Reaktorentwicklung, Kernforschungsanlage Jülich
*Institute of Nuclear Physics, Cracow

This paper presents the results of three special activities on SNQ shielding calculations: The neutron flux outside the accelerator tunnel from the view of earth activation, dose rates outside the SNQ target station and activation of air and earth in the surroundings thereof, and the radiation heating of the near target parts of the SNQ shield were calculated.

1. Shielding of the Accelerator

Neutron fluxes in order to determine the production rates of some important nuclides (guide nuclides, Table I) in the earth shield of the SNQ accelerator were calculated using high energy secondary particle cascade theory and group Monte Carlo techniques for low energy neutron transport. The HETC KFA version /1/ together with MORSE /1/ were run for this problems on CRAY-XMP.

The accelerator tunnel was modelled as a channel of virtually infinite length and with the cross section shown in Fig. 1 which is an adequately simplified model of the technical layout given in Fig. 2.

Table I

^{151}Eu (n,γ) ^{152}Eu
and the following neutron induced
threshold reactions

^{24}Mg -> ^{22}Na, ^{24}Na
^{25}Mg -> ^{22}Na, ^{24}Na
^{26}Mg -> ^{22}Na, ^{24}Na
^{27}Al -> ^{22}Na, ^{24}Na

For the beam losses, which are the source of radiation in this shielding problem, the following assumptions were made: The lost protons of the beam amount to $3x10^{11}$ per meter and have energies of 1100 MeV each. They will interact with massive parts of the accelerator structure mainly made of steel. This was simulated by assuming a stopping iron target in the beam line.

The neutron fluxes were calculated in different areas (see Fig. 1) in order to obtain the spatial dependence. The area of highest flux is marked in Fig. 1 and the according spectrum is given below in Fig. 3. The broken line denotes the high energy part of the spectrum calculated with HETC, and the low energy spectrum calculated by MORSE is given by the solid curve.

2. Radiation Protection Problems Connected with the SNQ Target Station

The bulk shield calculation that were performed for the SNQ target station do not predict the radiation doses outside the shield and should, therefore, be completed by taking into account the so-called "skyshine" and "groundshine" effects, which are due to the backscattered radiation from the atmosphere and the earth. To study this problem, the neutron yield from an ^{238}U target irradiated by an 1100 MeV proton beam has been considered as a source. Neutron/secondary gamma transport calculations have been performed through the shield and in the neighbourhood up to 1 km from the target station. Unfortunately, the recently performed Monte Carlo hadronic cascade calculations are restricted to the region close to the target assembly and are not able to account for the albedo effects and the phenomenon of neutron spectra transition between different media. Therefore, for the problem with a large spatial range to be solved here the two-dimensional discrete ordinates computation remains the favourable calculational technique.

The procedure of analysis required considering the following three items: (a) the space, energy and angular dependence of the secondary radiation source, produced by the beam interaction with target and other irradiated materials, (b) description of the transport process of the secondary radiation through the shield, ground and atmosphere, and (c) using the response functions relevant to the radiation interaction with elements of environment, human tissue, radiometric counters, etc. The management of the system of applied computing codes and data files is shown in fig. 4. For the source step the KFA version of the INC Monte Carlo code HETC /1/ was run for the three-dimensional model of the ^{238}U target. The spallation events from HETC scored by the SIMPEL code /1/ to the volume-averaged secondary neutron yields versus angle and energy were

then input to the GRTUNCL code /2/, calculating analytically the first-collision neutron source. The SNQ facility was modelled in the cylindrical "r-z" geometry, as is shown in fig. 5. The target station consisted of a 5.5 m thick iron shield, surrounded by a 1 m thick concrete layer. The target was considered to be a point source of secondary neutrons from the spallation, with yields equivalent to the thick target, located on the height 1.5 m above the ground level, on the "z" axis. Azimutal symmetry was assumed with the beam direction representing all the azimutal angles. The angular anisotropy was taken into account for the different vertical angles with the "z" axis. There was a graphite moderator of 2 m height and 3 m diameter, placed above the source position. The atmosphere and the ground surface were included up to a distance of 1.5 km away from the SNQ facility and up to 1.5 km above. The LAHI /3/ multigroup neutron cross-section library (KFA combination of the ORNL and LANL libraries) was connected. The highest energy group (700-800 Me) was uniformly extended to the proton source energy of 1100 MeV.

The DOT.4 /2/ two-dimensional discrete ordinates code system was used to solve the neutron and secondary gamma transport equation. The P_3 order Legendre expansion and the S_4-S_8 angular quadrature sets were applied. The results from DOT, the space and energy-dependent neutron and γ fluxes (e.g. Fig. 6) were integrated over energy with several multigroup response functions. The low energy part of the responses (below 17.5 MeV) was collapsed from the MACKLIB-IV library /4/. The high energy parts of the same responses were obtained using the so-called thin target option of the HETC code (Ref. 5). Some radiation protection responses, like the flux-to-dose conversion factors, were appended from the literature /6/. Dose equivalents at various points are given in Table II. The space dependence of the neutron flux, the dose equivalent, the absorbed dose and the induced reactivity are shown by Figs. 7 and 8.

Table II

	low-energy neutrons	high-energy neutrons	gammas	total
below the ground level	4.01×10^{-2}	4.21×10^{-4}	5.69×10^{-3}	5.00×10^{-2}
at the beam level	1.13×10^{-1}	6.03×10^{-3}	1.84×10^{-2}	1.32×10^{-1}
above the roof	3.61	1.91×10^{-3}	5.03×10^{-2}	3.68

3. Radiative Shield Heating

The near target regions of the SNQ shield are intensively exposed to radiation from the target. The layout of the necessary cooling system is strongly dependent on the distribution of the energy deposition which has large gradients and peak values of about 1 W cm^{-3}.

The material in the part of question in the shield is mainly lead shot with some steel structure. As the density of steel is not far away from the density of lead shot, it was, for simplicity reasons, assumed that the whole inner part of the shield was made of lead of density 8.0 g cm^{-3}. Voids and ducts like the beam tubes and the proton channel were considered to be of some importance for the radiative energy transport, and thus taken into the simplified modelling of the SNQ target station. The geometric model was covered by a mesh grid to attain space dependence of the results of the energy distribution calculations. The calculations were also performed using the HETC/MORSE code system for the high and low energy fractions of the energy deposition, respectively. Figs. 9 and 10 show cuts through the target station giving a rough picture of the distribution of energy deposition. The values of the energy deposition in these originally coloured pictures may

not be clearly recognized. A more detailed report on the subject of this section is being prepared. The energy depositions in the target, the moderators and the reflector are not considered here, as these components have own cooling circuits.

4. References

/1/ P. Cloth, D. Filges, G. Sterzenbach, T.W. Armstrong, B.L. Colborn
Jül-Spez-196, March 1983

/2/ W.A. Rhoades et al.
ORNL/TM-6529, Oak Ridge National Laboratory (1978)

/3/ H. Schaal
SNQ 3j./BH 120783, KFA Jülich GmbH (1983)

/4/ Radiation Shielding Information Center
RSIC/DLC-60, Oak Ridge National Laboratory (1978)

/5/ J.M. Zazula, P. Cloth, D. Filges
SNQ A1015.1, KFA Jülich GmbH (1985)

/6/ E.A. Belogorlov, V.T. Golowachik, V.N. Lebedev, E.L. Potjamkin
Nucl. Instr.Meth. 199: 563 (1982)

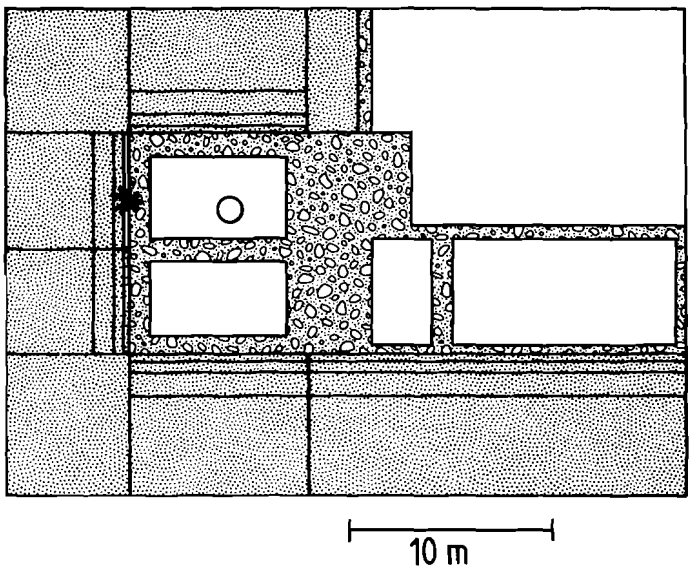

Fig. 1: 3-D computer simulation of accelerator tunnel

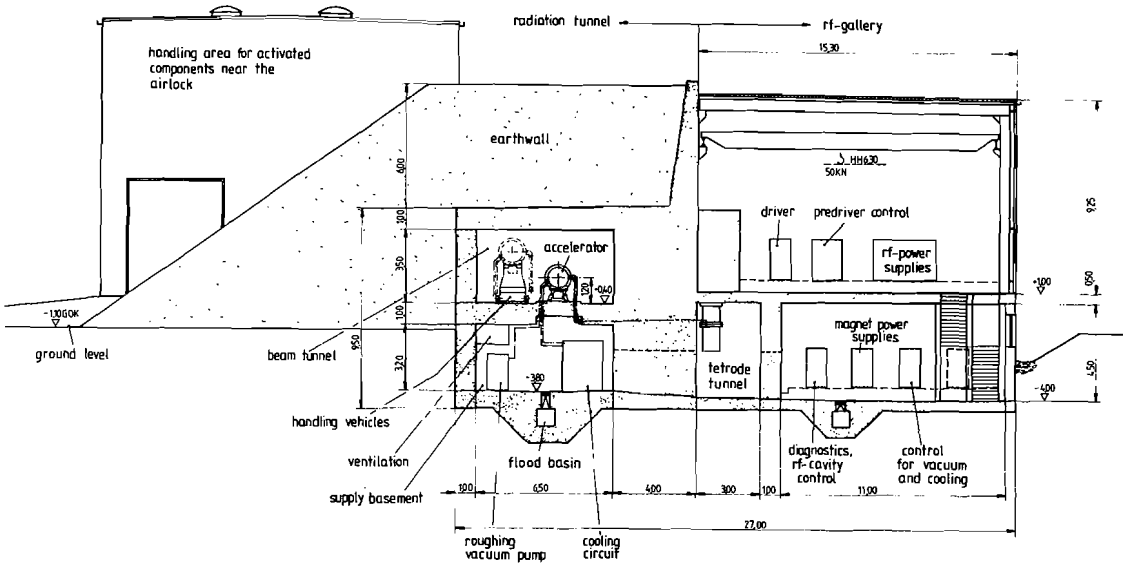

Fig. 2: Technical layout of accelerator tunnel

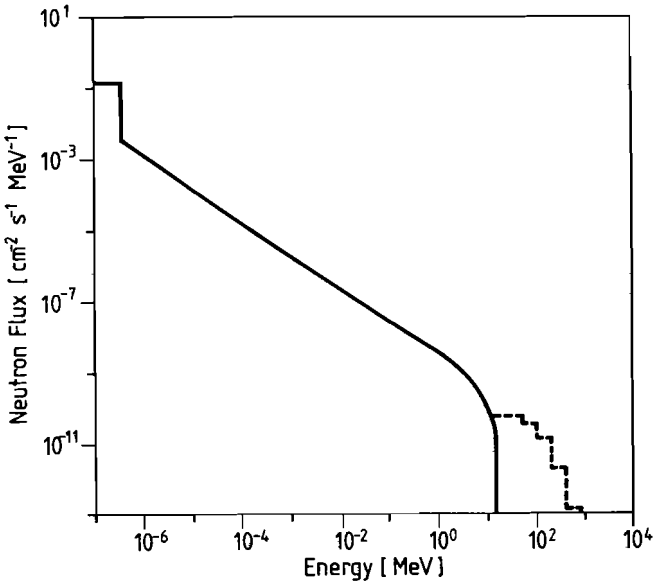

Fig. 3: Typical neutron spectrum in the soil around the accelerator shielding (*marked area in Fig. 1)

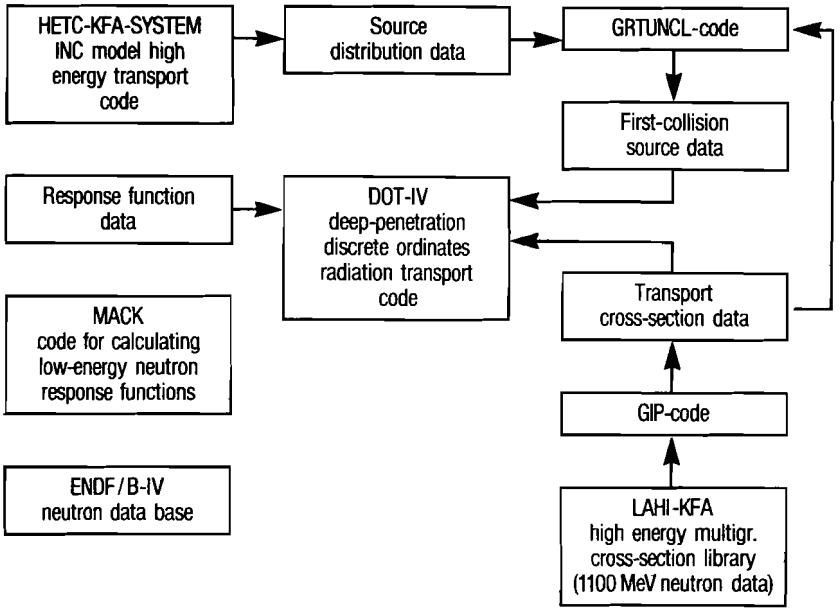

Fig. 4: Management of the computing codes and data bases in the system of Analysis

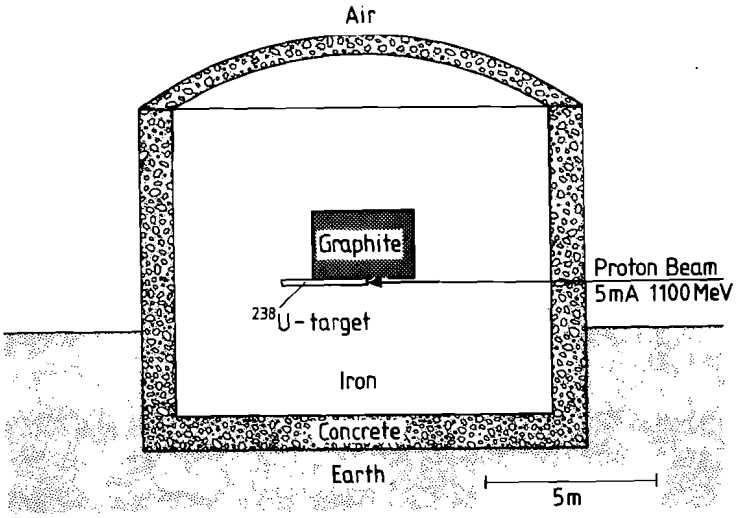

Fig. 5: The geometrical model for 2-D transport calculations (in principle)

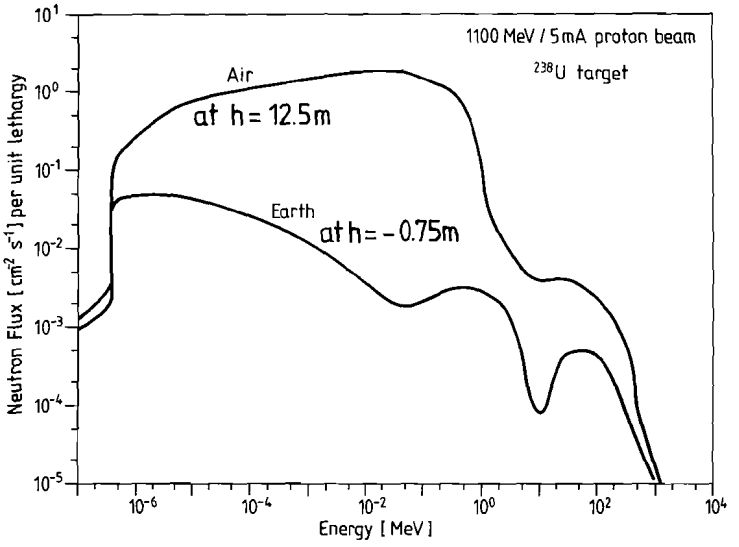

Fig. 6: Comparison of neutron spectra in air and in earth, outside of the shield

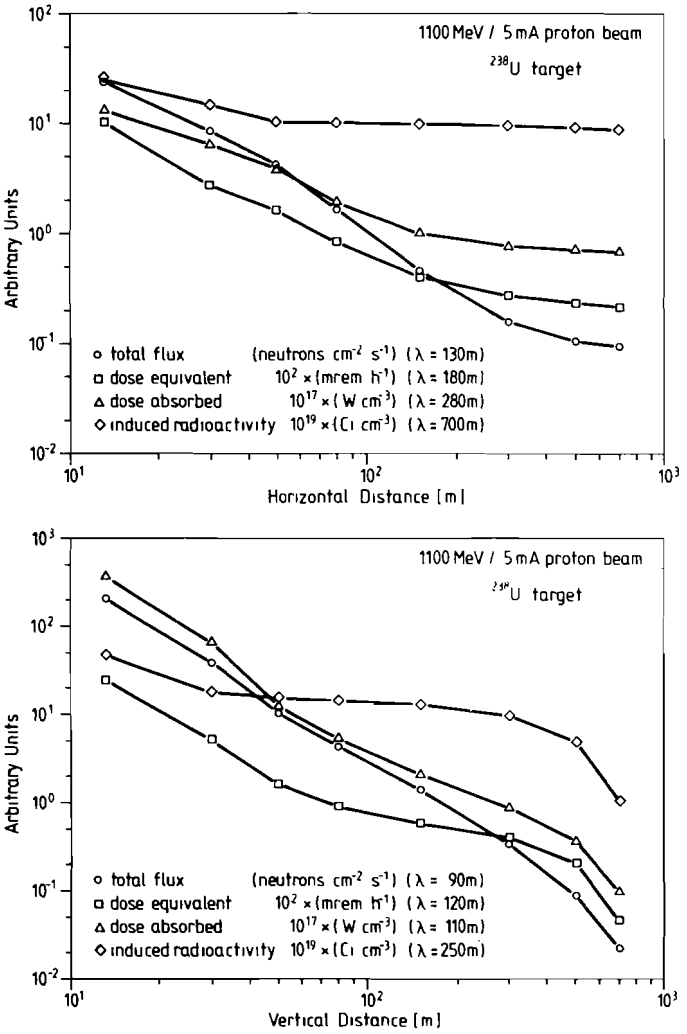

Fig. 7, Fig. 8:
Horizontal and vertical dependence of the total flux, dose equivalent, absorbed dose and induced radioactivity in air, outside of the target station with shield

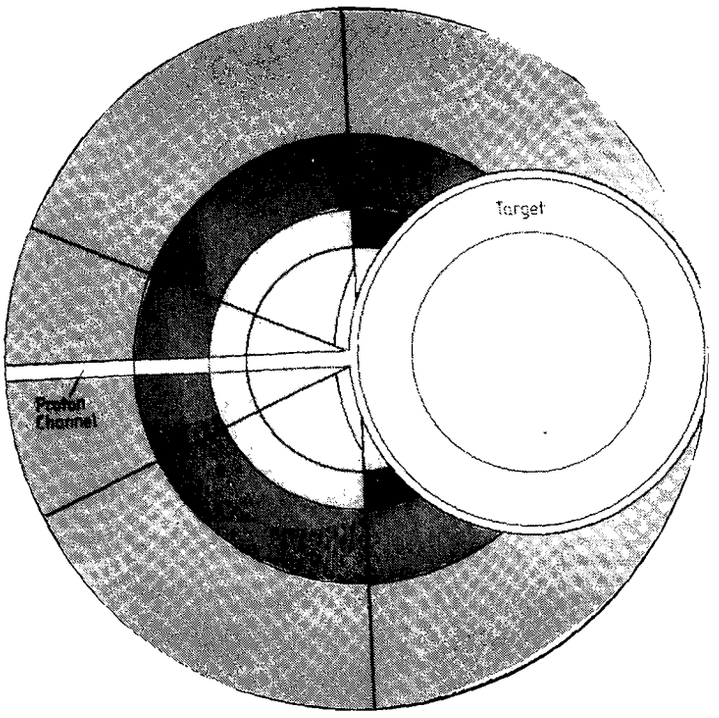

Fig. 9:
Horizontal cut in target level

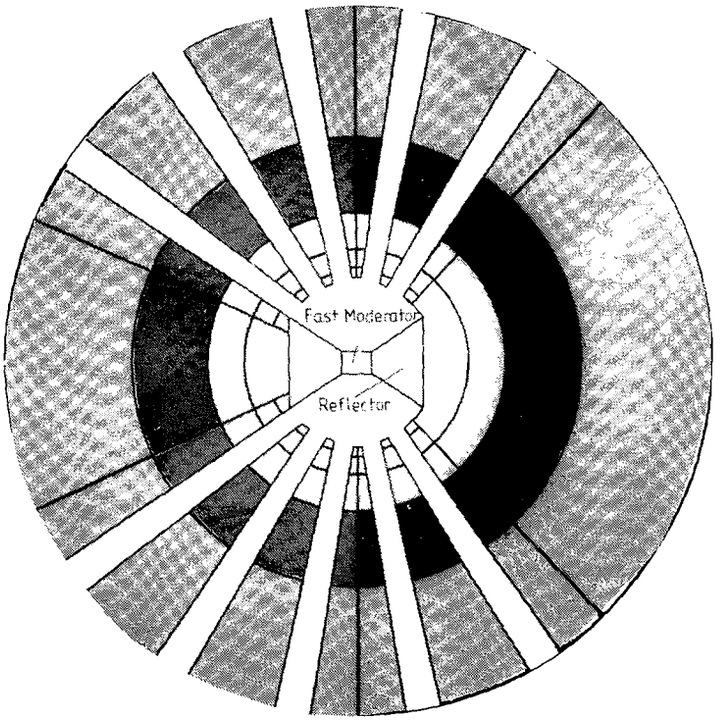

Fig. 10:
Horizontal cut in beam tube level

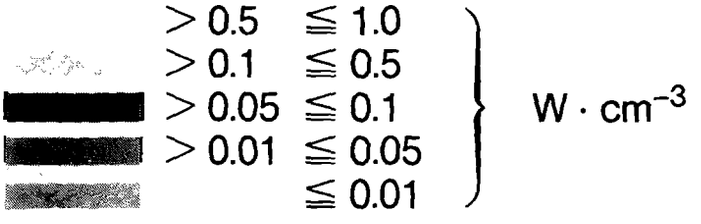

Proceedings of the Eighth Meeting of the International Collaboration on Advanced Neutron Sources (ICANS-VIII)
8-12 July 1985, Rutherford Appleton Laboratory Report RAL-85-110

CRISPY MIX and *FLEXI MIX* - HIGH BORON CARBIDE CONTENT, RESIN BONDED, NEUTRON SHIELDING MATERIALS

V T Pugh and B W Hendy
Rutherford Appleton Laboratory

INTRODUCTION

The most difficult regions to provide neutron shielding for a neutron scattering instrument are the inner surfaces of collimators, sample environment chambers and detector banks. In these regions some of the neutrons that enter the shielding will be partially thermalised and scattered out of the shielding. These neutrons may then find their way to the detectors and cause errors in the recorded data. This effect is more of a problem with epithermal neutrons than thermal neutrons because the neutron capture to scatter ratio increases with energy and average interaction lengths are longer at higher energies. It is therefore necessary to ensure that the neutron capture to scatter ratio of the shielding material in the critical regions is high when epithermal neutrons are present.

Boron carbide has been used in many forms for neutron shielding because of the large thermal and epithermal neutron capture cross-section of boron-10 and because it is an inert material. However boron carbide is difficult to machine so other methods of shaping it for neutron shielding have been used. Boron carbide grit can be poured into a container such as an aluminium can or a thin polyethylene bag, it can be sintered to form sheets, or it can be bonded together with a binder.

Resin bonded boron carbide tiles have been used for neutron shielding for some time. Resins have small neutron capture cross-sections and contain hydrogen which is efficient at thermalising neutrons, but if the resin content is minimised the composite material has a large neutron capture to scatter ratio for both thermal and epithermal neutrons. Professor N Watanabe of KENS Japan has developed a recipe and technique for producing a composite with a resin content of 6%-10% by weight. In attempting to repeat these results the authors have developed two forms of resin bonded

carbide that have good mechanical properties, fairly uniform density and allow for simple fabrication techniques.

"Crispy mix" and "flexi mix" are mixtures of various boron carbide grits with resin that form solid composites when heat cured. Crispy mix has a rigid structure and a boron carbide content of 97% by weight. The same mixture of grit sizes can be used with a 2% resin content, but this gives some loss in mechanical strength and the resultant composite has a crumbly surface. Flexi mix is easily bent but the penalty for this flexibility is a lower boron carbide content (90%) and therefore a much higher resin content (10%).

CRISPY MIX

Most of the techniques, described below, for producing the composites were developed using the crispy mix recipe. Three grit sizes of boron carbide were used (coarse F20, medium F40 and fine F60). Various percentage combinations of the three sizes were prepared and tested and several resin binders were tried. All test samples had a small amount of fine grit, 1% to 7%, a coarse grit content of 20% to 90% with the remainder of the mix made up from medium grit and resin. The best resin of those tested was a Ciba-Geigy Araldite resin with a Thikol Chemicals hardener in the following ratios :

Epoxy resin	MY 740	100 parts
Hardener	EM 308	50 parts

Each test mix was cast into a 6 mm tile in an open mould and qualitatively tested for "strength" (can it be broken by hand?), "even density" (can light be seen through pinpricks in the tile?), "surface integrity" (does the surface crumble when rubbed with a finger?) and "surface resin" (is the surface glossy and resinous or dull and only lightly covered with resin?). The combination of grit sizes and resin that gave the lowest resin content by weight with good mechanical properties and a dull surface was :

Coarse grit	F20	38%
Medium grit	F40	56%
Fine grit	F60	3%
Resin		3%

FLEXI-MIX

To develop flexi mix the same ratio of boron caribe grit sizes were mixed with a more flexible resin. The ratio of epoxy resin to hardener and the percentage of resin in the final mix were adjusted until a 6 mm tile of flexi mix had the right combination of flexibility, integrity and low resin content. The best resin tested was made from the following ratio of Ciba-Geigy Araldite components :

Epoxy resin	CY 208	100 parts
Hardener	HY 219	25 parts
Accelerator	DY 219	2 parts

The mixture must then be oven cured at 120°C for 2 hours.

The best mix had the following ratio of boron carbide grit sizes and resin:

Coarse grit	F20	35%
Medium grit	F40	52%
Fine grit	F60	3%
Resin		10%

PREPARATION OF THE UNCURED MIX

Preparation of the two mixes is similar. The resin components are preheated to 60°C before mixing. Preheating reduces the viscosity of the resin and produces a more even distribution of resin when mixed with boron carbide grit. The boron carbide grits are dry mixed before adding hot resin and mixing. Great care must be taken to ensure that all globules of fine grit are broken up and evenly mixed with the rest of the grit and that the grit is evently wetted by the resin. All test batches were hand mixed with a steel spatula. To ensure even mixing no more than 400g of the mix were made in one batch, the grits were mixed for at least 4 minutes and the resin mixed with the grit for a further 10 minutes. A power-assisted mixer should raise the batch size limit. The raw mix has a damp appearance and no cohesive structure. It must be held in a mould and hot cured to produce the solid composite.

CRISPY MIX MOULDS

Three types of mould have been used to shape crispy mix during the curing stage: open moulds, closed moulds and hot-press moulds.

Open moulds have a base and sides made from aluminium and an open top. Shapes PTFE blocks have been inserted into some moulds to produce holes and surface profiles. The moulds are lined with thin sheets of PTFE, the mixture tamped into the mould and baked at 80°C for a time that depends on the maximum thickness of the mix (90 minutes for 60 mm and 4 hours for 50 mm). The moulds are then left to cool before removing the composite.

Closed moulds are used to produce awkward shaped structures such as thin curved pieces. The mixture is semi-cured for half the normal curing time in flat open moulds that have similar dimensions to the final shape. It is then transferred to the final mould in its green state, where it can be stretched, bent and joined surface to surface. The mix is enclosed on all sizes and returned to the oven to complete the curing.

Hot-press moulds were used to produce "high-density" flat tiles. A piece with the shape of the tile was removed from the centre of a 6 mm thick ground steel plate and the cut edge sprayed with PTFE releasing fluid. The mould was filled with crispy mix and placed between two ground steel pressure plates. To prevent the tiles sticking to the pressure plates 2 sheets of 1 mm PTFE were sandwiched between the plates and the side moulds. A pressure of 300 kg/cm^2 and a temperature of 80°C was applied for 1 hour. The moulds were then left to cool before removing the tiles.

FLEXI MIX MOULDS

So far flexi mix has only been used to cast 6 mm thick flast tiles in an open mould, but the authors see no reason why it should not be produced using the same range of techniques as crispy mix. The mixture must be baked in the mould at 120°C for 2 hours. The mould is then left to cool before removing the tile.

CRISPY MIX TESTING

Most of the testing done during the development of crispy mix has been a qualitative comparison of one tile with another and a subjective assessment of the various fabrication techniques. The major findings are outlined below :

- A resin with a little flexibility produces a more robust tile than a harder resin.

- If the resin content is reduced to 2% there is some loss of mechanical strength and the composite has a crumbly surface.

- When cast into an open mould the composite had a density of 1.45 g/cm^3 (cf 2.52 g/cm^3 for solid boron carbide). When hot pressed a density of 1.8 g/cm^3 could be achieved but the tile was difficult to remove from the mould and separate from the PTFE sheet. A hot pressed tile with a density of 1.7 g/cm^3 could be easily removed from its mould.

- While a minimum thickness of 6 mm is recommended for a robust tile, tiles have been cast with 3 mm thick by 10 mm wide lips. These lips can withstand minor knocks but break when flexed or roughly treated.

- A 6 mm thick tile was cast in an open mould and cut into five 20 mm wide by 120 mm long strips and submitted to a flextural test. The transverse modulus of rupture of the tile was 3.08 MNn m^{-2}.

FLEXI MIX TESTING

The criteria used to select a good flexi mix were that a 6 mm thick flat tile should not crack when bent through a radius of 200 mm, should not rip easily, should bend easily and have a low resin content. No quantitative tests of flexi mix properties have been made. Reducing the resin content to 6% produces a tile with a little flexibility but the tile can be easily cracked.

USAGE

Crispy mix was developed and first used to make neutron collimation irises and instrument shielding for the SNS eVS spectrometer. Open moulds have been used to produce detector shielding, flat 6 mm thick tiles to line the inside surface of the sample and detector chambers and 50 mm thick irises have been used to produce a low albedo collimation assembly. Closed moulds have been used to produce curved 6 mm thick tiles to line a flight tube that preceeds the sample chamber. Hot-press moulds have been used to produce flat 6 mm thick high density shielding tiles for regions close to the detectors. It has since found many uses on other SNS instruments and will be of great use in future SNS instruments such as SANDALS.

Flexi mix tiles are currently being used to make instrument shielding for POLARIS, the SNS polarised neutron spectrometer. The flexibility of the tiles allows them to follow the curvature of the inner walls of the instrument vacuum chamber. This saves the time that would otherwise be needed to prepare moulds for rigid crispy mix tiles, as a single mould can be used to cast standard shaped tiles which can then be cut, drilled and bent into the required shapes.

CONCULSION

While these experiments were qualitative rather than quantitative and have not exhausted the possibilities of grit ratios or fabrication techniques, a method of producing rigid neutron shielding in a variety of shapes from a 97% boron carbide/3% resin mix and flexible neutron shielding from a 90% boron carbide/10% resin mix has been developed. If a little care is used the shielding materials can be filed, drilled and cut.

Some ideas for further improvements to crispy mix include: development of a mix using a non-hydrogenous binder and introducing more flexibility into the mix without increasing the resin content. With a resin content of only 3% neutron scattering from the carbon in the boron carbide is greater than that from the resin. It may be possible to replace the boron crbide with another inert form of boron that has a lower scatter to capture ratio.

Because of their flexibility, flexi mix tiles , and presumably other moulded flexi mix structures, are easier to produce and install than crispy mix tiles but they contain three times as much resin. Where the lowest neutron capture to scatter ratio is not the sole criterion for choosing neutron shielding material, flexi mix provides a quick solution for shielding the critical areas of neutron spectrometers and diffractometers against thermal and epithermal neutrons.

ACKNOWLEDGEMENTS

The authors would like to thank Dr J M Carpenter of Argonne National Laboratory USA for informing RAL of Professor N Watanabe's recipe for crispy mix. We also wish to thank D Evans, R J Ellis and D Morrow of the RAL Resin Lab for their helpful advice and J T Morgan for flex testing the samples.

Proceedings of the Eighth Meeting of the International Collaboration on Advanced Neutron Sources (ICANS-VIII)
8-12 July 1985, Rutherford Appleton Laboratory Report RAL-85-110

The IPNS Chopper Control and Accelerator Interface Systems*

G. E. Ostrowski, L. I. Donley, A. V. Rauchas, G. J. Volk,
E. A. Jung, J. R. Haumann and C. A. Pelizzari*
Argonne National Laboratory
Argonne, Illinois 60439 U.S.A.

(*Now at Dept. of Radiation Oncology, University of Chicago)

Introduction

Several of the instruments at the Intense Pulsed Neutron Source (IPNS) at Argonne use rotating Fermi choppers. The techniques used to control the speed and phase of these rotating devices will be discussed in the following paragraphs.

Chopper Mechanical Overview

The neutron chopper rotor is of cylindrical Fermi design and constructed of hemicylindric beryllium lunes with a curved slot containing a slit package which permits neutrons to pass through[1]. The chopper rotation axis is vertical with high precision ball bearings being used both top and bottom. To remove heat generated by the motor and bearings, the chopper is operated in a 1 mm Hg He atmosphere. This provides adequate cooling, yet presents insignificant drag. The driving motor is of hysteresis-synchronous type and has a rated power of 90 W. The hysteresis-synchronous motor is attractive in demanding little sophistication of the drive system, and its torque is good during startup; however, its synchronous torque is low, and acceleration must also be done slowly to avoid hysteresis heating of the rotor which can damage the bearings. Fig. 1 shows a sectional view through the slit package assembly and provides parameters for the 5 chopper rotors currently in use at IPNS. The calculated geometric transmission efficiencies can be seen in Fig. 2 and the calculated neutron burst widths can be observed in Fig. 3. The IPNS chopper rotors are operated at a multiple of 30 Hz frequency (typically 270 Hz) and synchronously with the IPNS Rapid Cycling Synchrotron (RCS) which operates at a nominal frequency of 30 Hz [2]. The chopper drive and protection system provides the power required to operate the chopper at a chosen speed, monitors operating parameters and shuts down the chopper power if a potentially damaging condition exists. Amplifiers operated as constant current sources are used to supply the driving power to the chopper.

Chopper Drive and Phasing Systems

Monochromatization of the incident neutron beam is accomplished by opening the chopper at a well defined time after the proton beam hits the IPNS target. By this means, only neutrons whose velocities bring them to the chopper at the chosen time can pass through it and strike the sample. In order that energy resolution not be degraded, the chopper - proton beam phase (i.e., the above mentioned time delay between protons on target and the opening of the chopper) must be held constant to a tolerance of no more than 10 - 20% of the source burst time, or typically to a few microseconds. In order to accomplish this, systems to control both the chopper and certain functions of the RCS have been developed. These are divided operationally into a drive system, which provides the power required to run the chopper at a chosen speed, monitor chopper operating parameters and shuts

*Work supported by the U.S. Department of Energy

off chopper power (scram) if a potentially damaging condition exists; and a phasing system, which maintains the desired phase relationship by adjusting the chopper phase when necessary and by issuing extraction trigger signals to the RCS.

Chopper Drive System

The drive system provides power to run the chopper at a chosen frequency and scrams the chopper if a potentially damaging condition is sensed. The various components of this system can be seen in the block diagram displayed in Fig. 4.

System Master Clock -

The Master Clock provides signals to which the RCS and choppers can be synchronized. A 60 Hz square wave is sent to the RCS where it is converted to a 30 Hz sine wave to drive the ring magnet power supply. To the 30 Hz delay (see below) of each chopper phasing system are sent a 30 Hz square wave and a 3.93216 MHz clock. The high frequency is used in synthesizing audio frequencies to run the choppers; the 30 Hz signal provides a timing reference for phase locking of the chopper drive frequencies and for phase shifting during extraction control. There are actually two versions of the Master Clock, one which operates from a fixed crystal-controlled 3.93216 MHz oscillator and a Variable Frequency Master Clock (VFMC) unit[3] which allows the oscillator frequency to change slightly in response to slow changes in the power line frequency. The latter is used to minimize operating difficulties experienced by the RCS when the 60 Hz clock frequency differs significantly from the power line frequency. Also, development work is currently underway which will allow the chopper systems to operate synchronously with the (VFMC). This activity will be discussed further in the **Summary and Future Plans** section (see below).

In addition, a 60 Hz Backup Clock is located in the RCS control room. In the event of interruption of the master 60 Hz signal coming into the accelerator main control room, the Backup Clock synchronously switches the RCS over to its own 60 Hz reference signal. This is done to protect the Ring Magnet Power Supply System from possible damage due to sudden removal of its input signal, and to prevent the RCS shutting down when something goes wrong with the Master Clock or associated cabling.

Frequency Synthesizer -

This unit synthesizes two-phase sine waves with frequency between 1 Hz and 960 Hz. It is designed so that at any harmonic of 30 Hz its outputs can be phase-locked to an external 30 Hz reference. This allows both the Frequency Synthesizer and the RCS to be synchronized to the System Master Clock for chopper-RCS phasing. The Synthesizer can operate in a stand-alone mode using its internal frequency standard. For use with the phasing system, the required 30 Hz and 3.93216 MHz signals are brought from the Master Clock (see above) via the 30 Hz Delay Module.

An automatic frequency increase feature has been provided to simplify chopper acceleration. This feature is controlled by the FAST-STOP-SLOW switch on the front panel. With the switch in either the FAST or SLOW position, the synthesizer frequency will be changed from the current value to a specified harmonic of 30 Hz; the harmonic number is dialed in using thumbwheels. The frequency is increased (or decreased) in steps of 1/8 Hz; the rate at which step changes are made is controlled by a front-panel adjustment in the SLOW mode, or at a fixed rapid rate in the FAST mode. Adjustment of the SLOW rate is set to provide continuous chopper acceleration over a wide frequency range while maintaining a slip frequency of less than 1/8 Hz. This minimizes the hysteresis heating of the chopper and the potential damage to bearings during the acceleration process. The FAST mode is used to reset or preset the synthesizer to a desired frequency. The frequency ramping process can be frozen at any point by switching to STOP mode.

Damper -

Small variations in bearing frictional drag cause an increase in the chopper phase instability (hunting). This condition results in small changes in the

chopper speed. A fast acting logic circuit within the Damper Module[3] senses the variations in chopper speed and makes small phase shift corrections in the driving sinusodial waveforms to the chopper which minimizes the hunting effects, extends the useful bearing lifetime and improves data collection efficiencies.

Chopper Drive Regulator -

This unit controls two power amplifiers (see below) which actually drive the chopper. It is a constant-current regulator which maintains the rms current in both phases at a specified value. A sufficiently long time constant is built into the regulating circuit such that current fluctuations due to hunting oscillations of the chopper are ignored. The Regulator requires as input the two fixed amplitude sine wave outputs of the Frequency Synthesizer or the Frequency Synthesizer - Damper series combination, and a current sense signal from each power amplifier (see below). As output it produces two variable level sine waves, one to drive each amplifier. The two phases are regulated, independently of each other, to the same rms current value by controlling the amplifier inputs. Current monitor outputs are also provided for the chopper Scram Module (see below). The rms current of each phase is displayed on a front-panel meter reading 0-5 amps, and is adjusted using a front panel control.

Chopper Scram -

The Chopper Scram unit contains a microprocessor which cyclically monitors the current levels in the two phases, the vibration amplitude and the chopper-oscillator slip frequency. If any of these are outside the set trip levels, a scram signal is sent to shutdown the power amplifiers and secure the data acquistion system. A RUN-STANDBY switch is provided to defeat the scram function during chopper acceleration.

Power Amplifiers (California Instruments Co. Model 501TC) -

The Power Amplifiers, one for each phase, are 500 VA rated units with output voltage capability from 0-135 or 0-270 volts. Since we require large currents only during magnetization (4 to 5 amps.), the 0-135 volt taps are used. A solid state relay switches the AC power to the Power Amplifier. This relay is opened by the Chopper Scram Module to shut off the Power Amplifier when a scram condition exists (see above). A 0.1 ohm current sense resistor has been added in series with the output. The voltage across this resistor is monitored by the Chopper Drive Regulator (see above).

Zero Crossing Detector and Vibration Monitor -

This module converts the bipolar pulse from the chopper magnetic pickup to a logic pulse for use by the Chopper Scram and Chopper Phase Controller. In addition, it provides power to the accelerometer used to monitor chopper vibration and converts the vibration signal amplitude to a DC level for the Scram Module.

Chopper Phasing System

The control functions performed by the phasing system may be most readily understood with reference to the timing diagram of Fig. 5. For illustration we ignore the possibility of using a second chopper.

In order for the chopper to stay in phase with the accelerator, the chopper frequency (1/CHOP) must be a multiple of the 30 Hz RCS frequency (270 Hz is a typical value). The fundamental condition which must be met is that the chopper opening time follow the proton on target signal (T-o) by the specified time (Tc), with a tolerance (ΔTc) as shown. The phasing system controls proton beam extraction (EXM) and therefore (T-o), so all it needs do to establish the desired phase is to send an extraction trigger signal (EXM) such that (CpEx = CHOP - Dly - Tc).

There are limits, of course, on the times during the RCS cycle when the beam may be extracted. A window is provided by the RCS clock during which extraction

trigger pulses are accepted; if an extraction trigger pulse arrives within this window, then the chopper will control the extraction of the proton beam. This condition is operational only when the chopper can control (CCC) level being sent to the Chopper Controller is high. A low (CCC) level indicates that extraction is being controlled by the RCS and that extraction will take place at the center of the extraction window, which is the optimum instant from the machine's point of view. As long as the (CCC) level is high, the RCS clock will wait for a chopper extraction trigger pulse (EXM) until the last possible moment; if none arrives, the beam will be extracted at the trailing edge of the extraction window. Even with a high (CCC) level, it is not certain that every (EXM) will control extraction of the proton beam. The phasing system therefore checks every (T-o) pulse to make sure the phase condition is satisfied, i.e., that (T-o) arrives within the time interval equal to (CpEx + Dly ± ΔTc/2). If this condition is not satisfied, an inhibiting level is sent to the data acquisition system (DAS) front-end computer so data will be accumulated only for correctly phased pulses.

The final function of the phasing system is to adjust the phase of the chopper with respect to the RCS when necessary in order that legal extraction trigger pulses (i.e., within the extraction window) can be sent. This is accomplished by introducing a delay between the "Master" 30Hz signal used to drive the RCS ring magnets and the audio frequency (twice chopper frequency, typically 540 Hz) used to drive the chopper. Exactly when this phase shifting occurs will be described below in the discussion of the Chopper Controller Module.

Chopper Mode Selector -

The Chopper Mode Selector Module simulates several modes of accelerator operation. One of these modes is the normal running state of the RCS in which all system components are phase-locked to the 30 Hz Master Clock and all required signal information is communicated between the Chopper Mode Selector and the Chopper Controller Module. This mode is most frequently used to prephase choppers prior to accelerator start-up and also to test tne performance of chopper phasing equipment without wasting neutron beam time. Other available modes are used for the testing and evaluating of new chopper control and phasing circuitry, such as the variable frequency mode of operation which will be discussed later.

Priority Level Selector -

This module is the only one which actually communicates with the RCS. It receives the extraction window (EW), protons on target (T-o), chopper can control (CCC) signals and sends out the extraction signal (EXM).

The Priority Level Selector also communicates with up to six Chopper Controllers (see below) and prioritizes the information it receives from them. Each controller receives extraction window and protons on target information from the Priority Level Selector and sends back its own extraction trigger. The Priority Level Selector sends to the RCS the highest priority legal extraction trigger (EX) it receives for each RCS cycle. Thus if the first priority (EX) signal is not within the extraction window, the second priority (EX) will be used, etc. If there is no (EX) signal from any of the six inputs which is within the extraction window, the RCS will extract the beam at the trailing edge of the extraction window. At any instant, the highest priority chopper providing a legal (EX) pulse is defined to be the "Master", all others "Slaves". This status information is sent back to each Chopper Controller and is used during phase shifting (see below).

Chopper Controller -

Each chopper which is to be phased has one of these modules. The module contains a microprocessor and some timers which are used by the processor to gather the information it needs. The processor and timers are clocked using a 2 MHz oscillator. Upon initialization, the processor does the following:

a) Measure the chopper period (CHOP) (see Fig. 5).
b) Measure the extraction window (EW) width (typically 200 μs).

c) Measure the delay (Dly) from extraction (EXM) to (T-o) (typically 54 μs).
d) Read the desired value of Tc from the thumbwheel switches and compute the delay time (CpEx) by which the extraction trigger (EXM) must follow the chopper pulse.
e) If the resulting extraction pulse (EXM) does not fall within the limits of the extraction window, phase shift the chopper to bring (EXM) to the midpoint of the extraction window.

At this point the (EXM) is being sent at the optimum time (midpoint of the extraction window) and no futher corrective action is needed until the chopper - RCS phase changes. If such a phase change occurs, corrective action will only be taken if (EXM) has moved a distance equal to 25% of the extraction window width either side of the center of the extraction window. When this condition exists, the Chopper Controller will phase shift the chopper to return the (EXM) to the midpoint of the extraction window.

In addition, every incoming (T-o) pulse is checked to make sure it satisfies the chosen phasing conditions. If the phasing conditions are not met, a blanking signal is sent to the (DAS) to disable data collection for that burst of neutrons. A delayed (T-o) pulse (100 μs) is used to start the (DAS); this allows the Chopper Controller time to determine if the chopper is phased correctly and if not, to generate a data blanking signal.

30 Hz Delay -

This module provides the means by which the Chopper Controller can phase shift the chopper. A variable delay is introduced into the 30Hz sync signal from the Master Clock and the delayed 30Hz is used by the Frequency Sunthesizer to phase-lock the chopper driving waveforms. Thus the chopper can be phase shifted with respect to the Master Clock, while the RCS is locked to the undelayed master 30Hz signal.

Summary and Future Plans

The present IPNS Chopper Control and Phasing System was designed and constructed at Argonne during 1981-1982 and required about one year of on-line experience to recognize and eliminate system problems. Since that time, the original system has performed well with no loss of neutron beam time due to electronic failures in any of the Chopper Control or Phasing System hardware. As would be expected, areas for improvement have surfaced over the past 2 1/2 years of routine chopper operation; namely, the desirability to operate the RCS - chopper system in a 60Hz power line phase-locked configuration. This mode of operation is most efficient for the RCS as beam losses during the proton acceleration cycle are minimized and therfore, radiation activation rates for accelerator components are also reduced and neutron fluxes are maximized. Because of the low horsepower motors used to supply power to the choppers, it is not possible to maintain synchronous chopper operation while phase-locked to the 60Hz power line.

A Variable Frequency Master Clock (VFMC) unit[3] has been designed which allows the oscillator frquency to change slightly in response to slow changes in the power line frequency. Measurements made while operating phase-locked to the (VFMC) show that RCS porformance is not degradated by small phase shifts (±15°) relative to the 60 Hz power line; also, the chopper system data collection efficiency remains at the 98-99% level.

Recall that during initialization (see Fig.5), the chopper period (CHOP) and the extraction delay time (Dly) are measured and stored as constants. For each pass through the microprocessor software, the (Tc) value is read and the value of (CpEx) is computed from the relation (CpEx = CHOP - Dly - Tc) and used to generate the next extraction trigger pulse (EXM). The value of (Tc) is determined from a chopper calibration table and set into the front panel thumbwheel switches of the Chopper Controller. This allows an experimenter to change the neutron energy selected by the chopper at any time without impacting the stability of the chopper

control-phasing system. Operation using the Variable Frequency Master Clock (VFMC) requires continuous measurement of the chopper period (CHOP). As can be seen from Fig. 5, any variation in the chopper speed will change the time when the chopper window is open (Tn); therfore, (ΔCpEx) reflects the changes in (Tn) due to the variations in the chopper period (CHOP) and corrects for the smearing of the neutron energy which would result if a correction were not made for (Δ Tn).

A new Chopper Controller has been designed and built [4] at Argonne to function in both the fixed and variable frequency modes of operation. An 8 bit microprocessor and newly developed 100 MHz counting circuitry have been brought together to produce a controller having a 10 nanosecond clocking uncertainty. The spectral data displayed in Fig. 6 was produced by routing appropriately reshaped chopper Zero Crossing Discriminator (ZCD) pulses into a detector input of the (DAS). The resultant spectral widths indicate the total timing uncertainty of the Chopper Controllers plus 125 nanoseconds timing uncertainty of the data acquisition system (DAS).

Neutron measurements, obtainted while operating synchronously with the Variable Frequency Master Clock, indicate that the new Chopper Controllers are functioning as intended. Fig. 7 shows the agreement between Monitor 1 (located downstream of the chopper) spectra collected on the High Resolution Medium Energy Chopper Spectrometer (HRMECS) for both fixed and variable frequency modes of operation. These data clearly verify that spectrometer energy resolution is not deminished through the use of synchronous variable frequency chopper phasing techniques. It is expected that the Variable Frequency Master Clock will remain as the standard time base for the routine operation of the IPNS RCS-Chopper Phasing System.

Short bearing life (typically 25 to 50 days) continues to be the weak link in the reliability of the IPNS choppers. Given sufficient funds, we feel it would be advantageous to investigate the possible use of commercially available magnetic bearing systems.

References

[1] R. Kleb, C. A. Pelizzari and J. M. Carpenter, "Fermi Choppers for Epithermal Neutron Beams," (Argonne), in preparation

[2] A. Rauchas, G. Ostrowski, C. Pelizzari and G. Volk, "IPNS Accelerator System and Neutron Chopper Synchronization," (Argonne) Proc. ICANS-VII (1983), p157

[3] L. Donley, "Phase Locking the IPNS Neutron Chopper to the 60 Hz Power Line," (Argonne) Proc. ICANS-VIII (1985)

[4] E. Jung, "Precision Phase Control of High Speed Rotating Devices Using An 8 Bit Microprocessor and 100 MHz Timing Circuitry," (Argonne), in preparation

CHOPPER PARAMETERS

Rotor	50-2	160-2	500-2	250-3HR	500-3HR
f (rpm)	16200 -›				
f (hz)	270 -›				
E (meV)	50	165.3	500	250	500
R (in.)	35.886	65.253	113.480	80.244	113.480
D (in.)	6.063 - - - - - - - - - - - - -›			5.000 - - - - - - -›	
d (in.)	.100	.080	.062	.050	.040
τ(μs. fwhm)	9.72	7.77	6.03	5.89	4.72
Beam size (in.)	2w x 4h	2w x 4h	2w x 4h	3w x 4h	3w x 4h
Geomet. Trans.	0.82	0.79	0.74	0.78	0.74
Adsorber	3 ply B-Al - - - - - - - - - -›			2 ply B-Al - - -›	

Adsorber constructed by cross laminating 5.7 mil dia. Boron fibers produced by vapor depositing Boron on 0.5 mil dia. Tungsten wire.

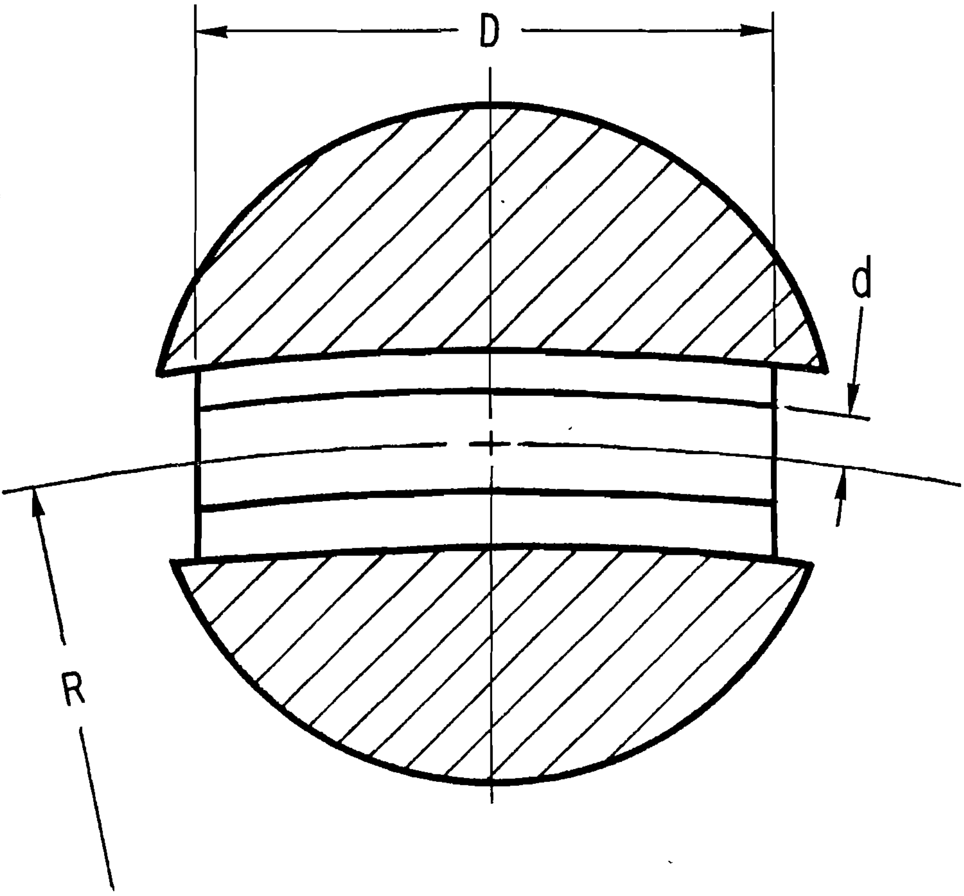

Fig. 1 - Parameters for the 5 IPNS Chopper Rotors

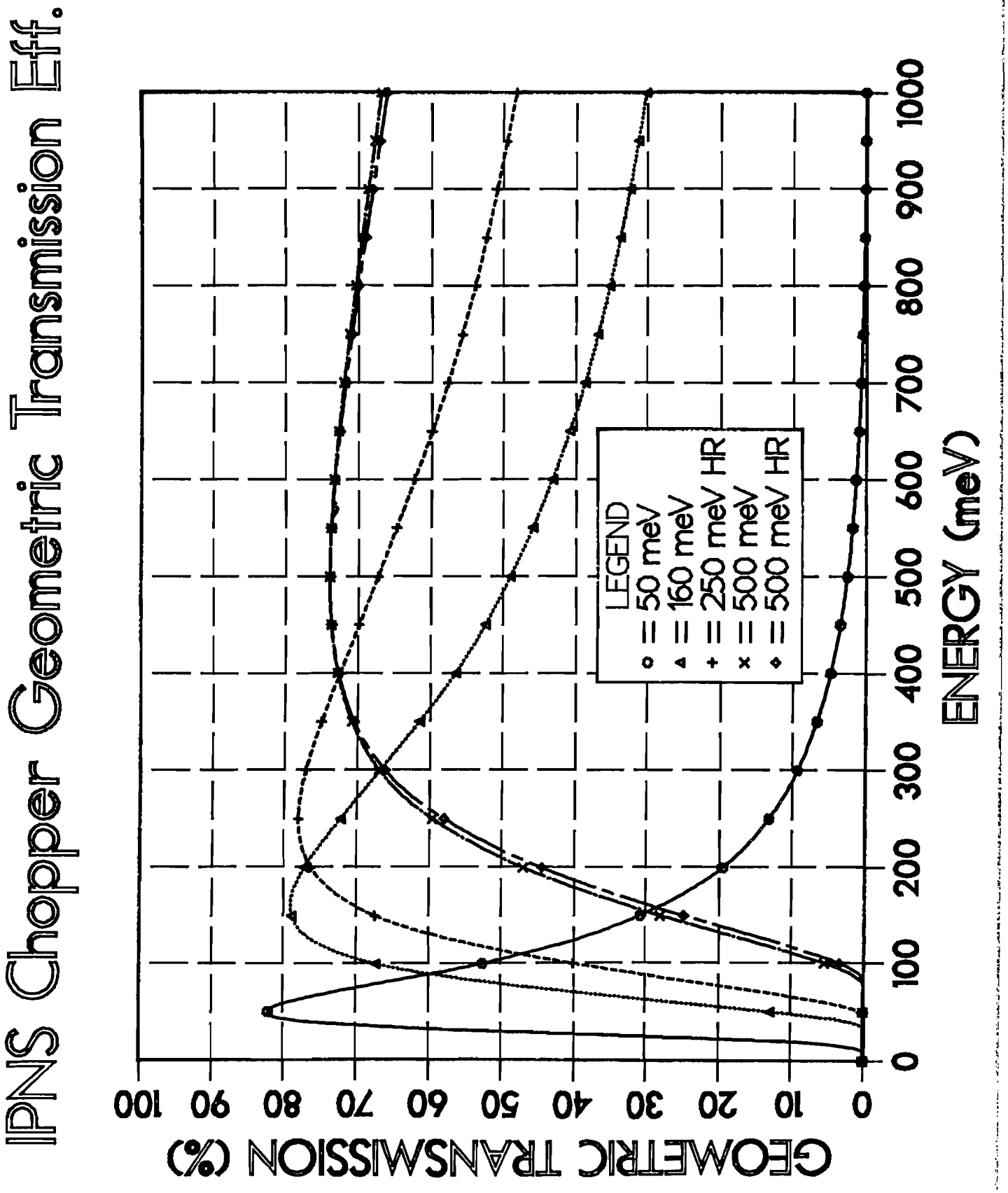

Fig. 2 - Computed Geometric Transmission Efficiencies for the IPNS Chopper Rotors

Fig. 3 - Computed Neutron Burst Widths (fwhm)
for the IPNS Chopper Rotors

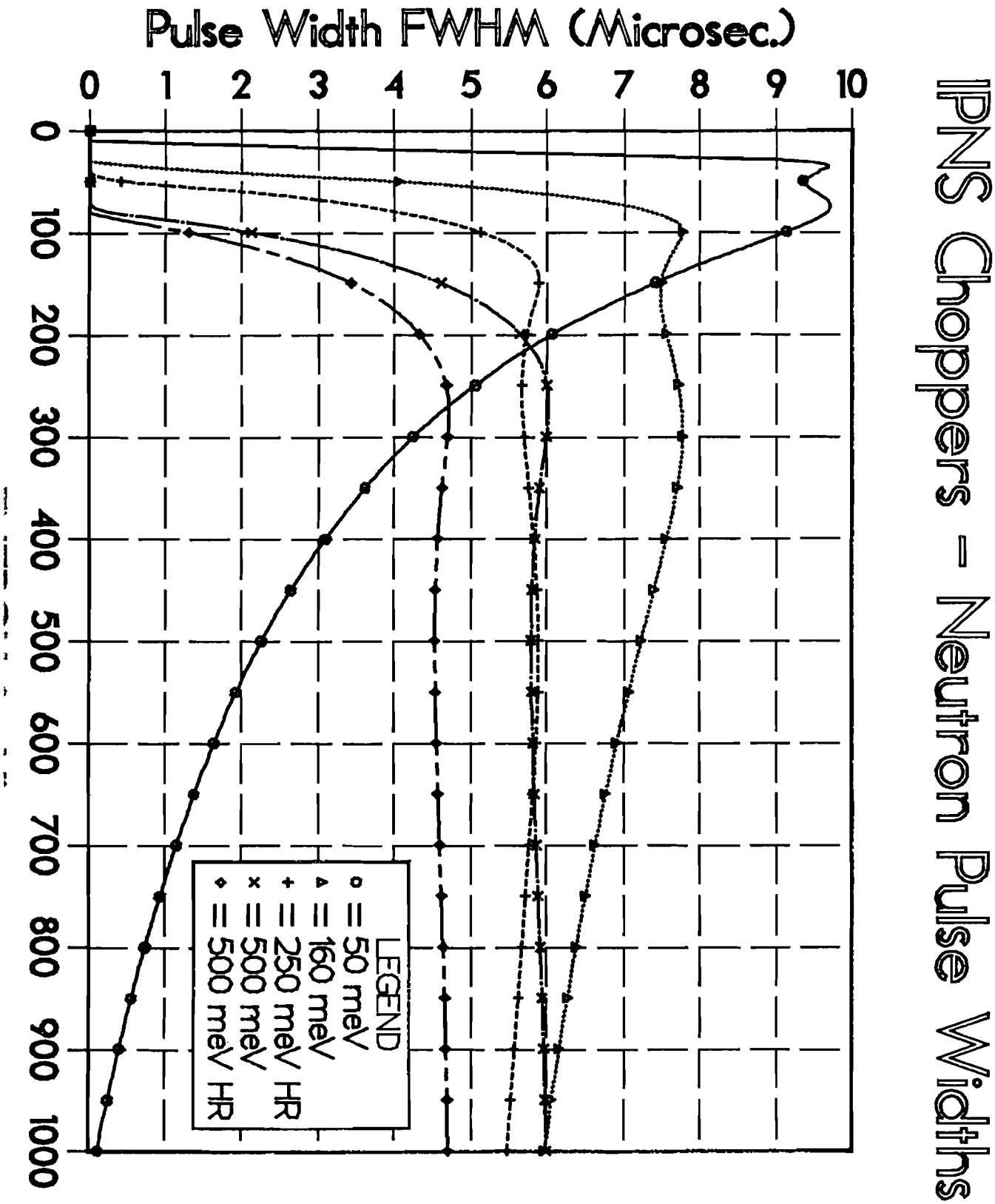

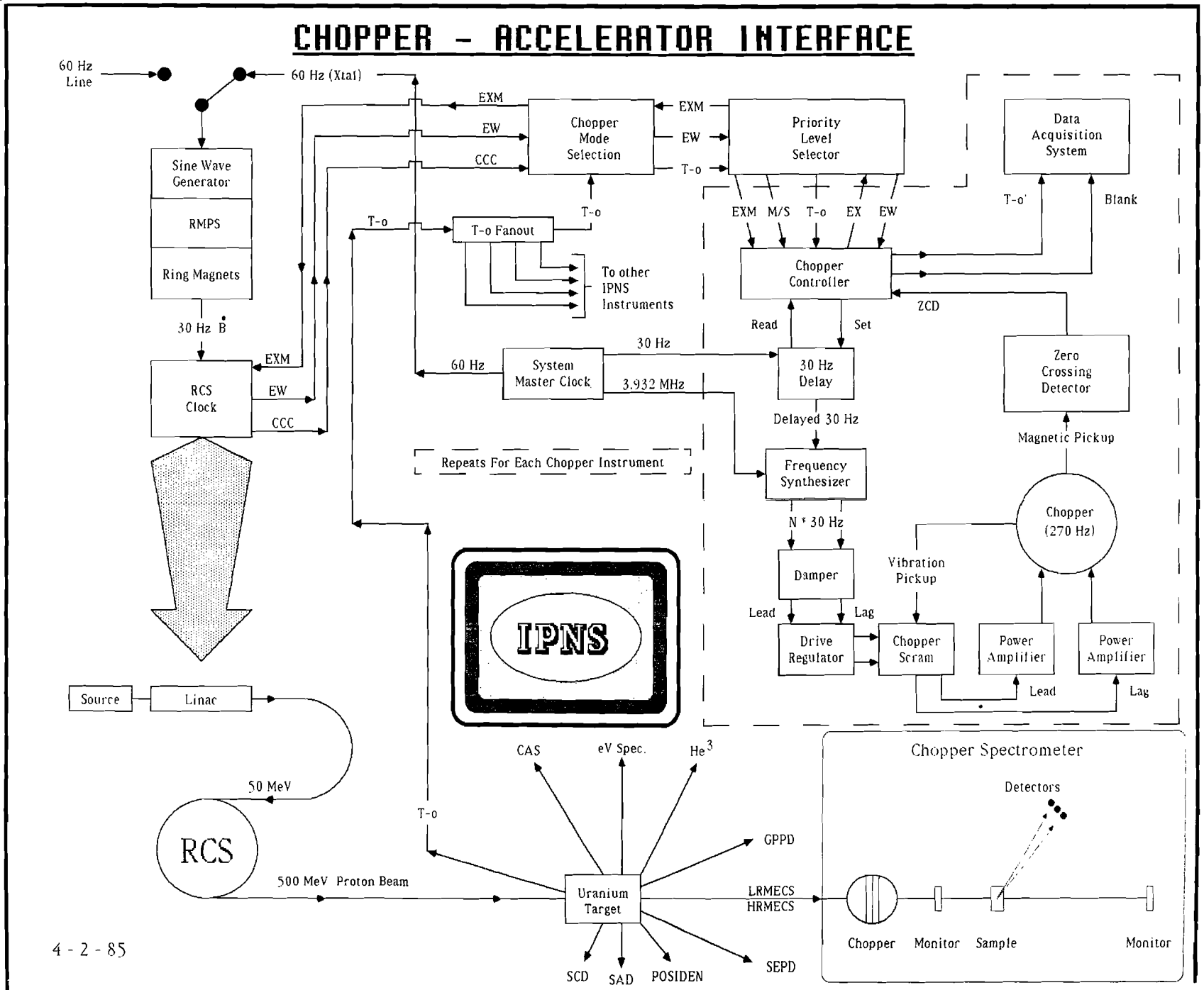

Fig. 4 - Block Diagram of the IPNS Chopper Control and Phasing System

4 - 2 - 85

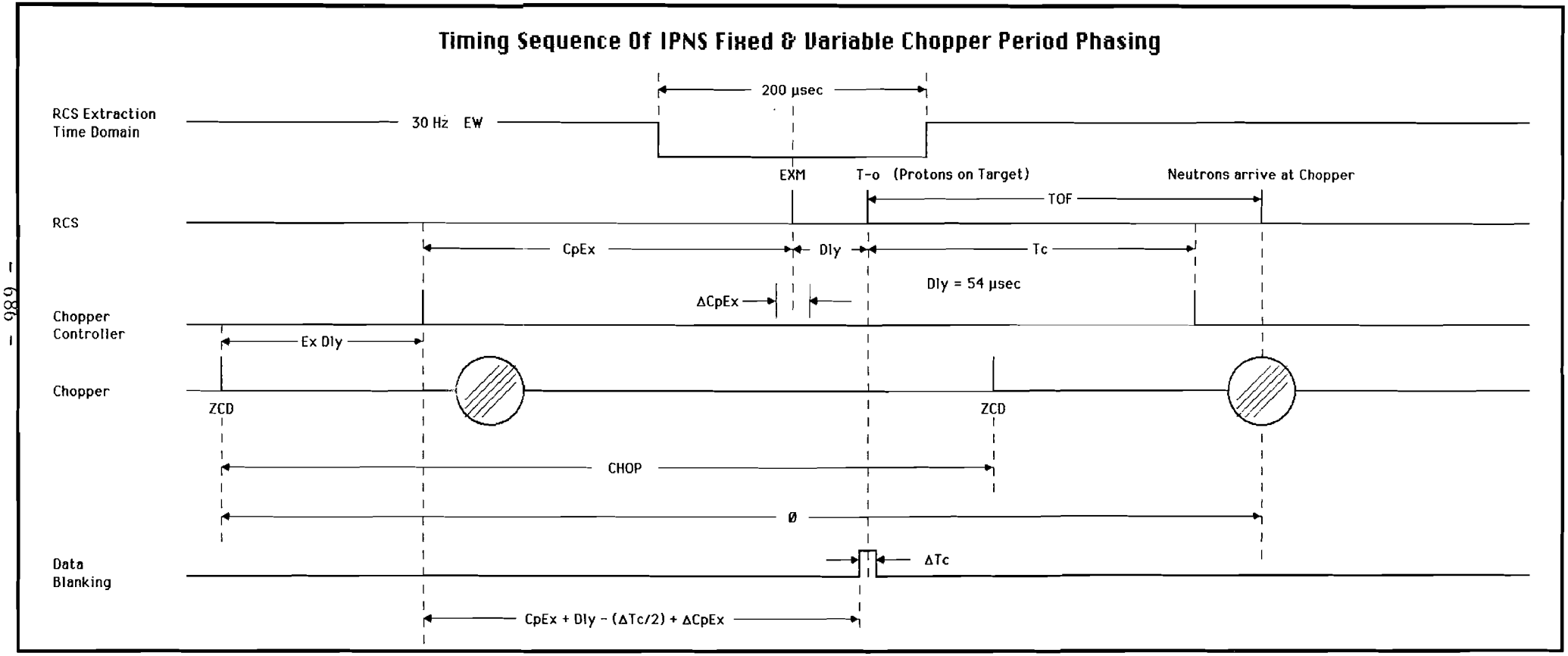

Fig. 5 - Chopper Phasing Timing Diagram

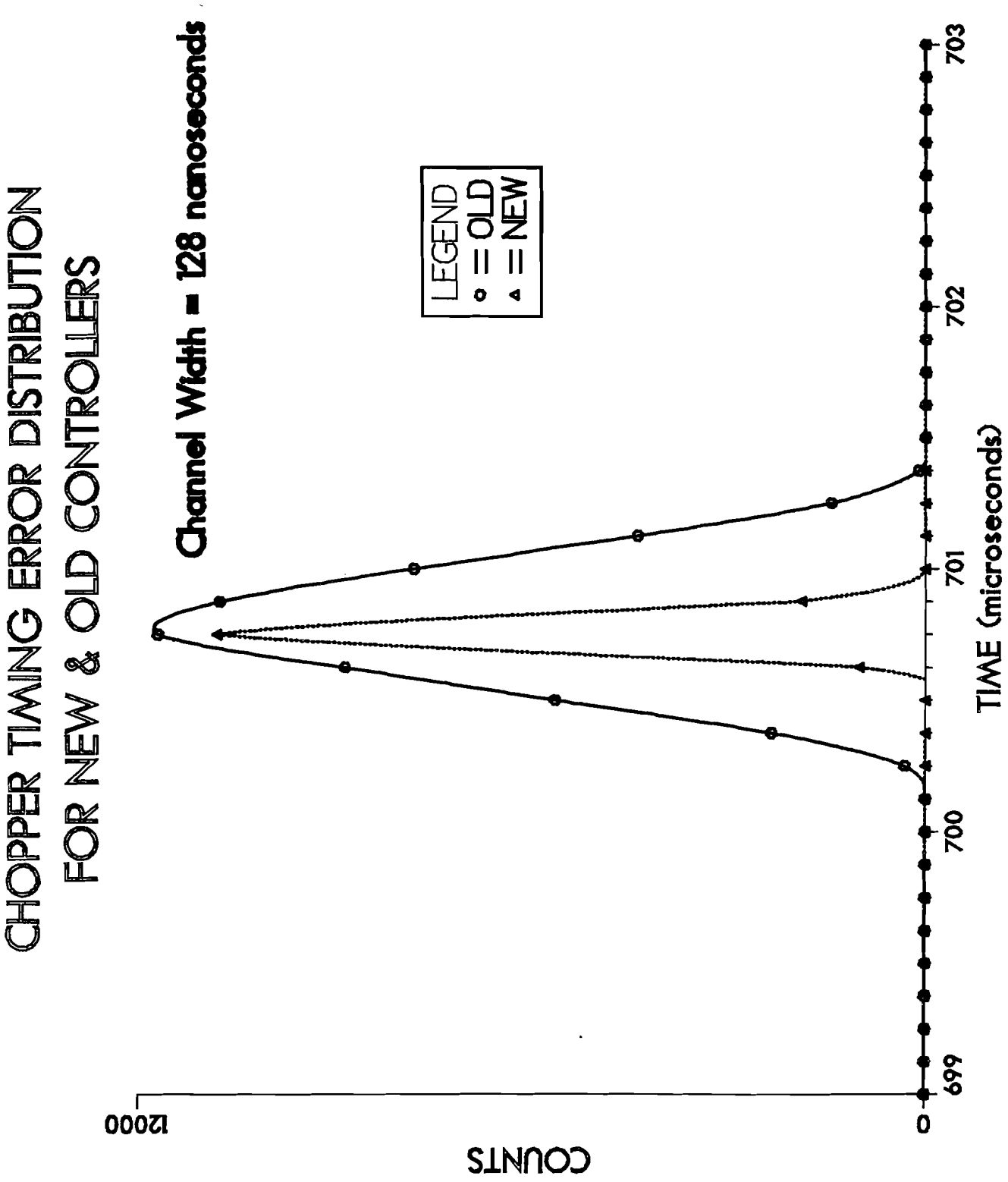

Fig. 6 - Time-of-flight Spectra of Neutron Chopper Pulses Showing Timing Uncertainties in Old and New Chopper Controllers

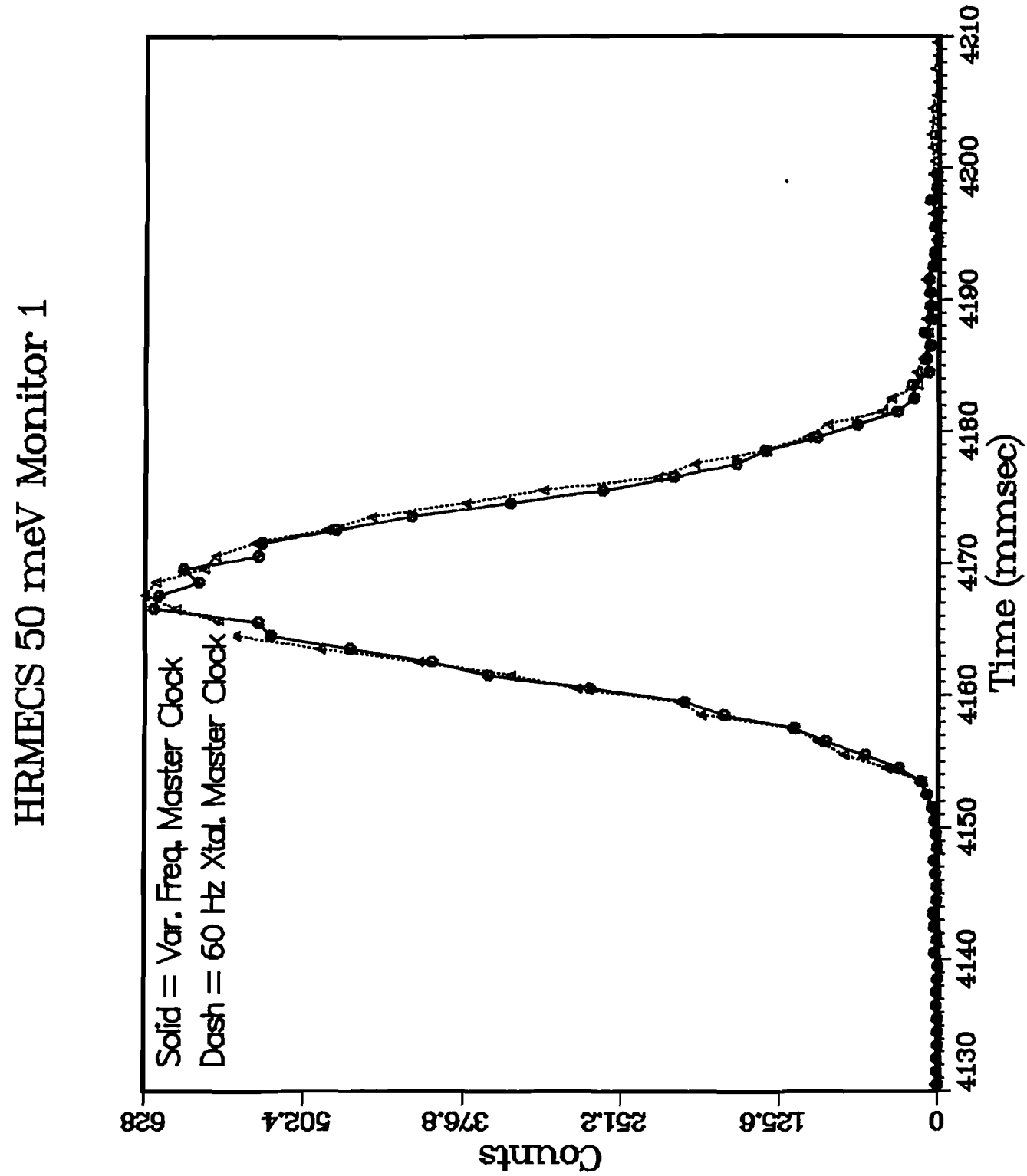

Fig. 7 - Time-of-flight Monitor Spectra for Fixed and Variable Frequency Chopper Operation

Proceedings of the Eighth Meeting of the International Collaboration on Advanced Neutron Sources (ICANS-VIII)
8-12 July 1985, Rutherford Appleton Laboratory Report RAL-85-110

Phase Locking the IPNS Neutron Choppers to the 60 Hz Power Line*

Lawrence I. Donley
Argonne National Laboratory
Argonne, Illinois 60439 USA

Introduction

The neutron beam chopper is a cylinder made of a neutron absorbing material with slits which permit neutrons to pass through. The revolution frequency (typically 270 revolutions per second) and the width and curvature of the slits determines the range of energies that can be transmitted to the experimental sample. The time from when neutrons are released from the pulsed neutron source to the alignment of the slits to permit passage of neutrons determines the energy of neutrons that will be passed by the chopper. The chopper operates in a partial vacuum and is rotated by a fractional horse power synchronous motor. The chopper rotates at a frequency multiple of 30 Hz. Several of the neutron scattering instruments at the Intense Pulsed Neutron Source (IPNS) at Argonne National Laboratory (ANL) use neutron choppers to select the energy of the neutron beam required for their experiment. Since the neutron burst is generated by the 100 ns proton beam extracted from the Rapid Cycling Synchrotron (RCS), precise synchronization must be maintained between the RCS extraction and the chopper slits. To accomplish this, a chopper rotor position signal is used to generate the RCS extraction pulse; therefore, the RCS must be synchronized to the chopper. The chopper master clock generates a 30 Hz reference signal that is used by both the RCS and chopper controllers for synchronization. The RCS operates at 30 Hz and performs best when synchronized to the 60 Hz power line. This paper describes equipment required to synchronize a chopper to the power line.

60 Hz Line Synchronizaton Requirements

Through operating observations it has been determined that the RCS performance increases as the RCS pulse rate approaches one half the 60 Hz power line frequency. Performance continues to improve as phase excursions are limited down to $\pm 15^{\circ}$, after which further tighter phase control is not expected to greatly improve RCS performance. Except for short periods of time the power line frequency ranges from 59.95 Hz to 60.05 Hz.

Rotor Stability Requirements

When more than one chopper is operating, one is denoted as the master chopper, the rest are slave choppers. A rotor position signal from the master chopper is used to produce an extraction master pulse (EXM) resulting in beam being extracted from the RCS. The slave choppers must rely on being precisely synchronized to the master chopper to determine energy resolution. TC is the time from when the proton beam arrives at the target and a chopper rotor position signal. If ΔTC is outside limits (typically ± 1.0 µs for a master and ± 2.0 µs for a slave, the data from the instrument will not be taken. Because of the method used to make phase corrections, the choppers may not be operating in the center of ΔTC. This further tightens the requirements on rotor stability. To maintain good data taking rates and high energy resolution from the chopper instruments, the rotor must maintain a phase stability to the master clock 30 Hz reference of ± 1.0 µs (approximately equal ± 0.1 degrees of rotation).

*Work supported by the U.S. Department of Energy.

RCS Chopper System Description

For the purpose of this paper a detailed understanding of how the chopper and the RCS are phased locked to each other is not necessary. It is only necessary to know that they both have phase control systems that seek to properly phase them with the 30 Hz reference from the master clock (Fig. 1). The Variable Frequency Master Clock (VFMC) has the ability to phase lock the 30 Hz reference to the 60 Hz power line. In response to the chopper controller, the frequency synthesizer produces chopper motor drive signals properly phased to produce the correct dynamic rotor position with respect to the 30 Hz reference. By measuring the period of the magnetic pickup the damper can detect positive or negative acceleration of the chopper rotor. The damper then phase shifts the motor drive signal in a direction to reduce the acceleration. The current regulator and power amplifier supplies a steady current to the motor windings in response to the drive signals.

The chopper controller system has several functions of which only the generation of a EXM and delayed 30 Hz are relevant to this discussion. After a programmable delay from the magnetic pickup, the EXM is generated. The amount of delay is calculated by the chopper controller to produce the desired neutron energy based on the time from EXM to beam arriving at the uranium target, chopper period, and the phase relationship between the magnetic pickup and the slits on the chopper rotor. A second programmable delay from the 30 Hz reference generates a delayed 30 Hz which causes the frequency synthesizer to position the chopper rotor so the proton beam will be extracted from the RCS at a preset phase of the 30 Hz reference.

The RCS controller synchronizes the RCS so that beam can be extracted from the RCS at a preset phase of the 30 Hz reference and generates an EXM acceptance window at that time.[1]

The three changes that were required to allow the chopper system to follow the 60 Hz power line are: 1) to make the master clock into a variable frequency master clock, 2) add chopper dampers to improve chopper rotor stability, and 3) update the chopper controller system to maintain monochromatic neutron beam as chopper period is changed. The purpose of this paper is to describe the circuitry of the VFMC and the chopper damper.[2]

Variable Frequency Master Clock Circuit Description

The VFMC contains a voltage controlled crystal oscillator (VCXO) with a center frequency of 3.93216 MHz (referred to as 4 MHz C). The 4 MHz C is divided by 2^{16} to get the 60 Hz clock (referred to as 60 Hz C). The 60 Hz C is divided by 2 (Fig. 2) to get 30 Hz clock (30 Hz reference). If the 60 Hz C is to be phase locked to the 60 Hz power line the 60 Hz C must have a frequency range that encompass the frequency range of the 60 Hz power line. Observations of the power line frequency at ANL reveal that a range from 59.95 Hz to 60.05 Hz would be sufficient for our purpose. From this the frequency range requirements for the 4 MHz C can be calculated:

$$\text{Minimum frequency} = 59.95 \text{ Hz} \times 2^{16} = 3.92888 \text{ MHz}$$

$$\text{Maximum frequency} = 60.05 \text{ Hz} \times 2^{16} = 3.93544 \text{ MHz}.$$

The VCXO is programmed to cover this frequency range by the output of a 12 bit digital to analog converter (D to A). This provides a method of programming the frequency between minimum frequency and maximum frequency in 2^{12} (4096) bits. The frequency change for each bit can then be approximated as

$$\text{Frequency maximum - frequency minimum/4096} \times \text{frequency center} =$$

$$3.93544 \times 10^6 - 3.92888 \times 10^6/4096 \times 3.93216 \times 10^6 = 1/2.46 \times 10^6$$

or one bit equals a change of one part in 2.4 x 10^6. This provides adequately small and predictable step changes for the chopper rotor to follow without creating rotor instability.

The output of a 12 bit up/down counter referred to in Fig. 2 as frequency register is connected to the D to A. This provides a method for stepping the input to the D to A up or down. The restrictions on stepping the frequency register are to step at a rate no faster than the chopper rotor can follow, and not to let the frequency register roll over (go higher than 2^{12} or lower than zero) and a correction must be required in the frequency of the VCXO. The parameters that determine if the frequency register needs to be changed are derived from comparing the 60 Hz C along with its source the 4 MHz C and the 60 Hz power line. A 60 Hz band pass filter and a zero crossing detector are used to get a low noise signal (60 Hz L) that represents the 60 Hz power line. If the 60 Hz C and 60 Hz L are correctly phased then the proper frequency for the VCXO is (60 Hz L) x 2^{16}. If phase correction is required then the proper frequency for the VCXO is (60Hz L) x (2^{16}) $\pm(\Delta$ F) when Δ F represents the frequency shift used to cause the phase correction.

The programmer and the cycle counter count all of the cycles of the 4 MHz C that occur in the period of one cycle of 60 Hz L. The phase comparator supplied the cycle counter with the 12 least significant bits of the number 2^{16} - K $\pm(\Delta$ F) where K is the number of cycles counted by the programmer. A comparison is made between the number supplied by the phase comparator and the number of cycles counted by the cycle counter. If the two are unequal the results are passed on to the frequency controller as an enable up count or enable down count.

The magnitude comparator compares the output of the frequency register to adjustable limits. If the frequency register is larger than the upper limit, the up count is disabled in the frequency controller. If the frequency register is smaller than the lower limit, the down count is disabled.

If the up count or the down count has not been disabled by the cycle counter of the magnitude comparator then the frequency controller activates the corresponding count input to the frequency register when the frequency controller is strobed. Up counts and down counts are also distributed outside the VFMC for use in chopper damper circuitry.

The strobe is adjustable from 0.5 Hz to 60 Hz allowing the frequency register to be updated at a rate that the chopper rotor can follow. The functions of the programmer are to activate the strobe and reset the cycle counter, phase comparator, and selector. The selector sends the 4 MHz C to the programmer when it is set by the 60 Hz L. After being reset by the programmer the selector sends the 4 MHz C to the cycle counter.

Neutron Chopper Damper Theory of Operation

The chopper rotor is driven by a hysterises synchronous motor. As indicated by Fig. 3, the rotor would lag the stator magnetic axis by the stable rotor load angle. Within limits, as rotor load angle increases, motor torque increases. When the rotor velocity is changed it causes a change in instantaneous rotor load angle. Without damping, the instantaneous rotor load angle would oscillate about the stable rotor load angle. The phase shift amplifier has the ability to shift the stator magnetic axis. The damper measures changes in rotor velocity to generate an error signal to control the phase shift amplifier. When the rotor is accelerating, the phase shift amplifiers shift the stator magnetic axis in a direction to reduce the instantaneous rotor load angle. This reduces motor torque and acceleration.

Chopper Damper Circuit Description

The chopper period is measured by gating a 100 MHz clock into the accumulator (Fig. 4) for 28 revolutions of the chopper. A change in chopper period of approximately 1 part in 10^7 would cause the resultant number in the

accumulator to change by 1. The number in the accumulator is saved in the D to A register whose output is converted to analog by the D to A converter and is used as an error signal. The error signal is added to other correcting signals and used as phase control by the phase shift amplifiers. To keep the D to A converter operating in the center of its control range, the accumulator is preset to the value in the offset register. The D to A register is checked by the offset detector to see if it is in the midrange of the D to A converter. If it is not, the offset register is incremented or decremented in the direction to put the D to A converter in midrange. When the VFMC changes frequency, the chopper period will have to change. Without additional inputs the damper would try to prevent the chopper period change. The accelerator, responding to up or down counts from the VFMC, adjusts the offset register, so when the chopper reaches its new period, the D to A converter will be in midrange. To calculate the amount of change in the offset register note that when the VFMC frequency register is changed by one count the 4 MHz C changes by one part in 2.4×10^6. This will cause the same change in the chopper period. The calculation of the change in accumulator counts is then

28 revolutions x chopper period x clock rate x one part in 2.4×10^6 parts =

$28 \times (1/270) \times 100 \times 10^6/2.4 \times 10^6 = 4.3.$

Therefore, if a up count is received from the VFMC the accelerator would increase the number in the offset register by 4 counts. The accelerator also puts an offset into the error signal summing amplifier for a short time to help get the chopper to its new period faster. When the starter detects the 28 revolutions of the chopper, it sets the set reset. This action results in gating the 100 MHz clock to the accumulator off and on to the timer and programmer. The amount of time measured by the timer plus the amount of time measured by the accumulator is 28 times the chopper period. The timer measures a precise amount of time for the programmer to operate before resetting the set reset. The programmer loads the D to A register from the accumulator, updates the offset register,and loads the offset register into the accumulator.

Damper Tests and System Operation

In order to test the damper, the chopper drive signal period was increased to cause the chopper period to increase by 89 ns. This change was introduced linearly over 2 s (Fig. 5 - upper trace). The three time frames represent three conditions: 1) no active damping in circuit, 2) active damping added to circuit and 3) the addition of the accelerator function to the active damper. On June 13, 1985, the IPNS started operating on the VFMC with the VFMC tracking the 60 Hz power line. During the first seven days of operation, one master chopper and one slave chopper were operating. The master took data 99.4% of the time and the slave took data 98.8% of the time. This is within the range of efficiencies that would be normal if the IPNS were operating on a fixed clock. The 30 Hz reference has been between $\pm 40^o$ of the desired power line phase 96% of the time. Tests indicate that there would be little effect on chopper stability and data taking efficiencies if the VFMC were set to more tightly follow the 60 Hz power line. Measurements were taken of energy resolution of the neutron beam passed by the choppers while the IPNS was operating on a fixed clock and the VFMC. The measurements did not show any change in the energy resolution.[2] The purpose of operating the IPNS on the VFMC was to improve the intensity and stability of the proton beam in the IPNS. The beam current for the seven days of operation before the VFMC was installed was 11.70 μa. After the operators had been tuning on the line locked IPNS for four days, the average beam current was above 13 μa. The average current for the next four days was 13.63 μa. Other changes were made at the same time the VFMC was installed and it is not known how much each contributed to the increased beam current, but it is believed that the most significant gain came from operating the IPNS locked to the power line.

Acknowledgements

Without the help of G. E. Ostrowski and C. A. Pelizzari I would not have had a deep enough understanding of the chopper control system to have developed the VFMC or the active chopper damper. I would also like to thank M. Faber and R. Zolecki for flawless construction technique that saved hours of debugging circuitry.

References

[1] A. Rauchas, et al., "IPNS Accelerator System and Neutron Chopper Synchronization," Proceedings of International Collaboration on Advanced Neutron Sources (ICANS-VII), Atomic Energy of Canada Limited, Report AECL-8488 (Sept. 13-16, 1983) 157.

[2] G. E. Ostrowski, et al., "The IPNS Chopper Control and Accelerator Interface Systems," proceedings of this conference.

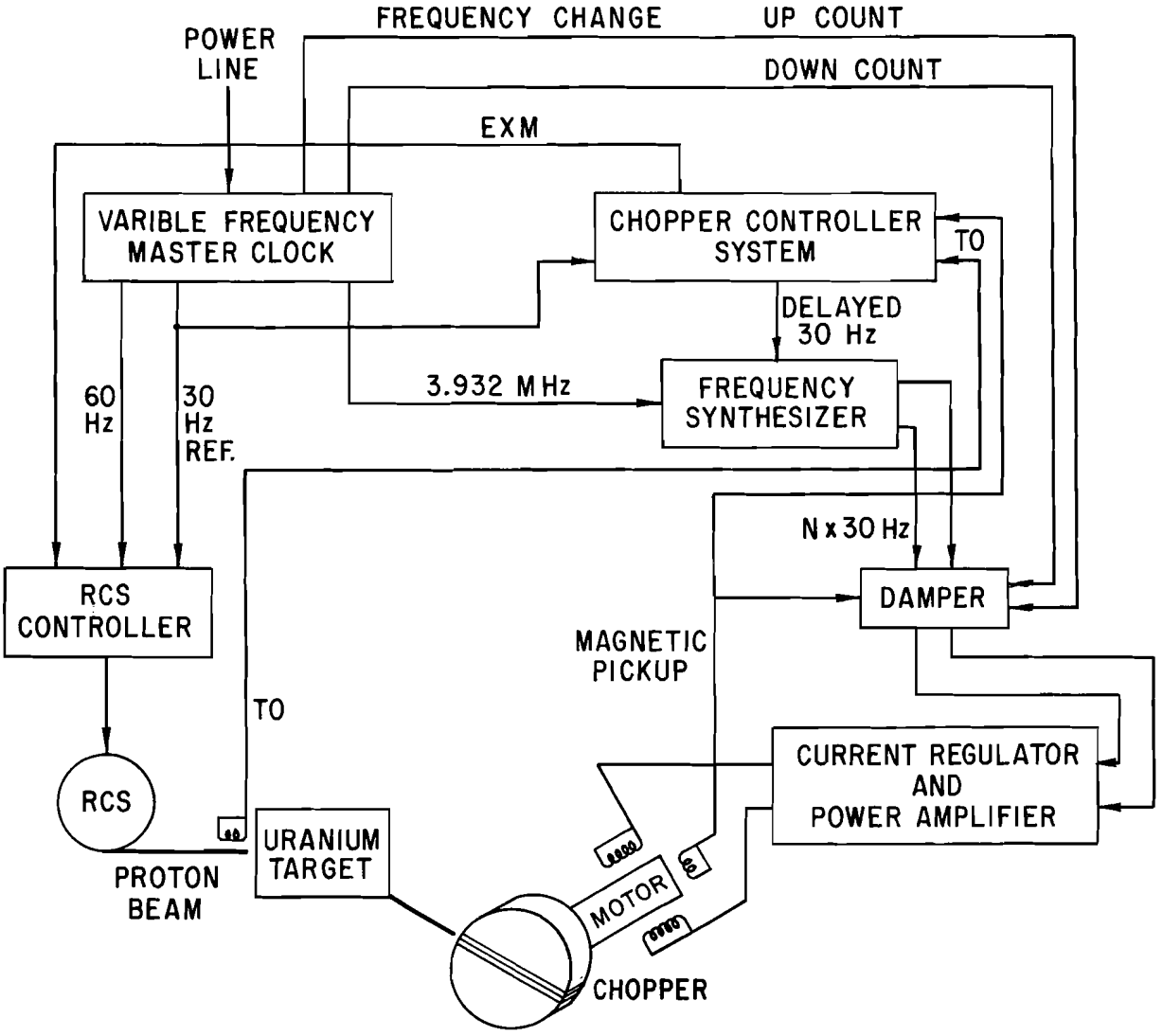

Fig. 1. Chopper IPNS control system.

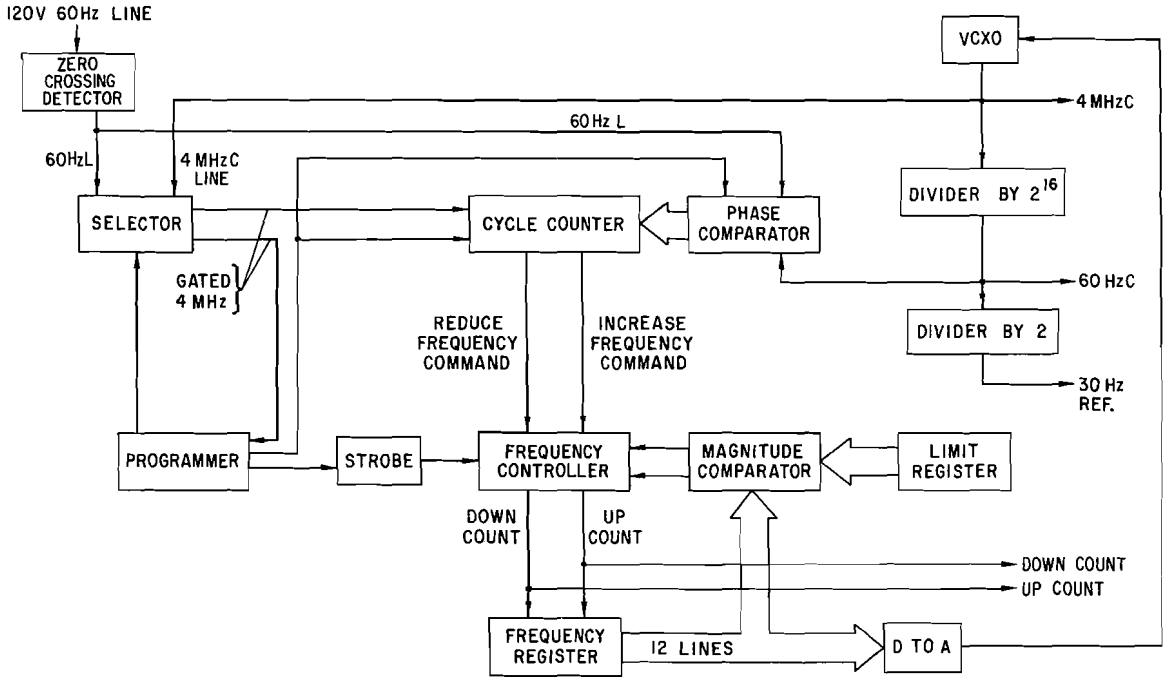

Fig. 2. Variable frequency master clock.

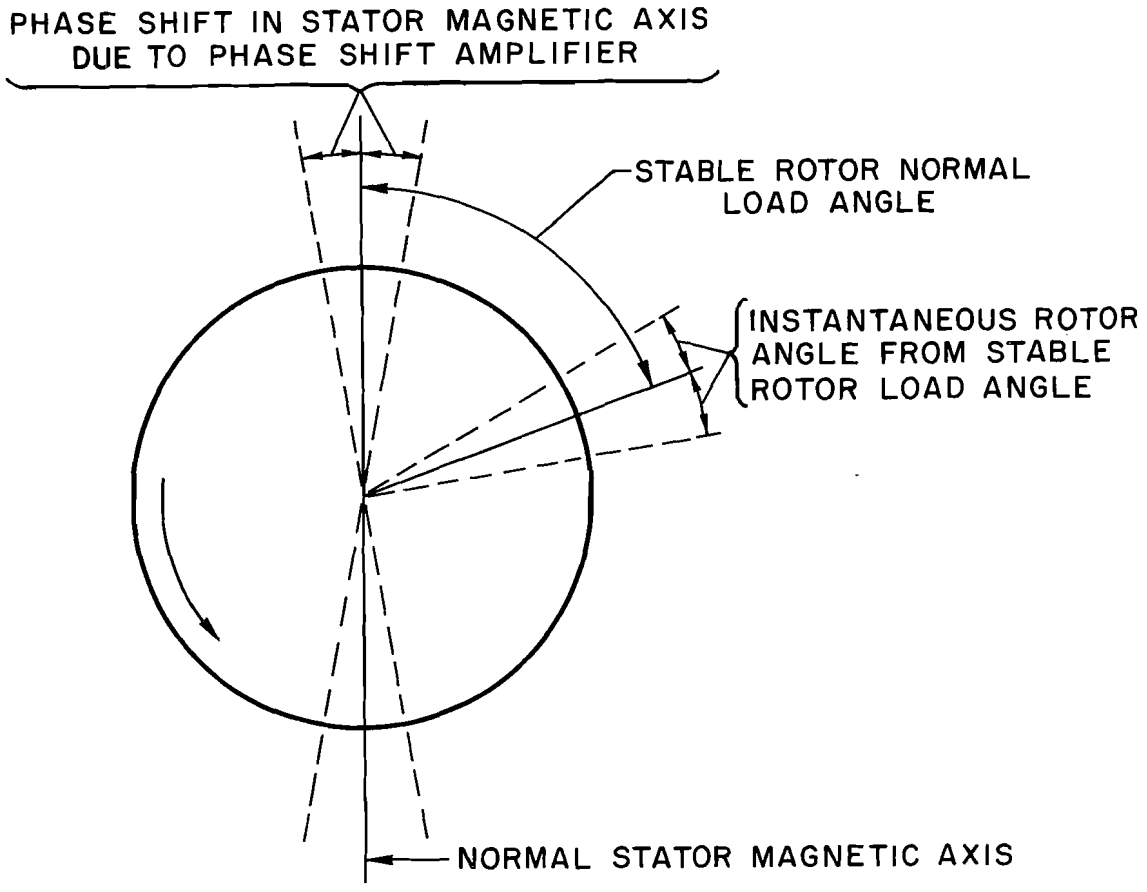

Fig. 3. Rotor load angle.

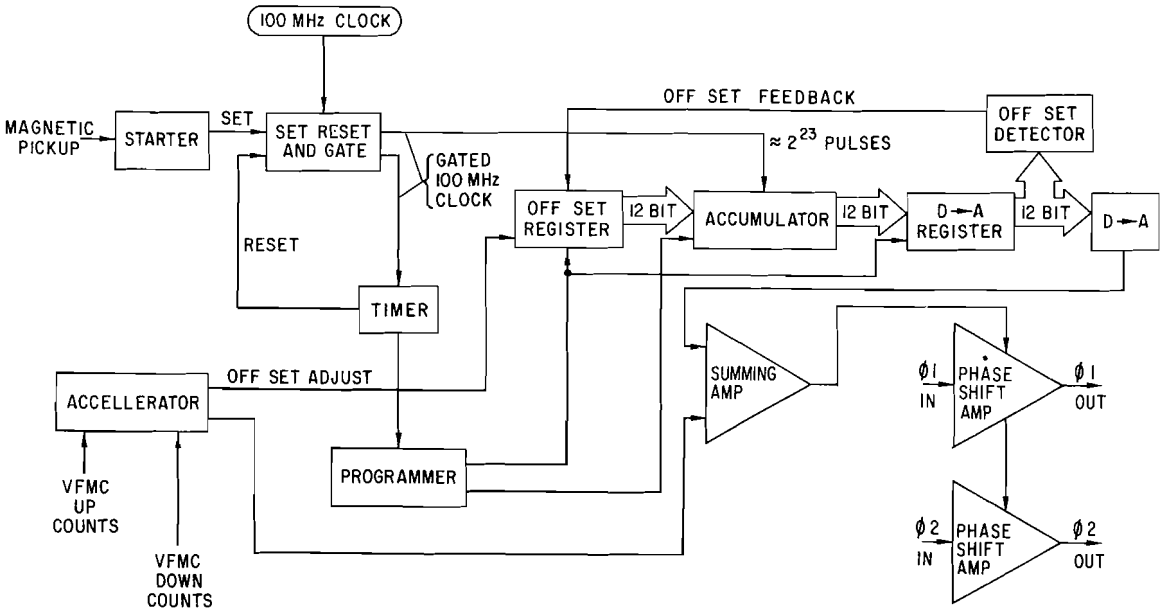

Fig. 4. Active chopper damper.

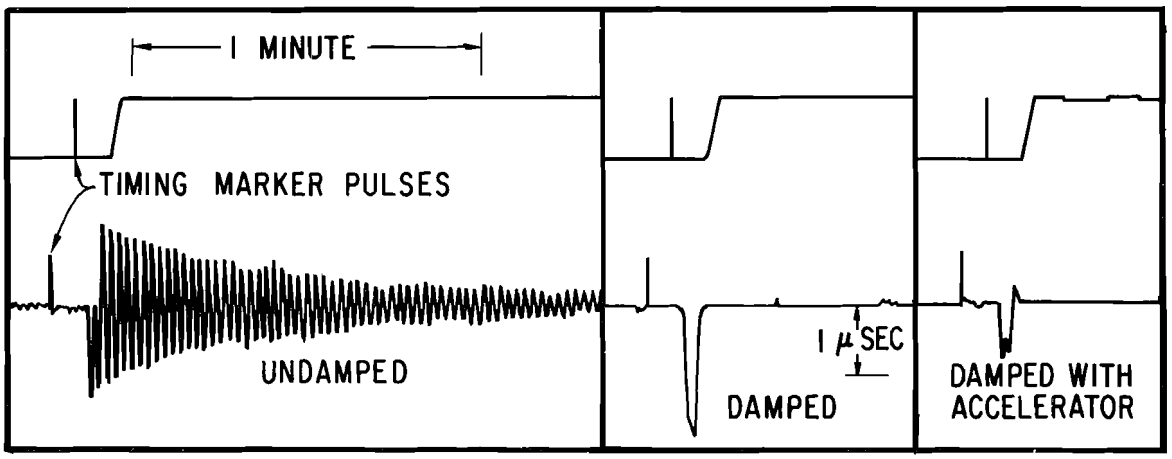

Fig. 5. Strip chart.

Proceedings of the Eighth Meeting of the International Collaboration on Advanced Neutron Sources (ICANS-VIII)
8-12 July 1985, Rutherford Appleton Laboratory Report RAL-85-110

NEUTRON CHOPPER DEVELOPMENT AT LANSCE

M. Nutter, L. Lewis*, S. Tepper*, R. N. Silver, R. H. Heffner
Physics Division, MS H805
Los Alamos National Laboratory
Los Alamos, New Mexico 87545

ABSTRACT

Progress is reported on neutron chopper systems for the Los Alamos Neutron Scattering Center pulsed spallation neutron source. This includes the development of a 600+ Hz active magnetic bearing neutron chopper and a high speed control system designed to operate with the Proton Storage Ring to phase the chopper to the neutron source.

I. INTRODUCTION:

Choppers for inelastic epithermal neutron scattering experiments at the Los Alamos Neutron Scattering Center (LANSCE)[1] must meet three criteria. First, they must operate continuously with minimal maintenance during the typically six months run cycle of the LANSCE facility. Second, they must provide the maximum transmission in a short pulse of neutrons of the order of 2 μsec FWHM to match the neutron source resolution, a feature which requires as high a rotation speed as possible.[2] Third, the chopper must be timed with the neutron source to transmit neutrons of only one time-of-flight (energy). This is difficult because the LANSCE pulsed neutron source is synchronized to the variations of the power line frequency and phase within time windows set by the limits of accelerator operations.

Previously, Los Alamos had reported[3,4] on a successful test of a control system for phasing neutron choppers to the proton bursts from the Los Alamos Meson Physics Facility (LAMPF) accelerator on the WNR facility target. This involved a partial PID control of a low speed (240 Hz)

*Engineering consultants to the Los Alamos National Laboratory

mechanical bearing chopper as well as triggering the LAMPF accelerator within an allowed 128 μsec window from a magnetic pickup on the chopper. This system would not allow more than one chopper to operate at the same time.

This paper is a report on progress on chopper systems at Los Alamos in the past two years. Los Alamos has acquired a high speed (600+ Hz) active magnetic bearing chopper. It has also developed a high speed control system which will operate with the Proton Storage Ring[5] and which will permit several choppers to be phased to the source simultaneously.

II. ACTIVE MAGNETIC BEARING NEUTRON CHOPPER:

To meet the first two criteria, a mechanical rotating chopper which uses active magnetic bearings (AMB) has been designed, manufactured by S2M Corporation in Vernon, France, and delivered to Los Alamos.

There were many reasons to choose magnetic bearing technology over more conventional mechanical bearing technology. The no-wear feature of magnetic bearings, due to the absence of metal-to-metal contact, will allow the unit to operate continuously for long periods of time without the need to shut down for bearing replacement maintenance. Because there is no need for lubrication, which can introduce varying frictional loads and limit the allowable surface velocity, the rotating member can be large and still operate at very high speeds (i.e., at 600 Hz and above). Because such a system is stiff, the operating speeds can still be below the critical frequencies of the mechanical system (870 Hz in the present case), greatly simplifying the acceleration and deceleration. By eliminating the variable frictional load of mechanical lubricated bearings and the flexibility of the mechanical system, the control problem is reduced to that of following the variations in neutron pulse timing primarily caused by power line variations.

There are many additional advantages for a magnetic bearing system. The rotor is self-balancing, turning around its principal axis of inertia rather than around the axis of the bearings. This results in vibration free, silent operation because there is no stress on the bearings. There is a very low heating of the bearings, a very low power consumption, and a very wide temperature operating range. The bearing stiffness is adjustable electronically, providing great precision in setting the rotor equilibrium position. The suspension damping is also adjustable, which enables passing the rotor critical speeds without difficulty. (However, as mentioned earlier, in the initial design the first critical speed (870 Hz) is above the design operating speed (600 Hz).) It is also possible to permanently monitor the machine during operation because the data from the AMB

electronic position sensors provide constant information on rotation characteristics. The system provides all the information required for in-situ balancing. There is also electronic information to initiate an automatic shutdown in the case of excess machine vibration or malfunction.

Figure 1 is a schematic drawing of the active magnetic bearing neutron chopper which was acquired from S2M Corporation in Vernon, France. These systems now can also be manufactured by Inland Motor Corporation in the U.S., which has licensed the technology from S2M. The neutron chopper consists of a vertically oriented shaft supported by an axial thrust bearing and two radial bearings. The 3 KW, 3 phase induction motor squirrel cage rotor is an integral part of the vertical shaft and provides the rotational driving force. The neutron chopping Fermi slit package is contained in a replaceable aluminum drum which forms a part of the vertical shaft. The radial bearings are located near the top of the shaft and at the bottom below the slit package. The entire shaft assembly runs in a vacuum, thus reducing the windage and power consumption, and is compatible with operation in an evacuated beam line. In case of power failure of the mains, battery back-up is provided to maintain the magnetic bearing operation until the unit is decelerated and comes to a stop. There are also mechanical back up bearings.

III. CONTROL SYSTEM OVERVIEW:

The major system elements and associated controls are illustrated in Fig. 2. Proton macropulses are generated in the LAMPF linear accelerator with the 2nd harmonic (120 Hz) of the incoming power grid. These proton pulses are typically 750 μsec in length with the leading edge occurring 200 μsec after the zero voltage crossover of the phase of the grid power.

Every 10th proton macropulse is injected into the recently constructed Proton Storage Ring (PSR) at a pulse repetition rate of 12 Hz. The macropulse is chopped into segments 0.27 μsec long separated by 0.09 μsec, each segment of which is fed into an electromagnetic bucket for protons in the PSR which makes a revolution about the ring every 0.36 μsec. When the macropulse injection is completed, PSR specifications require that the stored proton bunch of 0.27 μsec length be extracted within 200 μsec onto the high Z spallation target to produce neutrons. The neutrons from the target are slowed down in hydrogenous moderators to the energies required for neutron scattering research. This produces a neutron burst with FWHM pulse width of approximately 2 μsec/ $\sqrt{E(eV)}$, where E is the neutron energy, for epithermal (E > 0.1 eV) neutrons. The neutrons travel down the beam line toward the chopper, whose purpose is to select a neutron time of flight, i.e., monochromate the beam. The chopper has a aluminum boron fiber composite Fermi slit package optimized[2] for intensity and resolution.

The primary specifications of the chopper control system arise from the need to achieve the best energy resolution by controlling the time-of-flight to much better than the neutron pulse width. The desired neutron time slice is a function of the chopper angular velocity; for this system, the control provides a selectable angular velocity ranging from 120 Hz to 600 Hz in steps of 60 Hz. The control system divides the time taken for a complete chopper revolution in 0.1 μsec increments. The control system is capable of allowing the selection of any desired time-of-flight, with a 0.1 μsec granularity. In practice, the system can be no more precise than the PSR circulation time of 0.36 μsec. The control system design specification has been set at ± 0.3 μsec root sum square (RSS) control accuracy in the time-of-flight.

Bolie et. al.[3,4] described an experimental system which phased a 240 Hz mechanical bearing chopper to LAMPF. The results were in general agreement with theoretical expectations; however, they fell far short of the required accuracy. A major limitation on the accuracy was shown to be the random variability of the grid power which, via the LAMPF synchronization with the grid, produced a random variability in the proton macropulse repetition rate. Bolie et. al. showed that the grid power variability was dominated by two terms. The first is a high frequency crossover to crossover jitter of ± 8 μsec; the second is a slow periodic variability of ± 8 μsec at a rate of approximately 1.2 radians/second. This level of variability was far beyond the tracking capability of the control system. Of even greater significance was the random nature of the variability which eliminated the opportunity to predict the arrival time of the next pulse based on data from the previous pulse. To circumvent this problem, a feedback signal was taken from a magnetic stud pickup on the chopper, the function of which was to modify the LAMPF trigger point to be compatible with the chopper instantaneous position. This approach substantially enhanced system accuracy but was still below the accuracy objective. Furthermore, it limited the facility to the use of a single chopper.

Further analysis conducted on the chopper control dynamics showed that a system bandwidth in excess of 1200 radians/sec would be required to track the jitter component on a pulse-by-pulse basis and that this bandpass requirement would require a motor drive power in excess of 10 kilowatts. In contrast, tracking the slow periodic variability requires a control system bandwith of 12 radians/sec and a motor drive power on the order of 1 kilowatt.

In view of these widely disparate requirements, we decided to reconfigure the system to treat the two variability components separately. The reconfigured system eliminates the jitter component through electronic

filtering techniques and uses a 3 kilowatt motor to track the low frequency periodic variability. The revised configuration is illustrated schematically in Fig. 3. In this configuration the control system is a combination forward loop control of LAMPF and PSR coupled with a closed loop feedback control of chopper speed and phase.

The control system takes grid power zero crossings as its input. This signal is passed through a loosely coupled phase lock loop which has a zero gain bandwidth of 12 radians/sec. The output signal is 120 Hz in phase with the input signal for all input frequency perturbations up to 1.2 radians/sec and progressively rejects increasing levels of high frequency input perturbations. This produces a 20:1 attenuation level which reduces the 16 μsec jitter to 0.8 μsec. Attenuation levels beyond this magnitude have no benefit since LAMPF has an inherent jitter of 1 μsec. The output is a 120 Hz carrier frequency that is essentially jitter free and is overmodulated with a low frequency component corresponding to the grid power behavior. This signal is used to trigger LAMPF in a predictable manner. In practice, this trigger signal is well within the $\pm$ 64 μsec range of the zero crossings set by LAMPF operations requirements.

The time interval between triggering LAMPF and total capture of the proton macropulse by the PSR is a constant of 950 μsec for a 750 μsec wide macropulse. PSR specifications limit the storage of the macropulse for a maximum of 200 μsec after capture. To take account of these characteristics the output of the jitter filter is passed through a time delay, the value of which corresponds to the LAMPF/PSR delay plus half the allowable PSR storage time, and then passed on to a programmable frequency multiplier.

This multiplier takes the form of an additional loosely coupled phase locked loop, again with a bandwidth of 12 radians/sec. Thus it provides a further 20:1 attenuation on grid jitter reducing its level under worst case conditions to less than 0.04 μsec. The output of the multiplier is in phase with its input signal, synchronized through the delay action to be at the mid-point of the PSR holding time, and its frequency is that at which the chopper is required to run. By taking a function of the multiplier output as the PSR trigger, the PSR proton release is synchronized to the motor control system.

Control of the neutron time-of-flight is achieved by placing a programmable time delay between the motor control system and the multiplier output. The chopper assembly incorporates a stud type position reference which passes a magnetic monopole speed sensor when the slit package is in line with the neutron source. The monopole produces a fast leading edge pulse under line up conditions. The motor control system is a tightly coupled phase lock loop, having a bandwidth of 87 radians/sec, and acts to

modulate the motor excitation frequency such as to keep the stud feedback signal precisely in phase with the delayed frequency multiplier output. By placing the time-of-flight delay in the forward loop as opposed to the feedback path, time-of-flight can be directly dialed. More importantly, time-of-flight accuracy is not affected either by selected chopper speed or low frequency perturbations of grid frequency.

Provisions are incorporated in the chopper assembly for a laser position feedback signal to supplement the magnetic monopole system. This provides a higher accuracy position feedback, if required.

This control architecture allows the use of multiple choppers through replication of the frequency multiplier and motor control system in as many installations as required. Synchronization of additional choppers is achieved by driving each additional chopper from the PSR trigger signal.

IV. CURRENT STATUS:

S2M supplied the active magnetic bearing chopper system to Los Alamos along with a dummy rotor and control cabinet in February, 1985. Initial commissioning tests began in May and the early test results were encouraging. The chopper operated at all power line harmonic speeds from 60 Hz to 600 Hz with no observable limitations due to unexpected vibration criticals. Velocity command changes from minimum to maximum speeds are executed in 120 seconds.

So far there have been only four days of testing of the control system with the S2M chopper. The jitter filter, LAMPF trigger, frequency multiplier, PSR trigger, and delay network are validated. Phase control of the chopper encountered a stability problem due to an additional lag associated with the motor drive system. This lag limited the motor drive bandwidth to 11.8 radians/sec and produced a cyclic time-of-flight wander of $\pm$ 10 usec. Subsequent analysis of the revised dynamics have shown good theoretical agreement with the test results. Modifications are in process to the motor drive system to provide the required bandwidth and stability. Testing is expected to resume in July with the system becoming available for operation concurrent with PSR availability during the last quarter of 1985.

Testing of the system with neutrons from the PSR is scheduled to begin in October, 1985. Based on the success of these tests, Los Alamos will proceed with the design and development of a chopper spectrometer for 1986 construction.

V. ACKNOWLEDGEMENTS

We thank the staff of S2M Corporation, in particular M. Brunet and M. Dussaux, who have worked with us so patiently in developing the active magnetic bearing neutron chopper. We also thank H. Bowen and A. P. Key for their excellent technical support.

REFERENCES

1. R. N. Silver, "The Los Alamos Neutron Scattering Center," LA-UR 85-...., submitted to Physica, Schull Festschrift Supplement

2. For a discussion, see C. Windsor, Pulsed Neutron Scattering, Taylor and Francis, London (1981)

3. V. Bolie, R. M. Brugger, R. N. Silver, "A Phased Chopper at WNR," Proceedings of the Sixth Meeting of the International Collaboration on Advanced Neutron Sources, Argonne National Laboratory, June 28-July 2, 1982, ANL-82-80, p. 191

4. V. Bolie, R. M. Brugger, R. N. Silver, LA-UR 83-3718, "Neutron Chopper Phasing for a Quasi-Periodic Pulsed Neutron Source," Accepted for Publication in Nuclear Instruments and Methods 236 (1985)

5. G. Lawrence, R. Cooper, D. Hudgings, G. Spalek, A. Jason, E. Higgins, R. Gillis, "LASL High Current Proton Storage Ring," Proceedings of the XI International Conference on High Energy Accelerators, Geneva, July, 1980, Published in Experimentia: Supplement 40, 103 (1981); G. P. Lawrence, R. A. Hardekopf, A. J. Jason, P. N. Clout, G. A. Sawyer, "Los Alamos High Current Proton Storage Ring Status Report," Proceedings of the 1985 Particle Accelerator Conference, LA-UR 85-1613

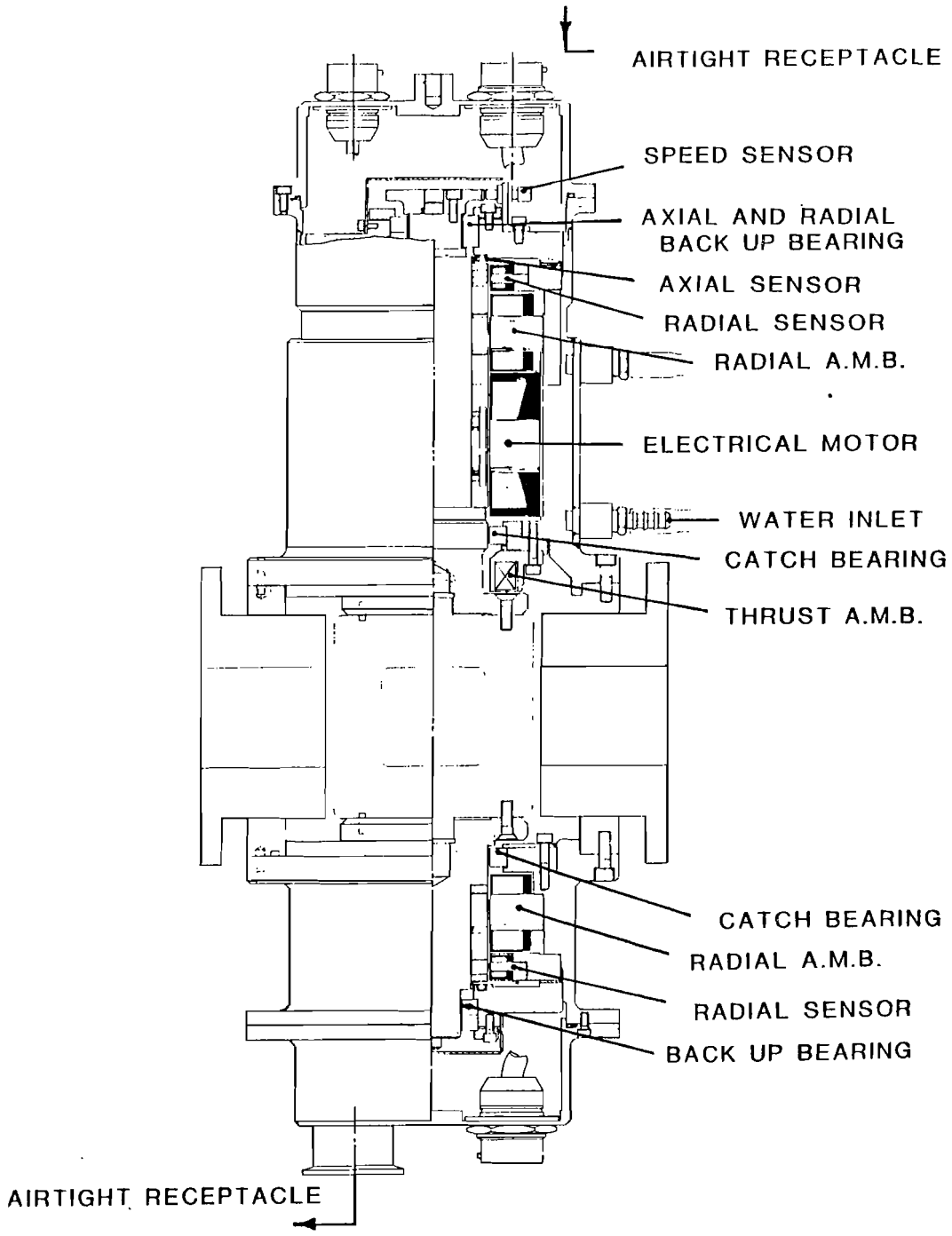

Fig. 1 Schematic diagram of the active magnetic bearing neutron chopper supplied by S2M Corporation.

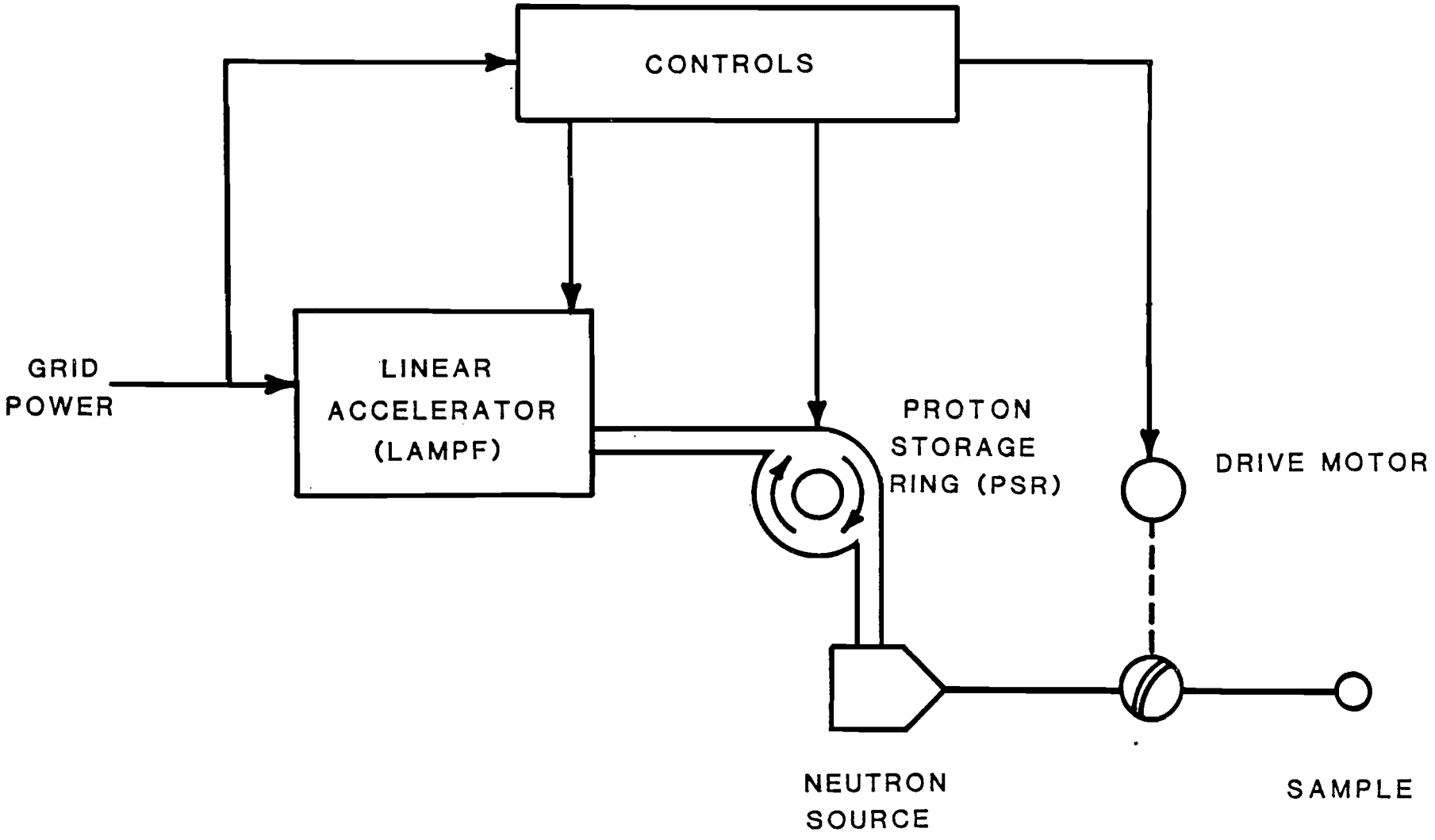

Fig. 2 General arrangement of acclerator, chopper, and controls.

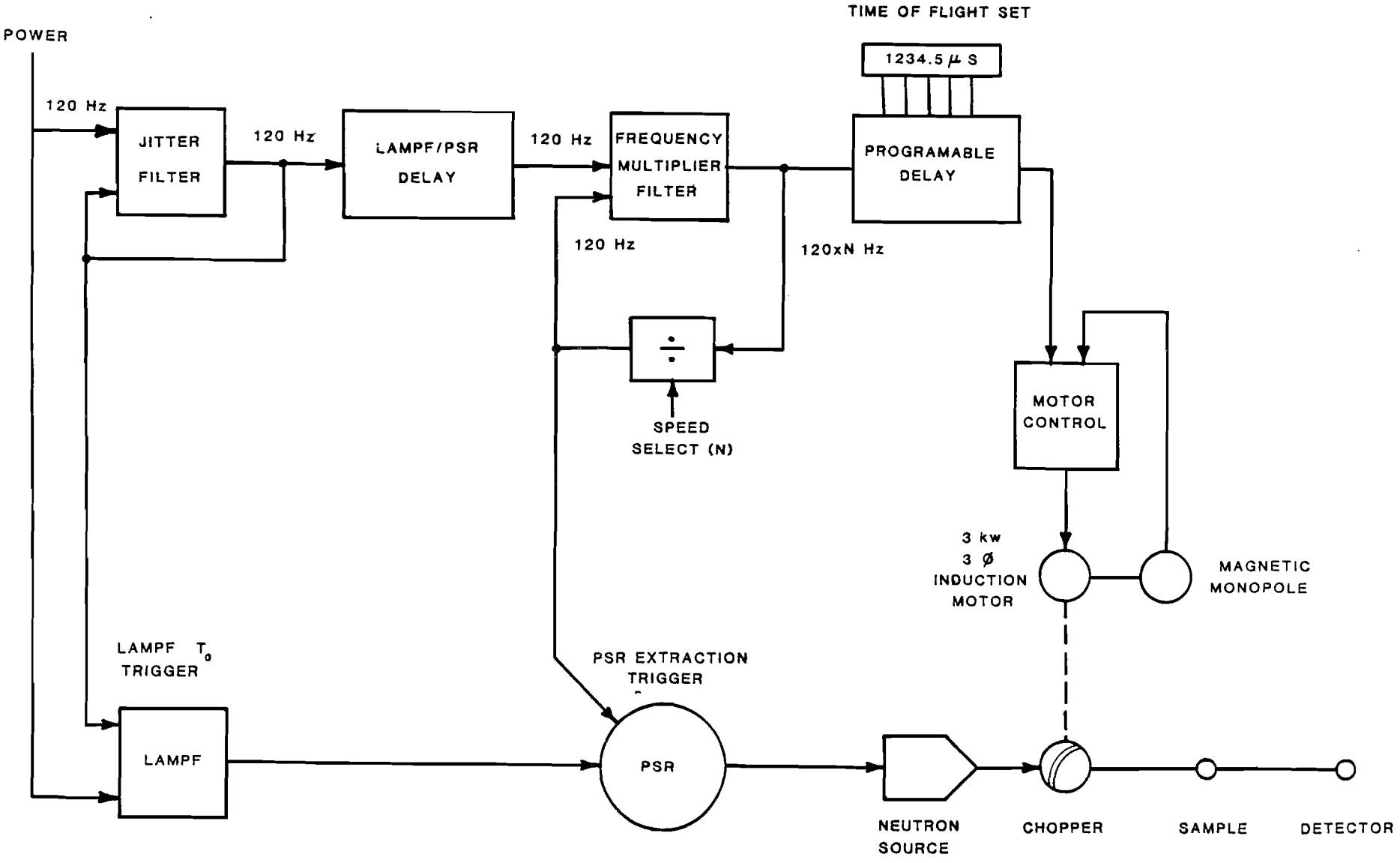

Fig. 3 Reconfigured chopper control system architecture.

Proceedings of the Eighth Meeting of the International Collaboration on Advanced Neutron Sources (ICANS-VIII)
8-12 July 1985, Rutherford Appleton Laboratory Report RAL-85-110

EXPERIENCE WITH THE KFA/IGV (JUELICH) MAGNETIC BEARING SYSTEM ON AN SNS NEUTRON CHOPPER

T J L Jones, J H Parker and I Davidson
Rutherford Appleton Laboratory

K Boden and J K Fremery
IGV, KFA Jülich

1. Introduction

The chopper described is the fast Fermi neutron beam chopper which has been designed to select the incident neutron energy for the High Energy Transfer Spectrometer (HET) on the SNS, the magnetic suspension system for which has been developed and manufactured as the result of a collaborative contract between the Rutherford Appleton Laboratory (RAL) and the Institut für Grenzflächenforschung und Vakuumphysik at Kernforschungsanlage Jülich (KFA/IGV).

Figure 1 shows a sectional assembly drawing of the chopper. It consists essentially of 4 major components:

i) An evacuable spinning tank.
ii) The chopper rotor.
iii) The upper magnetic bearing assembly.
iv) The lower magnetic bearing assembly to which is attached the stator assembly of the hysteresis motor which drives the chopper rotor.

Figure 2 is a photograph of the chopper assembly with the top cover of the vacuum tank and upper bearing assembly raised to show the top end of the chopper rotor.

2. The Construction of the rotor and slit packages

The chopper is furnished with a family of 3 rotors containing curved-slot slit packages. These are assemblies of neutron opaque 'slats', formed from a triple laminate of boron fibres diffusion bonded into an aluminium matrix, interleaved with neutron transmitting 'slits' built up from appropriate thicknesses of etched aluminium foil. Cylindrically profiled cheek plates are used to curve the packages so that, at the rotor speed of 600 Hz, their transmissions and resolution are optimised. to neutron energies of 1 eV, 500 meV and 250 meV respectively.

Because the magnetic bearings operate with a large physical clearance between rotor and stator the rotors are easily interchanged in the spinning tank and so, by choice of appropriate rotor and electronic rephasing of the chopper, incident neutrons with energies ranging from ~ 100 meV to almost 4 eV can be selected for the spectrometer at ~ 1% energy resolution.

The construction of a rotor can be clearly seen in Figure 3 which is a photograph taken just before the insertion of a slit package into the central body of the rotor. To the left of the slit package examples of the component 'slats' and etched 'slits' are shown and the rods, which fit into the reamed grooves in the package securing it centrally in the rotor body, can be seen protruding from the upper side. (The plates which can be seen screwed to the ends of the package are only mounting jigs to hold the assembly together during manufacture and are removed after the package has been press-fitted into the body.) The upper and lower shafts, to the left and right of the central body in the photograph, which are integral with the aluminium rotor body, are fitted with steel collars which are the moving components of the magnetic bearing and hysteresis motor systems. At the extremities of these shafts dry-lubricated ball races are fitted which act as touch-down and safety bearings in the event of failure of the magnetic suspension.

3. The Magnetic Bearing and Control System

Frictionless suspension of the rotors is achieved using an axially-passive, radially-active permanent magnet bearing system developed by KFA/IGV.

Magnetic bearing stator units are mounted on the upper and lower flanges of the spinning tank. The passive part of each unit is a toroidal barium-ferrite permanent magnet which provides the force to support the weight of the rotor and much of the force to centre it. The active part of each stator consists of two pairs of horizontally opposed magnetoresistors, which sense the off-axis deviations of the rotating steel collars attached to the rotor, and two pairs of horizontally opposed force coils which are powered by the electronic servo control to provide the restoring forces needed to re-centre the rotor.

The drive stator of the hysteresis motor is attached to the outer end of the lower bearing stator. The stator assemblies are sleeved internally with, 'O' ring sealed, thin stainless steel liners which isolates all components from the vacuum within the spinning tank.

The only bearing components attached to the rotors are a set of mild steel cylindrical collars which are push-fitted and clamped to the upper and lower shafts. The motor drive collar is made of a special hysteresis material which is encapsulated in a titanium shield.

A schematic circuit illustrating the principal of operation of the bearing and its control unit is shown in Figure 4. Outputs are also provided on the control unit which allow the magnitude and phase of the axial deviations of the upper and lower bearings to be monitored on an oscilloscope. Any changes in the dynamic balance of the rotor resulting from distortion or movement of the slit package due to the spinning forces are easily detected by this monitor.

4. Drive and Phasing Control Electronics

The chopper drive motor is of the hysteresis type with 3 phases. The stator is connected in a 4 wire 'star' configuration. At 120 Volts a:c line to starpoint it draws 1.2 Amps/phase and is capable of accelerating the chopper to its operational speed of 36000 rpm in ~ 20 minutes. After the chopper drops into phase at 600 Hz the motor current reduces to ≃ 0.6 Amps in order to protect the stator from overheating.

The motor is powered and controlled by a digital electronic control and drive system developed at RAL. The phase can be set in steps of 1.67 μs and under fixed frequency operation a phase stability of ± 0.2 μs has been achieved.

The drive and control system was fully described in a paper by T J L Jones and J H Parker presented at the ICANS IV Meeting.

5. First Results from Operation of the Chopper System

i) General conclusions on the magnetic bearing chopper

Because of the sealed modular construction of the magnetic bearing and motor stator units the chopper has been extremely easy to manufacture, install and operate. Interchange of the rotors has proved to be an easy task which can be performed in ~ 1 hr by the operational scientific staff, without the aid of fitters or mechanics.

ii) Results from operation in the test laboratory

Before installation on the HET Spectrometer the chopper was tested in the laboratory. All 3 rotors were spun at 600 Hz for periods of several days. Operation was silent and vibrationless and in all 3 cases the axial and phase stability of the rotors were within design specification. From observations of the monitor signals from the operating bearings and from visual examinations of the rotor packages after spinning, there were no indications of distortion or displacement of package components due to the action of the spinning forces.

iii) Neutronic performance of the chopper

Because the SNS only came into operation 1 week before this conference a full appraisal of the neutronic performance of the chopper has not yet been possible. To date only the 500 meV peak rotor has been used to monochromate neutrons to the HET Spectrometer.

In a series of short experiments the phase of the rotor was altered, with respect to the SNS neutron pulse, to sweep the neutron peak energy transmitted by the chopper from 310 meV to ~ 1 eV. A low efficiency scintillation detector, ~ 1.5 m in front of the chopper, was used to monitor the intensity of the incident neutron beam and observations were made of the signals from 2 monitor detectors situated in the direct beam 20 cm and ~ 7 m beyond the chopper and of simultaneous signals from the HET detector banks observing the scattered neutrons from a sample of ZrH_2 at the instrument sample position.

Due to interference from the stray magnetic fields (~ 20 Oersted) from the magnetic bearings the data from the monitor 20 cm beyond the chopper has proved non-valid. From the other data we make the following conclusions:

c) Neutron Pulse Characteristics

The duration of the neutron pulse transmitted by the chopper is 2 μs (FWHM) entirely consistent with the design of the 500 meV slit package. There is also transmission by the chopper ~ 833 μs before the main pulse. This corresponds to $\frac{1}{2}$ revolution (π phase) of the chopper and, when the chopper is phased for 500 meV neutrons, represents transmission of neutrons with energies of ~ 17 eV. A full investigation of this will be undertaken but the most probable explanation is that the tips of the slats are not completely neutron opaque at these energies and allow a direct line of sight through the rotor.

b) Relative Transmission of the Rotor

From these provisional data we have attempted to obtain the transmission of the rotor as a function of its opening time (t_{ch}) relative to the SNS pulse (transmitted peak neutron energy). This is shown in Figure 5. The results, which have been normalised for detector efficiency, whilst not entirely self consistent, show a peak transmission near the design energy of the rotor (500 meV). However the shape of the transmission curve is not in agreement with that predicted and further experiments are proceeding to resolve these differences.

6. Acknowledgements

The authors extend their thanks to all colleagues at the RAL and KFA laboratories who have aided with the design, installation and testing of this chopper, especially to Mr M Fisher, Dr A D Taylor and Mr W Rubner.

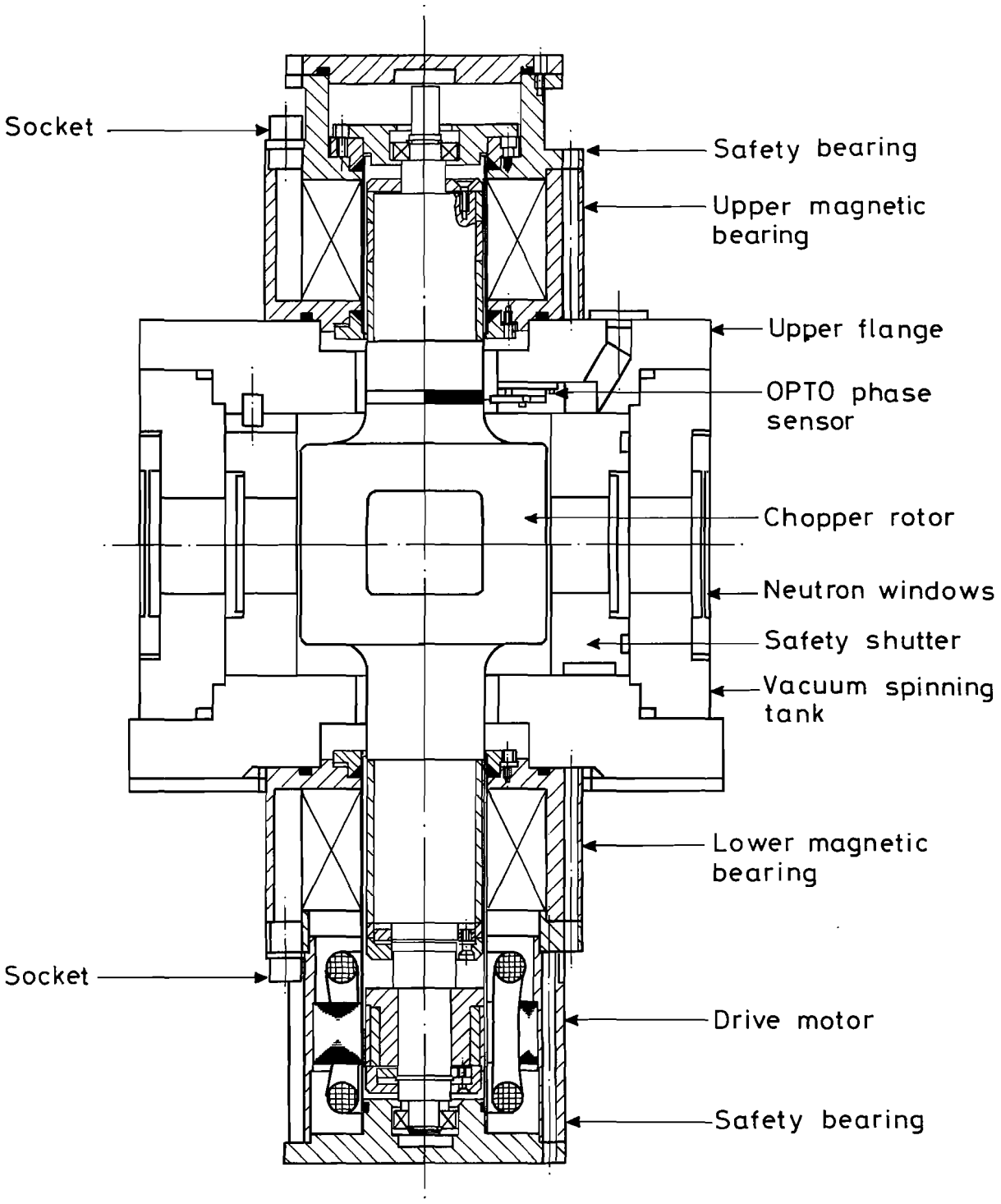

Figure 1 Sectional Assembly Drawing of the HET magnetically suspended chopper.

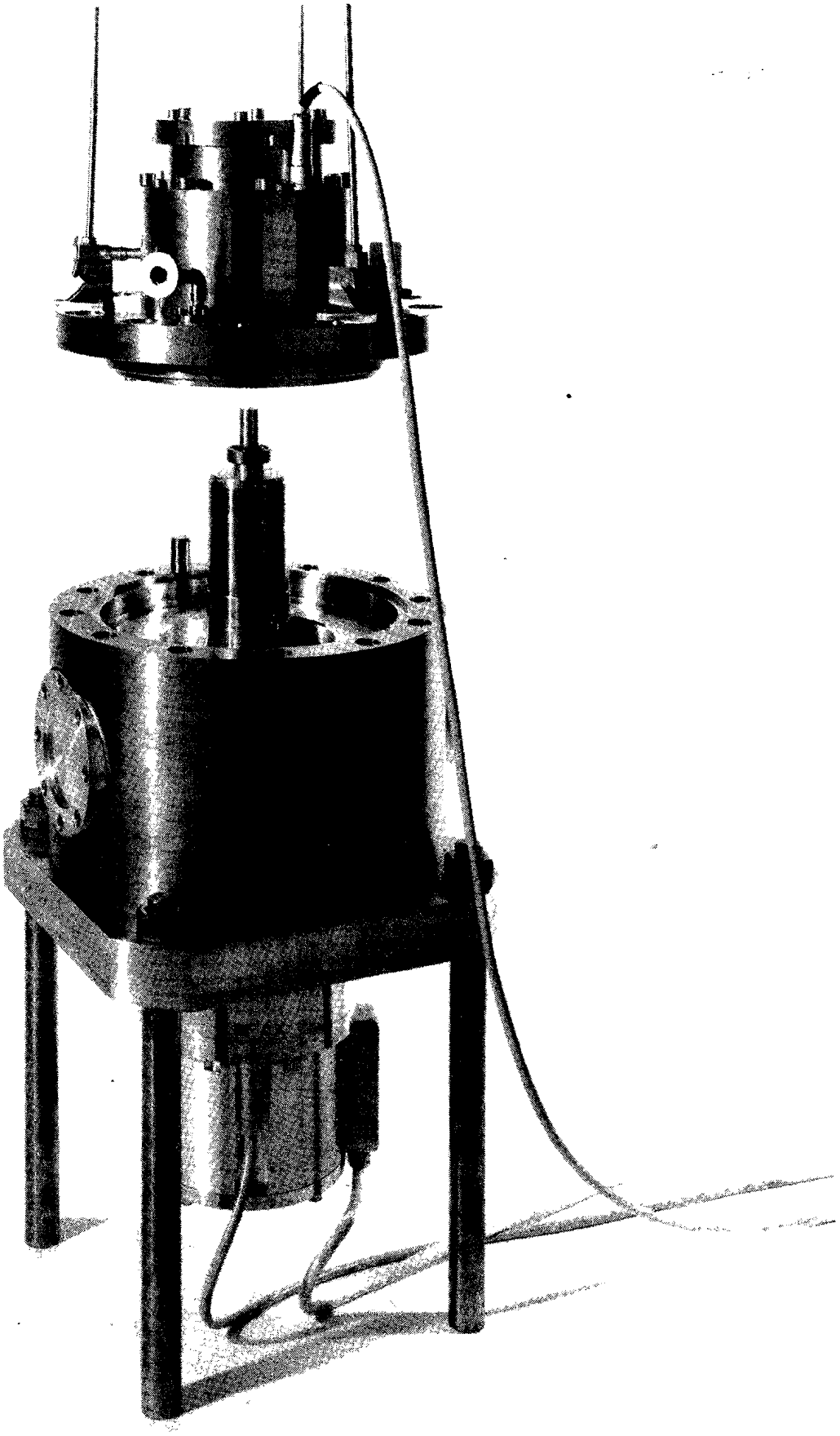

Figure 2 The chopper assembly with the upper bearing assembly and vacuum flange raised to show the mounted rotor.

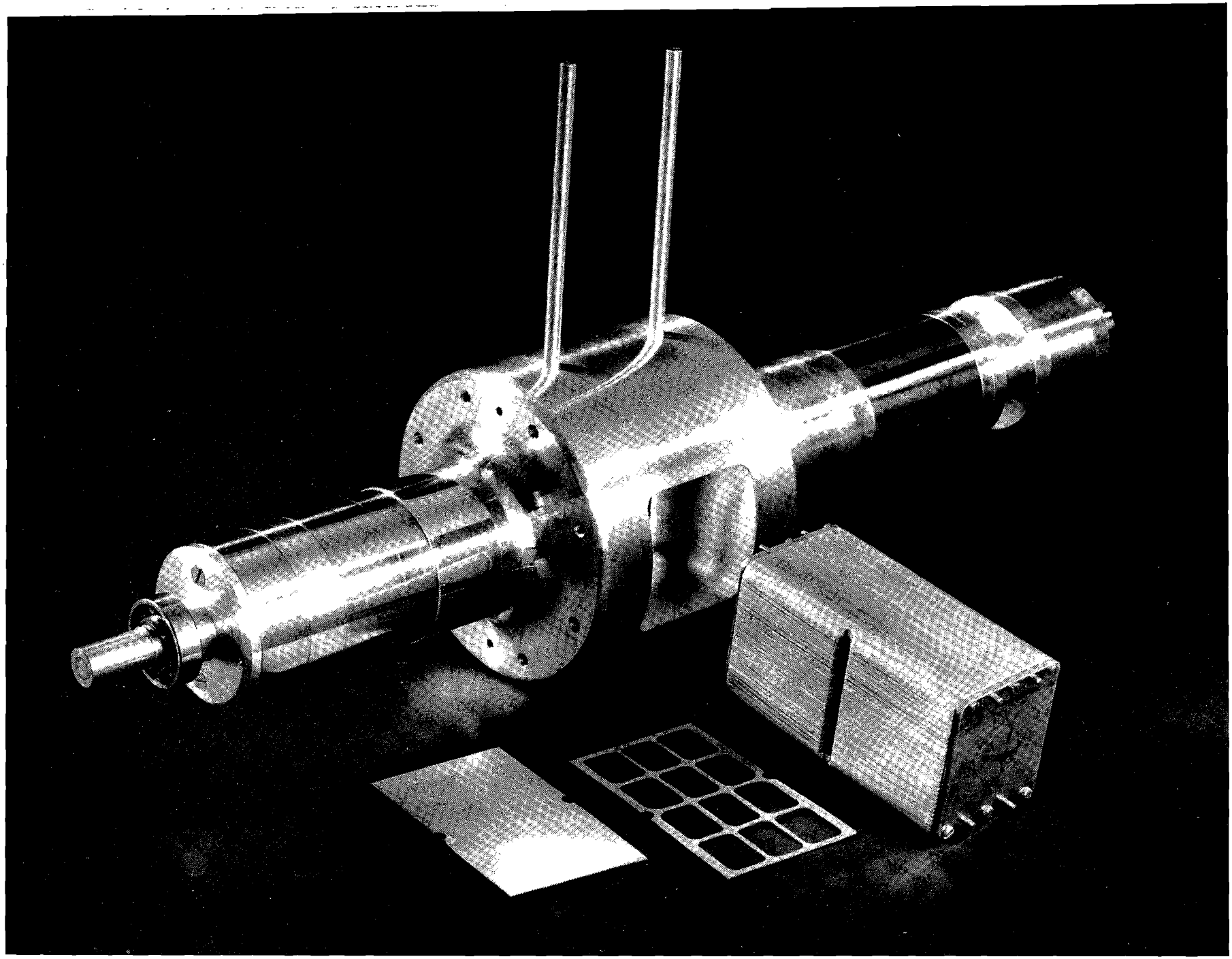

Figure 3 Construction of the chopper rotor and slit package.

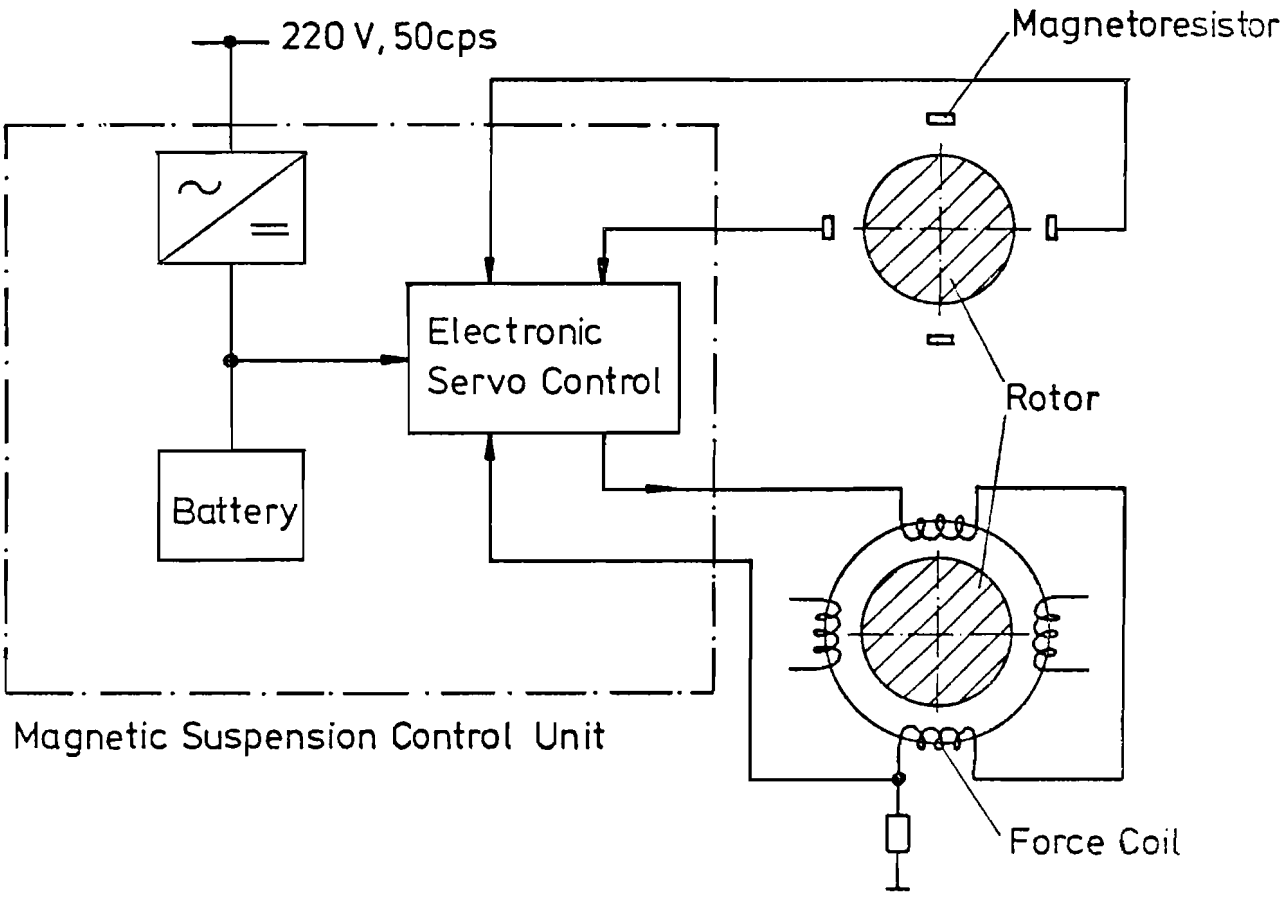

Figure 4 Schematic diagram of the magnetic bearing and its control circuit.

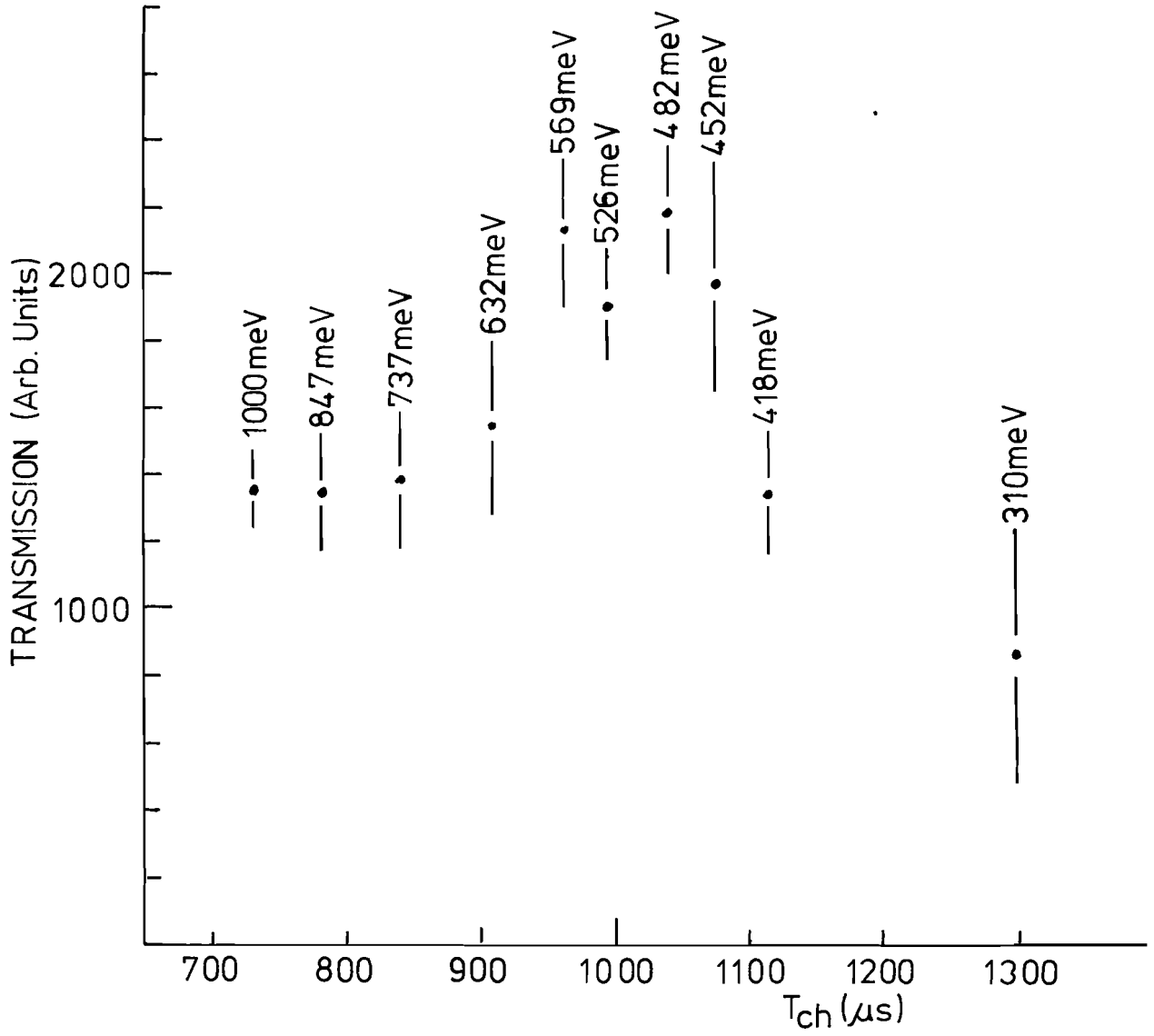

Figure 5 Provisional data for the relative transmission of the 500 meV chopper rotor.

Proceedings of the Eighth Meeting of the International Collaboration on Advanced Neutron Sources (ICANS-VIII)
8-12 July 1985, Rutherford Appleton Laboratory Report RAL-85-110

STATUS OF THE LOS ALAMOS ANGER CAMERA

P. A. Seeger and M. J. Nutter
Los Alamos National Laboratory, Los Alamos, NM 87545, U.S.A.

Abstract

Results of preliminary tests of the neutron Anger camera being developed at Los Alamos are presented. This detector uses a unique encoding scheme involving parallel processing of multiple receptive fields. Design goals have not yet been met, but the results are very encouraging and improvements in the test procedures are expected to show that the detector will be ready for use on a small-angle scattering instrument next year.

1. Introduction

The Anger camera, originally invented for use as a gamma-ray imaging detector for medical applications [1], has been successfully adapted for neutron use at the Argonne National Laboratory [2]. The Los Alamos version differs significantly in its encoding scheme [3]. Fig. 1 is a diagram of a detector with 13 photomultipliers (PMs). Scintillating material is placed in front of only the central PMs, however. An optical glass dispersing plate allows the photons from a neutron capture event to reach a group of seven PMs (a "receptive field"), in varying amounts depending on where the event was. The detector illustrated has three overlapping receptive fields. The linear combinations of signals which determine the position within each field are formed in parallel for all fields in the camera. Position determination is then a two-step process: first, determine which field, and second, interpolate within the field. Since the precision needed for the interpolation is much less than that needed in the standard Anger camera to find a centroid over the entire active area, the electronics may be much faster. The total encoding time per event in our present detector is 400 ns. Furthermore, in a large detector it is possible to analyze events simultaneously in different fields, and so the counting rate may be very high.

The present prototype detector at Los Alamos has 29 PMs and 13 receptive fields. The active area is 150 mm x 255 mm.

2. Calibration

Our present problems with the camera stem largely from lack of an adequate calibration procedure. It is essential that all PMs have the same gain, which is usually accomplished by adjusting the individual high voltages. The calibration and the subsequent tests described here were done using a monochromatic (1.257 Å) neutron beam from the Omega West Reactor at Los Alamos. We have made a mask, 1-cm thick, filled with ^{10}B powder, with ten circular plugs of Aℓ to provide neutron spots 6 mm in diameter at precisely determined positions. (See fig. 2.) By reflecting the mask about the horizontal and vertical centerlines and using all four orientations, 29 unique beam positions are defined. We attempt to adjust the PM gains till the pulse height spectra are the same for all 29 readings. Unfortunately, since the scintillator does not extend over the peripheral PMs, the observed signals do not have a one-to-one correspondance with the photomultiplier gains. At best, we can assure that the linear combinations we measure are linearly independent, so that we can invert a 29 x 29 matrix to find the adjustments. Our matrix does not converge very rapidly, however, and does not behave well when one PM is sick, or has bubbles in its optical coupling grease, etc.

For the tests reported here, the calibration had been carried through 3 iterations, but it was clear that at least one photomultiplier was not responding properly, and that our matrix had inadequate sensitivity to determine the extreme top and bottom PM gains. Thus the following tests were carried out under conditions far from optimum.

3. Test Procedure and Results

The camera was mounted on a translation stage driven by a stepping motor. The mask (described above) was mounted in a fixed position, so that only one of its apertures was illuminated by the neutron beam. The camera was set to an arbitrary height and a scan was made in the X-direction, as shown in fig. 3. The translation motor was driven 1000 steps (5 mm) and neutrons were counted for 100 s. The data were stored in a LeCroy 3588 histogramming memory at data rates of about 10000 s^{-1}. After completing the X traverse the camera was turned on its side and the Y scan was made.

Since the memory was not large enough to hold a histogram with full resolution in both dimensions simulataneously, the camera's encoder was set to record only 7 bins in the transverse dimension, and the full resolution capability (1.15 mm per bin) in the direction of interest. Data were subsequently summed in the transverse direction, so the entire detector area contributed to the background. (No background subtraction was made, but only the data near the peak were used in determining the second moment.) The quantities to be determined were uniformity of count rate, linearity of position encoding, and resolution of the spot as a function of position.

The results of these two scans are summarized in fig. 4. The uniformity, or integrated intensity, is most affected by the gain calibration of the PMs. We note a dip at Y = 225 mm, corresponding to the portion of the scan in field 24. We subsequently discovered that the PM in the upper left corner of field 24 was not completely optically coupled. The dip at X = 60 mm corresponds to the triple-point between fields 0, 1, and 9, and probably resulted from events being analyzed in field 9 when they should have been in field 1. If we neglect the one bad X point, the rms uniformity is 3%, which we confidently expect to improve with better calibration. Remembering that the spot size was 6 mm, the linearity and the resolution results are surprisingly good. (The known variance of the circular spot was subtracted from the calculated second moments to estimate the standard deviations.) There are features in the linearity plots at the same places that the count rate was low. Both linearity and resolution require that the position determination be continuous as we cross from one field to the next. There is only a single global adjustment available for all field overlaps in the entire camera; these scans give our first indication that one knob is enough.

4. Future Improvements

The alumina powder reflector on the scintillator glass had partially separated, and also may have contributed to a background pedestal around each reading. We have now aluminized that surface of the glass; Monte-Carlo simulations indicate this may also increase our position sensitivity slightly.

A revised calibration scheme is being developed. We propose first to adjust the 13 PMs over which we can center the beam, and then to use a 16 x 16 matrix of readings for the others.

For complete testing, it is obviously necessary to take many scans in each direction, rather than one. We must improve the automation of our data collection system to make this practical.

This prototype detector will be installed on the LQD flight path for further testing this fall. We will then be prepared to test for two other properties of the Anger camera, which must be answered before we can commit to using it in the final LQD instrument. These are stability (both short term and long term), and gamma-ray response in the environment of the pulsed source.

Acknowledgments

We greatly appreciate the cooperation we have had in this project from M. G. Strauss and his co-workers at Argonne, and from R. Lawrence and others

from Rutherford Appleton Laboratories. This work was performed under the auspices of the U. S. Department of Energy, Office of Basic Energy Science.

References

[1] H.O. Anger, Rev. Sci. Instr. **29** (1958) 27.

[2] M.G. Strauss, R. Brenner, F.J. Lynch and C.B.Morgan, IEEE Trans. Nucl Sci. **NS28** (1981) 800.

[3] P.A. Seeger, IEEE Trans. Nucl. Sci. **NS31** (1984) 274.

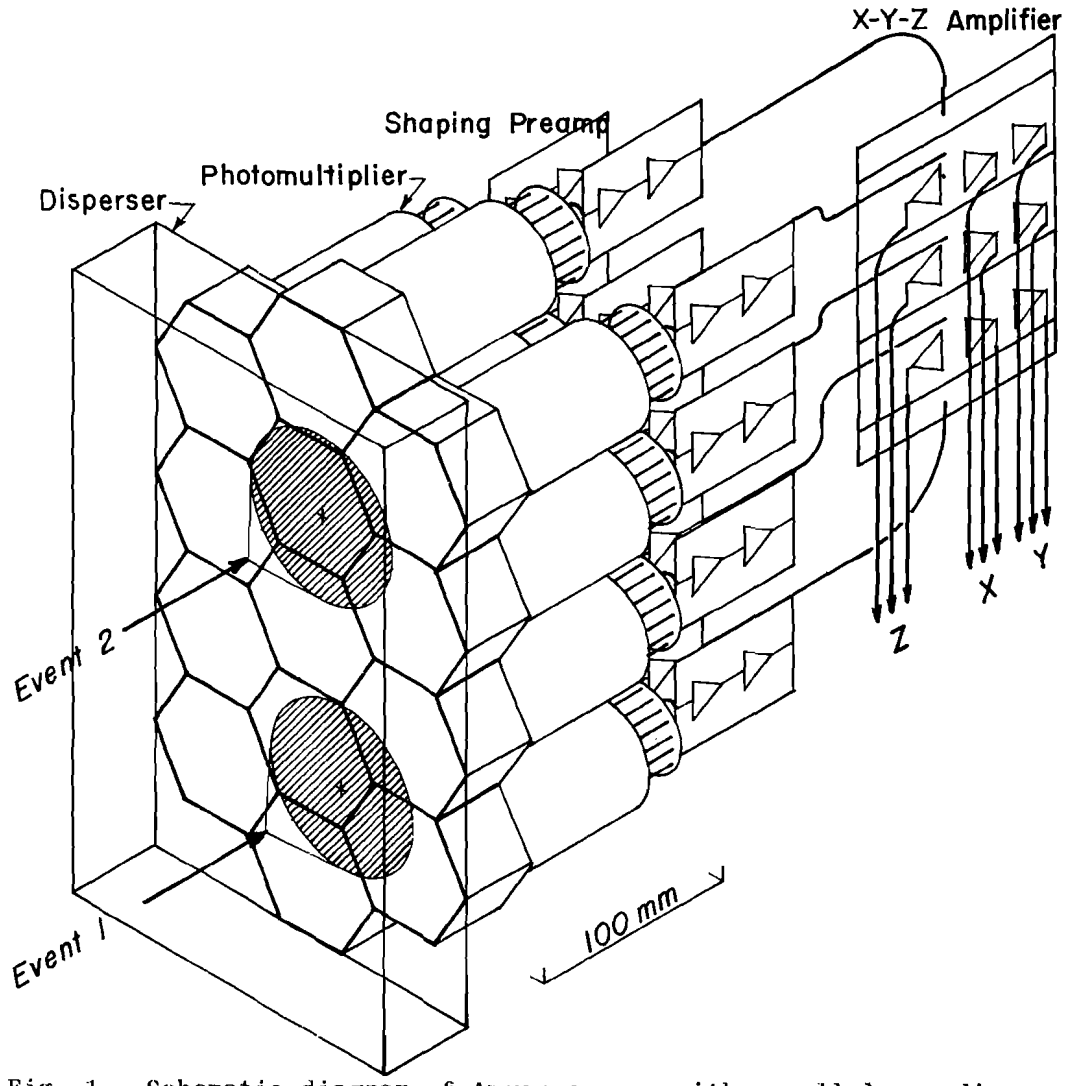

Fig. 1. Schematic diagram of Anger camera with parallel encoding. Encoding is done in two steps: choice of one of the possible receptive fields, and interpolation within the field.

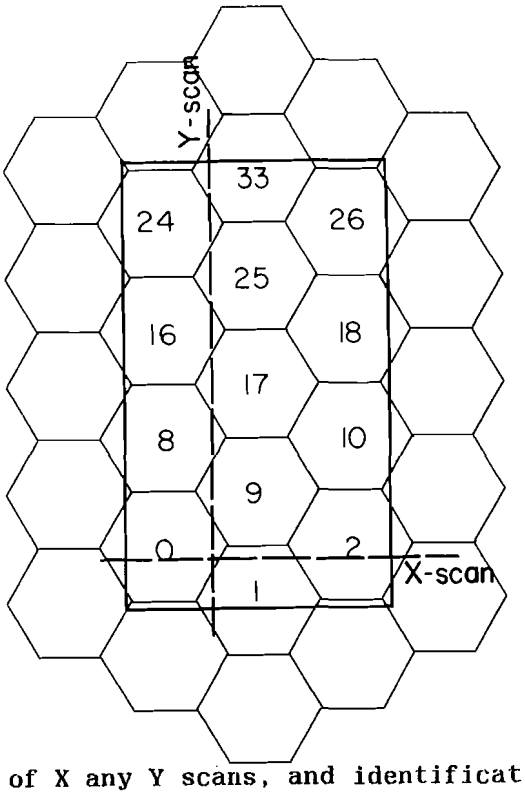

Fig. 3. Locations of X any Y scans, and identification of receptive fields.

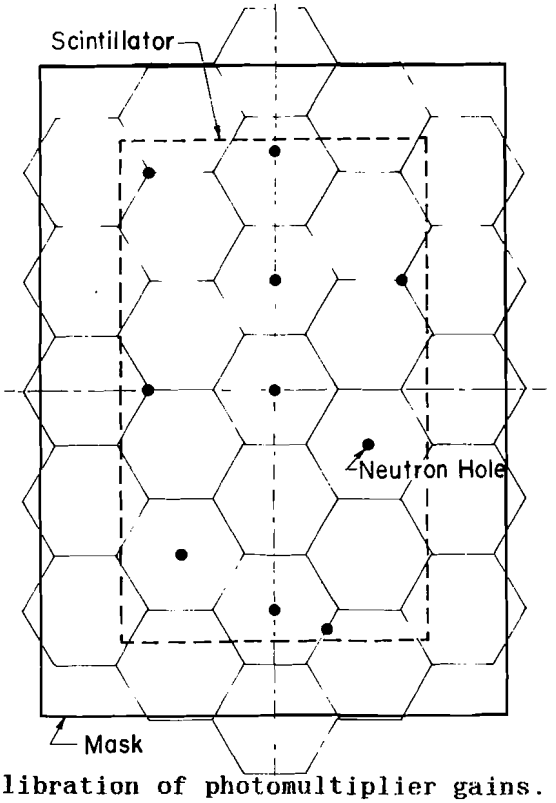

Fig. 2. Mask for calibration of photomultiplier gains. Reflections about horizontal and vertical axes result in 29 unique beam positions, to be used to determine the 29 gains.

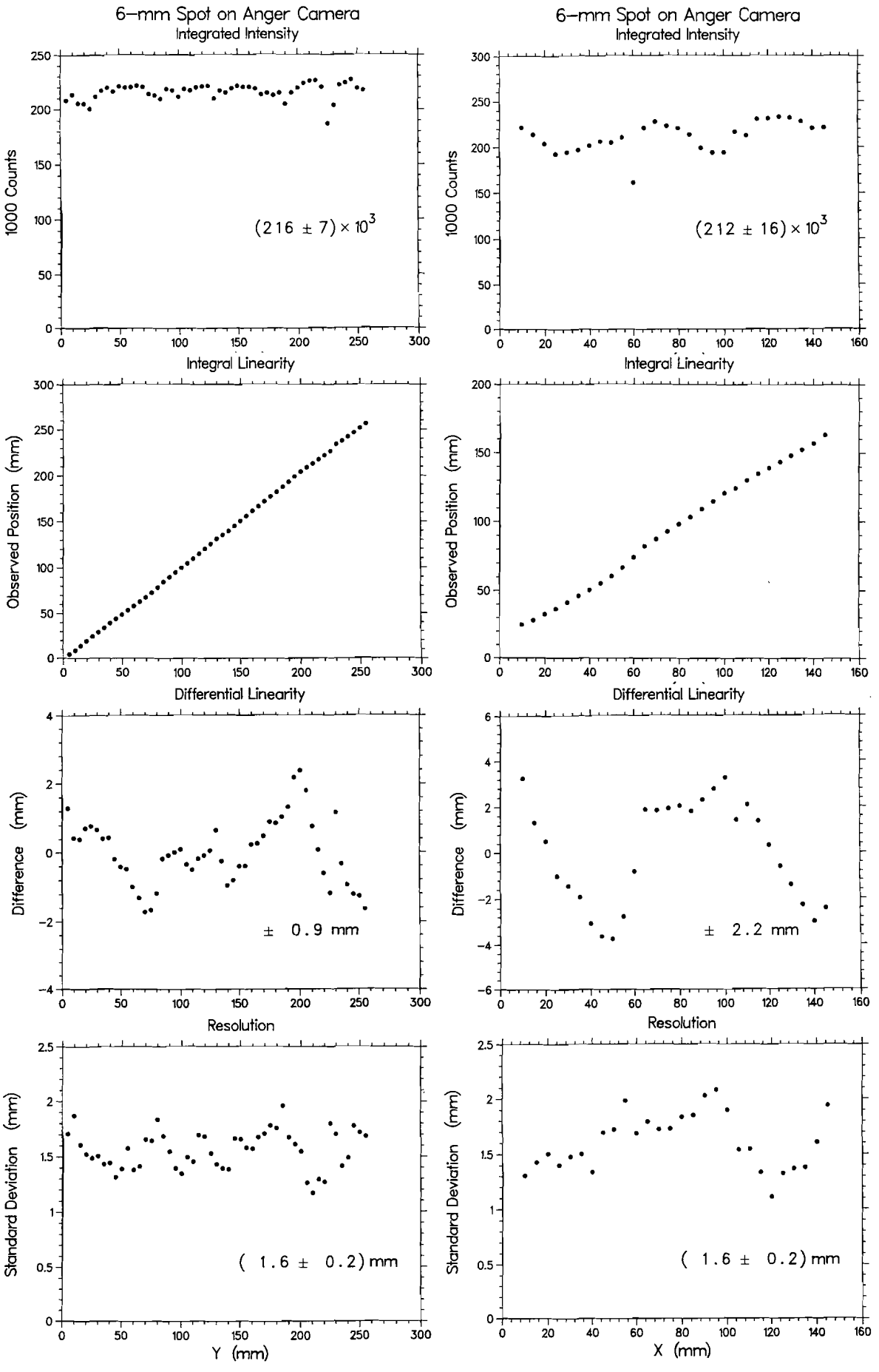

Fig. 4. Test Results

Proceedings of the Eighth Meeting of the International Collaboration on Advanced Neutron Sources (ICANS-VIII)
8-12 July 1985, Rutherford Appleton Laboratory Report RAL-85-110

THERMAL NEUTRON BEAMLINE MONITOR

P L Davidson
Rutherford Appleton Laboratory

Abstract

A detector has been developed which has characteristics that make it suitable for use as a neutron beamline monitor on the Spallation Neutron Source. Efficiency has been reduced to 10^{-4}, pulse pair resolution is 50 nSecs and it presents minimal obstruction to the neutron beam.

Published as Rutherford Appleton Laboratory report
RAL-85-032 (April 1985)

Proceedings of the Eighth Meeting of the International Collaboration on Advanced Neutron Sources (ICANS-VIII)
8-12 July 1985, Rutherford Appleton Laboratory Report RAL-85-110

FIBRE OPTIC CODED DETECTOR SYSTEMS ON THE SNS

P L Davidson, N Rhodes and H Wroe

1. INTRODUCTION

The principle of the fibre optic coded scintillator detector has been described elsewhere[1],[2]. Systems using this principle have been built for two SNS instruments, the High Resolution Powder Diffractometer (HRPD) and the Low Q Spectrometer (LOQ). This paper gives brief details of these detector systems together with some early results.

2. HRPD DETECTOR

2.1 Geometry and Construction

The main features of the HRPD were given at the ICANS IV meeting[3] and a more recent summary of the instrument parameters is given in reference [4] from which the schematic representation shown in Figure 1 is reproduced.

The detector has an annular ring geometry and is used in backscattering, the incident neutron beam passing through a central aperture. The main dimensions are shown in Figure 2. The detector is constructed in identical octants each with 20 rings. Each ring is in the form of 2 layers of 1 mm thick lithium glass scintillator. These layers are coded as separate detectors, the total number of rings thus being 40. The cross-section shown in Figure 2 illustrates the method of gluing the rings together, resulting in a conical shaped nest of rings (see Figure 3). The fibre optic bundles, after coding, are potted in resin and machined off as shown in Figure 4. This face forms a vacuum seal so that the photomultiplier tubes (PM's) can be operated at atmospheric pressure, thus avoiding any vacuum breakdown problems. The detector is mounted in a vacuum vessel which is separated from the sample chamber by an aluminium window (0.5 mm thick). The vessels are pumped down simultaneously to avoid a pressure differential across the window. This arrangement allows a low

pressure to be achieved in the sample volume without the outgassing load produced by the detector itself. The window also completes the lighttight enclosure for the detector - there is no separate lighttight window over the scintillator array itself.

The electronic system is the same as that described in reference [2].

2.2 TOF Spectra from SNS

Two octants of the detector are installed in HRPD at the time of writing. The first results were obtained in December 1984 when the SNS operated for a brief run at very low intensity. Two samples were simultaneously in the beam viz: Ni powder at the 1m sample position and a pyrolitic graphite single crystal at the 2m position. A presentation of these results is given in Figure 5 which shows sections (about 1/40 of the total) of the time-of-flight spectra from each of the 20 rings on an octant with the 2 layers of scintillator in each ring summed. These results show that the backgrounds seen by the detector are acceptably low and that there is negligible crosstalk between rings, i.e. a T-O-F peak in one ring does not lead to significant counts in another ring at the same time.

The detection efficiency has not yet been carefully measured. The stopping power, η, of a 2 mm thickness of GS20 scintillator is given by.

$$\eta = (1-e^{-1.66\lambda})$$

where λ is the neutron wavelength in Å. Approximately 10% of the stopped neutrons do not produce counts due to optical and discrimination losses. Using these values, a comparison between the theoretical and measured intensities of several reflections from nickel powder was made in reference [5] with fair agreement.

The intrinsic background count rate from the detector, i.e. the count rate with no neutron soruces present, is about 0.4 counts per minute per cm^2 of scintillator. There has been no evidence of any problems due to γ-ray background.

3. LOQ DETECTOR

3.1 Geometry and Construction

The general arrangement of LOQ is shown schematically in Figure 6 and a description of the instrument as it will be for early SNS operations is given in reference [4]. The main detector consists of concentric rings of scintillator elements of annular width ΔR at radius R such that $\Delta R/R$ is constant at 0.0358. The azimuthal resolution varies from 20° in the centre of the detector to 2° at the outside as shown in Figure 7 which is a diagram of a 1/9 module. The number of elements per module is 560 coded to 16 PM's, i.e. 5040 elements and 144 PM's in the whole of the main detector. A central aperture allows the unscattered incident beam to pass through to a beam stop.

The detector modules are constructed by first cementing a row of 0.5m diameter fibres side by side in a jig to make up a single layer bundle equal in width to a particular scintillator tile. The scintillator tile itself is then cemeted, by its edge, to the fibre bundle via a 5 mm long , 0.5 mm thick, glass light guide. The purpose of the latter is to ensure that the intensity of the scintillator light pulses entering the fibres is reasonably uniform from fibre to fibre. If this is not done, a neutron capture in the scintillator close to a fibre causes a large light pulse input to that fibre but only a very small one into other fibres, since light can only arrive at these within the acceptance angle by transmission through the scintillator tile and reflection back from an edge.

It is believed that in these circumstances the intense light can be reflected from the PM end of the fibre bundle back along other fibres and then back into other PM's giving rise to crosstalk between elements. Two other precautions are taken to minimise this effect. Firstly the edges of the scintillator tiles are coated with a white diffuse reflector to avoid specular reflection of returned photons back into the fibres. Secondly, at the PM end, the fibre bundles are cut at an angle so that light emerging into the PM is not reflected normally (from bright surfaces inside the PM) back up the fibres.

Each arc of elements, with its fibre optic bundles attached, was glued to a backing made as a B_4C/resin casting to provide some absorber for neutrons not stopped in the scintillator. For the first module, each arc was tested separately on a laboratory neutron source in a special test rig. Good results for uniformity of response were achieved for all the arcs. Figure 8 shows the result of exposing the arc of elements beginning with number 281 to an approximatley uniform neutron flux from a Pu/Be source.

The scintillator used is GS20, 0.5 mm thick, giving a stopping power for neutrons of wavelength 2Å (the minimum for LOQ) of 57%.

As for the HRPD detector, the fibre optic bundles are taken, after coding, through a vacuum seal so that the PM's can operate at atmospheric pressure. Since the whole secondary flight path and detector are in a large vacuum vessel, the PM's are housed in a sealed box connected to the outside of the vessel by long flexible bellows, which carries the high voltage supplies and signal leads. This arrangement circumvents any problems associated with operating high voltage equipment in vacuum. Since there are signal cable runs of about 10m between the detector modules and the first signal processing electronics situated outside the detector vacuum tank, a preamplifier is built into each PM base. A low airflow is driven through the flexible bellows to remove the small amount of heat (about 70W) generated by the PM dynode resistor chains and the pre-amplifiers.

3.2 Results of Laboratory Tests

Figure 9 shows the result of exposing the whole detector module to the laboratory source. The counts seen vary as the area of the elements, as expected.

An overnight background count in the laboratory with the detector module shieded with a 15 cm thickness of borated resin blocks and no neutron sources present showed an intrinsic background between 0.5 and 0.8 counts per minute per cm^2 of scintillator.

Exposure to a ^{60}Co source showed a γ-ray counting efficiency of 1.3×10^{-3}.

4. CONCLUSIONS

First results from the HRPD detector system on the SNS have been encouraging. This instrument operates on the end of a 95m long guide tube and is thus in a low γ ray field, an environment particularly suitable for this type of detector system. The intrinsic background counts produced by the detector and the degree of crosstalk between channels have, so far, been adequately low.

First results from the LOQ module on test with a laboratory source have also been good. It is expected that this detector will also operate in a low γ-ray field since the LOQ beam line does not have a line of sight to the SNS cold moderator but incorporates a supermirror bender.

At the time of writing further commissioning tests will be made on both systems, especially at higher neutron beam intensities, before constructing the remainder of the detector modules.

6. ACKNOWLEGEMENTS

The authors would like to thank Mr B Holland for his highly skilled assistance with the construction of the LOQ module and Mr A Gibbs for his careful work on the HRPD construction.

7. REFERENCES

1. KENS Report II, March 1981, pp 642-654

2. Position-Sensitive Detection of Thermal Neutrons, P Convert and J B Forsyth (Eds), Academic Press (London), p166 (1983)

3. KENS Report II, March 1981 pp 549-555

4. Neutron Scattering Instruments at the SNS - A Guide for Potential Users, February 1985

5. First Neutron Results from SNS, A J Leadbetter et al, RAL-85-030

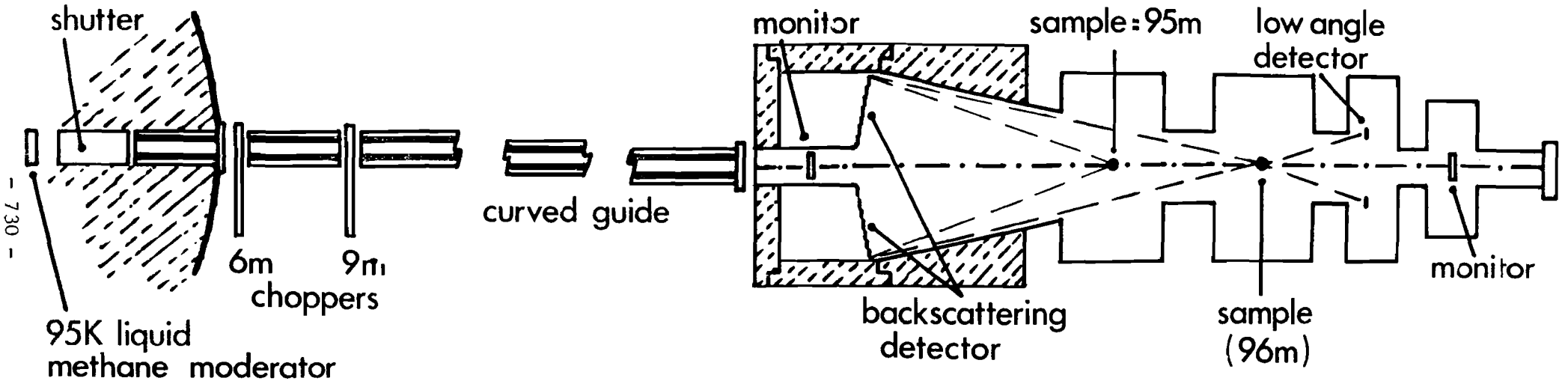

FIG. 1. Schematic layout of HRPD.

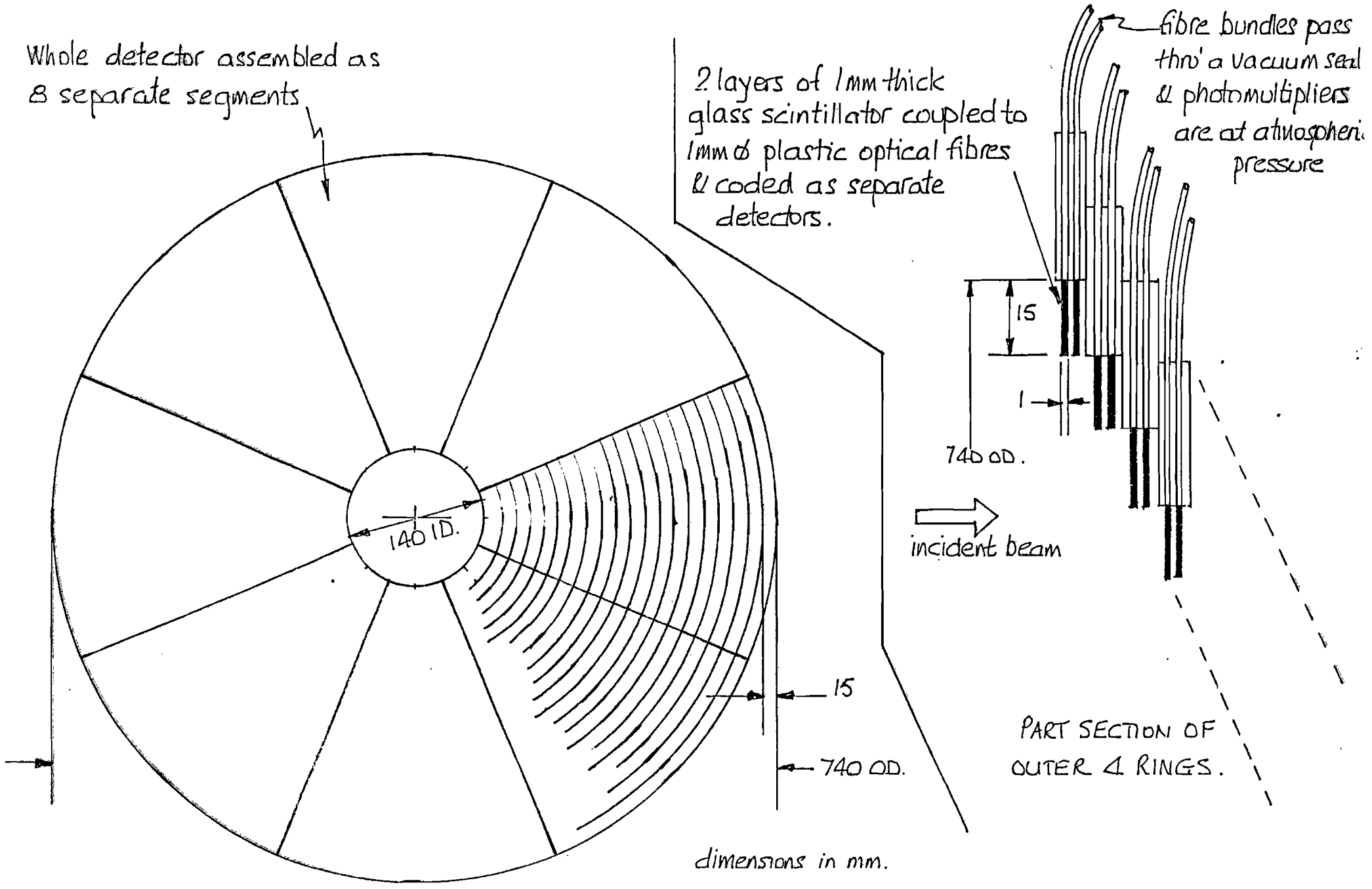

FIG.2 Geometry of HRPD detector

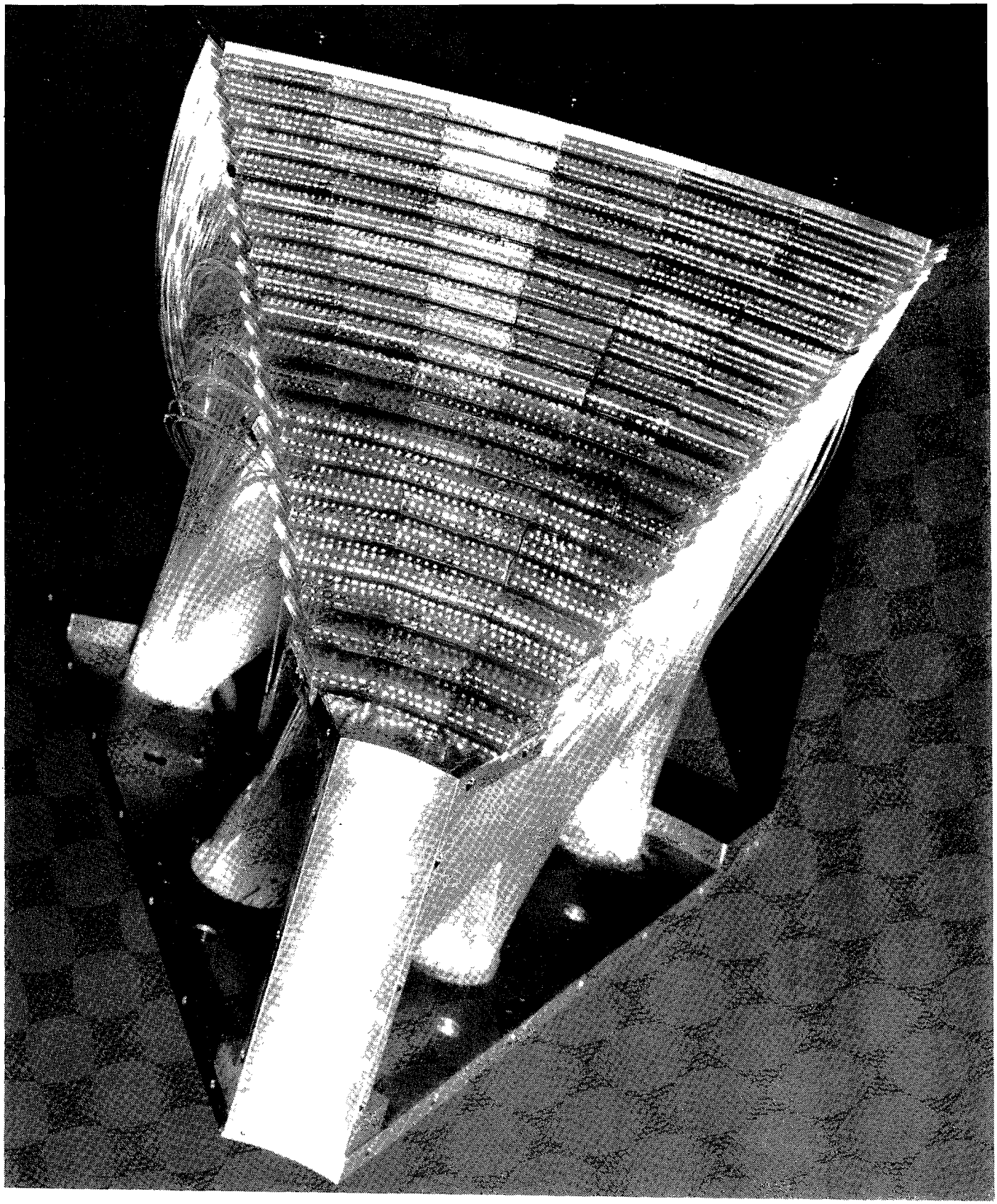

FIG.3 HRPD encoder showing scintillator end before cementing on scintillator tiles.

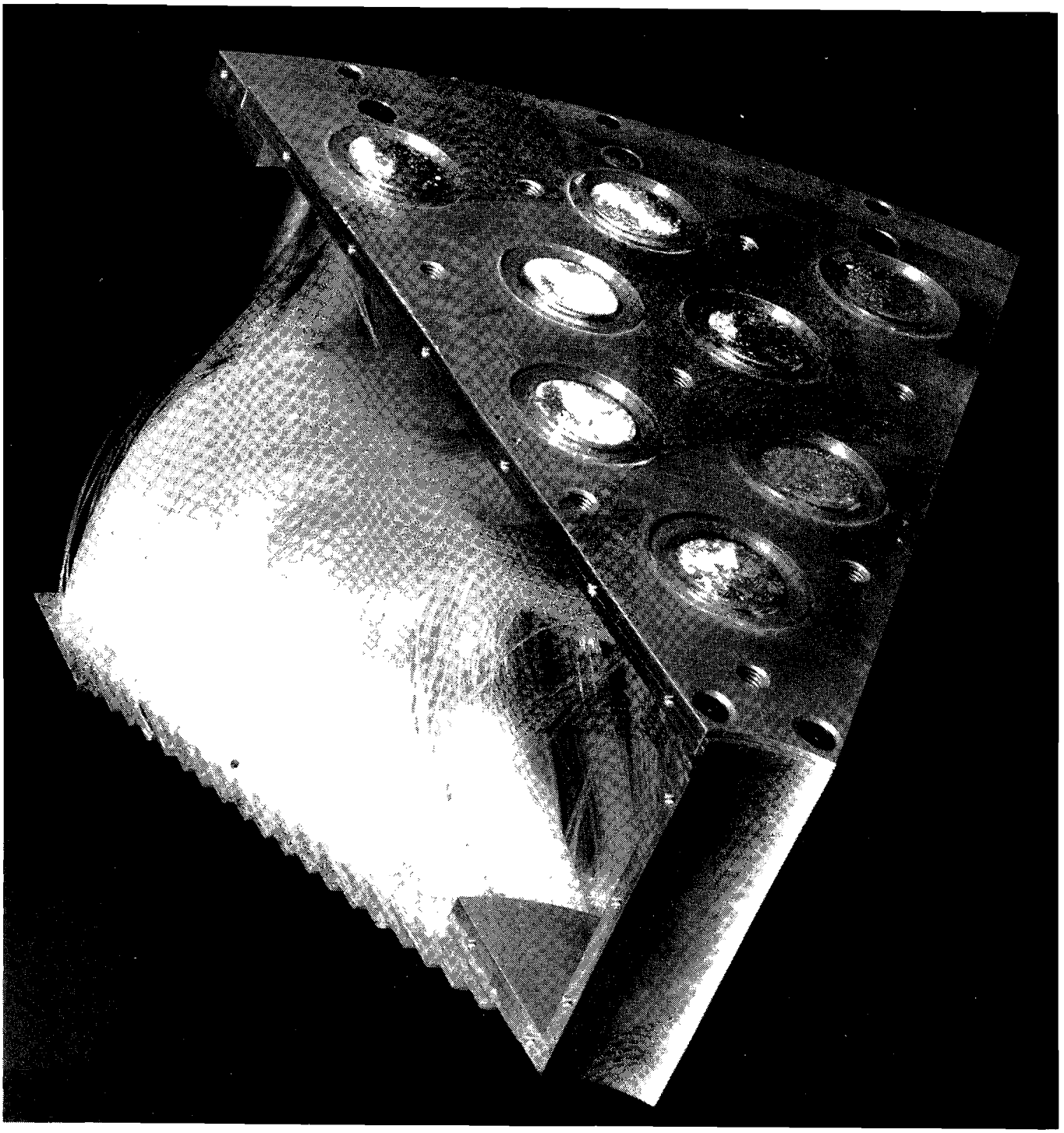

FIG.4 HRPD encoder showing PM end of fibre bundles before installing P.M. tubes.

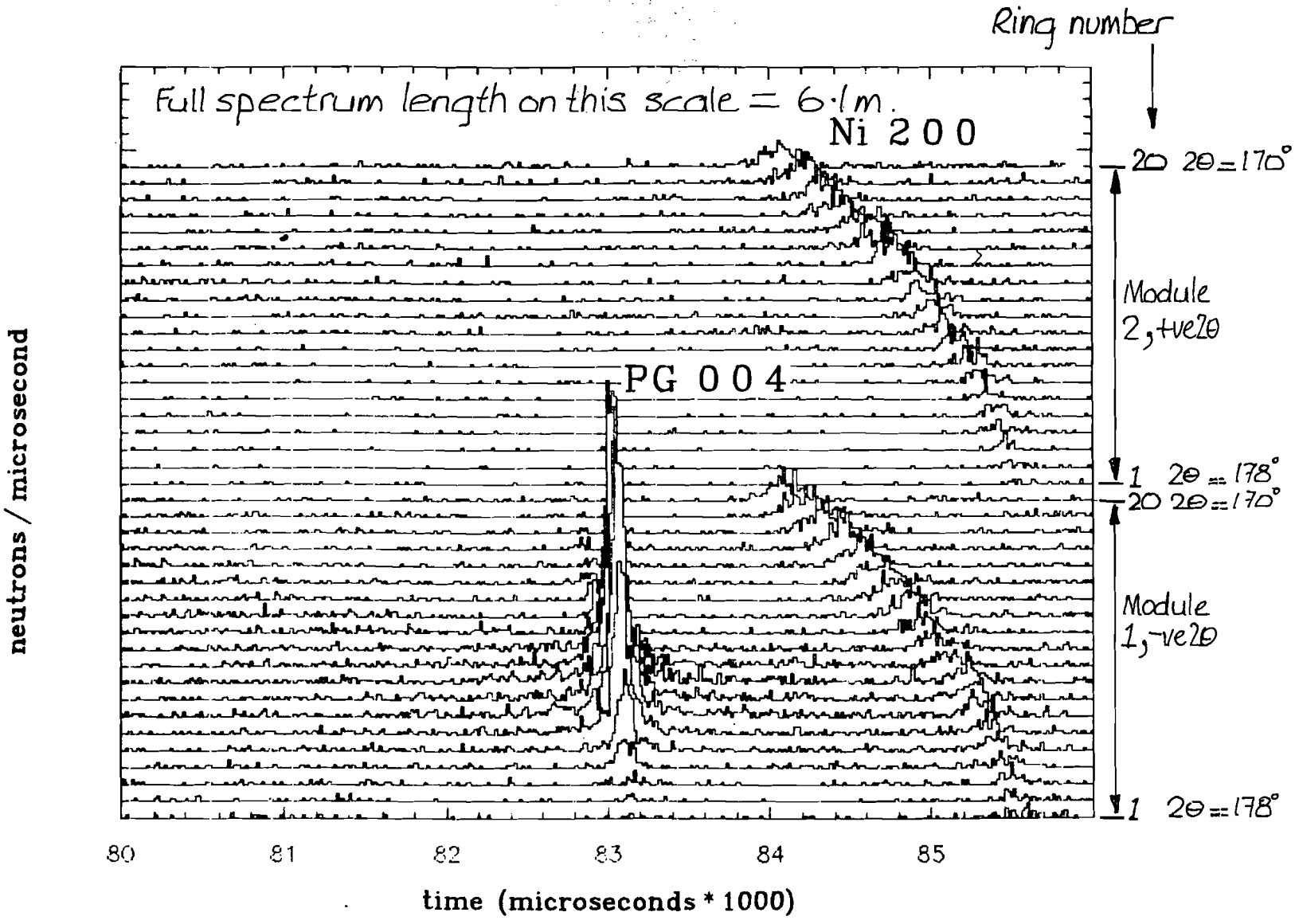

FIG. 5 Time of flight spectra from HRPD with nickel powder and pyrolitic graphite single crystal samples.

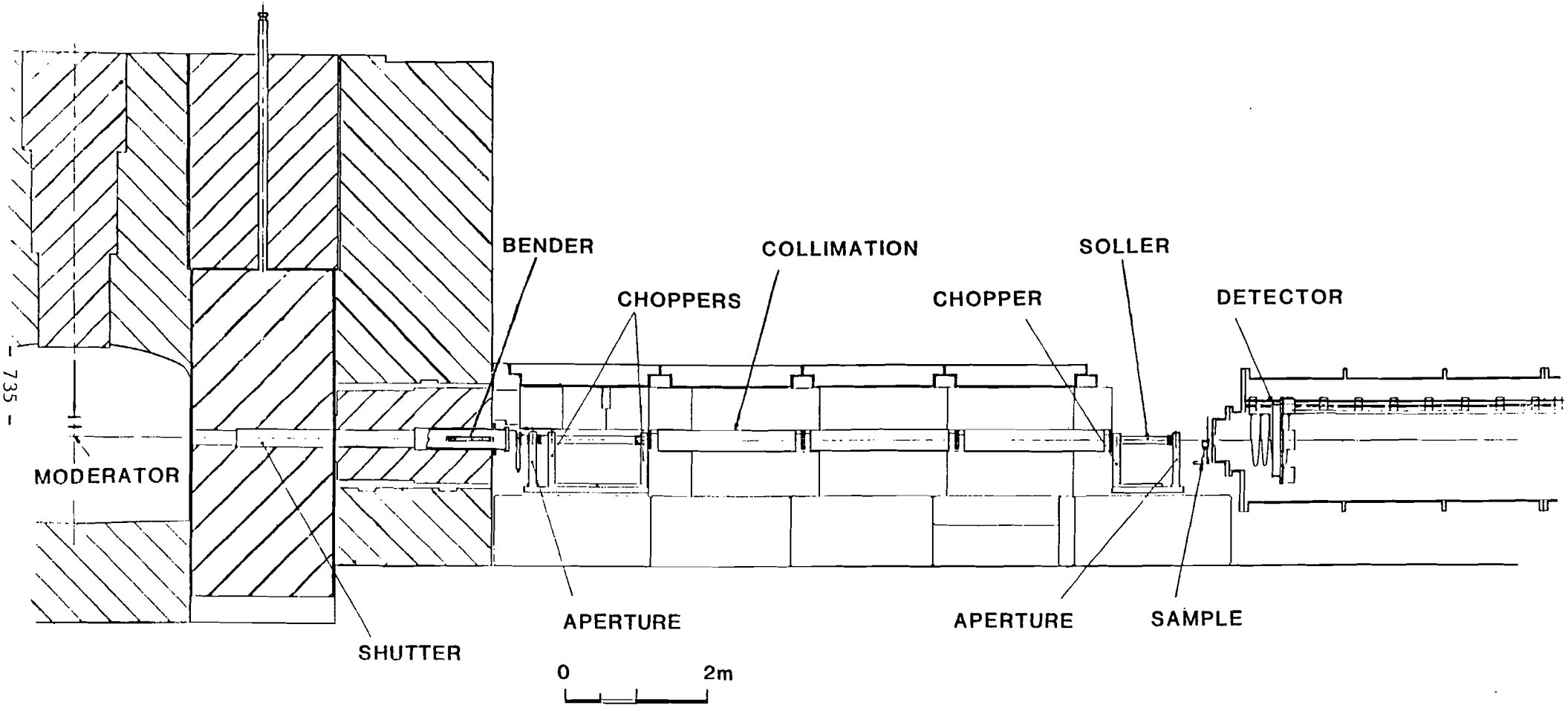

FIG. 6 Schematic layout of LOQ

FIG. 7 Geometry of a 1/9 module of the LDQ

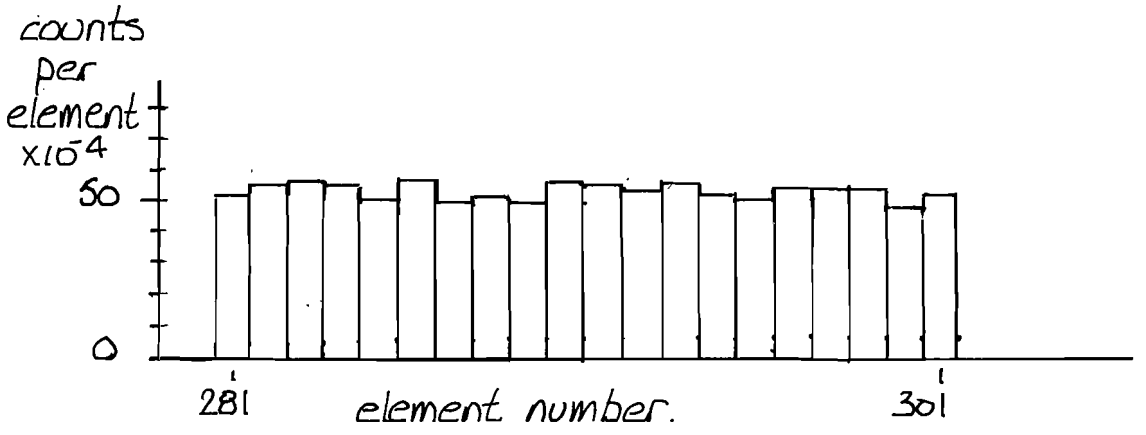

FIG. 8 Response of an arc of LOQ detector elements to a laboratory neutron source.

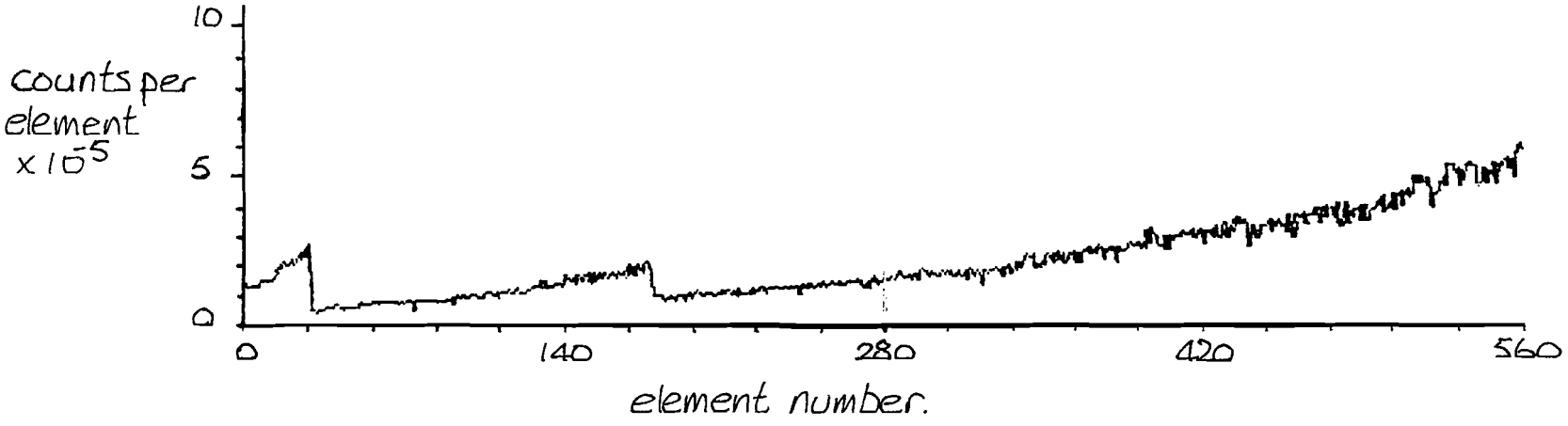

FIG. 9 Response of a 1/9 module of the LOQ main detector to a laboratory neutron source.

Proceedings of the Eighth Meeting of the International Collaboration on Advanced Neutron Sources (ICANS-VIII)
8-12 July 1985, Rutherford Appleton Laboratory Report RAL-85-110

CONFIGURATION FOR THE WNR DATA ACQUISITION SYSTEM FOR NEUTRON MEASUREMENTS

R. O. Nelson, D. M. Barrus, G. Cort, J. A. Goldstone,
D. E. McMillan, L. B. Miller and R. V. Poore

Los Alamos National Laboratory

and D. R. Machen

Scientific Systems International

Abstract

The configuration for a new data acquisition system for the Weapons Neutron Research Facility at the Los Alamos National Laboratory is introduced. The system utilizes a FASTBUS front-end for real-time data collection and DEC computers for the experiment control and analysis. A local area network is used extensively within the overall system.

Introduction

In recent years the Weapons Neutron Research (WNR) facility has developed into one of the nation's principal neutron scattering centers for nuclear physics and condensed matter measurements. Neutron flux intensities and pulse characteristics will be substantially enhanced when the Proton Storage Ring (PSR), which circulated first beam this spring, becomes fully operational in the fall. Flux intensities are generally expected to increase by a factor of approximately 250, thus rendering the present data acquisition system inadequate. The PSR repetition rate may be adjusted as low as 12 pulses per second without sacrificing average intensity. With this capability new measurements using slow neutrons are practical and may increase memory requirements for data storage up to an order of magnitude over that now employed. Using the current facility repetition rate, these slow neutrons arrive at the detector after the start of the next burst of neutrons (frame overlap) thus creating ambiguity. Because of growth in the measurements program, it is further desired to increase the number of instruments served by the new system to a dozen.

From these neutron source characteristics, from the strengths and weaknesses of our present system as well as those at other laboratories, and from the availability of high performance computer and communication equipment at reasonable costs, five basic guidelines for our new system evolved. 1) Service each instrument with its own dedicated system. 2) Support real-time data acquisition in dedicated hardware outside the general purpose computer environment. 3) Link the instrument system together loosely with a local area network. 4) Include within the network a more powerful computer to serve data reduction and analysis needs and oversee data archiving. 5) Modularize both software and hardware to enable the broadest use of modules in support of diverse instruments and experiments.

Upon examining options available in the computer market, the preferences of users, and software and hardware from other installations that might be incorporated within our system, a solution based on DEC equipment was dictated. To handle the estimated count rates which, time averaged, may reach 1 MHz and instantaneously reach 45 MHz, our design required the speed and flexibility afforded by FASTBUS[1]. This paper introduces the factors which motivated our design, the resulting data acquisition configuration, and the current status of the work. Discussion begins with the system wide perspective and proceeds toward the FASTBUS hardware at the detector interface.

Network

At the highest level of generalization, our system may be viewed as a network which links a relatively powerful central host system to a set of less complex front-end systems, each dedicated to data acquisition for a single neutron scattering instrument. The network, shown schematically in Figure 1, provides the hardware communication path and software control for the data transport from the front-end systems to the central data archive, as well as for the flow of software modules in the opposite direction. As the staffing support for the project is established at a minimum level, we prefer to buy commercial products whenever possible. Thus, the network is necessarily considered to be an off-the-shelf item.

At this time the network is largely in place. The local area network linking our systems together is an Ethernet system consisting of both fiber optic and coax sections. The coax sections are used within a single building and the fiber optic sections are used for geographically isolated buildings and sites where differing grounds may pose problems. Presently, the fiber optic portion is installed between six buildings. It links together two VAX 11/750 computers and one microVAX I computer. A connection to the laboratory wide broadband network is provided through one VAX 11/750 system. We still are in the development phase of the project so the new systems and the coax joining them do not yet exist. Software control is provided with DECNET. Should performance issues arise in the shipment of large data files, some work to adapt a locally defined protocol to the existing drivers would be acceptable at some point in the future.

Print servers and terminal servers will be connected to the network and will provide network resources not associated with any particular computer system. Two terminal servers are currently installed.

Host System

The central host system is designed to provide added capability for the experimental program in three major areas: data archive management, data reduction and analysis where extensive numeric calculations may be involved, and software development and maintenance support. This system will have no real-time data acquisition role and is intended primarily to support experiments which have been completed, in contrast with those in progress. The central host system will be a VAX 8600 class machine.

After data collection, data obtained with the front-end system will automatically be forwarded to the host system where it is archived and retained on-line for the duration of the run cycle. Not less than 10 Gigabytes of disk storage is envisioned for this system. Powerful color graphics terminals supported with DMA access will be provided to assist with data interpretation and analysis. Through the laboratory network (XNET), it will be possible to access powerful computing resources with Crays, 7600s, etc., as well as exotic peripherals such as high speed laser printers and photo-plotters. More routine peripherals like magnetic tape drives will be available locally for archive, backup, and data export functions.

Presently, the host is an overloaded VAX 11/750. However, much of the host functionality is present in this system including connection to the laboratory network and a single color graphics terminal. Disk storage capacity is limited to 1 Gigabyte at this time. To extend this system to the desired configuration requires a significant amount of funding.

A second VAX 11/750 dedicated to software and hardware development and maintenance has been added to the local area network. While originally perceived as an integral component of a single host computer system, the separation of many of the maintenance aspects of system support to this computer will likely prove highly beneficial over the lifetime of the data acquisition system.

Front-end Systems

Each front-end system exists to service the needs of a single neutron scattering instrument. Although each computer will likely have sufficient resources to service several experiments, this approach seems unwise at present system costs in view of the risk of disruptive user interaction. These extra CPU cycles should be regarded as a resource available to the experimenter which, for example, may allow him to determine the health of the experiment via some detailed on-line analysis. Other experiments may be able to finish data collection and at the same time be finished with data reduction and analysis.

Powerful as it may be, the front-end computer is incapable of handling the expected worst case data rates from the detector arrays. Scaling current WNR counting rates to the expected PSR levels indicates that burst rates of 45 MHz for a period of 10 us early in the neutron pulse are possible. Of course these count rates drop at later times in the pulse finally reaching an average count rate of 1 MHz for the worst case. Additional requirements that dead-time corrections not exceed 0.5% and constant dead-time be enforced (drop all data from a neutron burst if any event cannot be processed within a user defined fixed time interval) force an implementation with custom hardware for buffering events as they arrive from the detector. In our judgement it is reasonable to complete the data capture process, including data compaction and histogramming, in hardware and dedicate the computer to control and analysis tasks. This hardware is described at length in the following section.

Development of these front-end computer tasks is extremely software intensive and has been the focus of considerable effort over the past year. As the subject of other papers[2,3], the main data acquisition tasks are listed below as background for the hardware requirements. They include configuration initialization, instrument control, data collection, data cataloging, automatic run sequencing, and graphics for monitoring the health of the experiment and data analysis.

The basic hardware configuration for each front-end is shown in Figure 2. As delivered , each microVAX II will be contained within a 5.25" rack mount chassis which includes 2 Megabytes of memory, a 71 Megabyte hard disk, a 95 Megabyte cartridge tape, 4 serial ports, and an Ethernet interface. We anticipate that in the future it will be necessary to upgrade this disk to increase the local storage capacity to at least 120 Megabytes. At the completion of each run, control information and data selected by the experimenter will be written to the local disk in a generalized and flexible format. These files may be as large as 4 Megabytes, so even large local disks could be filled quickly. Local storage is mandatory since reliable operation of the network and host system should not be taken for granted. At a minimum, local storage capacity for files created during a day of running is required. Should the network/host remain unavailable, the local cartridge tape

could be used to make copies of all data from the preceding day. Normally, the cartridge tape is reserved for disk backup operations.

Since the data obtained with the front-end systems can be subtle and complex, high resolution color graphics will be included here as well as on the more powerful host system. This graphics capability enables rapid inspection of the quality of the data and allows in near-time an experimenter to select measurements that make best use of his beam time. Initially, a combined command/graphics terminal will provide experiment control and data monitoring capability. Later a second high resolution dedicated graphics terminal with color and a parallel DMA interface will be added.

A simple register driven I/O interface for a CAMAC system crate will be included on the front-end system. Since no preset scalers for FASTBUS systems are commercially available at this time, existing scaler and preset scalers will be used in the CAMAC environment. Likewise, motor control interfaces and monitoring equipment distributed throughout the facility on various CAMAC serial highway systems will continue in use with a serial driver located in the system crate.

As delivered, our current prototype front-end system consists of a microVAX I CPU with 1 Megabyte of memory, a 31 Megabyte hard disk, two 400 Kbyte floppy drives, a four-port serial interface, and an Ethernet interface. We have added a register I/O interface, Model 3912 from Kinetic Systems, and a CAMAC crate for the support of existing CAMAC modules which will continue in use. Also installed in the CAMAC crate is a register driven FASTBUS interface, the FIORI, from CERN[4]. To date this system has been used exclusively as a FASTBUS hardware development workstation.

FASTBUS Systems

Each front-end will also connect with a FASTBUS subsystem, the truly real-time component of the system. The interface for FASTBUS will be a QPI (Q-bus Processor Interface), currently under development at Kinetic Systems. The unit is essentially the UPI designed at Fermilab[5] for use with the DEC Unibus, but adapted for the 22-bit wide address/data multiplexed Q-bus. Within the FASTBUS crate, the interface connects to a set of five custom module types. Details of these modules have been presented elsewhere[6], and only the basic functionality is summarized here. Note, however, that the histogramming memory module has benefited from the introduction of 256K RAM technology and now each module contains 2 Megawords of 24-bit memory.

As in most neutron measurements, the flight time over a fixed length path characterizes the neutron momentum and is the primary parameter of any measurement. Three of the FASTBUS modules are directly involved with the time interval determination, one acting as a master clock and two as time-of-flight input buffer modules. The fourth module type provides a limited event processing capability and the last type is an auto-incrementing histogram memory.

Figure 3 illustrates the basic data flow of the FASTBUS system. Stepping through the operation of the system briefly, the master clock is initialized through the host interface, and begins counting time bins when triggered at the leading edge of the neutron burst (TO). The time information and optional parallel information is strobed into the time-of-flight (TOF) input buffer by a pulse from the detector system. Data is accumulated in the buffer for the duration of the neutron burst. At the start of the next neutron burst the data is read for a complete frame of events into the mapper processor which compacts the data. Compaction is accomplished primarily through substitutions from a map loaded into the mapper processor through the UPI interface. Individual

events are reduced to addresses which are presented to the bulk store module for histogramming. The histogram may be read by the front-end microVAX for data monitoring or recording.

The modularity of FASTBUS and the flexibility of the design allow the experimenter to configure the module set to accommodate a wide spectrum of counting rate environments. Additional modules may be added to provide independent parallel paths from TOF buffers to bulk store memories. Should dead-time reach an unacceptable level during the burst, additional TOF buffers may be introduced to reduce multiplexing at the TOF module. If average count rates saturate the capability of the mapper processor, then additional mappers may share the TOF service load. If the histogramming bandwidth becomes the limitation, then as with the others, more modules can be installed. Maximum system performance is finally limited by the speed of the FASTBUS backplane for inter-module communication.

With ECL implementation of modules, random FASTBUS data transfers can achieve rates of 10 MHz. In our designs, the block transfer mode is used extensively and transactions between the mapper and bulk store utilize only the address cycle. Effectively, only one half as much data passes on the bus as with random cycles, but it always passes twice: once from buffer to mapper and again from mapper to bulk store. Neglecting the overhead of bus arbitration and some setup delay incurred once for each block transfer, the data might be expected to flow at the 10 MHz rate for ECL implementations. As mixtures of both ECL and TTL, our design goal is set at 5 MHz for time averaged histogramming rates.

Design and fabrication of prototypes of the module set has been completed and only the mapper module remains to be debugged. Since the mapper timing remains uncharacterized, actual system performance figures are not yet available. Unless more than one bulk store is used, however, the read/increment/write cycle time, 300 ns, is the limiting factor. A future design which enables memory interleaving will eliminate this performance problem.

Buffer performance in the TOF greatly exceeds the design specification. Pulse pairs with time spacing as low as 20 ns may be accepted without loss of data in a pair of registers preceding a 64 word deep FIFO. Data then flows into this FIFO at its maximum rate, 20 MHz. Data is removed from the bottom of the FIFO at 10 MHz and deposited in one of two static RAM frame buffers that toggle between neutron bursts. The logic which monitors the event strobes can resolve strobe separation times down to 10 ns and thus any dead-time in excess of this amount can be flagged. Assuming Poisson statistics, the dead-time correction for the highest count rate of 1.7 MHz for a single detector element and for a duration of 10 us is less than 0.02%.

Summary

To date our experience with the coalescing system is very positive. The partitioning of the system architecture is perhaps its greatest feature: 1) data capture and histogramming within the excellent real-time FASTBUS environment relieves the front-end computer from time critical functions and therefore 2) enables the use in the front-end systems of a familiar and robust operating system (VMS) not known for its impressive real-time characteristics. Finally, 3) the network, in addition to providing a loosely coupled system, also allows gradual growth which matches well our funding outlook.

Acknowledgements

This work was performed under the auspices of the U. S. Department of Energy.

References

[1] D. McMillan, R. Nelson, R. Poore, M. Meier, and R. Woods, "P-9 Proposed Weapons Neutron Research Facility Data Acquisition System for the PSR Era", 1982.

[2] G. Cort, J. A. Goldstone, R. O. Nelson, R. V. Poore, L. Miller and D. M. Barrus, "Dynamic Structures and Concurrency in a Real-Time Data Acquisition System", presented at the Fourth Real-Time Conference on Computer Applications in Nuclear and Particle Physics, Chicago, Illinois, May 20-24, 1985.

[3] R. V. Poore, D. M. Barrus, G. Cort, J. A. Goldstone, L. B. Miller and R. O. Nelson, "A Data Acquisition Command Interface Using VAX/VMS DCL", presented at the Fourth Real-Time Conference on Computer Applications in Nuclear and Particle Physics, Chicago, Illinois, May 20-24, 1985.

[4] C. F. Packman, "FIORI - CERN FASTBUS to Register I/O Interface User Guide", CERN Report FBDOC/M007, 1982.

[5] M. Larwill, E. Barsotti, T. Lagerlund, R. Pordes, L. Taff, D. Brown, M. Haney, B. Jackson, D. Lesney, K. Nater, and J. Wray, "UNIBUS Processor Interface to FASTBUS", Fermilab Report FBN008.2, 1982.

[6] R. O. Nelson, D. M. Barrus, G. Cort, J. A. Goldstone, D. E. McMillan, R. V. Poore, and D. R. Machen, "FASTBUS Data Acquisition System for Neutron Time-of-Flight Measurements", IEEE Transactions on Nuclear Science, NS-32, No.1, 248(1984).

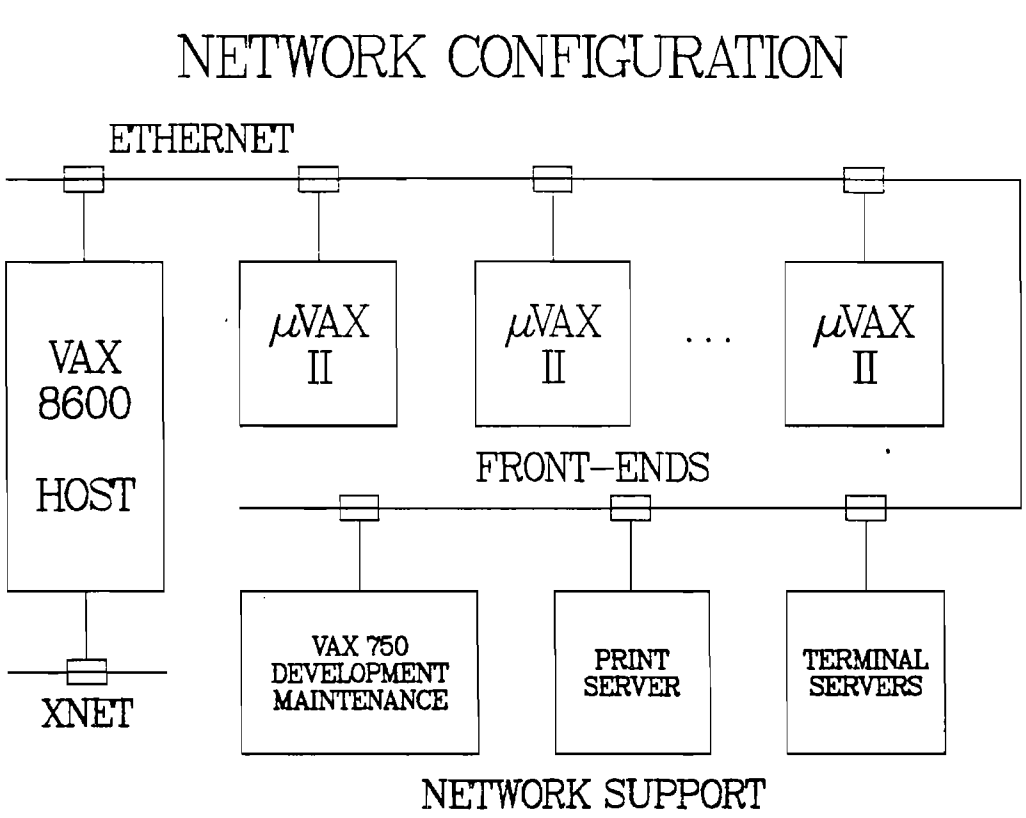

Figure 1. Block diagram for the major system components of the WNR local area network. No attempt is made to distinguish between the cable and fiber optic portions. The host acts as a gateway to the laboratory wide network, XNET.

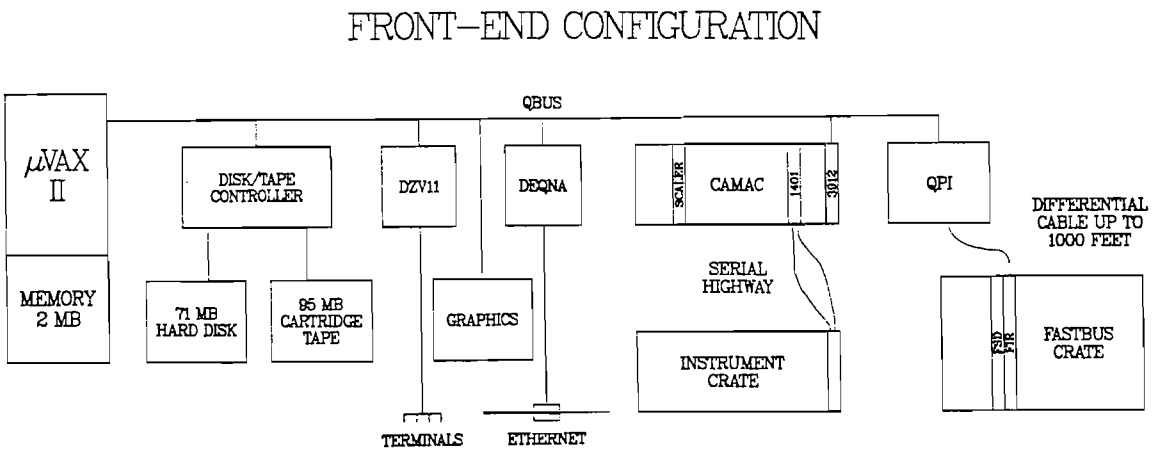

Figure 2. Block diagram for the front-end system. Contents of the FASTBUS and CAMAC crates depends on the instrument and/or the experiment.

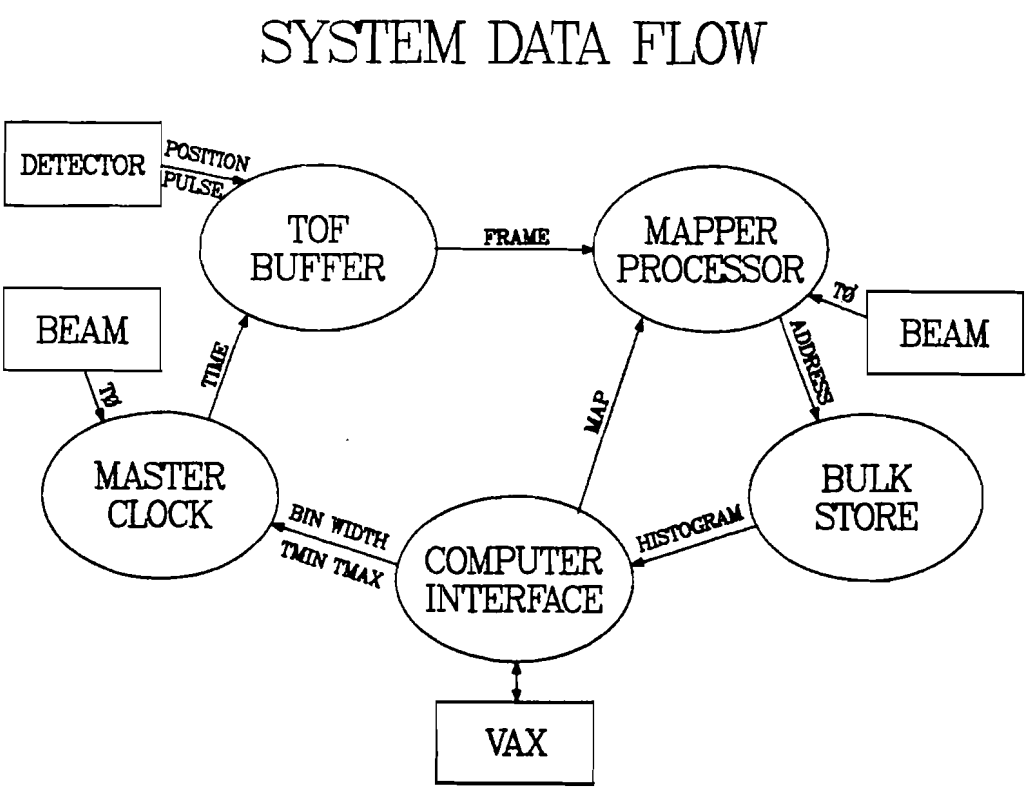

Figure 3. Schematic flow of data through the FASTBUS module set. Before data acquisition begins, modules are initialized through the computer interface. Once begun, the data flow proceeds from the master clock in the clockwise direction.

Proceedings of the Eighth Meeting of the International Collaboration on Advanced Neutron Sources (ICANS-VIII)
8-12 July 1985, Rutherford Appleton Laboratory Report RAL-85-110

The SIP Program for the Evaluation of Neutron Scattering Experiments.

Colin G. Windsor

Materials Physics and Metallurgy Division, B 418 AERE Harwell , OX11 0RA.

Summary. This computer program aims to make the evaluation of the count-rate and resolution of neutron scattering experiments a routine task. The Shelter Island Program (SIP) was conceived to estimate the performance of new neutron sources, new instruments and new experiments in a realistic way. Its data bases and default parameters include the performance characteristics of the 18 principal existing and proposed reactor and pulsed sources, typical instrumental configurations for the 10 most common elastic and inelastic instruments, and the tables of neutron cross-sections for the elements. Given the sample atomic or weight fraction, the most common scattering laws are evaluated analytically. These include the small-angle defect, liquid hard sphere, Bragg, Einstein oscillator, phonon, magnon and crystal field cross sections.

Neutron beam time represents an expensive resource. This program aims to optimise its utilisation by the evaluation of experimental count-rates and resolution before an experiment is performed. It aims to avoid both the waste of beam time resulting from extravagant statistical precision, as well as the possible failure of an experiment caused by too low a count-rate or resolution. The prudent experimenter *SIP's* before he drinks. The program was conceived for the Shelter Island Workshop set up to evaluate the relative performance of the new reactor and pulsed neutron sources proposed for the United States. Comparisons of performance are only realistic if made in terms of the count-rate expected for particular experiments at given values of the scattering vector Q and energy transfer $\hbar\omega$ and their resolutions ΔQ and $\Delta\hbar\omega$. The comparison of count-rates using different methods at the same resolution was the original aim of the program.

The program works simultaneously in two modes. The experimenter can specify an *actual* instrument configuration, and evaluate the corresponding count-rate and resolution for a given value of Q,ω and experimental cross-section. At the same time he is requested to specify the required Q,ω value and the resolution $\Delta Q,\Delta\omega$ and is given the *best* possible count-rate consistant with this resolution. Simple matching methods are used to specify the corresponding best values of intrumental parameters such as the flight paths and

collimations. A serious approximation is that no consideration is taken of focussing. A comparison between the *Actual* and *Best* values enables a judgement to be made of the degree of optimisation of the present instrumental configuration.

The data-bases accessed by the program contain a parameterisation of the flux-distribution and pulse width of 9 reactor and 9 pulsed sources. Both include Maxwellian and epithermal terms specified in the conventional way as the energy-integrated Maxwellian flux $cm^{-2}s^{-1}$, and the epithermal flux from the whole moderator surface at 1 eV $s^{-1}sterad^{-1}eV^{-1}$. A novel method is used to specify the performance of the most commonly used instruments on neutron steady and pulsed sources. The final count-rate is expressed as a product of 5 terms:

1. The moderator flux in $s^{-1}sterad^{-1}eV^{-1}$ units.
2. A generalised *monochromator element* expressing in units of sterad eV the fraction of neutrons transmitted to the sample in terms of the incident solid-angle and energy window.
3. The sample macroscopic cross-section expressed in units of $sterad^{-1}eV^{-1}$.
4. A generalised *analyser element* expressing in units of sterad eV the fraction of neutrons transmitted from the sample to the counter.
5. The counter efficiency.

The 10 instruments chosen include the small angle, reactor crystal monochromator and pulsed time-of-flight diffractometers, and for inelastic scattering, the reactor triple axis, the pulsed source rotor, crystal analyser, crystal monochromator, beryllium filter and resonance detector spectrometers. These instruments have many monochromator and analyser elements in commmon. For example the same crystal monochromator element is used for a reactor diffractometer, triple axis and pulsed crystal monochromator instruments. The *actual* monochromator element for a crystal monochromator is defined by the program in the conventional notation as

$$E_M^A = 2E_0 \cot\theta_M \frac{\alpha_I \alpha_0 \eta_M}{\sqrt{(\alpha_I^2 + \alpha_0^2 + 4\eta_M^2)}} x \frac{\beta_I \beta_0}{\sqrt{(\beta_I^2 + \beta_0^2 + 4\sin^2\theta_M \eta_M^2)}} x R$$

where R is the crystal reflectivity, which is evaluated from a data base containing the properties of the most common analyser crystals. The *best* value for the monochromator element is evaluated using the value of the incident wavelength resolution $R_0 = \Delta k_0/k_0$ where the wavevector resolution Δk_0 is calculated from either the specified scattering vector resolution ΔQ or the energy resolution $\Delta\hbar\omega$, which ever gives the lowest value.

$$E_M^B = 2E_0 \tan\theta_M R_0^2 \beta_I \; x \; R$$

For time-of-flight experiments in either direct or inverted geometry the program evaluates the count-rate per *resolution element* . This is roughly the counts per time channel integrated over a resolution broadened peak in the time-of-flight spectrum. Many time-of-flight instruments can employ many resolution elements along the time-of-flight scan, and possible many counters simultaneously. The number of useful resolution elements (*publishable points*) must be evaluated separately for any given experiment and used to multiply the count-rate per element to give an overall count-rate before comparing with say a single counter triple axis count-rate.

The program has been checked successfully against several well documented experiments. It was developed on a Sinclair QL home computer but uses standard IBM PC BASIC code of some 13000 lines. At present an extensive manual is being prepared. This will include the extensive set of equations relating the final count-rate for the most common types of experiment to the source, instrumental and sample variables — all specified in a consistent set of units with appropriate default values. It is hoped that these will prove valuable in other calculations.

Proceedings of the Eighth Meeting of the International Collaboration on Advanced Neutron Sources (ICANS-VIII)
8-12 July 1985, Rutherford Appleton Laboratory Report RAL-85-110

THE SNS DATA ACQUISITION ELECTRONICS

S Quinton (Technology Division
M Johnson (Neutron Division)
Rutherford Appleton Laboratory

1.0 INTRODUCTION

All neutron scattering instruments at the Spallation Neutron Source (Rutherford Appleton Laboratory) are connected to the PUNCH Data Acquisition and Display System. The PUNCH system encompasses all the hardware and software necessary to control instruments, acquire, manipulate, display and archive data. This paper describes the Data Acquisition Electronics (DAE) which is a subsystem of the PUNCH Data Acquisition System. The operation of the DAE within the overall system and functions of the individual modules of the DAE are described. The detailed circuit descriptions of the modules and the user guides for setting up and programming them are in preparation.

2.0 THE DATA ACQUISITION SYSTEM

Figure 1 shows a block diagram of the Data Acquisition System.

The scattering angles of the diffracted neutrons are defined by the detector positions. The outputs of these detectors are digitised, and in some cases encoded, by the detector electronics. This digital information is presented to the front end Instrument Crates of the Data Acquisition Electronics.

The input modules within the Instrument Crates generate a bit partitioned space - time descriptor for each detected neutron. The spatial information is provided by the detector electronics and the time information is a measure of the elapsed time since the SNS neutron pulse was produced, ie the time of flight of the neutron. Descriptors are stored on a frame by frame basis in the Instrument Crates (where a frame is a SNS cycle or number of cycles) before being transferred to the System Crate. This allows data for a frame to be rejected, if it is corrupted in some way, before being added to the total data acquired for the run.

Up to 20,000 neutron descriptors can be acquired in a frame, which when using 20mS frames corresponds to a 1MHz data rate. The Instrument Crates can acquire this data in a 10MHz burst. Peaks of up to 20MHz can be absorbed by FIFOS in the input modules.

The System Crate controls data acquisition and data transfer from the Instrument Crates via the Instrument Bus. The timing information used to generate the time partition of the neutron descriptors by the Instrument Crate is provided by the System Crate.

Descriptors transferred from the Instrument Crates have further information added to them relating to the elapsed time since the start of the run and are then processed to form the address of a large store. Data transfer then consists of incrementing the store location corresponding to each descriptor.

Facilities to monitor run parameters and implement test features are included in the System Crate. A computer interface allows the Data Acquisition Electronics to be controlled by the VAX 11/730 Front End Minicomputer and for data to be downloaded at the end of a run.

The Front End Minicomputers on each instrument are connected to a Cambridge Ring Local Area Network, as is a central hub computer and gateways to the laboratory central computers and SERC network.

3.0 THE DATA ACQUISITION ELECTRONICS (DAE)

In order to accommodate the needs of different instruments a modular system has been developed.

Figure 2 shows a block diagram of the DAE. Most of the modules use wire-wrap construction and have been designed using the laboratory's CAD facility. The Instrument Crate input modules use multi-layer printed circuits.

3.1 INSTRUMENT CRATE

The Instrument Crate uses CAMAC standard mechanical components together with a custom design printed circuit backplane, the Instrument Crate Bus. Power supplies are mounted on the back of the crate. A system can contain up to 16 Instrument Crates, each crate containing an Instrument Crate Controller, a pair of Ping-Pong Frame Memories and up to 16 Data Input Modules.

3.2 DETECTOR INPUT MODULES (DIM)

There are 3 types of DIM modules:

DIM1 A module with 8 parallel inputs, each with its own FIFO. The output descriptors contain the time information and a 3-bit position code for the corresponding event.

DIM2 A module with a 12-bit binary coded input and a single FIFO handling 4096 channels. The output descriptors contain the time and position code for the corresponding event.

MIM A Monitor Input Module with 4 parallel inputs designed for neutron beam monitoring. Each input has an 8-bit binary prescaler, presettable by switches in the module. The output descriptors contain the time information corresponding to the last event in a prescaled group, and an associated 2-bit position code.

If a FIFO in any of the DIM modules overflows during data taking a flag is set in the Instrument Crate Controller.

3.3 INSTRUMENT CRATE BUS

The bus uses ECL technology and can read data from the DIMs at up to 10 MHz. Modules will issue requests to the Instrument Crate Controller when they have data to transfer. They will be serviced on a fixed priority basis. The bus is 24 bits wide and partitioned as shown in the diagram:

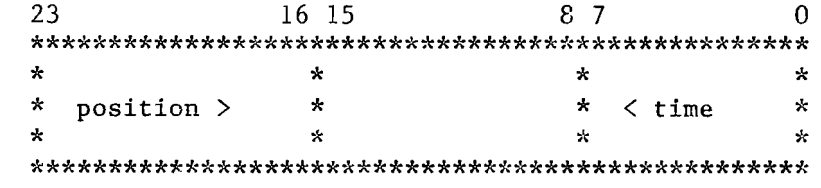

The position of the partition can be varied over the centre 8 bits on a crate by crate basis. The timing parameters for the instrument must be set to prevent overflow into the position partition and the Descriptor Generator in the System Crate must be set up appropriately. There is also a 16 bit time channel bus driven by the Instrument Crate Controller to provide Gray coded time information to the DIMs.

3.4 INSTRUMENT CRATE CONTROLLER (ICC)

The ICC controls data acquisition in the crate and provides the interface to the Instrument Bus.

The synchronous data acquisition controller carries out the priority arbitration on the DIM request signals, and generates the necessary timing signals to read the descriptors from the DIMS and load them into the Ping-Pong Frame Memories.

The module contains the Gray coded time channel counter which is incremented by the external time channel increment signal. The time channel counter is reset by the frame synch (t0) or when a preset maximum time channel count is reached. This maximum value is set in the ICC by the host computer via the Instrument Bus. Data acquisition is inhibited when the time channel counter = 0.

Timing definitions are illustrated below:

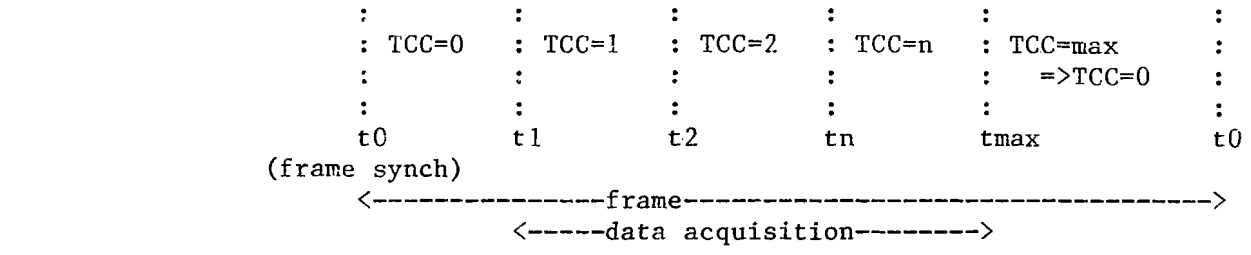

TCC=Time Channel Count

3.5 PING PONG FRAME MEMORY (PPFM)

The PPFM is linked to the ICC by a front panel Instrument Crate Controller Bus. The Instrument Crate contains two modules each containing 20k*28 bit (24 bits + 4 bits module address) of RAM for one frame of data. Data acquisition and data transfer alternates between the two modules on a frame by frame basis. Data acquisition refers to the real time acquisition of data using the Instrument Crate Bus where the descriptors are stored sequentially in a PPFM. Data transfer refers to the downloading of a PPFM to the system Crate and subsequent operations including the Read-Increment-Write operation on the Bulk Store.

Registers within the PPFM's contain the word count, and flags to indicate if the PPFM overflowed or if a FIFO overflowed in the corresponding data acquisition cycle. These registers are normally read by the Instrument Bus Interface via the Instrument Bus and ICC prior to data transfer.

3.6 INSTRUMENT BUS

The Instrument Bus is a daisy chain bus linking the ICCs to the Instrument Bus Interface (the bus controller). It is used to set up the maximum time channel count in the ICCs, read the ICC status registers, and download data during data transfer operations. Data can also be written to the PPFMs for the test purposes.

The bus uses twisted pair cable carrying ECL balanced signals with a maximum length of 30m. Data transfer can take place at up to 1MHz.

3.7 SYSTEM CRATE

The System Crate uses Intel Multibus standard cards and signal definitions. The crate is a custom design and incorporates power supplies.

10 card slots are provided at a 1" pitch for wire wrap cards, 8 slots are provided at the standard 0.6" pitch for printed circuit cards, this section being intended primarily for the Bulk Store memory cards.

Only serial priority arbitration is supported since there are only two bus masters, the Computer Interface and the Incrementer.

Up to 16 System Crates, and therefore 16 sets of Data Acquisition Electronics, can be attached to each Front End Minicomputer.

3.8 INSTRUMENT BUS INTERFACE (IBI)

The IBI controls Multibus access to the Instrument Crates via the Instrument Bus. The Instrument Crate registers are mapped directly into Multibus I/O address space.

The IBI also controls data acquisition and transfer.

A bit in the IBI control register determines whether or not the system is acquiring data. Data acquisition is not allowed for part frames and the IBI carries out the necessary synchronisation to avoid this. When the data acquisition bit is negated the IBI will generate an interrupt (which can be disabled via the control register) and reset a data acquisition status bit when data acquisition has finished and the last acquired frame of data has been transferred to the Bulk Store.

At the start of each data transfer frame the IBI reads the status register in each ICC and determines the total number of descriptors acquired in the previous frame, and whether any of the PPFMs or FIFOs overflowed. Under certain conditions the frame will be vetoed, ie. the data will not be transferred and will be lost. The conditions are:

(1) An external veto was received during the frame.

(2) The total descriptor count exceeded 20,000.

(3) A PPFM overflow was flagged.

(4) A FIFO overflow was flagged.

(5) A proton count underflow was flagged.

(6) A chopper out of phase veto was received.

Each of the 6 conditions can be enabled or disabled by bits in the IBI control register. The system is designed to eliminate, as far as possible, the loss of part of a frame of data. If data transfer from a particular frame is still taking place when a frame synch is received the data transfer will continue until complete. Meanwhile data acquisition will be halted. The halting and restarting of data acquisition will only take place on frame boundaries.

If a frame's data is lost due to overrun of data from the previous frame or if there was an enabled veto condition present the IBI will generate an interrupt (this can be disabled via the control register). A status register will contain the reason for the interrupt.

The IBI transfers data from the PPFM in each Instrument Crate to the Incrementer via the Neutron Proton Monitor and Descriptor Generator. The IBI adds the crate address (4 bits) and the frame count (8 bits) to the incoming descriptors, making a total descriptor of 40 bits.

There is a frame count prescaler (up to /256) presettable from the Multibus. The value of this prescaled frame count, which forms the frame count position of the descriptor, can be read from the Multibus.

There are also registers containing the frame count during the run and the number of frames of data transferred.

3.9 DESCRIPTOR GENERATOR (DG)

The 40-bit descriptor passed to the DG by the IBI is compacted to form an address within the range of the Bulk Store. The following functions are performed and are programmable from the Multibus.

(1) bit partitioning of the 24 bit time/position component of the descriptor from the DIMs, using a look-up table addressed by the crate address to control a multiplexer.

(2) concatenation of the position descriptors, by adding constants from a look-up table addressed by the module and crate addresses. Up to 16 bits are allowed for the concatenated position descriptor.

(3) a 64k*16 bit look-up memory addressed by the concatenated position descriptor, allows any ganging or bit routing patterns to be set up for the position descriptor.

(4) position and time descriptors are merged using a t+(tmax*p) algorithm.

(5) position time descriptors are concatenated and the frame number included by adding a constant from a look-up table addressed by the frame count and crate address.

The compacted descriptor is passed to the Incrementer.

3.10 INCREMENTER (INR)

During data transfer the INR controls the Multibus and performs Read-Increment-Write operations on the Bulk Store locations corresponding to the incoming descriptors. The INR supports 8, 16 or 32 bit word length in the Bulk Store. If a Bulk Store location overflows the location is set to zero, the address stored in a 32 word FIFO accessible from the Multibus and an interrupt is generated.

3.11 NEUTRON PROTON MONITOR (NPM)

The Frame Synch pulse provides the basic time reference for data acquisition and transfer and for neutron time of flight measurement. The NPM normally derives this signal from an external source but an internal oscillator and Multibus controlled single shot facility are available for test purposes. The external source can either be the SNS control system,

or the chopper control system in cases where a chopper is being used to delete pulses of neutrons. The Frame Synch can be delayed with respect to the source by up to 256mS with 4μS resolution (programmable from the Multibus).

In addition the NPM accumulates externally generated neutron and proton counts and the neutron count from predetermined DIMs or MIMs.

A ten bit proton count for each frame is passed to the NPM which compares the count with a presettable value. If it is below this a proton count underflow veto is passed to the IBI. The total proton count for the run is accumulated as a raw proton count, the counts associated with frames of data transferred are accumulated as a good proton count.

The neutron count for the frame is passed to the NPM as a series of pulses which are counted after passing through a programmable time gate. As with the proton count raw and good neutron counts are accumulated for the run.

The NPM monitors the descriptor transfers between the IBI and DG. Descriptor and mask registers allow two separate selected descriptor counts to be accumulated. The 16 bits of the descriptor position partition and the crate and module address partitions are monitored. The mask register allows 'don't care' bit positions to be programmed into the descriptor selection.

For test purposes the NPM can drive the DG input directly, the IBI output drivers can be turned off for this purpose.

3.12 TIME CHANNEL GENERATOR (TCG)

The TCG uses a RAM look up table to generate the time channel increment pulses to be routed to the ICCs.

A 20 bit scaler is clocked by a 32MHz crystal clock giving 32nS resolution and 32mS full scale. A 32k*20 bit RAM is loaded with the required time channel boundaries from the Multibus. These are fetched in sequence, the

increment pulses being generated by comparison with the scaler output. The minimum time channel width is determined by the memory access time and is 500nS. There is a 3 bit binary clock prescaler, programmable from the Multibus, to accommodate frames longer than 32mS. Using the prescaler frames of up to 8x32mS may be accommodated. The time channel increment pulses are transmitted on 16 separate ECL twisted pair lines to the ICCs.

Instruments can have more than on time regime (but not crossing crate boundaries) by adding more TCGs.

3.13 BULK STORE

The Bulk Store is implemented using commercial memory modules. In current technology these are available in sizes of up to 4 Mbytes. The Multibus can support up to 16 Mbytes of memory.

The memory cards have error detection circuits which will generate an interrupt if a parity error occurs. These interrupts can be disabled.

3.14 COMPUTER INTERFACE (CI)

The CI interfaces the DEC Unibus from the VAX 11/730 Front End Minicomputer (FEM) to the Multibus.

The Bulk Store appears directly in the memory address space of the Multibus using all of the 16 Mbyte address range if required. The Unibus accesses Multibus memory address space via an auto-incrementing address register and a memory data register in Unibus user I/O address space. Other System Crate module registers will be in Multibus I/O address space accessed using the same address register (but not auto incrementing for I/O accesses) and an I/O data register. These module registers include auto-incrementing address registers and associated data registers to access look up table memories.

Bidirectional DMA transfers are supported between the FEM and Multibus memory and I/O address space. Block, burst and single shot DMA modes are provided.

An interrupt can be generated to the FEM through a hardware presettable vector and at a hardware presettable priority level in response either to a Multibus interrupt or the end of a DMA operation.

The interrupt sources can be individually disabled. In the case of a Multibus sourced interrupt a register in the CI contains the bit pattern of the Multibus interrupt level(s) that crused the FEM interrupt.

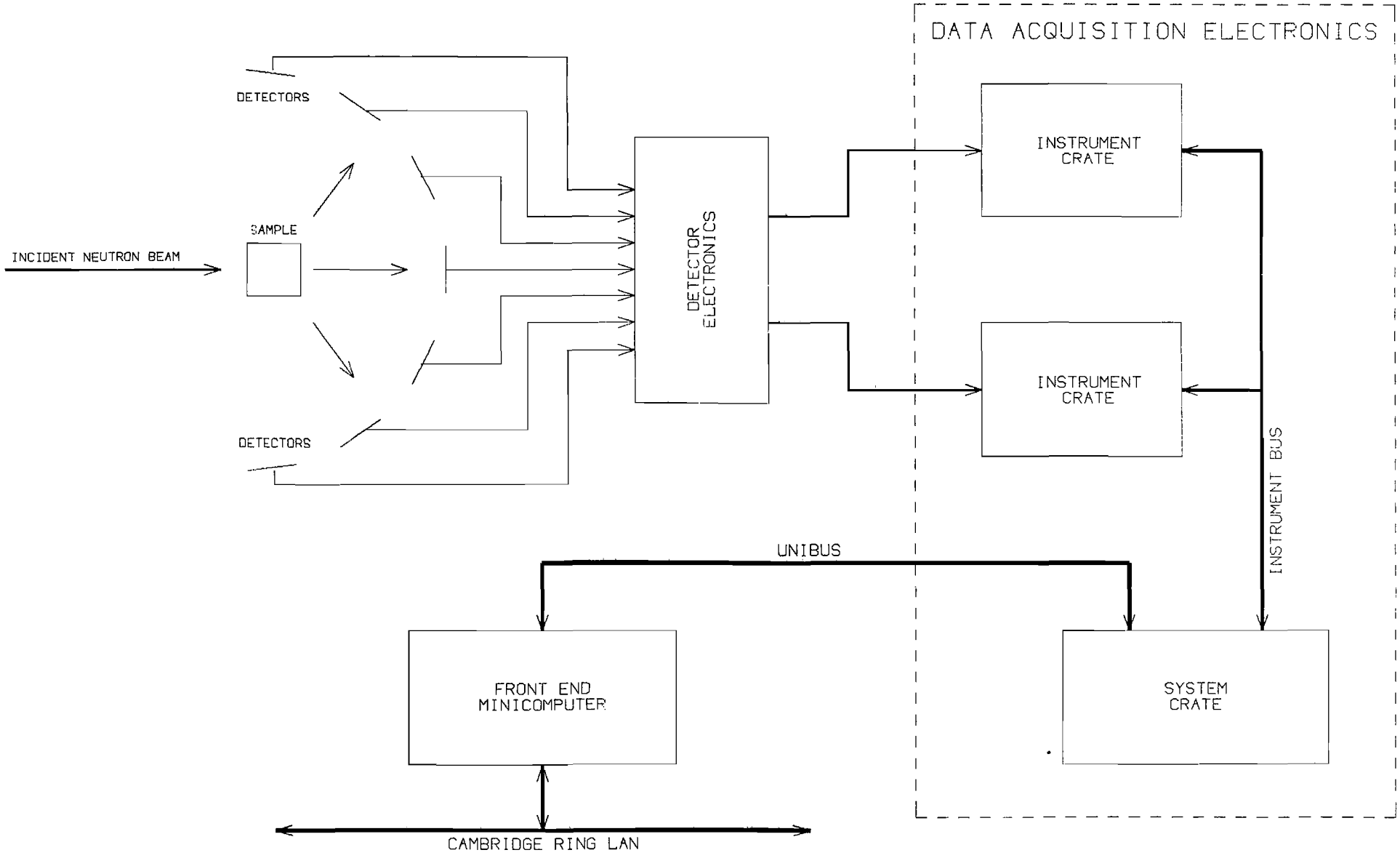

SNS DATA ACQUISITION SYSTEM

FIGURE 1

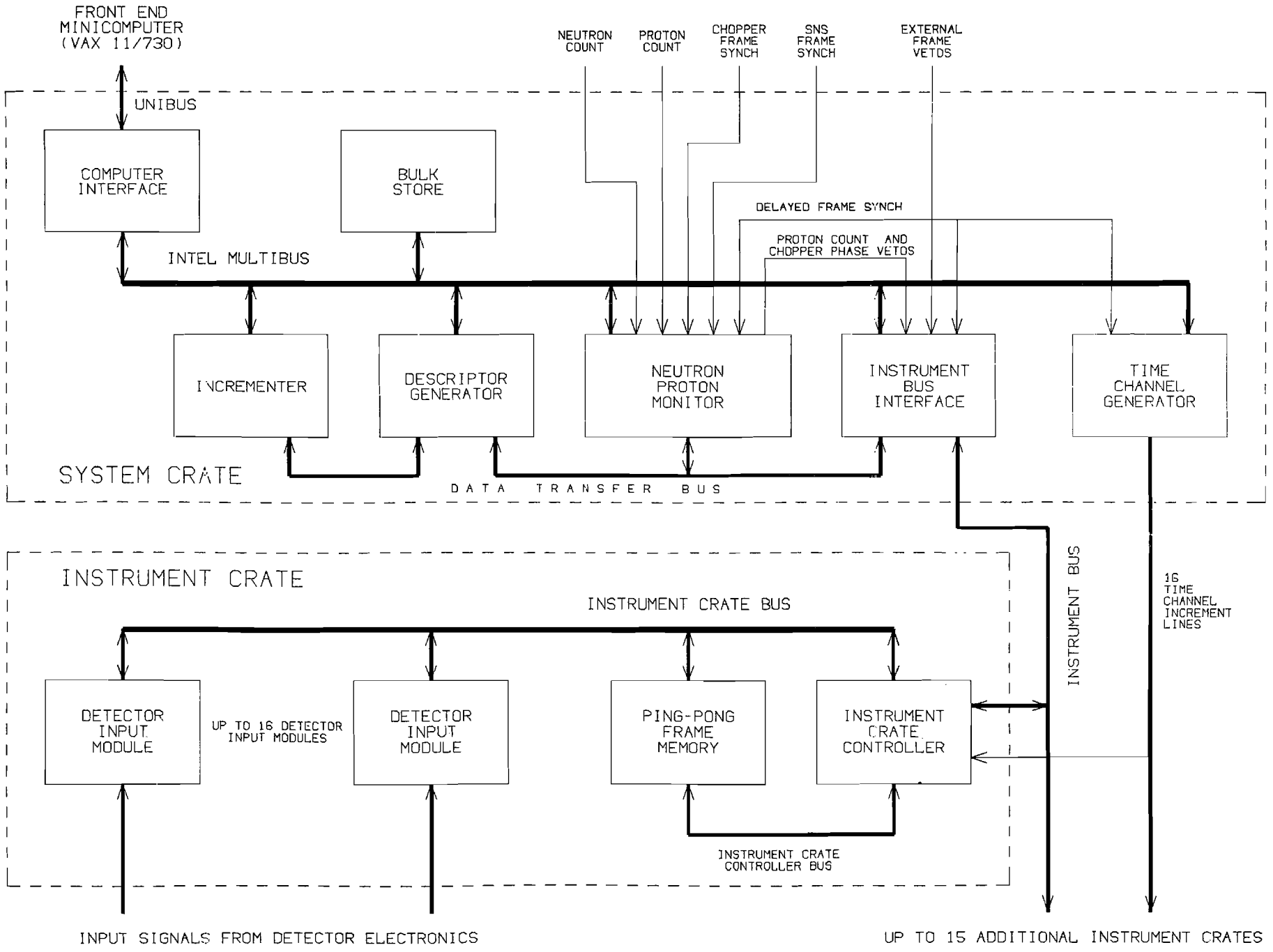

SNS DATA ACQUISITION ELECTRONICS

FIGURE 2

Proceedings of the Eighth Meeting of the International Collaboration on Advanced Neutron Sources (ICANS-VIII)
8-12 July 1985, Rutherford Appleton Laboratory Report RAL-85-110

PUNCH: THE SNS DATA ACQUISITION SYSTEM

M W Johnson, W I F David, A W Joines, K J Knowles,
R T Lawrence, W C A Pulford, S P H Quinton, E G Smith

PUNCH is the name given to the interconnected systems of data acquisition electronics (DAE), CAMAC, front-end minicomputers (FEMs) and HUB computer which provide the control, acquisition, display, storage and analysis functions required by SNS neutron scattering instruments.

It can conveniently be divided into 3 major sub-systems :

1. Data acquisition and instrument control
2. Data flow (networking and archival)
3. Data display and manipulation

The hardware and software components of these three subsystems are shown in table 1.

TABLE 1

System	Hardware	Software
Data Acquisition and Control	FEM (VAX 730) DAE CAMAC	Instrument Control Program (ICP)
Data Flow	Cambridge Ring (CR82) HUB (VAX 750) (VAX 8600 Sept 85)	PUNCH PROTOCOLS PUNCH ARCHIVAL
Data Display and Manipulation	HUB, FEM Pericom VT200/t4014	GENIE 72.1

The following sections give a brief overview of these systems.

1. Data Acquisition and Control

Each SNS instrument is equipped with the following hardware configuration :

DAE	Instrument Crate System Crate
CAMAC	Camac Crate Intelligent Crate Controller
VAX-11/730	730CPU (VAX/VMS) FP730 floating point accelerator 1-2 Mbytes memory 10 Mbytes removable disk 121 Mbyte fixed disk 3010 SEEL Cambridge Ring DMA interface console Pericom 1000 x 1000 graphics terminal Pericom VT100 control/edit terminal NDK dot-matrix printer (graphics)

This is shown in the block digaram Figure 1.

The DAE 'time-stamps' neutron events and increments the appropriate word in a large (1-16 Mbyte) histogramming memory. The time channel boundaries may be set by software to any multiple of a basic 32 MHz clock. Individual detectors may be mapped to any spectrum providing a totally flexible detector ganging procedure.

The principal parameters of the DAE are :

- up to 64k detectors
- up to 32k time channels
- up to 16M channels
- 20 MHz peak rate/detector
- 1 MHz max mean rate/system crate
- up to 16 system crates

The DAE is the subject of a subsequent paper at this meeting and further details are given there.

A CAMAC crate, containing an intelligent crate controller and associated modules, is connected to each FEM via an asynchronous RS232 serial line.

This enables beam-line and sample-environment components (such as stepping motors, vacuum sensors, etc) to be activated or measured. Measurements may be on user demand or by continuous monitoring. All control of the DAE and CAMAC is via the VAX 730 FEM computer.

This configuration, described above, enables the user to :

- control the course of a series of runs from high level commands entered through the FEM keyboards
- view the data
- manipulate and merge data sets
- store the data on disk (20-100 runs)
- transfer data to the HUB computer (via the Cambridge Ring local area network)

At present there are five VAX 11/730 computers installed as FEM computers. They all use the VAX/VMS operating system and are therefore totally software compatible with the HUB computer, presently a VAX 11/750. The HUB computer will be upgraded to a VAX 8600 in September 1985 by which time a total of nine FEM computers should be in operation (8 x 730, 1 x 750).

2. Data Flow

The network joining the FEM and HUB computers is a 3.5 km Cambridge Ring running CR82 protocols at levels 0,1,2. The network provides for two types of traffic, terminal and file-transfer, and different protocols are used for the two - to provide the most efficient for each one. A schematic of the network is given in Figure 2.

The terminal traffic is presently between some 53 terminals distributed geographically between R3, R6, R69 and R55 and 6 VAX computers sited in R69 (1), R55 (4) and R3 (1). This traffic is carried on the Cambridge Ring using a locally developed [1] 'single-shot' protocol and back-to-back terminal multiplexers (SEEL model 3012). This protocol transmits individual bytes as generated at the terminal or computer interface and is particularly effective in transparently supporting full-screen editing and graphics input. The protocol also provides :

- a multi-source, single-sink service (enabling line-printers and status displays to be accessed from many computers)
- a computer-name server
- distributed architecture (no centrally stored lists)

Although developed 'in house' this system is now marketed by SEEL as the DISTRIBUTED NETWORK SWITCH.

File transfer is accomplished using SEEL DMA interfaces (model 3010 single Hex UNIBUS board) and non-standard network/transport/service layers (3,4,5). Currently disk to disk copying is achieved at total elapsed rates of 200 kbits/sec.

Raw data created at the FEM computers is staged to HUB disks using the file-transfer protocols described above. The data is then archived to tape using PUNCH ARCHIVE software.

The upgrade of the HUB to a VAX-8600 (September 1985) with a high-speed (4 Mips) processor, 12 Mbyte or memory and a disk store of 3 Gbytes will provide users with the necessary facilities to enable computer on-line data analysis to be performed.

3. Data Manipulation and Display

We have attempted to provide a common solution to the problem all instruments pose for the first stages of data analysis. All instruments require spectra to be added, subtracted, normalised and adjusted to different scales. In the early stages of an instrument's development it is especially necessary to be able to follow novel data reduction routes unsuited to standard data reduction programs.

The solution is in the form of the program GENIE which essentially provides the user with a LANGUAGE for data manipulation.

GENIE has grown rapidly since October 1984 when it started life as a display package for SNS data running over the graphics system GKS 6.2. This original program was written by W I F David. From January to June 1985 the initial program has been transformed (by the efforts of WIFD,

MWJ, KJK, SPG, GDC) to become a language for displaying and manipulating spectra. The program now runs over the Rutherford Appleton Laboratory standard GKS Mk 7.2.

The program deals with the usual requirements of primary neutron analysis packages :

- Graphical display with
  - routing to hard-copy devices
  - selection of log/linear axes, x/y limits, header, binning, markers/histogram, screen resolution, graticule, screen size, error bars
  - cursor x,y location
  - cursor zoom
  - multiple spectrum plotting

- REBIN and UNITS commands to transform x axes from time-of-flight to physical units of interest.

- FUNCTION commands to enable y-value transformations. These may be user supplied without program relinking.

- FITTING commands to enable least-squares fitting of standard or user-supplied functions (e.g. peak fitting)

However the features which render GENIE a language rather than a simple program are the following :

- Operation from a stored list of instructions
- Flow control (DO, END DO, GOTO)
- Algebraic manipulation of spectra
- Parameter substitution
- I/O to screen or disk files

As an example, Table 2 gives the complete listing of a command file which includes comments describing its operation and purpose.

The GENIE program is provided on the HUB and each FEM computer where it can access both stored data on disk and 'live' data accumulating in the DAE.

References

[1] A Single Terminal Multiplexer for a Cambridge Ring, W C A Pulford and R T Lawrence, J of Microcomputer Applications (1984) 7 139-147

TABLE 2

```
**************************************************************************
 Directory:            SYS$SYSDEVICE:[HRPD]
 Filename:             FOCUS.COM
 Time:                 10-JUL-1985 18:05
**************************************************************************

!
!     ***** SOFTWARE FOCUSSING OF HRPD DIFFRACTION SPECTRA ******
!
!   This command file focusses NOSPEC spectra from run number IRUNNO.
!
$ INQUIRE IRUNNO "  Which run number do you wish to look at"
$ INQUIRE IPOS "  Is the sample at the 1m. or 2m. position (1/2)"
$ INQUIRE ISP "  Which spectrum do you wish to start with"
$ INQUIRE NOSPEC "  How many spectra do you wish to add together"
!
> @FOCUS'IPOS' IRUNNO ISP NOSPEC
!
$ IRUNNO= P1          ! Run number passed from FOCUS.COM
$ ISP= P2             ! Initial spectrum number
$ NOSPEC= P3          ! Number of spectra to be added together
> ABB 'IRUNNO' AA     ! Abbreviate data-file to AA for convenience
> W1= AA(S'ISP')      ! Fill workspace 1 with initial spectrum
$ ! Evaluate secondary flight path and two theta for each spectrum
$ PATH2= 1.100774 - 0.626785E-02*ISP + 0.1236448E-03*ISP*ISP
$ TTH= 176.7727 -0.814087*ISP - 0.305026E-02*ISP*ISP
> SET PAR 1 95 'PATH2' 'TTH' 0 2
> U/D W1              ! Convert to d scale
$ NOSPEC= NOSPEC-1
$ DO I= 1,NOSPEC      ! Do loop beginning
$ ISP= ISP-1
> W2= AA(S'ISP')      ! Fill workspace 2 with next spectrum
$ ! Evaluate secondary flight path and two theta for each spectrum
$ PATH2= 1.100774 - 0.626785E-02*ISP + 0.1236448E-03*ISP*ISP
$ TTH= 176.7727 -0.814087*ISP - 0.305026E-02*ISP*ISP
> SET PAR 2 95 'PATH2' 'TTH' 0 2
> U/D W2              ! Convert to d scale
> REB W1 W2           ! Make W2 bins commensurate with W1 bins
> W1= W1+W2           ! Add W2 to W1
$ END DO              ! End of Do loop
> W3= W1              ! Make W3 equivalent to W1
$ ! Find the middle spectrum and associated L2 and 2 theta
$ JSP= ISP + 0.5*NOSPEC
$ PATH2= 1.100774 - 0.626785E-02*JSP + 0.1236448E-03*JSP*JSP
$ TTH= 176.7727 -0.814087*JSP - 0.305026E-02*JSP*JSP
> SET PAR 3 95.0 'PATH2' 'TTH' 0 2
> U/T W3              ! Convert W3 back to time-of-flight
> D W3                ! Display W3
```

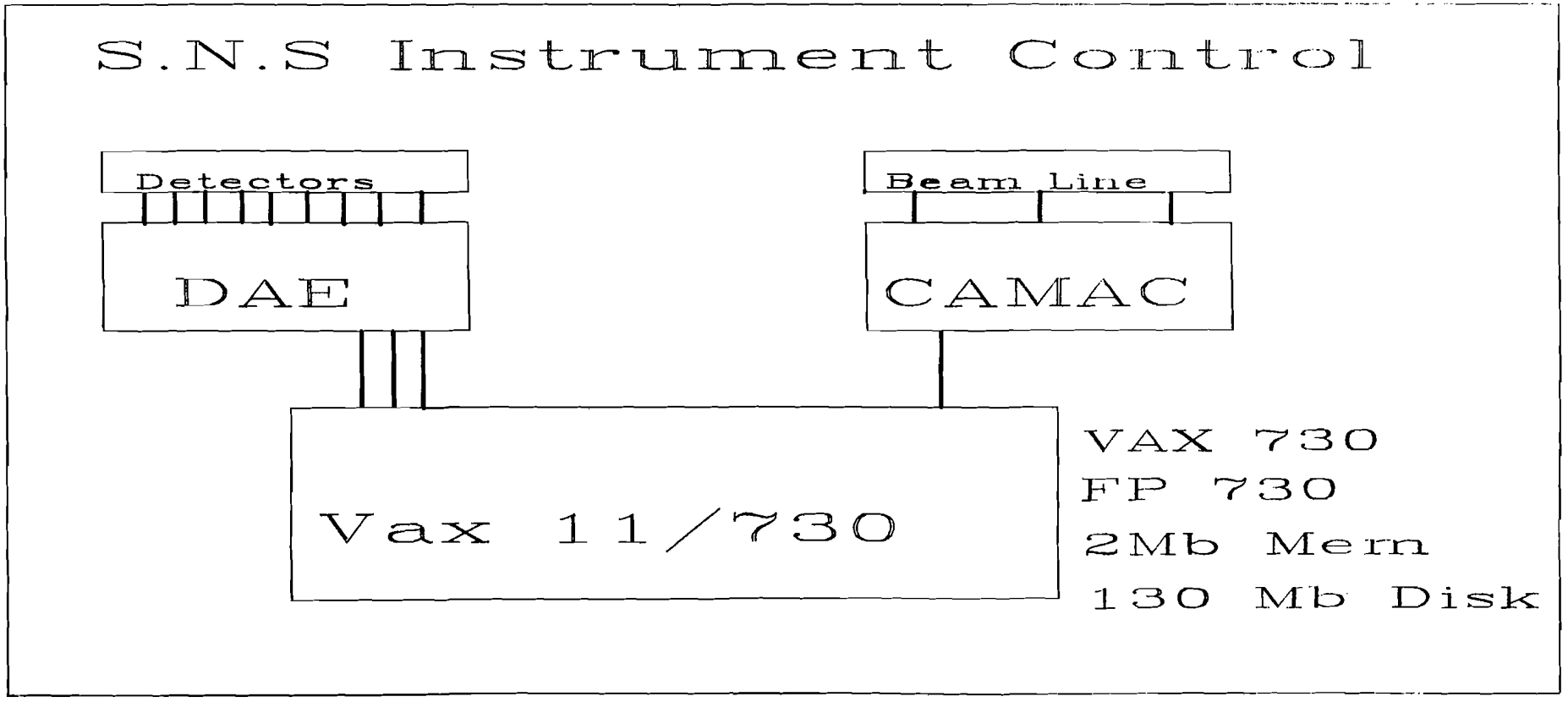
S.N.S Instrument Control
Detectors
Beam Line
DAE
CAMAC
Vax 11/730
VAX 730
FP 730
2Mb Mem
130 Mb Disk

FIGURE 1

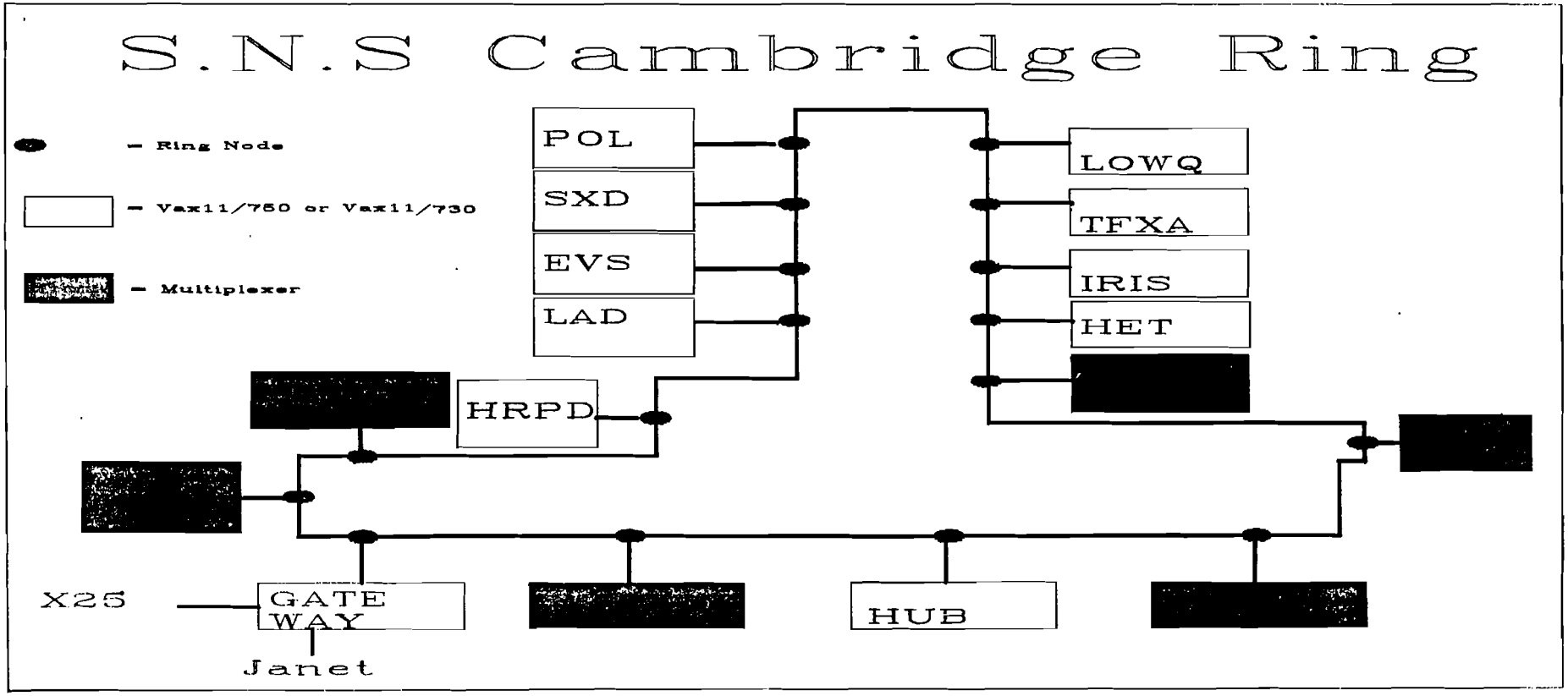
S.N.S Cambridge Ring
- Ring Node
- Vax11/750 or Vax11/730
- Multiplexer
POL
SXD
EVS
LAD
HRPD
LOWQ
TFXA
IRIS
HET
X25
GATE WAY
HUB
Janet

FIGURE 2

Proceedings of the Eighth Meeting of the International Collaboration on Advanced Neutron Sources (ICANS-VIII)
8-12 July 1985, Rutherford Appleton Laboratory Report RAL-85-110

THE PERFORMANCE OF THE IRIS AND HRPD GUIDES ON THE SNS

J C Sutherland, E Steichele*, W I F David, M W Johnson,
J L Altrip, R C Ward and C J Carlile

Rutherford Appleton Laboratory

*Technical University Munich

ABSTRACT

Two of the eighteen beam ports on the SNS are furnished with neutron guide tubes. These guides supply neutron beams to the High Resolution Powder Diffractometer (HRPD) and the Quasielastic Spectrometer (IRIS). The performance of these guides was able to be evaluated during the initial operating period of the SNS.

COMMON FEATURES

Each guide comprises 1m glass sections closely abutted to approximate the required curved geometry. The 1m sections were mounted inside steel vacuum vessels with mounting and adjustment points accessible from the outside. Each 1m section is closely fitted with steel shield plates within the vacuum vessel to prevent fast neutrons streaming along the sides of the guide. The vacuum vessels are supported on concrete plinths at approximately 3m intervals. Both beams are completely shielded externally with 60 cm thickness of steel and 30 cm thickness of borated wax out to a distance of 30m approximately. The remaining length of HRPD to the diffractometer itself is shielded with 30 cm of concrete.

The alignment of the guide is carried out with respect to survey datums on the floor of the experimental hall. Datum lines which represent a tangent to the emergent neutron beam (the prime tangent) and a 45 cm translation of this line have been laid down for both beams. HRPD, because of the

shape of the concrete shielding, also has a 1° offset line to the prime tangent. Mirrors and metre scales perpendicular to the prime tangent are set up on the target shielding wall and at the end of the guides. HRPD has an intermediate set of scales midway along the guide. This arrangement enables any angular line to be defined.

Guide heights are adjusted by means of 1/5' arc second spirit levels and horizontal settings by a theodolite set along the prime tangent at the beam height and able to view the side of each guide element through glass ports along the guide vacuum vessel.

The surface quality of the vertical faces of each of the guide sections has been measured optically with a 0.1 arc second precision [0.5×10^{-6} radians] auto-collimating telescope. The best overall guide elements were selected for installation, each element being located with its flatter surface to the outside of the curve where more reflections take place. The RMS average value σ_R of the standard deviation σ of all vertical faces for the installed set of 87 HRPD guides was 35×10^{-6} radians compared with the specification of 60×10^{-6} radians. The resultant σ_R values for the outer and inner surfaces are 26×10^{-6} and 44×10^{-6} radians respectively. A frequency distribution for the HRPD guide elements is shown in Figure 1. The IRIS guides were selected in a similar manner.

THE IRIS GUIDE

Situated on beam N6, IRIS views a liquid hydrogen moderator at 22K. The moderated neutron spectrum peaks at 3Å on an equal wavelength scale. The guide transmits neutrons to the spectrometer sample position at 31.4m. The design parameters of the guide are given in Table 1. The early section of the IRIS guide is fabricated from highly polished steel sections in order to minimise the effects of radiation damage at the guide entrance which is only 1.7m from the moderator. This small separation is necessary in order to ensure full illumination of the guide at 6-7Å.

The neutron spectrum at the entrance to the curved guide section at 6.4m as measured with a 1% scintillator monitor is shown in Figure 2a. This clearly shows the epithermal and thermal regions of the moderator spectrum. The intensity detected at this position includes a contribution from neutrons travelling at angles which would preclude them reflecting

from the subsequent guide sections. Accordingly when the neutron spectrum measured at the guide exit at 30.6m (Figure 2b) is normalised to the incident spectrum the resultant ratio (Figure 2c) is disproportionately low at short wavelengths. Despite this fact the throughput at longer wavelengths approaches 70%. The average number of reflections along the 24m curved section for 6Å neutrons is ~ 6.25.

HRPD GUIDE

Situated on S8, HRPD views a 10 x 10 x 2.5 mm liquid methane moderator at 90K. The details of the HRPD guide are given in Table 1. During the December test run of SNS, measurements were taken at both 9m and 92m using Davidson scintillator monitors [1] thus offering the possibility of determining guide transmission.

The two spectra are shown in Figures 3a and 3b. Taking a simple ratio between these measurements, and correcting for their different efficiencies provides an illustration of the transmission by the guide (Figure 3c). However, this is not a good measure of the guide's performance since many neutrons will be present at the 9m position that are non-transmittable, even by a perfect guide.

It shows that the expected characteristic wavelength has been realised and that the transmission exhibits a plateau at around 70%. The low-wavelength transmission is especially good, reaching down to 0.5Å. This indicates that the abuttment errors are well within the specified tolerance of 0.001" s.d.

[1] P L Davidson 'Thermal Neutron Beamline Monitor' RAL-84-120 (1984)

Table 1 The geometrical design parameters of the IRIS and HRPD guides

	IRIS	HRPD
Moderator	Liq H_2 22K	Liq CH_4 105K
Moderator to Guide Entrance	1.7m	3.65m
Initial Straight Section	4.45m	2.28m
Curved Section	24m	55m
Final Straight Section	--	32m
Guide Aperture	65 mm x 43 mm	80 mm x 25 mm
Characteristic Wavelength λ^*	3.5Å	0.98Å
Cut-Off Wavelength	1.0Å	0.5Å

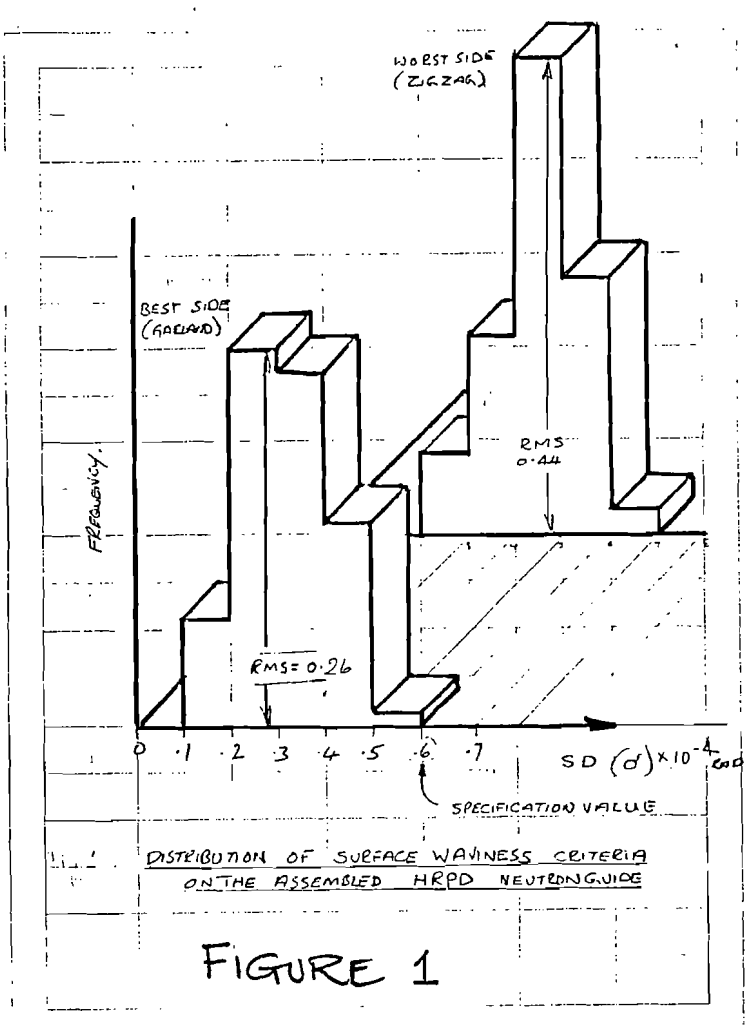

FIGURE 1

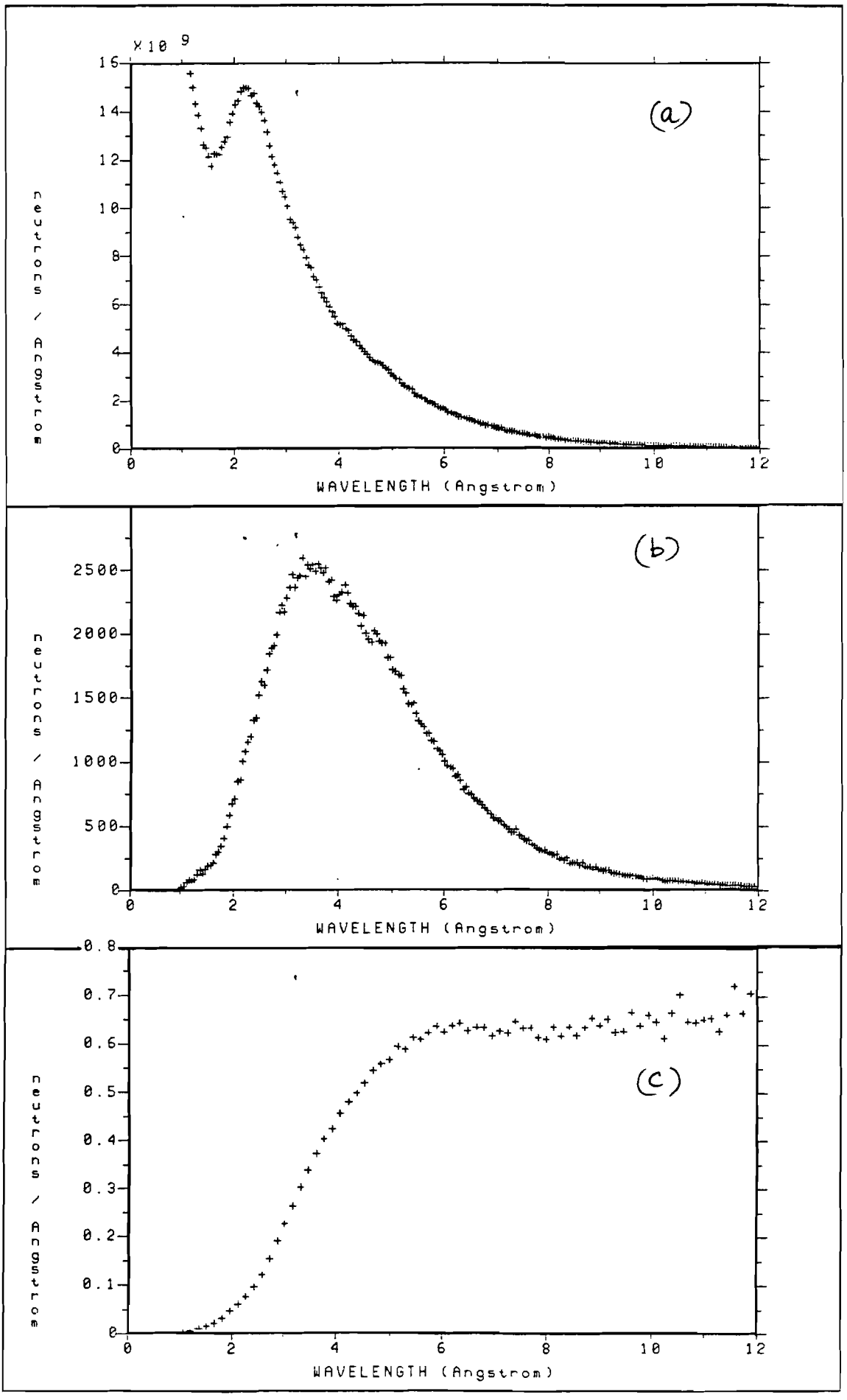

FIGURE 2 IRIS

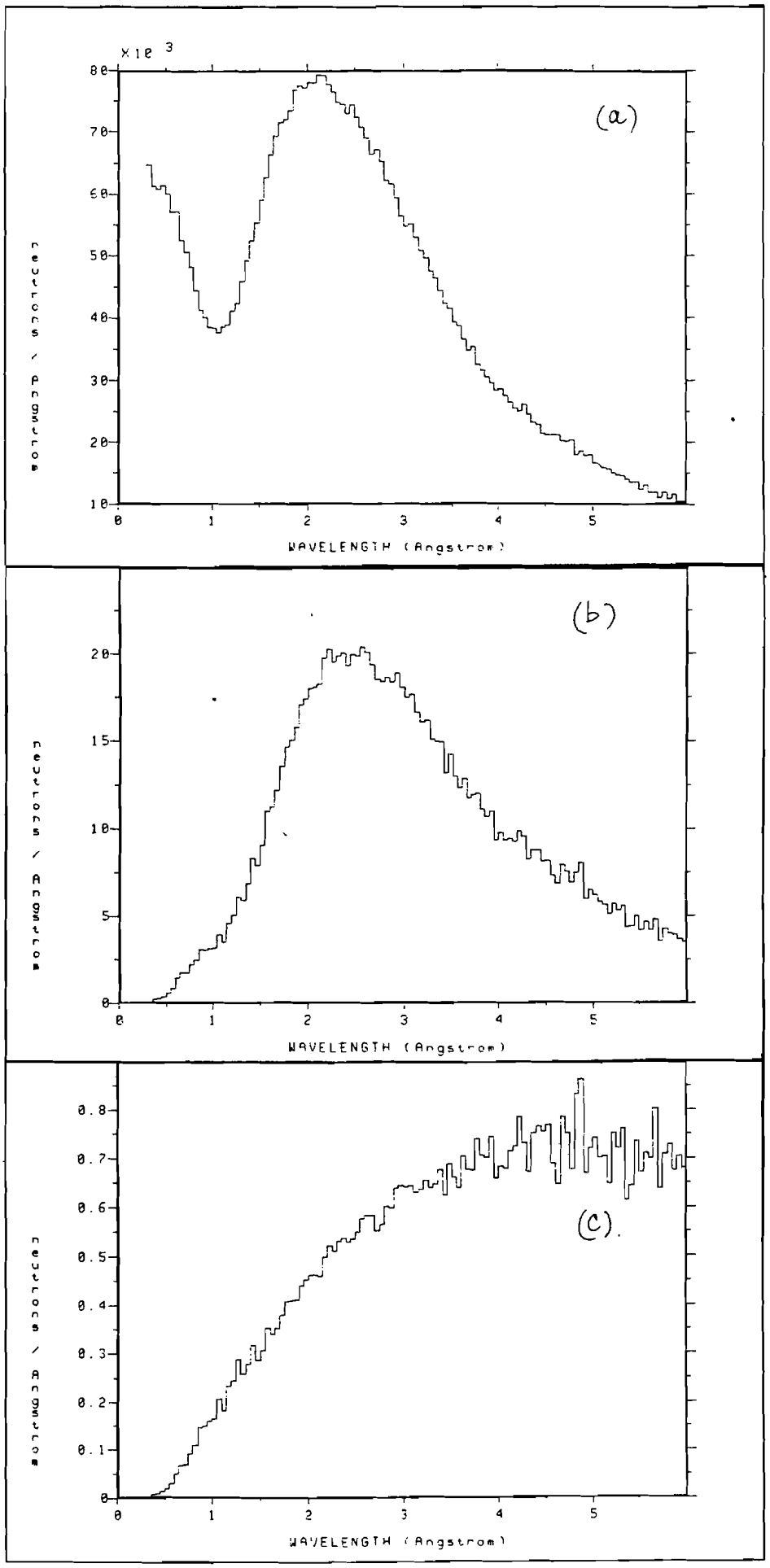

FIGURE 3 HRPD

Proceedings of the Eighth Meeting of the International Collaboration on Advanced Neutron Sources (ICANS-VIII)
8-12 July 1985, Rutherford Appleton Laboratory Report RAL-85-110

AN EXPERIMENTAL STUDY OF THE PERFORMANCE OF CRYSTAL MONOCHROMATORS ON PULSED NEUTRON SOURCES

C J Carlile, R Cywinski, V Wagner*, R C Ward and W G Williams

Neutron Division, Rutherford Appleton Laboratory

* Physikalisch-Technische Bundesanstalt, Braunschweig, Federal Republic of Germany

Abstract

An experimental programme carried out over the past 3-4 years and aimed at assessing the performances of single crystals as monochromators in a pulsed neutron source direct geometry spectrometer is described. As well as discussing the experience gained with a mock-up instrument we present measurements on a) the effect of cooling copper monochromators, b) crystal reflectivities, c) in-plane or horizontal focussing, and d) coherent resonance scattering of eV energy neutrons.

1. Introduction

In previous reports (1,2) we examined the feasibility of using crystal monochromators in a direct geometry inelastic scattering spectrometer on a pulsed neutron source. The principle of a stationary monochromator illuminating a scattering sample which is out of the direct beam offers some advantages over the use of a rotating chopper. These advantages include:

(i) the elimination of the complex electronic and mechanical frequency and phasing units required by a chopper, a problem which is compounded if the neutron source is not absolutely periodic, and

(ii) the possibility that a crystal spectrometer geometry may give lower backgrounds.

Although a cold neutron pulsed source crystal spectrometer has been built at the Tohoku Linac (3), no experimental data exists for an equivalent thermal or epithermal instrument. In this paper we describe the first tests of such a pulsed source spectrometer which were carried out at the Harwell electron linac. Our initial experience led us to make a more detailed examination of other aspects of using crystal monochromators in a direct geometry pulsed source instrument: the deleterious effect of simultaneous reflections; the effect of cooling crystals; the intensity gains in focussing geometries; and the possibility of using resonance scattering to enhance the monochromatic fluxes in the epithermal neutron region. The results of these investigations are also included in this paper.

2. Test Spectrometer

A schematic diagram of the experimental layout at the pulsed neutron source HELIOS at Harwell is shown in Figure 1. It was used to examine a copper monochromating crystal which was placed in a cryostat at 7.6m from the moderator.

The first tests were aimed at characterising the monochromatic beam and for these the copper crystal was oriented such that the diffracted beam from the [420] family of planes could be examined. Measurements in this geometry were carried out at temperatures of 260K, 107K and 15K. The

results are shown in Figure 2. At 260K three orders of reflection can be seen, with neutron energies ranging from 250 meV for the 420 reflection to 2.2 eV for the 12,6,0. Decreasing the temperature results in a marked increase in the integrated intensities of the Bragg peaks as illustrated in Figure 3. At the lower temperatures the 16,8,0 reflection at 4.0 eV is also clearly visible. The relative intensities of all the 420 orders at all temperatures were found to be in qualitative agreement with the theory of Popovici and Gelberg (4). The increase in Bragg intensity towards lower temperatures is mirrored by a decrease of the thermal diffuse scattering (TDS) background between the Bragg peaks. However at low temperatures, the rate of increase of Bragg intensity and decrease of TDS is limited by zero point motion; the rate of change of these quantities between 260K and 107K is greater than that between 107K and 15K. At 107K the contributions to the TDS from zero point motion and classical motion are approximately equal.

It is apparent from our results that a copper monochromator on a pulsed source crystal spectrometer should be cooled to at least 100K: a gain in intensity of 40% in the 420 reflection at 250 meV and 110% in the 840 reflection at 1 eV was observed on reducing the temperature from 260K to 15K with a consequent reduction in the background level between the peaks of ~ 30%. Cooling the crystal thus increases the signal to background by a factor of between 2 and 3.

The test spectrometer was then used to measure the inelastic scattering spectrom from zirconium hydride. This material exhibits a sharp optical vibration at 140 meV which has been used by Harling (5) and subsequently other workers to characterise inelastic scattering spectrometers. A 25% scattering sample of ZrH_2 powder in an aluminium can was placed at the sample position in transmission geometry. At a 30° scattering angle the cross section for single phonon scattering with E_o ~ 250 meV is close to a maximum. The copper monochromator was first aligned to provide the 420 reflection at E_o = 250 meV and maintained at 15K. The data from a 48 hour run is shown in Figure 4. The monochromator was then reset to the 200 reflection. Using the second order 400 reflection at an energy of 200 meV a further 48 hour spectrum from ZrH_2 was collected; this is shown in Figure 5. The data converted to double differential cross sections on an energy scale are shown in the insets to the figures. While the inelastic

mode measured with the lower incident energy is fully resolved, the scattered beam flight path of 1m is too short to resolve fully the equivalent elastic and inelastic features observed in the experiment using the higher incident energy.

The presence of the monochromator in the incident beam increased the background at the sample position by a factor of 4 at higher energies (~ 10 eV) and 2 at lower energies (~ 200 meV). However the background levels at the detector bank remained constant when either the monochromator was misaligned or when the scattering sample was removed. A comparison of the energy dependence of the background at the two positions indicated that, whilst the epithermal component at the sample was reproduced exactly at the detector bank, the Maxwellian component seen at the sample was absent at the detector bank. These observations indicated that the background level at the detector did not arise from the monochromatic beam falling on the sample. Instead it was concluded that the major part of the background at the detector bank could be attributed to the direct scattering (multiple Bragg and incoherent) of epithermal neutrons in the incident beam by the monochromator. Whilst the shielding around the experimental set-up was adequate against thermal neutrons it was relatively weak for epithermal neutrons. In particular the area of the shielding channel around the monochromatic beam was ~ 30 times greater than the sample area. It is evident that in a properly engineered instrument great care is essential in the design of the shielding around the monochromator, the monochromatic beam and the sample position.

3. Crystal Reflectivities

In the experiments described in Section 2 no attempt was made to measure absolute reflectivities and only relative peak intensities were used in evaluating the data. The absolute reflectivities of copper monochromators were determined using reactor measurements at the PTB Braunschweig (6), and the effect on reflectivity of beam losses due to simultaneous reflections was investigated at the Harwell electron linac.

3.1 Reactor Measurements

Integrated reflectivities R_θ from two selected homogeneous copper monochromators in transmission geometry were obtained for the 331

reflection and its higher orders. The measurements were carried out on the S3 neutron diffractometer at the 1 MW research reactor at the PTB Braunschweig using neutron energies up to 1.08 eV. The incident spectrum from the graphite monochromator was determined by time of flight techniques in order to assign the proportion of neutrons in the incident beam belonging to each of the orders reflected from the graphite. The experimentally determined values of the integrated reflectivity R_θ for two crystals of FWHM mosaic spread 1.8' and 4.8' (as determined by γ-ray diffraction) are summarised in Figure 6. Also shown are the calculated values of R_θ from the theory of Popovici and Gelberg (4). The mosaic widths β of these crystals were determined by γ-ray diffractometry and, together with the R_θ values, this allowed the peak reflectivities r_p to be obtained. These are also shown for the two crystals in Figure 6 as a function of neutron energy.

The experimental values of R_θ are lower than the theoretical estimates by up to 50%. Geometrical arguments such as inhomogeneous illumination of the copper crystal or deviations of the mosaic distribution from the ideal situation could account for a certain proportion of this discrepancy. However, it seems that the main reason for the difference between theory and experiment is the loss of neutrons in the reflected beam due to competing Bragg reflections being partially satisfied.

3.2 Pulsed Source Experiments

White beam time of flight investigations into the efficiency of the monochromators were carried out on the Harwell electron linac pulsed neutron source. Again two crystals were selected for the measurements; the crystal of mosaic spread 4.8' previously used at the PTB and a further crystal of mosaic spread 5.7'. Both crystals were aligned on goniometers with their <116> direction along the goniometer axis using the Badger neutron diffractometer on the DIDO reactor at AERE Harwell before transferring to the 3-circle sample table of the Linac High Symmetry Spectrometer.

Measurements were made in transmission geometry of the 331 and higher order reflections from the 4.8' crystal and also of the beam transmitted through the crystal. The transmitted beam spectrum is

shown in Figure 7 and reveals the presence of a series of reflections taking place at different times of flight, t, proportional to d sin θ.

Transmission measurements using the white beam time of flight technique can give precise information on the effect of simultaneous reflections in degrading the efficiency of selection of the required monochromatic beam, provided the instrumental resolution is sufficiently good. In particular by rotating the crystal about the scattering vector, not only can the fluctuation in intensity in the reflected beam be followed, but the transmitted beam gives direct information on the reflections contributing to this degradation. This type of "Renninger Scan" was carried out by Kuich and Rauch (7) in order to maximise the intensities available from the monochromator on a reactor-based spectrometer. Their conclusion was that intensity gains of ~ 25% were obtainable at low incident energies whereas no gain was possible at higher incident energies ($>$ 100 meV). However, the apparent gain in reflected intensity using this technique is highly dependent on the instrumental resolution.

Kuich and Rauch's data in fact indicates that losses through parasitic reflections are equally bad at high energies for all orientations of the crystal about the scattering vector on a poor resolution spectrometer. This is illustrated in Figure 8 where Ewald spheres for high incident energies and low incident energies are shown. It is evident that the higher energy Ewald sphere has a higher probability of intersecting more than one reciprocal lattice point than the lower energy sphere. At high energies it is practically impossible to avoid simultaneous Bragg reflections even with a high resolution instrument since the vertical collimation is generally relaxed to ~ 1° in order to increase the neutron current at the sample.

Transmission measurements on the 5.7' mosaic spread crystal carried out in parallel with reflection measurements indicated experimentally the importance of properly taking the effect into account. The crystal was aligned with its $\langle 100 \rangle$ direction along the scattering vector in transmission geometry and its $\langle 011 \rangle$ direction perpendicular to the scattering plane. Reflections up to the 4th order were observed at a neutron energy of 1.31 eV. In the transmitted beam (Figure 9) the dips in the transmission due to the (2n 0 0)

reflections are evident together with numerous simultaneous reflections at different wavelengths. The 200 reflection is contaminated in the long time wing by a neighbouring reflection with a similar value of d sin θ. Rotating the crystal about the scattering vector in 5° steps, as shown in cruves 2, 3 and 4 of Figure 9 greatly varies the extent to which this reflection is degraded by simultaneous reflections. Figure 6 shows that the experimentally determined R_θ values for the 1.8' mosaic spread crystal are closer to the theoretical values at low incident energies than for the 4.8' mosaic spread crystal where the discrepancy remains significant. This trend is consistent with the hypothesis outlined above.

4. In-plane (Horizontal) Focussing

The use of focussing techniques to increase the fluxes at the scattering sample in continuous source instruments is well-known (8). Both vertical (out-of-plane) and horizontal (in-plane) focussing are in principle possible using multi-component monochromators, and together these can give order of magnitude gains in sample fluxes. We have recently studied the application of focussing for pulsed source spectrometers (9) and have demonstrated the feasibility of horizontal focussing. The method of vertical focussing on a pulsed source, though not demonstrated, is the same as that at a continuous source, since it simply involves a vertical extension of the monochromator array. Horizontal focussing cannot be achieved however by the accepted continuous source techniques because of the correlation between wavelength and time-of-flight on a pulsed source.

The principle of horizontal focussing on a pulsed source is shown in Figure 10. P is the point of intersection of a perpendicular from the focal point (sample position) to the incident neutron beam line. L_1 and ℓ_o are the distances to P from the moderator and focal point, respectively. Time focussing at the sample occurs when the term:

$$d_{hk\ell} \sin\theta_{hk\ell} \left[L_1 + \ell_o \tan\theta_{hk\ell}\right]$$

is arranged to be equal for a set of monochromators M_1, M_2, M_3 ... etc placed after each other. It can be shown that acceptable values of the wavelength spread and angular divergences of the incident beam can be achieved by using reflections from planes with progressively narrower

d-spacings as the distance from the moderator is increased. In practice this is most easily done by using higher order Bragg reflections from one type of crystal monochromator.

The feasibility of the method has been demonstrated using two copper monochromators cut so that they reflected from their [400] and [420] planes respectively. The measurements were performed on a four-circle diffractometer at the Harwell electron linac pulsed source. The important geometric parameters in these tests are listed in Table 1.

L_1	11.17 m
ℓ_o	0.79 m
Moderator - 1st monochromator	11.17 m
Monochromator separation	17.1 cm
θ_B for 1st Monochromator [Cu(400)]	45°
θ_B for 2nd Monochromator [Cu(420)]	51.1°
Angular Spread at Focus	12.2°
Monochromator 1 Wavelength	1.278 Å
Monochromator 2 Wavelength	1.258 Å
Wavelength Spread	0.020 Å

Table 1. Geometric Parameters in Horizontal Focussing Tests.

Figs 11(a) and 11(b) show the diffraction patterns obtained with the first and then the second crystals aligned. Note that the 200 reflection occurs at a longer time than the recorded time frame and does not appear. Only the higher order reflections from this plane are observed. The 420 and its orders are observed in the second pattern. Figure 11(c) shows the pattern obtained with both crystals aligned. The 400 and 420 reflections are coincident in time as are the 800 and 840 reflections. The 600 reflection from the first monochromator stands alone as does the 10,0,0. Figure 11(d) shows the effect of a slight misalignment of the second monochromator where the superimposed diffraction peaks of the previous pattern are now split.

Experimental limitations unfortunately did not allow us to measure the attenuation of the incident beam by the first crystal. We were therefore not able to evaluate the intensity of the beam falling onto the second crystal nor consequently to quantify the overall intensity gain of a focussing monochromator array compared to a single monochromator. However we can estimate this gain by using published single crystal cross-sections (10). Thus at a wavelength of 1.27 Å, as used in these tests, a gain of ~ 1.7 in intensity over a single monochromator could be expected. For a possible five crystal array at a wavelength of 0.74 Å (energy = 150 meV) the overall gain would be a factor of ~ 3.2.

In conclusion we have demonstrated a method for horizontal focussing on a pulsed neutron source using a wavelength of 1.27 Å. The angular spread of the monochromatic beam and its wavelength spread are acceptable for incoherent scattering spectroscopy. At shorter neutron wavelengths more crystals can be assembled in the monochromator array whilst still maintaining acceptable values of the wavelength and angular spreads. For example for a wavelength of 0.74 Å (E_o ~ 150 meV) five sets of copper monochromators reflecting from the [444] planes up to the [731] planes and within a space of 20 cms along the incident beam would reflect a monochromated beam whose wavelength varies only by 0.01 Å and whose angular range is 12°. At longer neutron wavelengths it is possible to produce sets of alloy monochromators (Cu-Ge for example) with a range of lattice parameters which are able to fulfill the conditions described above. Overall gains in the intensity of the monochromated beam from this technique should approach a factor of three over a single monochromator. As this increase can also be achieved with vertical focussing (8) a properly designed two-dimensional monochromator array on a pulsed neutron source would produce intensity gains of an order of magnitude over a single-crystal monochromator.

5. Resonance Scattering in Epithermal Neutron Crystal Monochromators

Brugger (11) was the first to suggest combining the effects of coherent Bragg diffraction with the enhanced scattering lengths which occur at nuclear resonances to produce a crystal monochromator suitable for use at resonance energies in the 1-10 eV range. Tests of this idea have now been carried out on the Harwell linac pulsed source at a neutron energy of 6.67 eV using a single crystal of uranium dioxide (12). Although coherent

resonance scattering was observed in these measurements (Figure 12) it was also evident that the benefit of the enhanced scattering in a practical crystal was lost due to the much higher absorption cross-section at the resonance maximum. The scattering cross-section at the peak of the 6.67 eV resonance in uranium-238 is approximately 1198 barns at^{-1} which is a factor ~ 20 lower than the absorption cross-section. This means, as was pointed out by Brugger, that the effective crystal thickness for diffraction purposes is only ~ 50 μm. In order to produce a viable electron volt energy crystal monochromator using this principle a higher scattering to absorption cross-section is needed. Since this only occurs for nuclear resonances at much higher energies ($\gtrsim$ 100 eV), when the Debye-Waller factor is prohibitively high for coherent reflections, we conclude that it is unlikely that a practical monochromator can be produced for the 1-10 eV region using this technique.

6. Summary

A series of experimental measurements relevant to the design and construction of a direct geometry crystal monochromator spectrometer on a pulsed neutron source has been performed. Data has been collected on crystal reflectivities, a horizontally focussed arrangement of two crystals, and the effect of coherent resonance scattering for eV energy neutrons has been examined. In addition a test crystal spectrometer has been built and used to show the advantage of cooling copper monochromators, as well as to provide first inelastic spectra for downscattering from the epithermal energy region.

The case for building a crystal spectrometer depends critically on the comparison of its performance relative to a chopper spectrometer. In parallel with the experimental programme described several comparisons of the performances of these two types of direct geometry spectrometer have been made (2), and in the latest (13) it is concluded that the chopper spectrometer is superior at all neutron energies higher than about 50 meV. The main reason for the poorer performance of crystals is the difficulty of providing full illumination in a practical geometry, rather than any deficiency due to the factors discussed in this paper. The measurements we have described are however important in optimising the design of a low energy crystal spectrometer, especially the effect of focussing.

References

1. C J Carlile and W G Williams, Rutherford Laboratory Report RL-81-028 (1981).

2. C J Carlile and W G Williams, Rutherford Laboratory Internal Report NDR/P6/83 (1983).

3. N Watanabe, Y Ishikawa and K Tsuzuki, Nucl Instrum and Meth 120 (1974) 293.

4. M Popovici and D Gelberg, Nucl Instrum and Meth 40 (1966) 697.

5. O K Harling, Rev Sci Instrum 37 (1966) 697.

6. C J Carlile, W G Williams and V Wagner, Physikalisch-Technische Bundesanstalt Report PTB-FMRB-104 (1984).

7. G Kuich and H Rauch, Nukleonik 9 (1967) 139.

8. R Scherm and V Wagner, Neutron Inelastic Scattering, IAEA Vienna (1978) 149.

9. C J Carlile and R C Ward, J Appl Cryst 18 (1985) 16.

10. A K Freund, Nucl Instrum and Meth 213 (1983) 495.

11. R M Brugger, unpublished (1983).

12. C J Carlile, R C Ward and B T M Willis, J Appl Cryst, in press.

13. C J Carlile, A D Taylor and W G Williams, Rutherford Appleton Laboratory Report RAL-85-052 (1985).

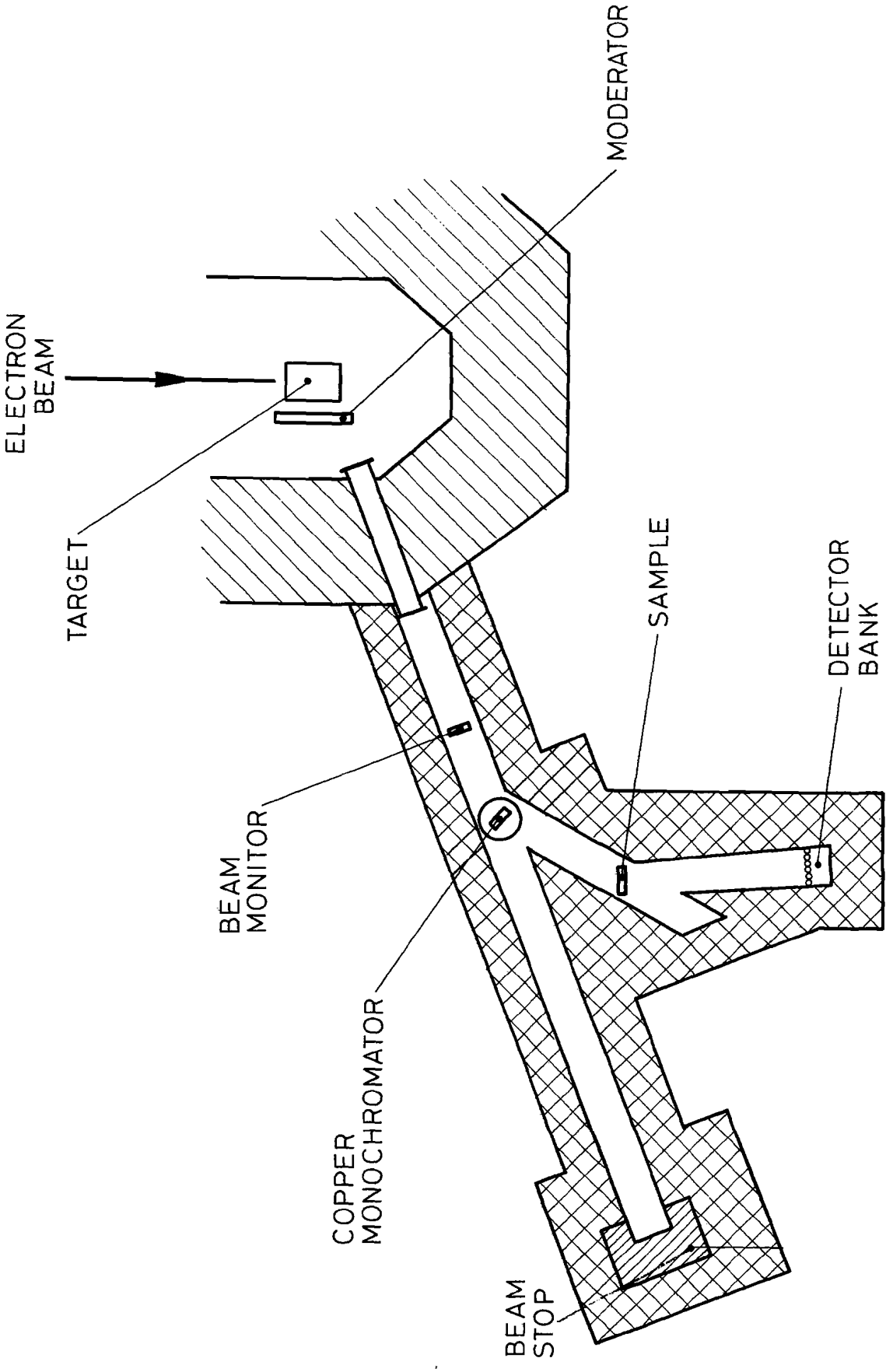

Figure 1. Test crystal spectrometer layout at the Harwell linac pulsed neutron source.

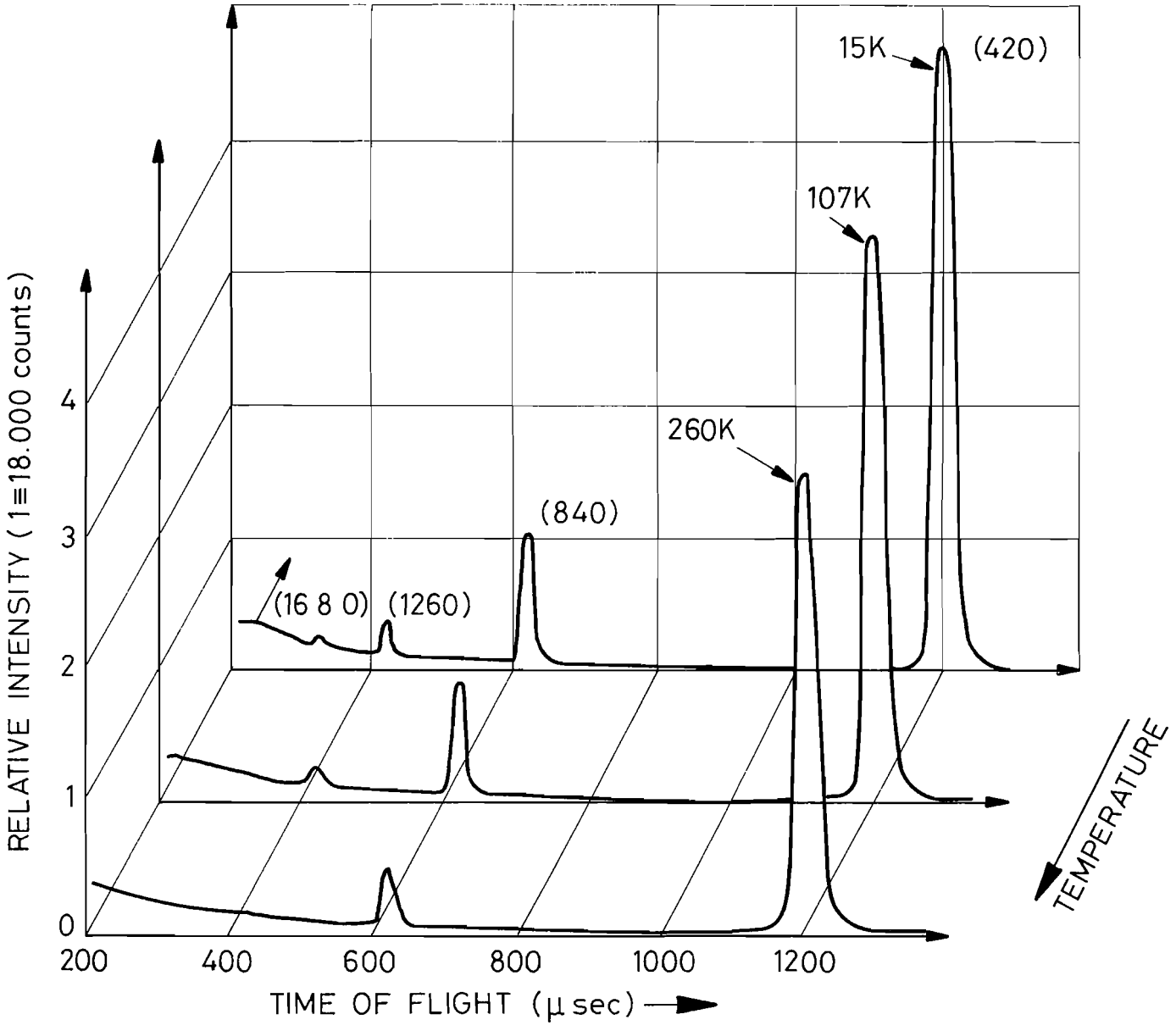

Figure 2. Diffraction peaks from the Cu [420] family of planes at different temperatures.

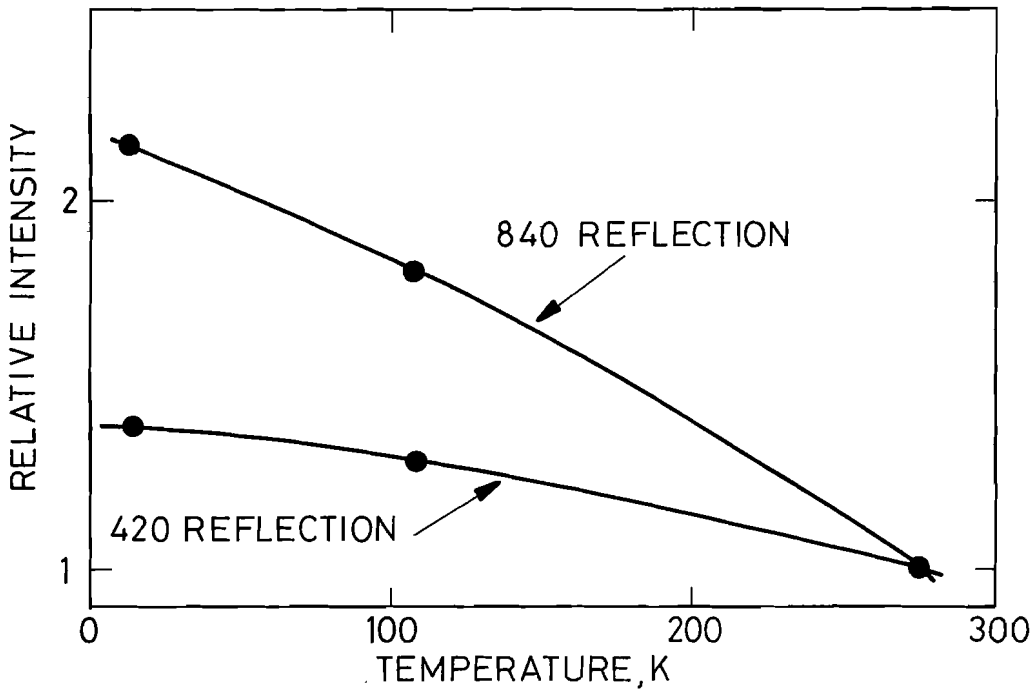

Figure 3. Relative peak intensities of Figure 2 normalised to values at 260K.

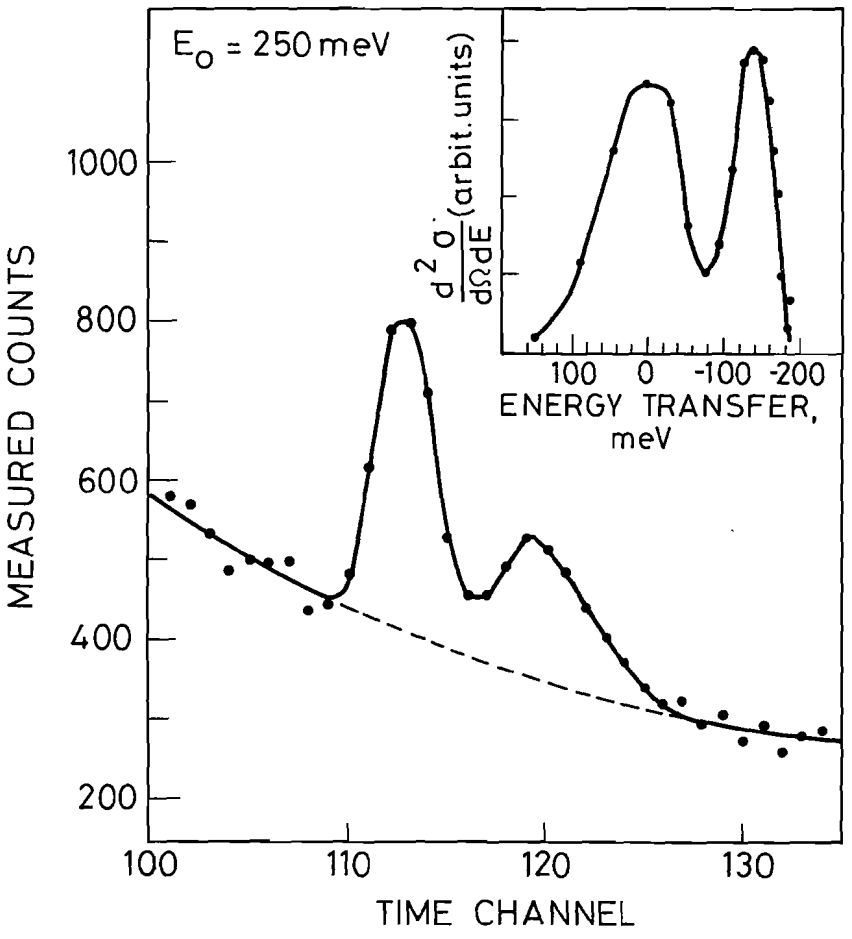

Figure 4. Inelastic spectra from ZrH_2 observed with the test spectrometer with incident energy E_o = 250 meV.

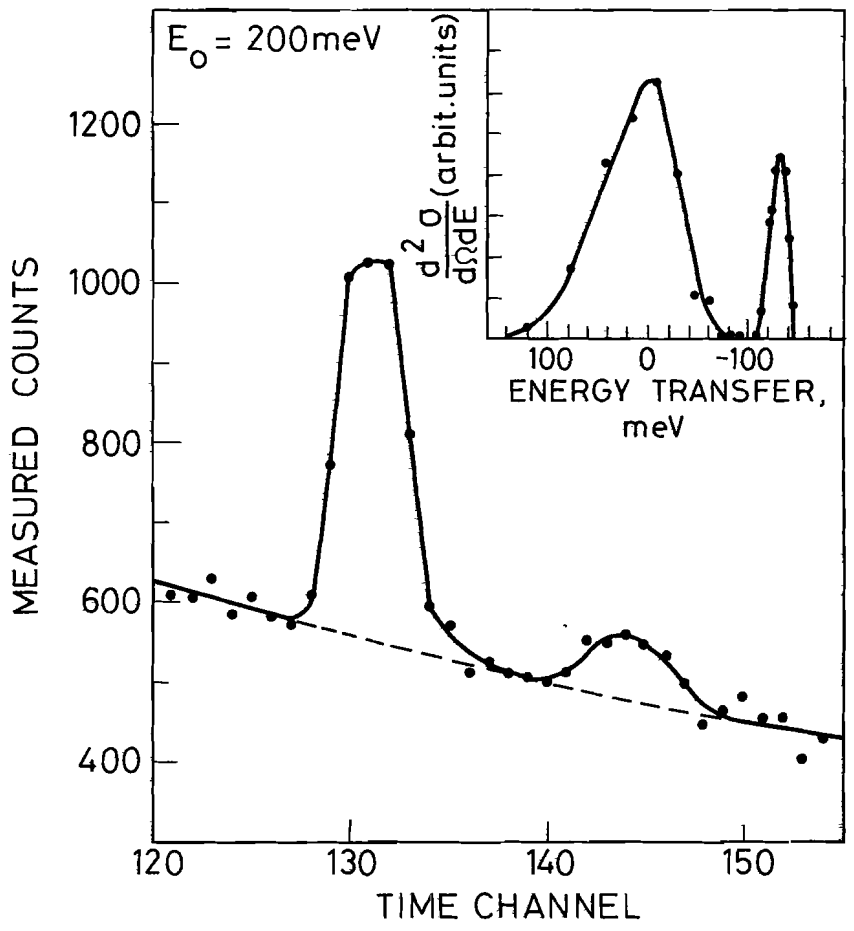

Figure 5. As Figure 4 with incident energy E_o = 200 meV.

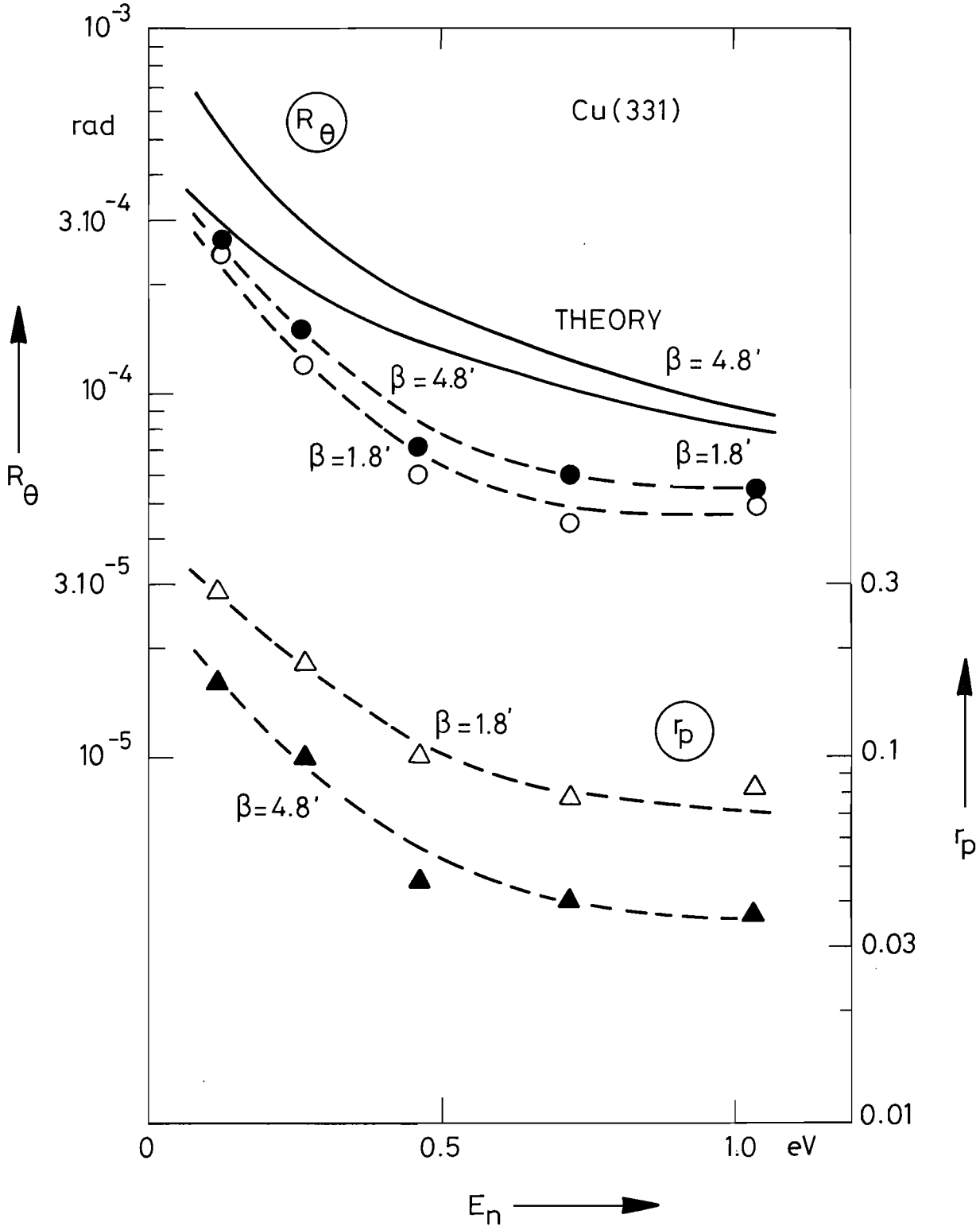

Figure 6. Integral reflectivity R_θ and peak reflectivity r_p as function of neutron energy E_n for two copper crystals. FWHM of the mosaic distributions are β = 4.8' and β 1.8'.

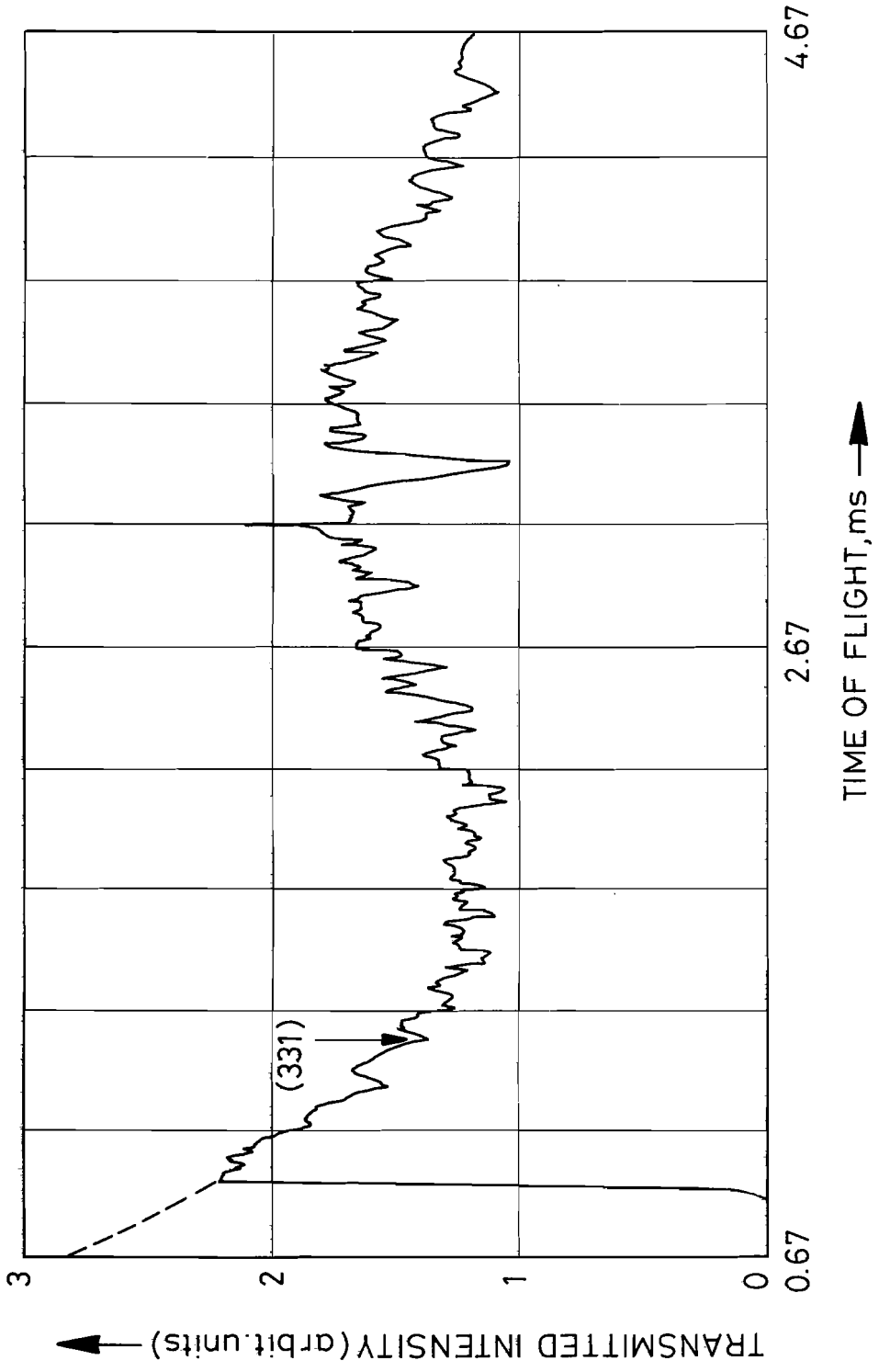

Figure 7. Time-of-flight spectrum of the transmitted beam of a Cu crystal with $\beta = 4.8'$ set for a 331 reflection.

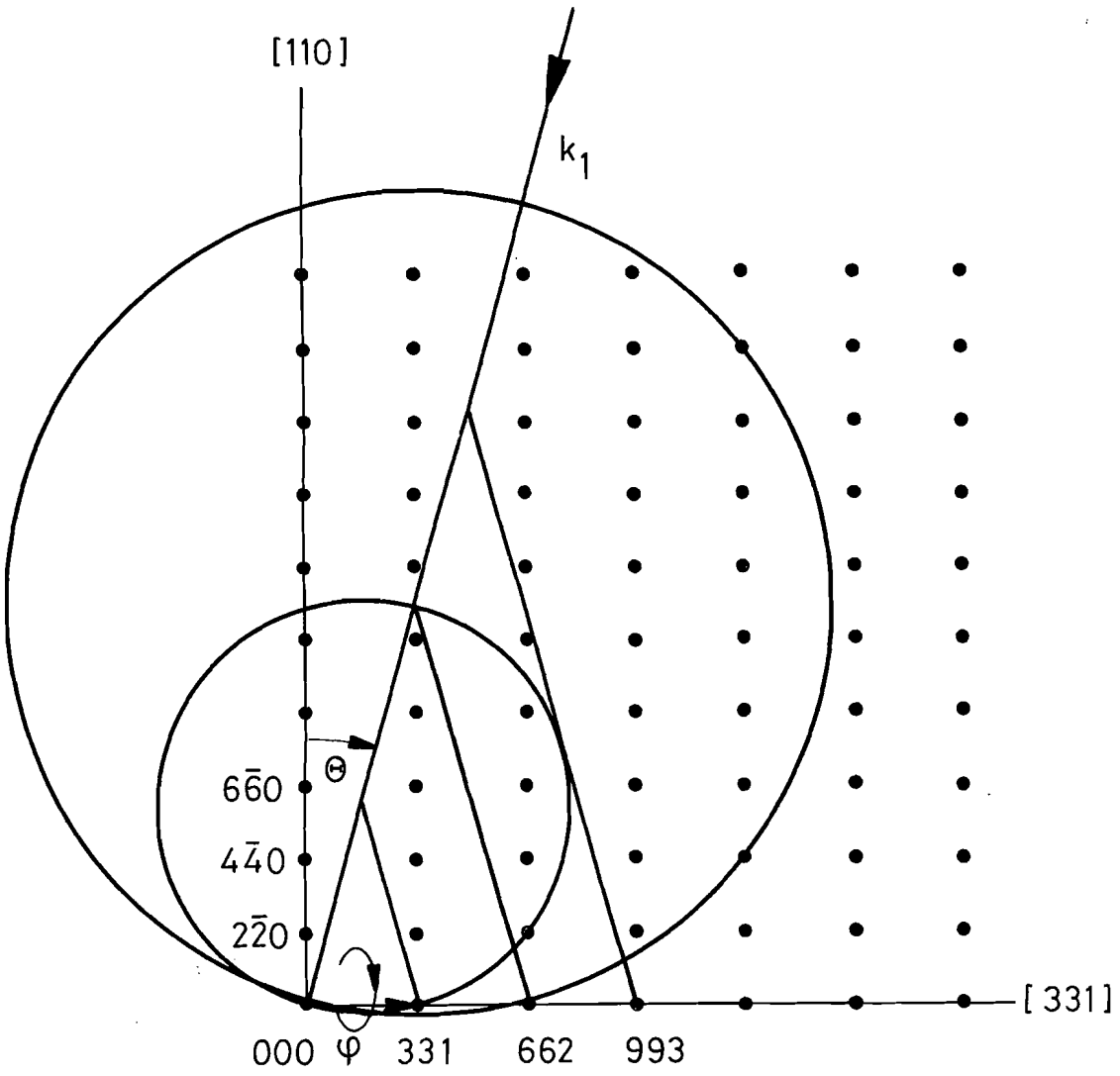

Figure 8. Section of the scattering plane (i.e. the [116] plane) with the reciprocal space showing the Ewald spheres for different incident energies.

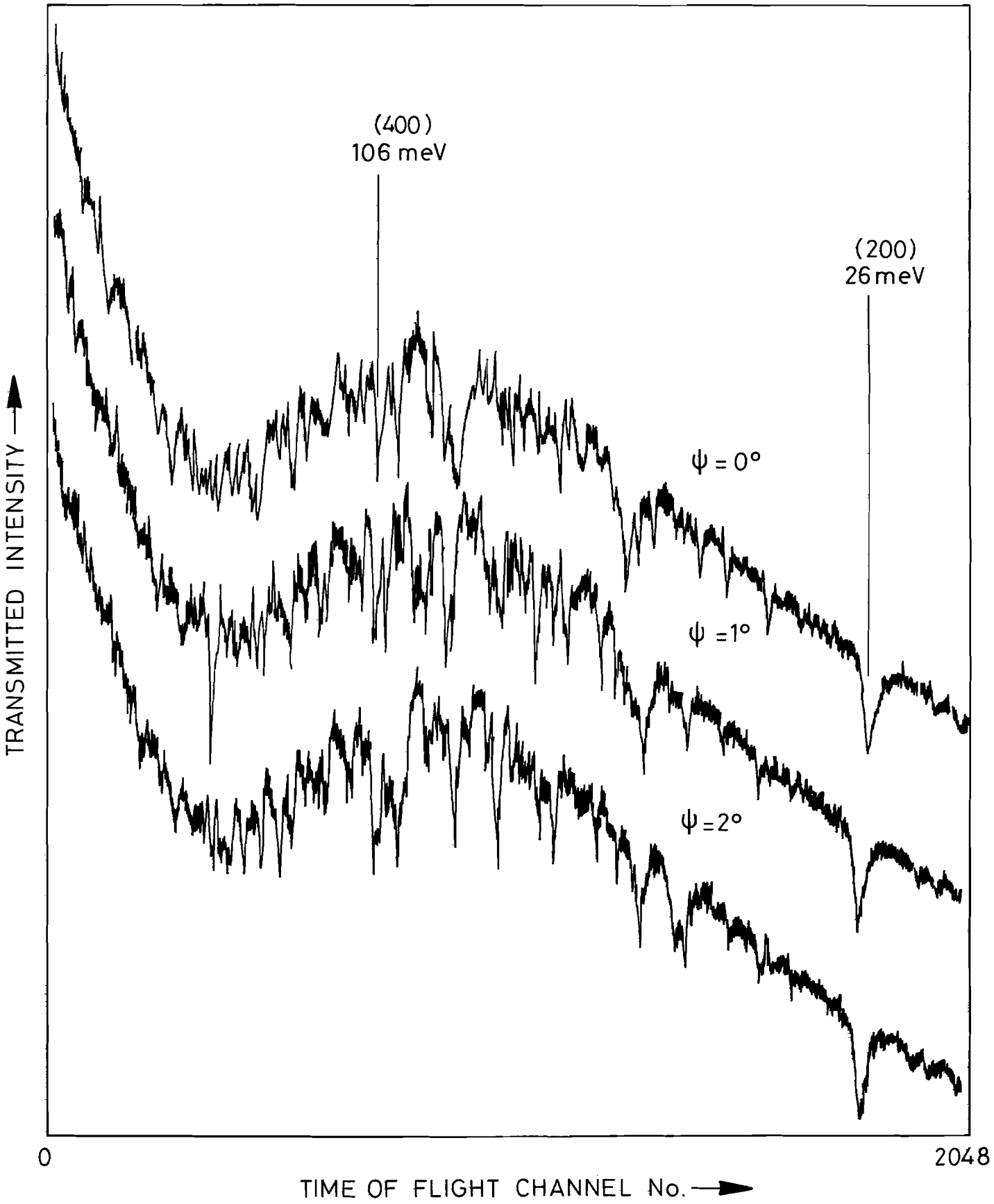

Figure 9. Time-of-flight spectrum of the transmitted beam of a Cu crystal with β = 5.8' set for the 200 reflection. ψ denotes the rotation around the scattering vector. For ψ = 0 the <011> axis of the crystal is vertical.

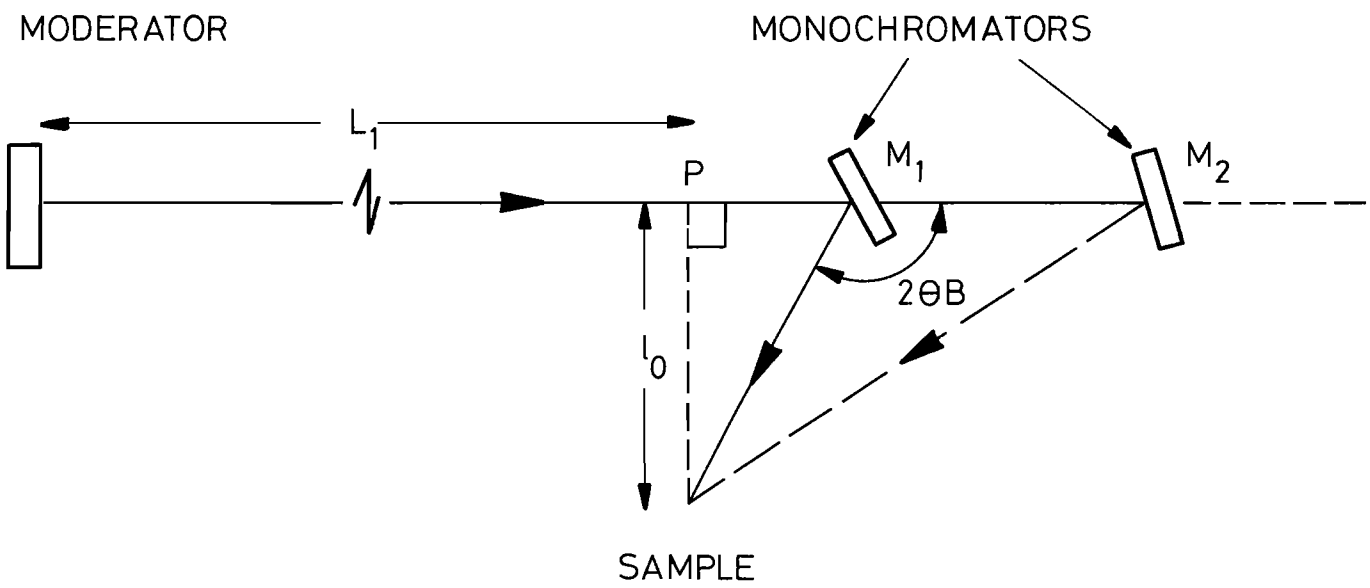

Figure 10. Principle of horizontal focussing using two crystal monochromators on a pulsed neutron source.

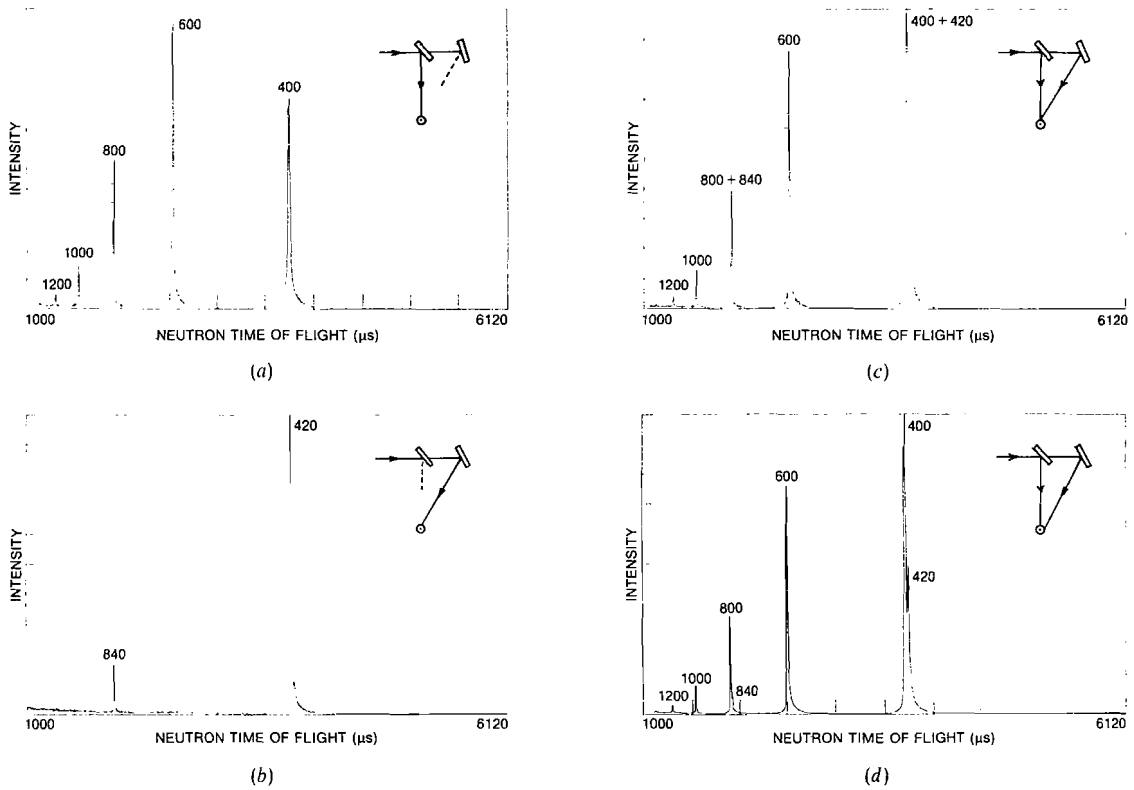

Figure 11. Observed diffraction patterns uncorrected for the incident beam spectrum and detector efficiency. Both crystals were copper, the first aligned with the <200> direction along the scattering vector, the second aligned with the <210> direction along the scattering vector. The hkl values of each reflection are as indicated. (a) The pattern with crystal 1 aligned and crystal 2 misaligned with the 400 and higher orders reflecting. (b) The pattern with crystal 1 misaligned and crystal 2 aligned. The 420 and 840 are visible. (c) The resultant pattern with both crystals aligned. (d) The effect of a slight misalignment of one of the crystals.

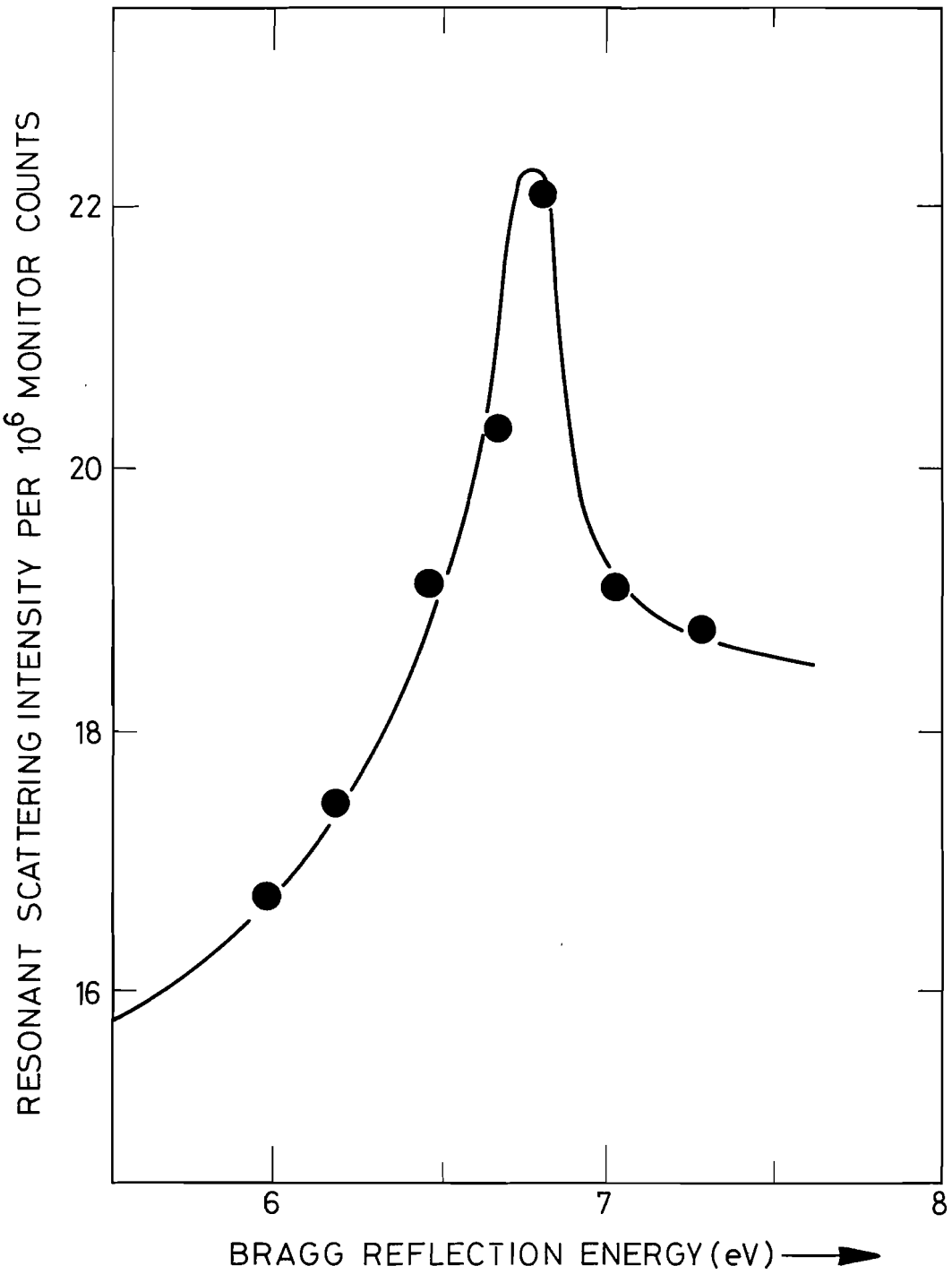

Figure 12. The integrated intensity recorded at the 6.67 eV resonance in uranium as the 18,6,0 Bragg reflection from UO_2 is scanned through the resonance energy. The scattered intensity is normalised to the incident beam intensity and the full line is a guide to the eye.

Proceedings of the Eighth Meeting of the International Collaboration on Advanced Neutron Sources (ICANS-VIII)
8-12 July 1985, Rutherford Appleton Laboratory Report RAL-85-110

DEVELOPMENT WORK FOR A DRABKIN-DEVICE AS A TIME-VARIABLE ANALYZER

G. Badurek[1+)], A. Kollmar[1], W. Schmatz[2]

1) Kernforschungsanlage Jülich, SNQ-Projekt, D-5170 Jülich, FRG

2) Kernforschungszentrum Karlsruhe, Institut für Angewandte Kernphysik, D-7500 Karlsruhe, FRG

Abstract

At a pulsed neutron source a new type of inverted geometry time-of-flight spectrometer can be realized by means of a so called Drabkin resonator which is placed between a pair of polarizing supermirros and thereby acts as an electronically tunable neutron energy analyser. Utilizing a broad incident spectrum scans of constant energy transfer can then readily be performed by proper variation of the resonator transmission function with time according to the different arrival times of neutrons of different energy.

[+)] On leave from Institut für Kernphysik, Technische Universität Wien, A-1020 Wien, Austria

1. Introduction

In polarized neutron scattering experiments one often appreciates the fact that the performance of most spinflip devices used to change the neutron polarization direction with respect to an applied magnetic field depends only weakly, if at all, on neutron energy or wavelength. Spatial spin resonance, first both predicted theoretically and confirmed experimentally by Drabkin and coworkers /1-4/, on the other hand allows to realize a neutron spinflip device with a remarkably pronounced wavelength dependence. When combined with a pair of neutron polarizers such Drabkin spin resonators therefore can serve as neutron monochromators or wavelength analyzers, respectively, whose spectral transmission characteristic can be varied easily by varying the strength of static magnetic fields, i.e. by purely electronic means. It is just this almost instantaneous tunability which makes them suited to conceive a new type of inverted-geometry neutron time-of-flight spectrometer with promising features as proposed recently by Badurek and Schmatz /5/. After a brief explanation of the most essential principles of the spatial neutron spin resonance method we will present in what follows our first conceptual considerations we have begun with in order to build a prototype of such an inverted geometry neutron spectrometer.

2. Principles of spatial spin resonance

As shown schematically in Fig. 1 a Drabkin neutron spin resonator consists of a zig-zag folded conducting foil which generates a static magnetic field $\vec{B}_1$ of periodically alternating direction orthogonal to that of an additonal homogenous field $\vec{B}_0$. This resonator system acts much in the same way as a conventional radio-frequency neutron spinflipper, but with the essential difference that each neutron in its own coordinate frame of reference

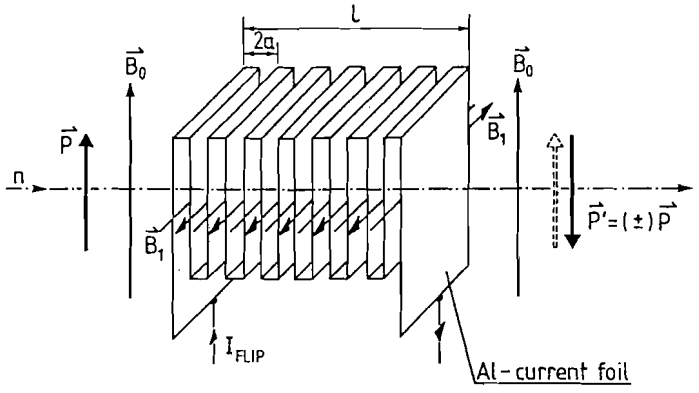

Fig. 1: Schematic arrangement of a magnetic neutron spin resonator.

creates its individual frequency of the tranversal field $\vec{B}_1$

$$\omega = \pi v/a \tag{1}$$

according to its velocity v. There the quantity a is half the period of the spatial oscillations of the conductor foil. The spinflip probability of such a magnetic resonator in close analogy to that of spinflip devices is found as

$$W(v) = \frac{\Gamma^2}{(\frac{\delta v}{v_o})^2 + \Gamma^2} \sin^2 \{\frac{\pi l}{2a} \frac{v_o}{v} \sqrt{(\frac{\delta v}{v_o})^2 + \Gamma^2}\} \tag{2}$$

where l is the active length of the resonator, $\Gamma = 2B_1/\pi B_o$ and

$$v_o = |\gamma| a B_o/\pi \tag{3}$$

is that neutron velocity which equals the Larmor frequency $\omega_o = |\gamma| B_o$ (with $\gamma = -1.83 \times 10^8$ rad/sT). This flipping probability is shown in Fig. 2 as a function of the neutron velocity. Its full-width at half maximum is given as

$$\frac{\delta v_{1/2}}{v_o} \simeq 1.59 \frac{a}{l} = \frac{0.8}{N} \tag{4}$$

that means it decreases with increasing number N of resonator oscillations. In defining the quantity Γ of Eq. (2) it is taken into account that only half of the amplitude of the oscillating field $\vec{B}_1$, which can be considered as a linear superposition of two fields rotating in opposite directions, effectively contributes to the resonant flipping process. It is furthermore included that according to the Fourier expansion of the "square-wave" resonator field oscillations the first harmonic enters with an relative amplitude $4/\pi$ whereas the influence of higher harmonics has been neglected. Complete flipping takes place at $v = v_o$ if the condition

$$\frac{l}{a} \Gamma = 2k + 1 \qquad (k = 0,1,2....) \tag{5}$$

is fulfilled. The occurrence of additional sideband maxima in the spinflip

probability vs velocity curve is highly unfavourable, however, for an actual application of the spin resonator as as a neutron monochromator. Two possibilities have been proposed to reduce these unwanted sidebands significantly to a level that can be tolerated.

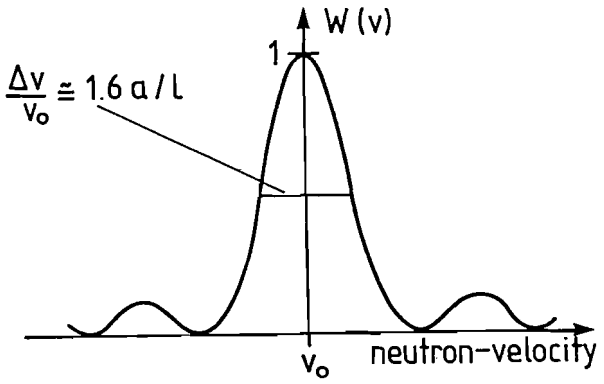

Fig. 2: Velocity dependence of the resonator spinflip probability.

The first method /6/ is based on the use of two successive polarizer-resonator-analyser cascades whose resonators have the same period but different number of oscillations. If the length of the two resonators are matched so that $l/l' = 1.56$, the side maxima of the first cascade happen to coincide with the corresponding minima of the second cascade and hence mutually cancel. Simultaneously the wavelength resolution is improved to

$$\frac{\Delta\lambda}{\lambda} = \frac{\delta v_{1/2}}{v} = 1.37\,\frac{a}{l} \qquad (6)$$

The signal-to-background ratio is significantly increased too as compared with a single cascade because of the doubled number of polarizing mirror reflections, although the latter is inevitably associated with a decrease of totally transmitted intensity.

The other, conceptually more elegant, method of sideband supression uses an amplitude modulated transverse field $\vec{B}_1$ which can be simply achieved by means of a smooth variation of the lateral width of the resonator foil /7/. The functional principle of this method can best be understood if one takes into account that the final reason for the occurencce of sidebands

is the finite duration of the "rf-pulse" the neutrons "see" on their passage through the resonator. This cut-off effect gives rise to sideband components in the frequency spectrum of the rf-pulse which in turn cause spinflip processes of others than the principal frequency ω_0. As usual in ordinary high- frequency technics the parasitic frequencies are eleminated by proper amplitude modulation of the pulse. Whereas the case of an idealized Drabkin resonator with exponential and Gaussian field amplitude modulation has been treated analytically in ref. /7/ we develop at present a numerical simulation programm that can be used to optimize such a resonator under completely realistic conditions as field inhomogenities, finite beam divergency etc. for arbitrary type of modulation /8/.

3. Inverted geometry TOF spectrometer

In a conventional inverted geometry TOF spectrometer only those of the scattered neutrons are allowed to reach the detector whose energy has a preselected fixed value within a given resolution interval. Thus only a small fraction of the incident polychromatic neutron spectrum is actually used if one wants to single out neutrons which have undergone a specific energy transfer upon scattering.

The neutron economy can be much improved, however, if the energy window of the analyser is continuously readjusted according to the different times of arrival at the analyser of neutrons of different inital energy /5/. With an ordinary crystal analyzer this is not possible in practice since it would require a prompt variation of the whole scattering geometry within several milliseconds. With the Drabkin resonator, on the other hand, which can be tuned without any mechanical manipulations simply by changing the currents of the magnet coils and the wiggler such a timevariable energy analyzer can actually be realized. The transmission window of this analyzer can consequently be adjusted properly at any moment so that all scattered neutrons with a certain energy transfer have a chance to reach the detector irrespective of their initial energy before scattering. In order to prove the practical feasibility of this method we are presently installing the experimental arrangement shown schematically in Fig. 3 at one of the new neutron guides of the DIDO reactor at the KFA Jülich.

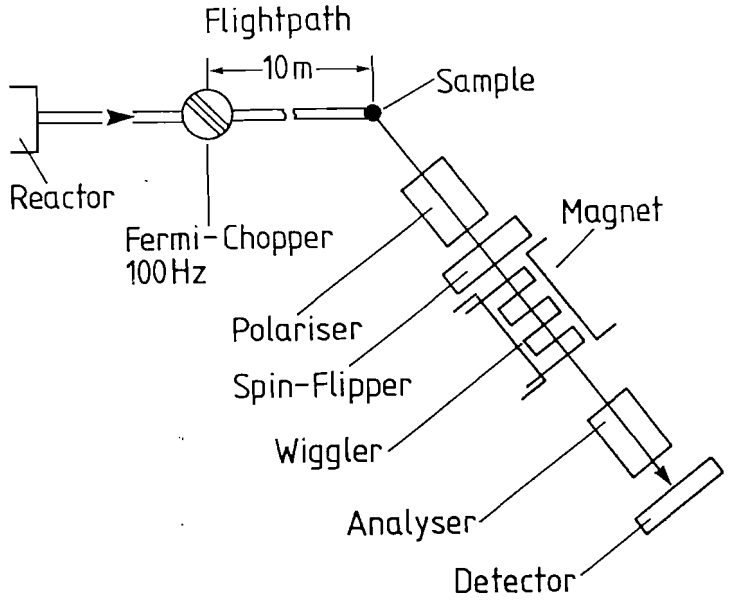

Fig. 3: Sketch of the experimental arrangement.

Since the spectrometer is placed at a continuous neutron source a mechanical chopper is necessary in order to simulate a pulsed source (which would be, of course, the much better choice for such a TOF instrument). The incident flight path from the "source" to the sample is about 10 m. To allow for as much flexibility as possible all components which have to be inserted into the scattered beam path are mounted on an optical bench (total length 2.5 m) that can be rotated around the sample axis. A pair of tranversally magnetized supermirror guides /9/ is used as spin polariser and analyser, respectively. Each consists of 60 curved Co-Ti supermirrors /10/ of 30 cm length stacked together with glass distance holders of 1 mm thickness, resulting in a beam cross-section of 30 x 60 mm^2. The shortest usable neutron wavelength is approximately 2.5 Å.

A current-sheet spinflipper /11/ is used to achieve a wavelength-independent polarization inversion of the beam by means of sudden field reversal as indicated in Fig. 4. In our arrangement the magnetic field produced by the current-sheet is oriented perpendicular to the guide field, which is only of the order of 0.1 mT at the position where the current-sheet is placed. This arrangement has the advantage that the fields of the polarizer and the analyzer need not to be oriented into opposite directions as was the case with the original current-sheet spinflipper and hence avoids beam depolarization problems in the flipper-"off" state. Our current sheet is made of 0.4 mm thick enamelled copper wires mounted on an aluminium frame in an

arrangement shown in Fig. 5. The wires an parallel across an area of 17 x 17 cm^2, the maximum current per unit length is about 10 A/mm.

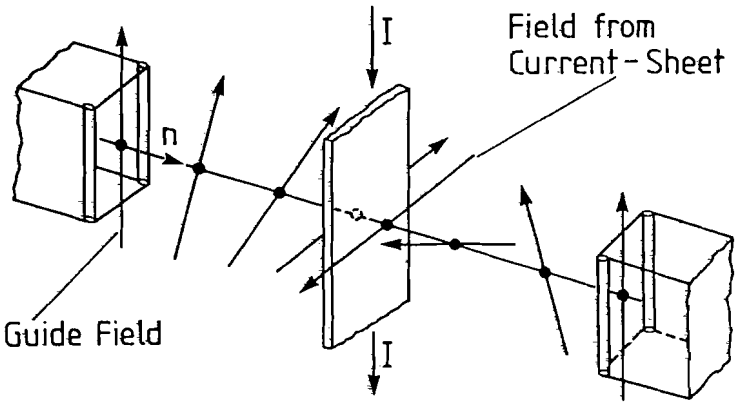

Fig. 4: Sudden field reversal arrangement with a current sheet neutron spinflipper for wavelength-independent polarization inversion.

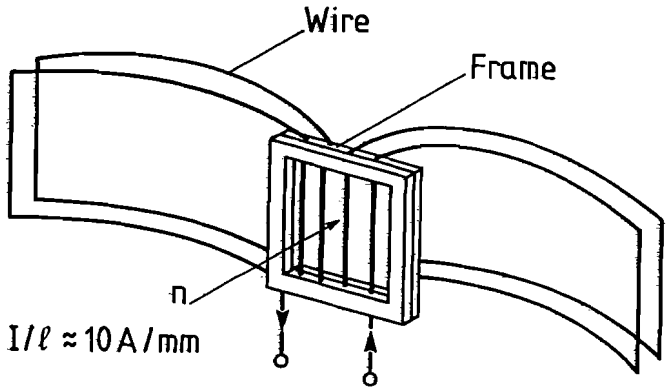

Fig. 5: Schematic sketch of the technical realization of the current sheet spinflipper.

The homogeneous magnetic field $\vec{B}_0$ of the resonator system is produced by means of an electromagnet shown in Fig. 6. To minimize eddy-current losses the magnet yoke is assembled of many thin iron sheets analogous to the core of electric AC-power transformers. Each of the two magnetizing coils has

30 turns. At the maximum current of 15 A a field of about 20 mT (200 G) is produced within the airgap (height 55 mm) of the magnet. The field homogeneity $\Delta B_0/B_0$ is approximately 1 %.

The spatially alternating field $\vec{B}_1$ is produced by means of a 0.1 mm thick zigzag-folded aluminium foil. Plastic frames of 2 mm thickness and 50 mm height are used to fix the 55 oscillations of this magnetic wiggler. Its total length is l = 231 mm at a period 2a = 4.2 mm.

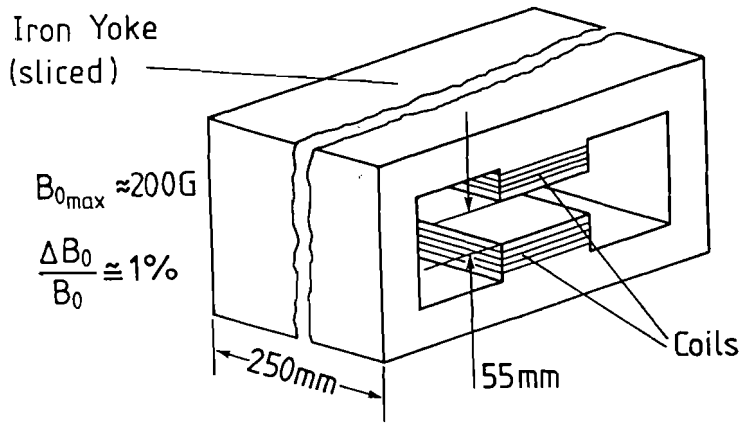

Fig. 6: The electromagnet producing the homogeneous field $\vec{B}_0$.

The foil width w (which is chosen to be constant in our first prototype arrangement) is 75 mm. The beam window of the plastic frames has the dimensions 55 x 30 mm^2. Calculations of $\vec{B}_1$ according to Biot-Savart's law of electrodynamics yields the relation

$$B_1 \simeq \frac{\mu_0}{2} \frac{I_1}{w} \qquad (7)$$

between the amplitude of the field and the foil current I_1. $\mu_0 = 4\pi \times 10^{-7}$ Vs/Am is the vacuum permeability. From Eq. (5) then follows the current which is necessary for complete polarization reversal

$$I_1^{flip} = (2k + 1) \frac{\pi^2 w v_0}{\mu_0 |\gamma| l} \qquad k = 0,1,2.... \qquad (8)$$

At $\lambda = 2.5$ Å ($v_0 = 1580$ m/s) first order (k = 0) spinflip requires hence in our case a current $I_1 = 22$ A, corresponding to a field $B_1 = 0.18$ mT (1.8G). By means of several clamping connections at every 5^{th} period the active length of our resonator and hence its wavelength resolution can be varied between the limits

$$1.4 \times 10^{-2} \leq \frac{\Delta\lambda}{\lambda} \leq 5.5 \times 10^{-2} \qquad (9)$$

if one takes into account the associated change of the flip current according to Eq. (8). However, not all of this resolution range is accessible in the dynamic mode of operation of the resonator with our spectrometer geometry, as will be pointed out later (see Eqs. 12 and 13).

In an inverted geomtry TOF spectrometer the energy transfer of the neutrons upon scattering of the sample is found from the relation

$$\Delta E = \frac{m}{2}\left\{\frac{L_I^2}{(t - L_F/v_0)^2} - v_0^2\right\} \qquad (10)$$

where m is the neutron mass, t the total neutron time-of-flight, v_0 the velocity which is transmitted by the analyzer and where L_I and L_F denote the distances from the source to the sample and from the sample to the detector, respectively. If the resonance analyzer is placed immediately behind the sample and if its active length is negligible as compared to the other flight path distances, a scan at constant energy transfer ΔE can be performed by varying the field $\vec{B}_0$ of the resonator with time according to /5/

$$B_0(t_I) = \frac{\pi L_I}{|\gamma| a t_I}\left\{1 - \frac{2\Delta E}{m}\left(\frac{t_I}{L_I}\right)^2\right\}^{1/2} \qquad (11)$$

where $L_I/v_{max} < t_I < L_I/v_{min}$ is the neutron time-of-flight along the primary path L_I. The velocity limits v_{min} and v_{max} belong the longest and shortest wavelengths in the incident neutron spectrum. An analogous time-dependence is required for the amplitude of the oscillating field. Fig. 7 shows schematically how the fields are varied during the measurement. At each source pulse (repetition frequency 100 Hz) the fields start with a maximum value

and then decrease gradually with time according to Eq. (11), which in case of elastic scattering ($\Delta E = 0$) yields a simple 1/t-dependence. At the end of each pulse cycle both fields are raised again to their initial value. As indicated too in Fig. 7

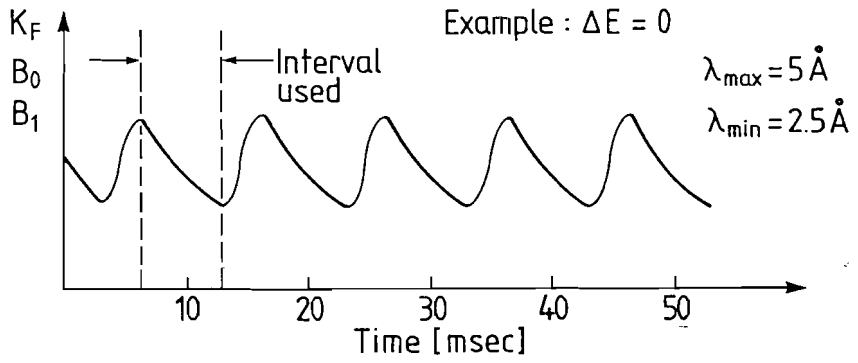

Fig. 7: Time-dependence of the fields $\vec{B}_0$ and $\vec{B}_1$ of the magnetic resonator for elastic scattering. Both fields decrease inversely with time synchronously with the repeated source pulses.

the wavenumber $k_f(t)$ of the scattered neutrons which are transmitted by this resonant analyzer consequently varies too, so that a certain energy transfer $\Delta E \propto k_I^2(t) - k_f^2(t)$ is measured with many pairs k_I-k_F simultaneously.

For a proper operation of such a spectrometer on has to take care, however, that the fields vary slowly enough with time to consider them as being constant and the resonance condition $v = v_0$ being fulfilled during the neutron transmission time interval $\Delta t = l/v$ through the resonator. This condition requires the fulfilment ot the relation

$$\left|\frac{dv_0}{dt}\right| \Delta t < \frac{\delta v_{1/2}}{2} \qquad (12)$$

which is turn leads to

$$\frac{\Delta t}{t} \cdot \frac{l}{a} = \frac{l^2}{L\,a} < 0.8 \qquad (13)$$

where L is the distance from the chopper to the resonator and t the corresponding neutron time-of-flight for that distance. In our case with $L \simeq 10$ m this means that the usable active length of our resonator is restricted to $l < 130$ mm or a wavelength resolution $\Delta\lambda/\lambda > 2.6 \times 10^{-2}$. Making use of its full resolution capability in the dynamic application would require an increase of the distance L to about 32 m.

References

/1/ G.M. Drabkin, Sov. Phys. JETP 16 (1963) 281

/2/ G.M. Drabkin, V.A. Trunov and V.V. Runov, ibid 27 (1968) 194

/3/ G.M. Drabkin, V.A. Ruban and V. I. Sbitnev, Sov. Phys. Techn. Phys. 17 (1972) 855

/4/ M.M. Agamalian, G.M. Drabkin and V.T. Lebedev, Sov. Phys. JETP 46 (1977) 200

/5/ G. Badurek and W. Schmatz, Proc. Int. Conf. "Neutron Scattering in the Nineties", Jülich 1985 (IAEA-CN46/85 Vienna 1985) p. 77

/6/ M.M. Agamalian, J. Schweitzer, Ya.M. Otchik and V.P. Khavronin, Nucl. Instr. Meth. 158 (1979) 395

/7/ M.M. Agamalian and V.V. Deriglazov, Sov. Phys. JETP 56 (1982) 166

/8/ G. Badurek, W. Neuhaus and A. Kollmar, to be published in Nucl. Instr. Meth.

/9/ O. Schärpf, in Neutron Scattering 1981 (J. Faber, Ed.), Proc. AIP Conf. No. 89 (Argonne Nat. Lab.), Am. Inst. Phys. (1982) 182

/10/ F. Mezei and P. Dagleish, Comm. Phys. 1 (1976) 81 and 2 (1977) 41

/11/ A. Abrahams, O. Steinsvoll, P.J.M. Bongarts and P.W. de Lange, Rev. Sci. Instr. 33 (1962) 524.

Proceedings of the Eighth Meeting of the International Collaboration on Advanced Neutron Sources (ICANS-VIII)
8-12 July 1985, Rutherford Appleton Laboratory Report RAL-85-110

NEUTRON MEASUREMENTS ON POLARISING FILTERS AT THE HARWELL LINAC

J Mayers, R Cywinski, T J L Jones and W G Williams
Neutron Division, Rutherford Appleton Laboratory

Abstract

Test measurements on resonance absorption neutron polarising filters containing Sm^{149} are presented. The temperature dependence of the transmittance was measured as a function of neutron energy using the time of flight method on the Harwell linac pulsed source. The results allowed the polarising efficiencies of a $SmCo_5$ filter to be determined at temperatures between 0.012K and 0.045K. Preliminary data was also obtained for a filter consisting of a 1% solution of samarium in palladium and gave encouraging results. Some of the practical problems encountered during the measurements are described and implications for future operations on the RAL Spallation Neutron Source discussed. Full details of this work have been reported in RAL-84-118.

Proceedings of the Eighth Meeting of the International Collaboration on Advanced Neutron Sources (ICANS-VIII)
8-12 July 1985, Rutherford Appleton Laboratory Report RAL-85-110

SAMPLE ENVIRONMENT EQUIPMENT FOR THE SNS

I Bailey, J R J Bennett and J Tomkinson

Rutherford Appleton Laboratory
Chilton, Didcot
Oxon OX11 0QX

GENERAL DESIGN PHILOSOPHY - STANDARDIZATION

It is intended to operate the neutron scattering instruments with the minimum of support personnel. Hence the sample environment equipment must be designed with the following requirements:

1. Reliability

Equipment is being designed to be fundamentally as simple as possible to aid reliability and minimise maintenance.

2. Interchangeability and standardisation

All instruments have been provided with a standard services panel to provide both single and three phase mains voltage, 50 Hz, socket outlets; cooling water flow and return with flow meter and trip level; bottled gas (Helium and Nitrogen) outlets; compressed air at 5 Bar; Helium recovery lines; and Helium lines from the compressors for the closed cycle refrigerators.

In addition there are standard sockets to the computer control interfaces in instrument cabins.

A single standard electronic control unit is available to measure and control temperatures in the range 1K to 2000K through the computer terminals in the instrument cabins.

The ILL design of "maxi orange cryostat" has been adopted as the SNS standard for almost all instruments. Closed cycle refrigerators will be used wherever possible down to temperatures of approximately 20K.

Instruments are equipped with a standard flange configuration of 400 mm diameter for entry of sample environment equipment. The distance of this flange from the neutron beam has also been unified at 300 mm to aid interchangeability of sample environment equipment.

3. Remote operation and automated sample changing

These are longer term aims but sample changers with remote control have already been developed for both ambient and low temperature sample environments.

SAMPLE ENVIRONMENT EQUIPMENT

A limited range of equipment has been designed and manufactured for use on the instruments: this is briefly listed below. Not included in the list is a range of sample cans and holders, which are intended to be provided as a central facility to users.

More sophisticated equipment is also being considered; a goniometer is being manufactured, a furnace for 3 samples at temperatures up to 1500K or 2000K is in design and magnets producing several Tesla have been requested. Table 1 summarises the equipment provided and its scheduled availability. Figure 1 shows a view of the carousel type sample changer; a version of this is to be used down to 90K.

Temperature

(a) Orange cryostat

These liquid helium cryostats, of ILL design, are suited to measurements from 1.7K to 80K. On the SNS, most will accept samples 100 mm diameter, 100 mm in length. They are provided with Rh/Fe resistance thermometers.

(b) Sorption cryostat

An Oxford Instruments sorption-pumped ^{3}He cryostat is available, with a base temperature 0.3K. The nominal sample size is 15 mm diameter and 50 mm length.

(c) Cryofridge cryostats

Seven Leybold-Heraeus closed cycle refrigerators (CCRs) are available, suitable for sample temperatures 20 - 300K. Three CCRs have been incorporated into cryostats for use on LAD, HET and TFXA. Another CCR is in a cryostat suitable for all standard instruments. All are provided with Rh/Fe resistance thermometers.

(d) Dilution refrigerator

A dilution refrigerator based on the design of Neumaier will give 25mK.

(e) Ambient temperature

A circulating water/glycol bath suitable for use from -40°C to 80°C is available. It is fitted with Pt thermometers, on a sample changer for the LOQ spectrometer.

(f) Furnaces

Suitable for temperatures ~ 100°C to 1400°C. Design to be fixed.

Sample changers

(a) Sample changer for LOQ spectrometer

An ambient temperature sample changer is being constructed in collaboration with Liverpool Polytechnic, primarily designed for use on LOQ in conjunction with the ambient temperature bath. The translation table of the device will have 60 cm movement across the neutron beam enabling up to 15 samples to be mounted. Both temperature control and sample translations will be controlled via the Falcon/CAMAC crate controller.

(b) Sample changer for LAD

A ten position sample changer, of a carousel design, is available. It is suitable for ambient temperature samples nominally 20 mm diameter and 50 mm long.

(c) Other instruments

A carousel design, capable of accommodating 10 samples, has been successfully tested; a cryogenic version is being developed.

Pressure

(a) 2 kbar unit

This is a single-stage unit utilising light oil as the pressurising medium, capable of 2 kbar. The system is only suitable for ambient temperature use.

(b) 5 kbar unit

This is a two-stage compressed helium system operating up to 5 kbar; a specially adapted cryostat operating down to 4.2K is available.

(c) Static loaded cell

This is a statically-loaded and locked cell utilising opposed pistons. Pressures up to 30 kbar can be generated; the cell is designed for use with a 100 mm bore helium cryostat.

Table 1

SAMPLE ENVIRONMENT EQUIPMENT

The following sample environment equipment will be available for scheduled use; all of this equipment is suitable for instruments which accept standard apparatus, unless otherwise stated.

	Available March 1985	Additional 1986-87	Comments
(1) Temperature			
(a) Orange cryostats	4	-	
(b) Sorption cryostat	-	1	
(c) Cryofridge cryostats (CCRs)	4	3	including LAD
(d) Dilution refrigerator	-	1	
(e) Ambient	1	2	LOQ initially
(f) Furnaces	-	3	
(2) Sample Changers			
(a) Sample changer for LOQ	1	-	LOQ
(b) Sample changer for LAD	1	-	LAD
(c) Other instruments	-	3	
(3) Pressure			
(a) 2 kbar Unit	1	1	
(b) 5 kbar Unit	1	-	
(c) Static loaded cell (McWhan) max 30 kbar	1	1	
(4) Magnetic Field			
Full requirement not yet defined	-	1	
(5) Control			
(a) Microprocessors (Falcon Units)	2	4	
(b) Temperature controllers	1	7	

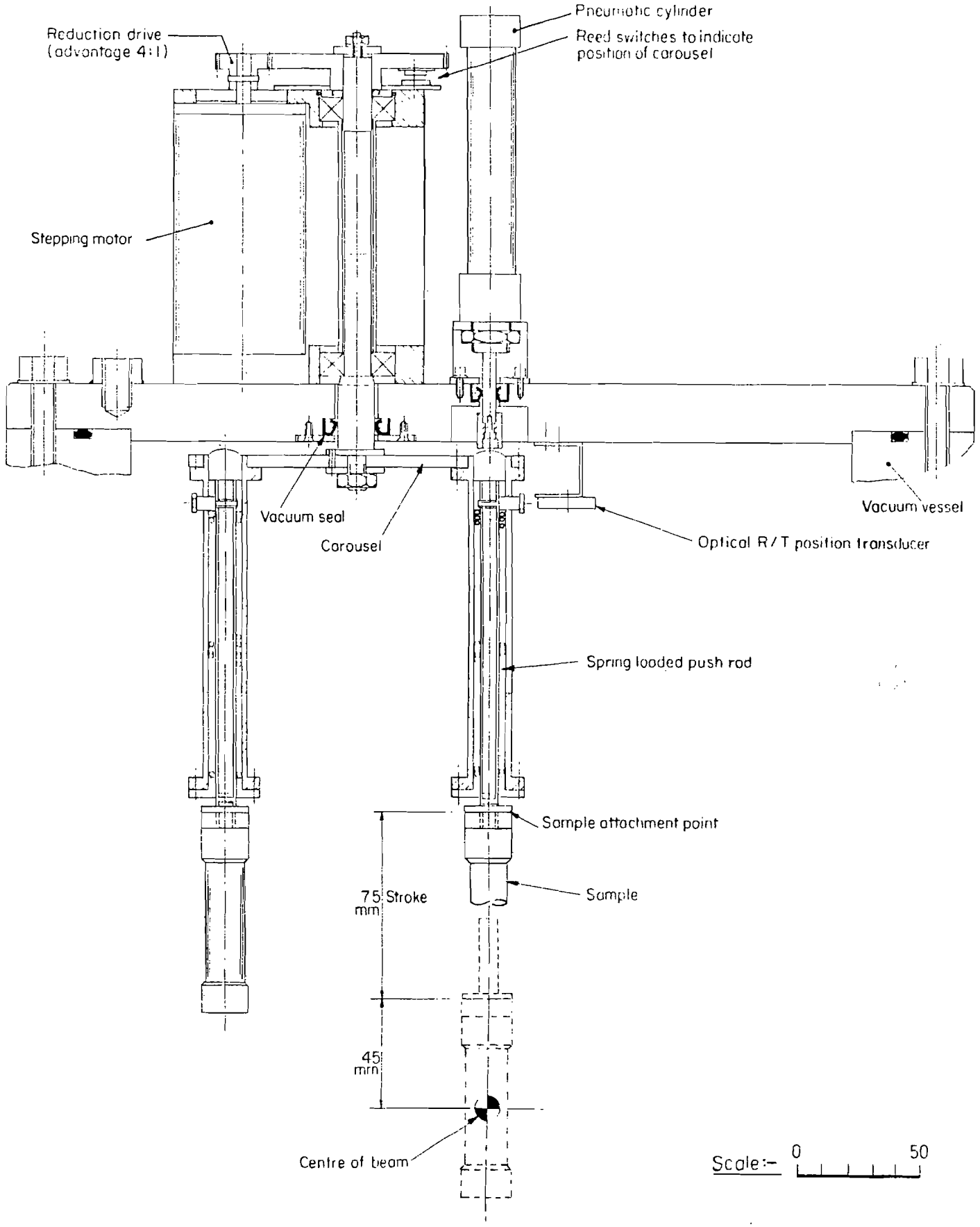

Fig 1. Sample Changer.

Proceedings of the Eighth Meeting of the International Collaboration on Advanced Neutron Sources (ICANS-VIII)
8-12 July 1985, Rutherford Appleton Laboratory Report RAL-85-110

Sample-related Peripheral Equipment at IPNS*

D. E. Bohringer and R. K. Crawford
Argonne National Laboratory
Argonne, Illinois 60439 U.S.A.

Introduction

This paper will briefly describe sample environment equipment provided by IPNS to visiting users and staff scientists. Of the twelve horizontal neutron beam stations, (ten now operational, two under construction) all use one or more form of such support equipment. An in-house support group devotes a significant fraction of its time to development, calibration, and maintenance of this equipment.

Vacuum Systems

Because of our many visiting neutron scientists and limited instructional time, simplicity is a key word. With sample change frequencies recorded in hours, easy vacuum control becomes a must. Our users have available a vacuum control station we like to refer to as user friendly. Operation of this control chassis is a simple two-step function of automatic-manual switch placement, plus a push button start. The control system will then rough pump the sample area, followed by a predescribed sequence to final vacuum of 10^{-6} to 10^{-7} torr. The control chassis can operate turbomolecular, diffusion or cryo pumps within the pump down routine. We now have five of these systems in operation.

Standardized Flanges

Maximum effective usage of peripheral equipment means interfacing IPNS instruments to ancillary devices. This has been accomplished via standardized flanges. With little or no adjustments, most IPNS instruments can cross use peripheral equipment, adding to user flexibility.

Furnaces

Listed in Table 1 are the furnaces we now use, plus a brief description. Due to the number of high temperature experiments submitted at IPNS, these units have had much use. Our first high temperature furnace built at IPNS was the "Wehrle Design". Since its preliminary test runs, many modifications in heater element material, thermo shield standoffs, and heater element geometry, have taken place. With the addition of 2 vanadium heat shields, our heater ribbon life increased from 50 x 10^3 C°-HR to over 100 x 10^3 C°-HR. Replacing the 2.36 mm x .05 mm tantalum ribbon with .5 mm tantalum wire further increases heater life to 180 x 10^3 C°-HR. (The temperature used to determine C°-HR was 1000°C x actual operating hours.) Considering this furnace's fragile design, the increase in running time was indeed progress. The above changes have made the "Wehrle" furnace an early workhorse for our high temperature users.

Since that time we have added two other custom built +1000°C furnaces, the "Miller" furnace and the "Howe" furnace. These new designs have provided us with giant steps forward in furnace performance and reliability. Testing is still being performed on updating the "Miller" furnace temperature vs. power requirements. To date, this unit has operated well over 200 x 10^3 C°-HR (operating temp. = 1200°C)[1]. Fig. 1 illustrates the progress of lower power -

*Work supported by the U.S. Department of Energy

higher temperature due to these modifications. One advantage this unit has over our other furnaces is the sample area is independent of the furnace element environment. Fig. 2 provides design characteristics.

The "Howe" furnace (Fig. 3) is the newest addition to our family of high temperature devices. Designed with a .05 mm vanadium foil heater element, the radiating surface area is ~ 200 cm^2. To insure low power requirements, dual .1 mm thick vanadium heat shields surround the heating element. This above combination has proven very sturdy, providing over 270 x 10^3 C°-HR of operation before a failure due to poor vacuum conditions. Another important feature of this unit is that the construction provides access to all scattering angles with minimum coherent scattering interaction in the vanadium.

Fig. 4 shows the custom furnace used at the Single Crystal Diffractometer (SCD). The temperature range of this device is from 200 - 800°C using a small platinum foil heater element. Due to its size, the power requirement at 800°C is ~ 30 amps at 10V. Sample size is approximately 10 mm^3 with scattering at 90° to the incident beam. The usable diffracted beam, as shown, covers approximately 60°.

Additional information of heater element life vs. temperature plus thermocouple longevity is of primary importance in establishing timely maintenance. Using the March 1984 to April 1985 running period as a ruler, our total down time due to furnace failures was 66 hours. The total furnace experimental hours were 1098 on two instruments giving our furnace experiments a +99% operating efficiency.[2] Closer evaluation of problem areas, plus better understanding of physical limitations of each piece of furnace equipment will improve our working knowledge while climbing the all important high temperature ladder.

Furnace Controllers

The variety of controllers available is large, but after some qualifications are made, the field of choice is narrowed somewhat. A decision to standardize our peripheral needs lowered the number of candidates. Our final selection, Micricon model 82300[3], best fit the projected needs regarding flexibility, reliability, accuracy and the ability to computer interface as discussed in the Automated Control of Peripheral Devices section.

The controller operating specifications using type K (chromel-alumel) thermocouple are 0-1370°C at 1°C selectability (tests have shown .2°C control accuracy).[4] Dual inputs, connected in a cascade configuration can further increase control accuracy, or these inputs can be arranged in the normal control feedback plus sample readout logic. In addition to the usual gain, rate, and reset capabilities, the options of preselected or adjustable heating ramps and multi level temperature plateaus are also available.

By changing preprogrammed input/output boards, additional choices of control and readout thermocouples can be operating. Our latest high temperature test has been with type S (platinum-platinum 10% rhodium), with an upper range of 1760°C. These tests are being conducted on our "Miller" (FM-1000C-V) furnace, for control and thermocouple longevity.

Displex Expander Module and Controllers

Displex closed-cycle He refrigerators are the workhorses for most low temperature experiments. With a proper maintenance schedule, our displex heads, Air Products Model DE-202K, and compressor units have had less than 1% down time.

Air Products Model K Series 5500[5] controllers with optional RS-232 communications are used for computer interfacing. These controllers now numbering 5, along with these displex units, have an operating range of 7 to 300 K. Using gold-chromel thermocouples, the experiment has two choices of control and readout location. These controllers are interfaced to the data acquisition computers as referenced in the Automated Control of Peripheral Devices section.

Cryostat and Controller

Our Thor variable temperature helium cryostat was designed to operate at temperatures as low as 2 K. To date, we have successfully operated at 2 K with more fine tuning needed. The cryostat can be operated on both powder instruments with minimum hardware setup. At the business end of the cryostat is a copper sample holder, extending from a cold plate. This holder can accommodate a sample size of x = 3.25 cm by y = 5.18 cm.

Silicon diodes, plus readout thermometry, regulate power needed to maintain temperatures above 2 K using T.R.I. Research T2000 controller.[6] This system has two level operational specifications of ± .01 K from 1.5 to 25 K, coupled with ± .1 K from 25 to 380 K coupled with internal heating control that operates at 0 to 25 volt with 0 to 2 amperes output.

Sample Changers

Until recently, we have had only one automatic multi-sample changer. This unit has performed well over the last 3 years at the Small Angle Diffractometer (SAD). The changer shown in Fig. 5 has two vertical rows of 6 sample positions in each. Two stepping motors are driven by a CAMAC XY motor controller with position accuracy ± .3 mm.

Our newest sample changer in Fig. 6 can hold 10 samples. This unit known as the Geneva Drive Sample Changer can be used in either the General Purpose Powder Diffractometer (GPPD) or Special Environment Powder Diffractometer (SEPD) and operates in a vacuum environment. With the addition of local cadmium skirts around each sample, plus collimation of the scattered beam by two large 9.5 mm thick boral discs, a quiet background is established. Due to the drive motor being located in a vacuum environment, the geneva drive system was chosen to position the samples. Final position repeatability is ~ .5 mm.

Camac control modual #3063[7] located in the PDP11/34 operates the drive system, along with an additional local-remote chassis with position readout residing at the instrument.

Sample Orienter

This single-axis orienter allows orientation of a sample in vacuum, and can be used on the High Resolution Medium Energy Chopper Spectrometer (HRMECS), Low Resolution Medium Energy Chopper Spectrometer (LRMECS), GPPD and SEPD. The sample is positioned on a feed thru shaft, adjustable in y position to beam center and can be rotated 360° in .01° increments. Operating a displex with the orientor is now an option that adds to this system's flexibility.

High Pressure Gas Cell

The SEPD has just completed its first experiment using a new high pressure gas cell.[8] The cell shown in Fig. 7 provides high count rates, low background, plus a large sample volume (5 cm^3). When attached to a displex or cryostat, the operating temperature range is from ambient to ~ 15 K. The latest operating parameters showed the pressure cell at 4 K bars with excellent neutron scattering results.

Another high pressure cell used on the SEPD is shown in Fig. 8. This room temperature piston-cylinder cell is well collimated at 90°. The sample volume of 0.25 cm^3 has a pressure range of 0 - 35 kbar, with a hydrostatic sample environment. This unit can also be used on the GPPD. A third pressure cell, now being developed, is listed in Table 2.

Chart Recorder/Data Logger

This system is called multipoint recorder/logger.[9] It is an 8 input channel (expandable to 48) multiple-microprocessor based, user settable data acquisition instrument with RS-232 option. In Fig. 9, the MRL uses a high

performance, low-power, 16 bit, CMOS microprocessor as the central hub. Also, two additional 8 bit microprocessor and additional high level integrated circuits control various peripheral functions internally.

Data reporting formats include chart recording, with paper speed from 1 through 12,000 mm-per-hour. The paper speed stepper motor drive advances paper at equivalent speed with printing trend line information. Each channel is easily identifiable. Another format is a peak-valley report. This report is generated at a user-selected interval to document in hard-copy the precise high and low values that have occurred for each selected channel and the times at which they occurred. An important feature is the ability to select a "both" mode. This provides both a selectable periodic data printout, with interconnected time selected chart recordings. Alarm function can be established on both data logger and recorder formats, with internal and/or external alarm capabilities. The model we selected is portable and is easily programmable.

Watchdog Timer

Fig. 10 shows the location of the Watchdog Timer WDT-1000[10] in data flow lines. Its function is to provide monitoring of real time environments at the front end of our data acquisition system. By adding commands that will direct control and select alarms of a furnace, displex, cryostat, etc., the Watchdog Timer will notify the main control room personnel if any of these commands are violated or if the data system crashes.

A simple software command energizes this system and might provide the cherished midnight call in. This devious device is available to all our instrument scientists.

Automated Control of Peripheral Devices

With a wide variety of ancillary devices now available, and more in the development stage, it was important to provide a unified framework for interfacing these devices to the data acquisition computers. The devices range from the sophisticated, such as the Micricon temperature controllers, with a high degree of local programmable intelligence and a consequently large number of settable parameters, all the way down to a "dumb" on-off device such as a Watchdog Timer which has no settable parameters. Since IPNS is a user facility, any such device control software has to be easy to use (and relatively foolproof) for the casual user. However the same software should allow the knowledgeable user (e.g., - instrument scientist) access to all the parameters and the full range of capabilities of the various devices. Furthermore, the software framework should allow for unlimited expansion to an even wider variety of future devices.

To simplify and standardize the required interfacing hardware and software, it was decided to limit controlled devices to two types of hardware interfacing, either RS-232 communications (so the device looks like a terminal to the computer) or communication via CAMAC modules of various sorts. Devices so far interfaced, or for which interfacing is in progress or currently contemplated are shown in Table 3.

In interfacing a device, all the device parameters which are to be accessible from the data acquisition computer are defined and entered into a master "device table" which is stored in each instrument computer and contains all such parameters for all interfaced devices. In order to maintain the ease of use for the casual user, these parameters are divided into two types, "user parameters" and "non-user parameters". User parameters are those which will typically be changed from run to run (e.g., - set point temperature and limits for a temperature controller, sample position for a sample changer, etc.). These are the only parameters with which the casual user interacts. The non-user parameters (e.g. - proportional, integral, and derivative settings for a temperature controller) may influence the operation of the device in ways transparent to the user, and may be changed as desired by specific commands.

In addition to this master device table, a second table, different for each instrument, contains the current device configuration for that instrument. This

includes the names of the devices available on that instrument, a device-number reference to the master device table for each of these available devices, the slot in the control CAMAC crate or the RS-232 terminal line being used to communicate with the device, and a parameter indicating whether the device is to be set up at the beginning of the run and then ignored during the run (as for a sample changer or a stepping motor) or is to be monitored during the run as well (as for a temperature controller, analog-to-digital converter, etc.). When setting up a run, the user selects which, if any, devices from this table are to be controlled for this run. Any number can be selected.

Devices being monitored during a run will cause suspension of data acquisition whenever they are outside the user-specified limits for that run. Data acquisition will automatically resume whenever all monitored parameters are back within their limits. If the Watchdog Timer has been selected as one of the controlled devices for this run, it will time-out and set an alarm alerting operators in the accelerator Main Control Room whenever a monitored device is outside its limits for more than four minutes. (See Fig. 10 for a typical application.)

Operating Experiences

Fig. 11 provides a percentage breakdown of equipment operating time on the GPPD. As can be seen, experiments involving altered sample environments dominate. Although GPPD is on the high side of the peripheral equipment usage scale, the trend extends to other instruments. Due to the increase, timely maintenance is all important. To provide a manageable system, a "maintenance data base" program was developed to fit our needs.[11] This program allows the operator to add, delete, modify, or update data records requiring periodic attention. These records range from annual qualification tests to weekly ordering of helium gas. This program also gives us a hard copy of completed tasks in chronological order, making maintenance and record keeping a breeze. These records (now over 500) also provide documented evidence of required procedures in the operation of IPNS.

Conclusion

In the last year of operation, 10 experimental beam lines comprised a total of 29,000 operating hours. Of this total, well over half involved the use of peripheral equipment. Our total lost time due to peripheral equipment failure was less than 1%. This is a strong reflection of the quality of this equipment and of experimental support personnel at IPNS.

Acknowledgements

The following individuals provided us with our high temperature furnaces; R. Wehrle, ANL; Harold Miller, E.G.G.; Alan Howe and Nigel Wood, Leicester University, England. For designing all other peripheral equipment, we thank R. Kleb and R. Stefiuk, ANL. Without the able support group, our operating record would be non-existing. Denis Wozniak has provided all important guidance in upgrading our ever growing furnace systems, and has shouldered the burden of troubleshooting the Thor cryostat. Assisting Denis and myself are John Urban, whose experience is tantamount to efficient operation. David Leach guided us thru the early experiments with the Wehrle furnace. Al Paugys's background is refrigeration and cryogenics. In the electronics spectrum, necessary individuals would be Joe Haumann, Donald Emery, Merlyn Faber, and Wally Czyz. Special thanks to Thomas Worlton and Mariangela Sanelli for their infinite patience in providing the programs and data base needed to establish operating trends and maintenance schedules.

References

[1] J. Faber, R. Hitterman (Miller Furnace, to be published).

[2] M. Sanelli and D. Bohringer (IPNS Operating Data, 1985).

[3] Research Inc., Box 24064, Minneapolis, Minnesota, 55424, U.S.A.

[4] F. Mezei and R. Ghosh (ILL), G. H. Lander (ANL) Small Angle Scattering From Fe in the Critical Regime (1983).

[5] Air Products and Chemicals Inc., Allentown, Pennsylvania, U.S.A.

[6] T.R.I. Research (St. Paul, Minnesota, 55114, U.S.A.).

[7] Kinetic Systems Corp. (Lockport, Illinois, 60441, U.S.A.).

[8] R. Kleb, D. L. Decker and J. D. Jorgensen, (High Pressure Gas Cell, to be published).

[9] Esterline Angus Instrument Corp. (Box 24000, Indianapolis, Indiana, U.S.A.)

[10] Standard Eng. Corp. (44880 Industrial Dr., Fremont, California, 94538, U.S.A.).

[11] T. Worlton (Operating Files IPNS Manual).

Type	Instruments	Temperature Range	Control Precision	Sample Volume	Computer Interface	Comments
"Miller"	GPPD, SEPD	~200-1400°C	0.2-2°C	~6 cm^3	Yes	90°±5° scattering only. Sample can be in controlled gas environment or in vacuum. Furnace is well collimated out of scattered beam.
"Wehrle"	GPPD, SEPD	~200-1000°C	0.2-2°C	~6 cm^3	Yes	Range of accessible scattering angles. Limited amount of heater and shield in beam.
"Howe"	GPPD, HRMECS, LRMECS, SEPD, EVS	~200-1000°C	0.2-2°C	~6 cm^3	Yes	All scattering angles accessible. Heater and shields are vanadium so very little coherent scattering from furnace.
SAD Tube	SAD	~200-1000°C	0.2-2°C	~2.3 cm diameter	Yes	No furnace parts are in the incident or scattered beam.
ILL	SAD and possibly others	~200-900°C	0.2-1°C	~6 cm^3	Yes	All scattering angles are accessible. Furnace parts are difficult to collimate out of scattered beam.
SCD	SCD	~200-800°C	~5°C	~10 mm^3	No	90°±30° scattering.
"300 K"	GPPD, SEPD, HRMECS	~30-300°C	0.2-1°C	~6 cm^3	Yes	All scattering angles accessible.

TABLE 1: Description of IPNS Furnaces

HIGH PRESSURE CELLS

Type	Instruments	Pressure Range	Sample Volume	Comments
Room Temperature Piston-Cylinder	GPPD, SEPD	0-35Kbar	0.25 cm^3	90°±2.5° scattering. Cell is well collimated out of scattered beam at 90°. Hydrostatic sample environment.
Low-Temperature Low-Pressure Gas Cells (1 cell now, 1 more in future)	GPPD, SEPD	0-5Kbar at present 0-8Kbar future	2 cm^3	90°±5° scattering. Cell is aluminum and is partially collimated out of beam. Can be mounted on displex or cryostat. Hydrostatic sample environment.
Low-Temperature Clamped Piston-Cylinder Cell	GPPD, SEPD	0-25Kbar	1 cm^3	90°±2.5° scattering. Can be mounted on displex or cryostat. Hydrostatic sample environment. (Quasi-hydrostatic at low T.)

Table 2 : High Pressure Cells

Table 3: Device Interfacing

Device	Interface	#	Module or Controller
*Furnace	RS-232	3	Micricon 82300 controller
*Displex	RS-232	5	Air Products Instruments 5500 controller
*Watchdog Timer	CAMAC	10	Standard Engineering WDT-1000 Watchdog Timer module
*SEPD/GPPD sample changer	CAMAC	2	Kinetic Systems 3063 16-bit input gate/output register module
*SAD sample changer	CAMAC	1	BiRa 3101A 15-channel stepping motor driver module
		1	Kinetic Systems 3473 24-bit change-of-state module
*Sample orienter	CAMAC	1	BiRa 3101A 15-channel stepping motor driver module
°SCD goniometer motors	CAMAC	1	BiRa 3101A 15-channel stepping motor driver module
°QENS table drive	CAMAC		BiRa 3101A 15-channel stepping motor driver module
°Proton current monitor	CAMAC	1	Kinetic Systems 3610 6-channel 50 MHz scaler module
°Digital to analog	CAMAC	1	Kinetic Systems 3112 8-channel 12-bit D/A module
Analog to digital	CAMAC	1	Standard Engineering AD-112 2-channel 12-bit A/D module
Multichannel analyzer	RS-232	1	Nuclear Data ND-100 Analyzer
		1	Nuclear Data ND-60 Analyzer
Thor cryostat	RS-232	1	TRI T-2000 Controller
Chart recorder/data logger	RS-232		Esterline Angus Multipoint Recorder/Logger
Chopper drive system	RS-232	2	System developed in-house

*Interfacing completed

°Interfacing in progress

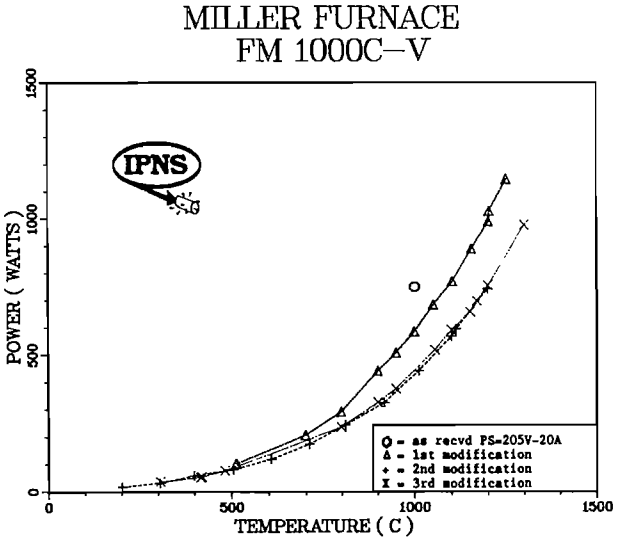

Fig. 1 - Modifications Improving Temperature vs. Power

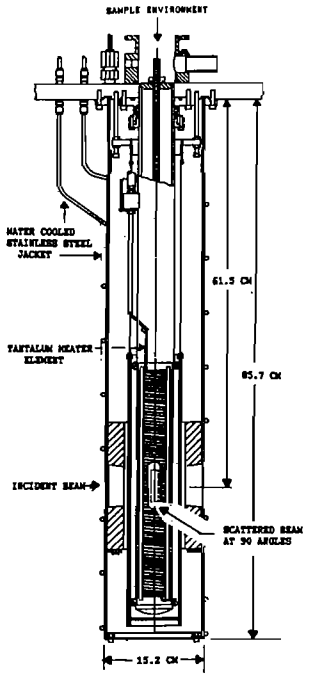

Fig. 2 - Miller Furnace

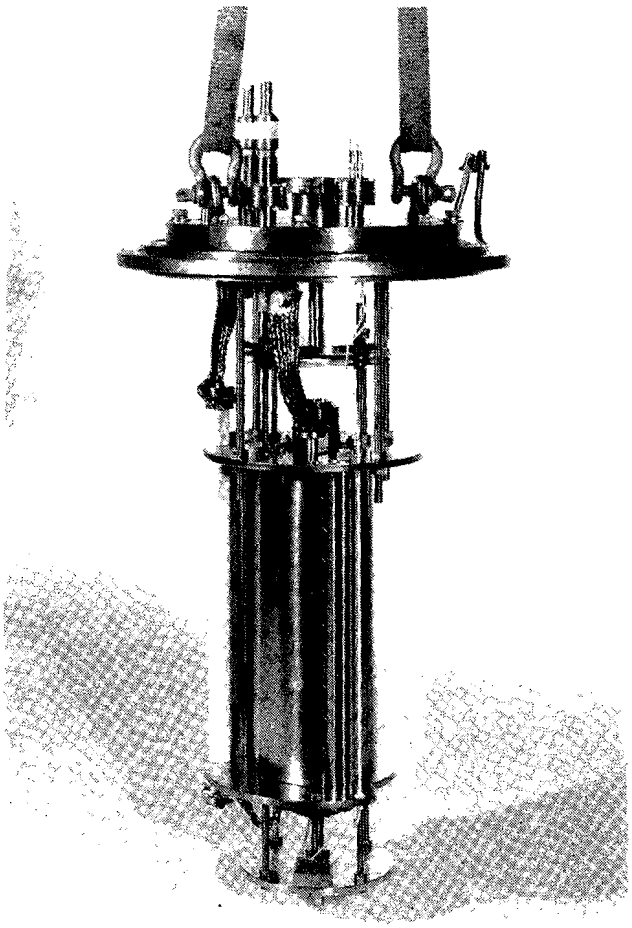

Fig. 3 - Howe Furnace

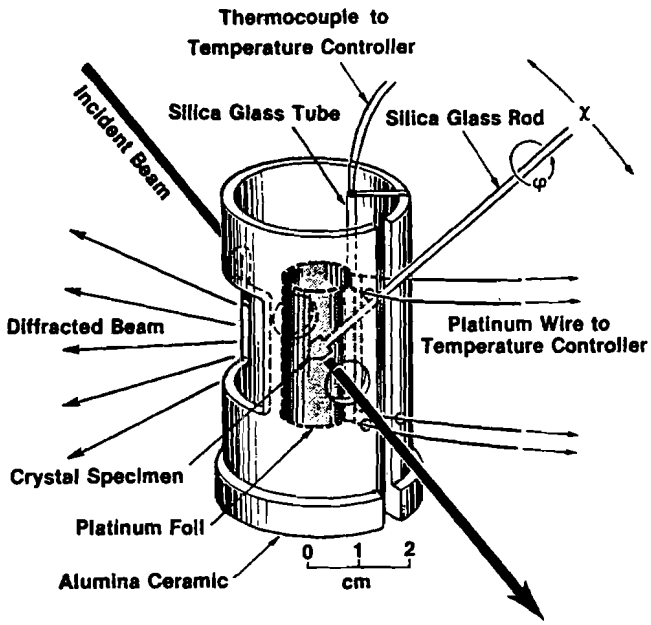

Fig. 4 - Single Crystal Diffractometer Furnace

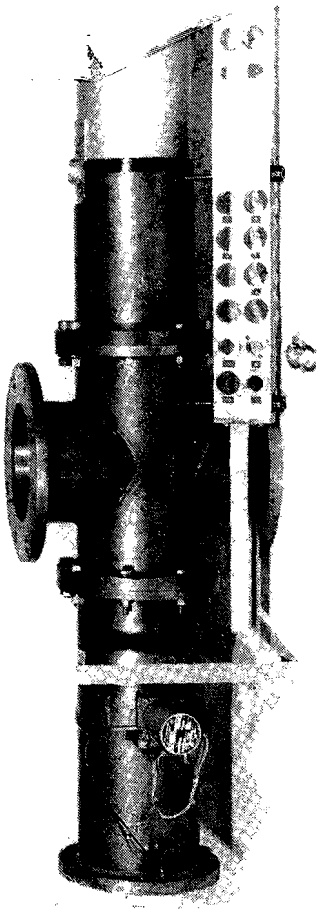

Fig. 5 - Vertical Cassette Sample Changer

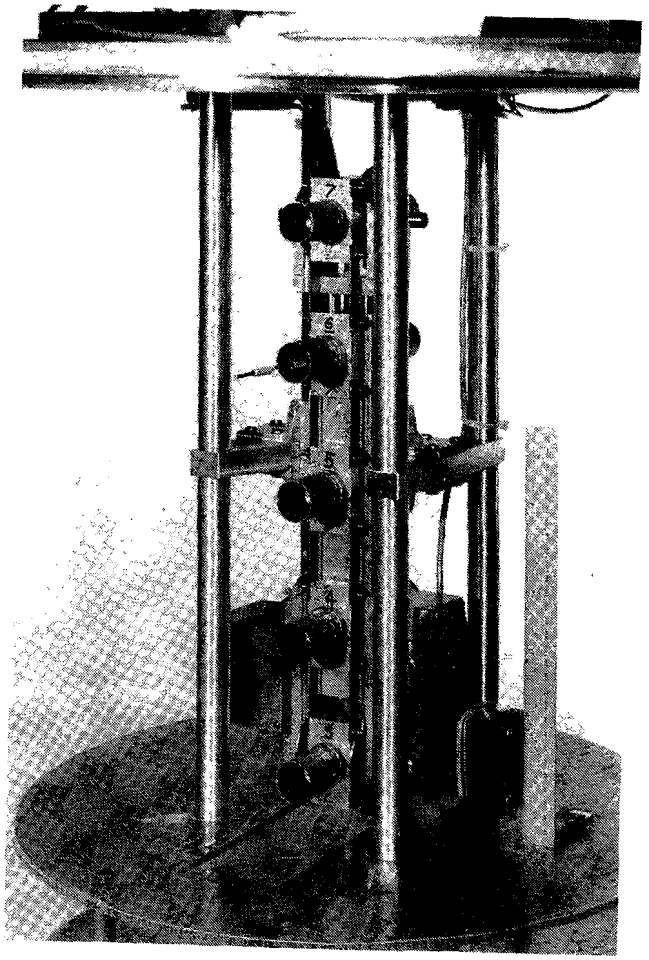

Fig. 6 - Geneva Drive Sample Changer

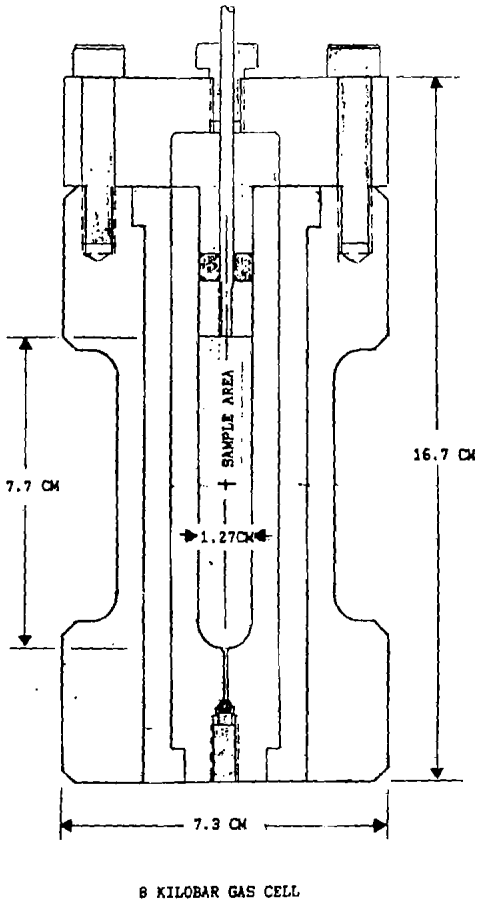

Fig. 7 - High Pressure Helium Gas Pressure Cell

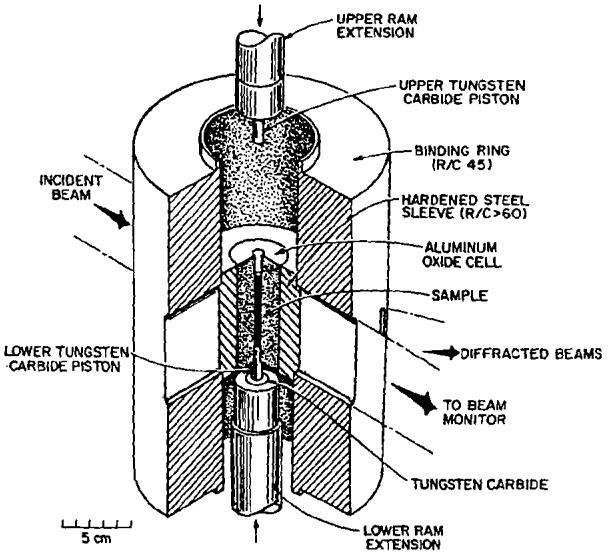

Fig. 8 - Room Temperature Piston-Cylinder

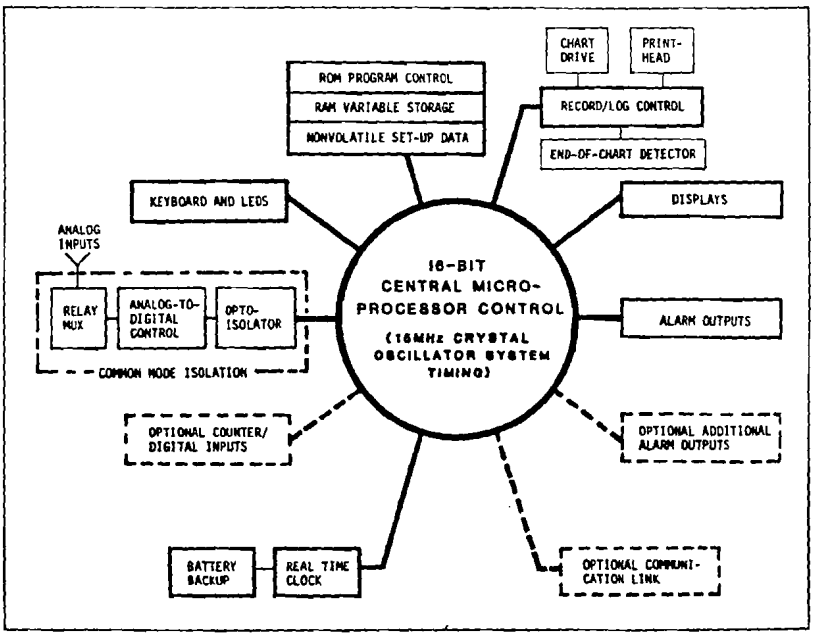

Fig. 9 - Chart Recorder/Data Logger

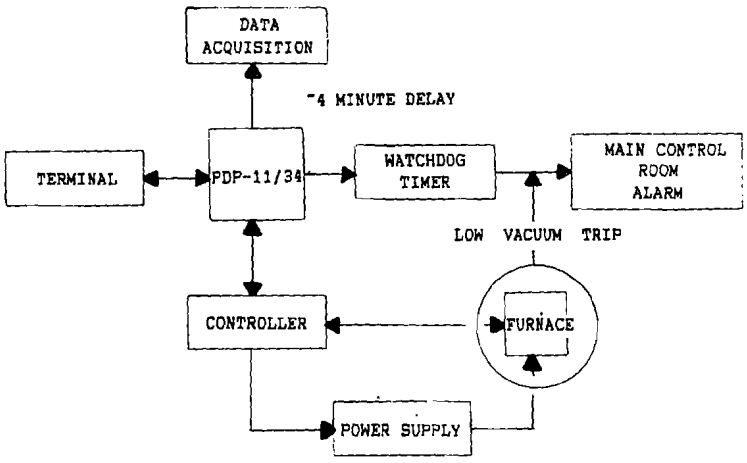

Fig. 10 - Furnace Controller Interface

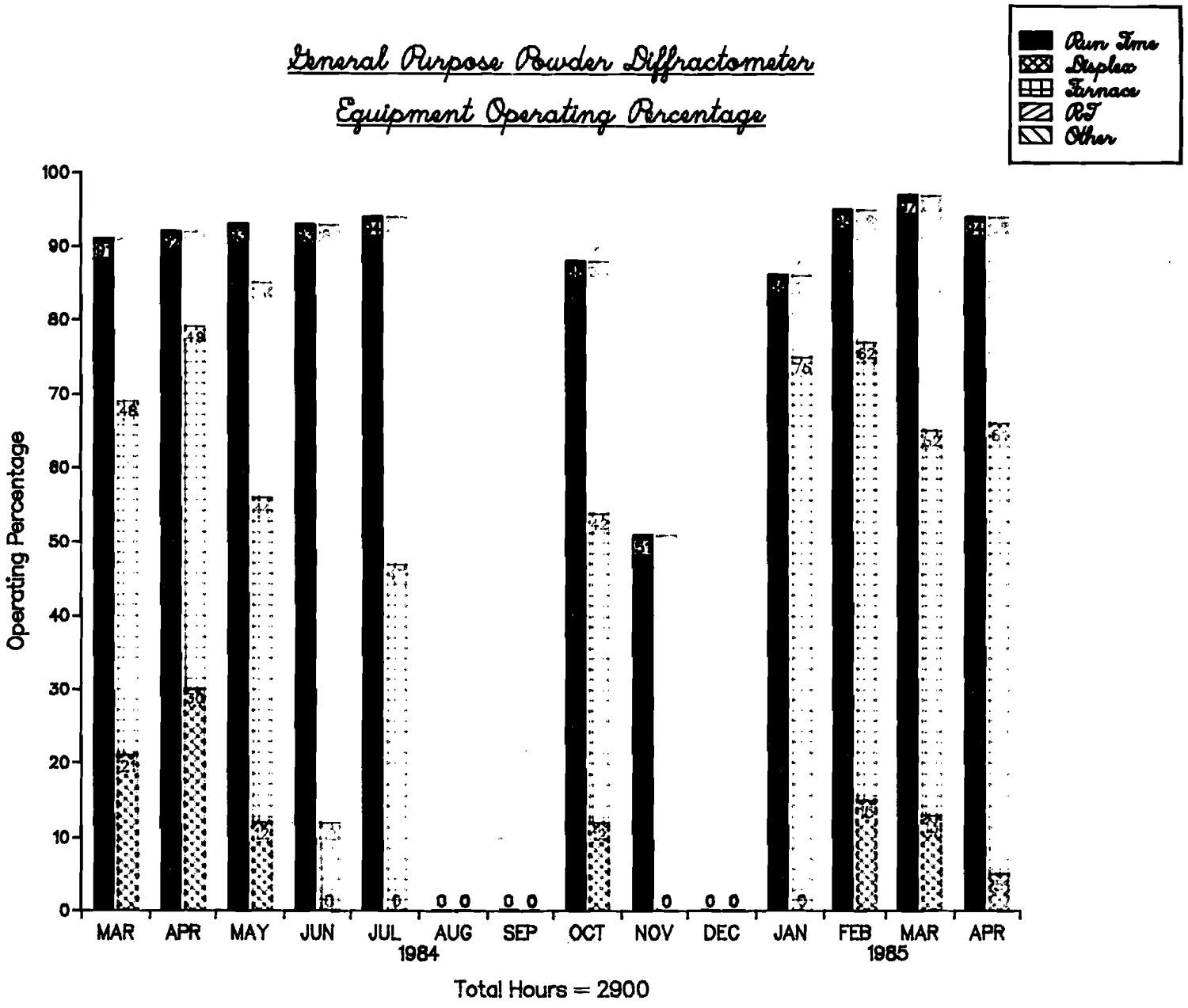

Fig. 11 - Stack Bar Graph of Peripheral Equipment (Displex, Furnace, Room Temperature, Other & Run Time) Usage as Compared with Monthly Operating Percentage

INDEX OF AUTHORS